Structure-based discovery of small molecule inhibitors of seeding activity in Alzheimer's disease biosamples using a fluorescence polarization-based amyloid-β aggregation assay

Inaugural-Dissertation
to obtain the academic degree
Doctor rerum naturalium (Dr. rer. nat.)

submitted to the Department of Biology, Chemistry and Pharmacy
of Freie Universität Berlin

by
Lisa Diez
from Schweinfurt

Berlin, June 2018

The work was conducted from June 2013 until June 2018 under supervision of Prof. Dr. Erich E. Wanker at the Max Delbrück Center for Molecular Medicine in the Helmholtz-Association.

I hereby confirm that I have written the thesis independently using solely the aids mentioned and without illicit assistance from third parties.

1. Reviewer: Prof. Dr. Erich E. Wanker
2. Reviewer: Prof. Dr. Stephan Sigrist

Thesis defense on 31.08.18

Content

1.

Summary

1

1. Summary

Alzheimer's disease (AD) is a progressive, neurodegenerative disorder that results in an irreversible impairment of cognitive functions due to a severe loss of neuronal cells. Characteristic hallmarks of AD are extracellular deposits of the amyloid-β peptide (Aβ) as plaques in affected patient brains and neurofibrillary tangles of tau protein within the cells. The number of affected patients is estimated to reach ~130 million in 2050 worldwide, making AD a major healthcare burden and one of the biggest challenges of the 21st century. However, even after decades of intensive research, the underlying molecular processes of this complex neurodegenerative disease have not been entirely elucidated and despite numerous drug trial studies, no causative treatment is available up to now. Especially the aggregation of soluble Aβ peptides into stable, β-sheet-rich amyloid fibrils that in the end deposit as plaques in AD patient brains is a presumed culprit of Alzheimer's. Several lines of experimental evidence indicate that so called 'seeds' of the Aβ peptide – small aggregate assemblies that can initiate an avalanche of Aβ aggregation – play a critical role in AD pathogenesis and contribute to the spreading of proteinaceous aggregates throughout the whole brain. Thus, a highly specific and sensitive *in vitro* method that facilitates the detection of Aβ seeds is crucial to understand the molecular principles of AD and potentially even to monitor disease progression.

Here, the establishment of a cell-free aggregation assay for the 42-amino acid long amyloid-β (Aβ42) polypeptide is presented named ^{FAM}Aβ42/Aβ42 co-polymerization assay or short Aβ42-FP assay as the readout is based on the principle of fluorescence polarization (FP). Briefly, the assay detects the co-assembly of a fluorophore-labeled monomeric tracer (^{FAM}Aβ42) with unlabeled peptide over time. As the relative molecular mass of the formed assemblies increases in the course of aggregation, the tracer mobility is reduced which results in a time-dependent increase of its FP signal. As a result, the assay enables to monitor the aggregation process of the Aβ peptide in a time-resolved manner and further facilitates the detection of seeding-competent Aβ species in complex biosamples. I also established a procedure for the enrichment of Aβ aggregate species from biological samples via immunoprecipitations and the subsequent amplification of seeds in Aβ42-FP assays. With this method, Aβ seeds in mouse brain homogenates of three different transgenic models and in human biosamples are detected. Furthermore, a direct correlation between Aβ seeding activity and metabolic impairment in cell models could be shown, substantiating the importance of nucleated Aβ aggregation in AD.

Importantly, the ^{FAM}Aβ42/Aβ42 co-polymerization assay can additionally be applied to screen for small molecules that interfere with the self-assembly of Aβ42 peptides. Furthermore, the assay allows not only high-throughput screening of whole compound libraries for potential Aβ42 aggregation modulators, but also facilitates the elucidation of structure-activity relationships. Until now medicinal

chemistry optimization of compounds in terms of their structural features critical for improved potency and pharmaceutical viability remained a challenge with state-of-the-art dye-binding aggregation assays. In this regard, the established FP-based assay represents an improvement as it allows the detection of compound effects without high concentration of binding dyes that might compete with the tested compounds in the Aβ42 reactions.

Systematic structure-activity investigations with derivatives of the known amyloid binder K114 allowed me to determine distinct substructural elements that empower a small molecule to delay the Aβ42 aggregation process, exemplarily shown with the hit compound LT1. LT1 potently reduces both spontaneous and seed-mediated Aβ42 aggregation at substoichiometric concentrations. Mechanistic studies demonstrate that LT1 targets small, on-pathway, seeding-competent Aβ42 assemblies and delays their extension into larger fibrillar structures. The intrinsic fluorescence of compound LT1 is further exploited to monitor Aβ42 fibril assembly. Finally, I could show that treatment with LT1 efficiently decreases seed-mediated nucleation of Aβ-fibrils prepared from brains of AD transgenic mice, indicating that it targets and influences the activity of disease-relevant Aβ aggregate species.

The established Aβ42-FP technology is a fast, efficient and powerful tool with many potential applications in the drug discovery field as well as in basic and applied research.

2.

Zusammenfassung

2. Zusammenfassung

Die Alzheimer Krankheit ist eine irreversible neurodegenerative Erkrankung, bei der Betroffene aufgrund eines fortschreitenden Absterbens von Nervenzellen im Gehirn unter einer sukzessiven Abnahme ihrer kognitiven Leistungsfähigkeit leiden. Charakteristische Merkmale der Erkrankung sind extrazelluläre Ablagerungen des Amyloid-β (Aβ) Peptids als Plaques im Gehirn und intrazelluläre Neurofibrillenbündel, die aus dem Mikrotubuli-assoziierten Protein Tau bestehen. Es wird angenommen, dass die Zahl der Betroffenen bis 2050 auf ca. 130 Millionen ansteigen wird, was Alzheimer zu einer immensen Belastung für das Gesundheitssystem und einer der großen Herausforderungen des 21. Jahrhunderts macht. Doch trotz jahrzehntelanger intensiver Forschung gibt es bisher noch keine wirksame Behandlung und auch der zugrunde liegende molekulare Prozess konnte noch nicht vollständig aufgeklärt werden.

Besonders die Aggregation von löslichen Aβ Peptiden zu stabilen Amyloid-Fibrillen, die sich als Plaques im Gehirn von Alzheimer Patienten ablagern, scheint maßgeblich zur Erkrankung beizutragen. Verschiedene Studien deuten mittlerweile darauf hin, dass sogenannte „seeds“ des Aβ Peptids, kleine Aggregatspezies, die die Kaskade von Aggregation und Ablagerung anstoßen können, eine entscheidende Rolle bei der Krankheitsentstehung und der Ausbreitung von Aggregaten im Gehirn spielen. Daher sind spezifische und sensitive *in vitro* Methoden essentiell, mit denen Aβ „seeds“ detektiert werden können. Nur wenn das gelingt, können die zugrundliegenden molekularen Prozesse überhaupt erst richtig verstanden und der Krankheitsverlauf auf molekularer Ebene verfolgt werden. In dieser Arbeit wird die Etablierung eines auf Fluoreszenzpolarisation (FP)-basierten Assays gezeigt, mit dem die Aggregation des Aβ42 Peptids zeitaufgelöst verfolgt werden kann, der Aβ42-FP Assay. Dabei fungiert ein fluorophor-markiertes Aβ42 Monomer als Tracer (^{FAM}Aβ42), der im Verlauf der Aggregation mit unmarkierten Peptiden co-aggregiert, weswegen auch die Bezeichnung ^{FAM}Aβ42/Aβ42 Co-Polymerisation Assay verwendet wird. Kurz zusammengefasst bewirkt die während der Aggregation auftretende Erhöhung der Molekülmasse eine Verringerung der Tracer Mobilität, die zu einer zeitaufgelösten Zunahme des Polarisationssignals führt. Neben der spontanen Aggregation von Aβ42 detektiert der Aβ42-FP Assay auch seeding-kompetente Strukturen in komplexen biologischen Proben, da die Aggregationsgeschwindigkeit aufgrund ihrer Anwesenheit beschleunigt ist. Dafür werden Aβ Aggregate zunächst mittels Immunopräzipitation isoliert und anschließend im Fluoreszenzpolarisations-Assay amplifiziert. Mit dieser Methode konnten seeding-kompetente Strukturen in Gehirnproben von drei verschiedenen transgenen Mausmodellen und in humanen Proben nachgewiesen werden. Weiterhin konnte eine direkte Korrelation zwischen Seeding-Aktivität und einer Beeinträchtigung des Zellstoffwechsels in einem Zellmodell gezeigt werden, was die Bedeutung der durch „seeds“ verstärkten Aggregation für den Krankheitsprozess unterstreicht.

Weiterhin von Bedeutung ist, dass der Aβ42-FP Assay auch für eine Anwendung im Bereich der Wirkstofffindung geeignet ist, da damit Moleküle identifiziert werden können, die in den Selbstassemblierungsprozess des Aβ42 Peptids eingreifen. So können mit dem Assay nicht nur ganze Wirkstoffbibliotheken im Hochdurchsatzverfahren nach potentiellen Aggregationsmodulatoren durchleuchtet, sondern auch deren Struktur-Wirkungs-Beziehungen aufgeklärt werden. Mit dem bisherigen Stand der Technik erwies sich die medizinisch-chemische Optimierung von Wirkstoffen hinsichtlich einzelner struktureller Komponenten für eine verbesserte Wirksam- und Verfügbarkeit als Herausforderung. Da man hierfür auf hohe Konzentration eines Reporterfarbstoffs angewiesen war und demnach kompetitive Bindungen zwischen Reportermolekülen und Wirkstoffen nicht ausgeschlossen werden konnten, stellt der neu etablierten Aβ42-FP Assay in dieser Hinsicht eine deutliche Verbesserung dar.

Systematische Struktur-Wirkungs-Analysen mit dem bekannten Amyloid-Farbstoff K114 und neu synthetisierten Derivaten ermöglichte es mir einzelne strukturelle Elemente zu identifizieren, die entscheidend dazu beitragen die Aβ42 Aggregation zu verlangsamen. Der Wirkstoff LT1 stellte sich hierbei als wirksamste Verbindung heraus. Der Substanz gelang es auch bei sub-stöchiometrischen Konzentrationen sowohl die spontane, als auch die durch „seeds“ beschleunigte Aggregation zu verzögern. In mechanistischen Analysen konnte weiterhin gezeigt werden, dass LT1, kleinere, „seeding“-kompetente Aggregate angreift und deren Elongation zu größeren Fibrillen verlangsamt. Die intrinsische Autofluoreszenz der Verbindung LT1 wurde ebenfalls genutzt, um damit die Aggregation von Aβ42 Peptiden zeitaufgelöst zu verfolgen. Abschließend wurde gezeigt, dass LT1 auch ich der Lage ist die Aβ42 Aggregation zu verlangsamen, wenn sie durch krankheitsrelevante „seeds“ stimuliert wurde, die aus transgenen Alzheimer Mausgehirnen isoliert wurden.

Der etablierte fluoreszenzbasierte Aβ42-Aggregationsassay stellt in jedem Fall eine neuartige und effiziente Methode dar, die aufgrund ihrer Leistungsfähigkeit für viele Anwendungen im Bereich der Wirkstofffindung und der molekularen Forschung geeignet ist.

3.

Introduction

3. Introduction

3.1 Alzheimer's disease

'A peculiar severe disease process of the cerebral cortex'[1,2], that is how Alois Alzheimer reported his findings at the *37th Meeting of South-West German Psychiatrists* in 1906 regarding the 50 year-old patient Auguste Deter who gained sad prominence as the first described case of Alzheimer's disease. Alzheimer's disease (AD) is a neurodegenerative disease, describing a group of disorders that emerge from abnormal protein interactions in the central nervous system (CNS) leading to death of neuronal cells[3]. Furthermore, AD belongs to the syndrome of dementia, an expression for a group of symptoms including a progressive decline in cognitive function and behavioral abilities[4,5]. AD is the most common form of dementia, accounting for an estimated 60-80 % of all cases. Besides AD, also vascular dementia, dementia with Lewy bodies (DLB), frontotemporal lobar degeneration (FTLD), Parkinson's disease (PD) and mixed dementia types can be found, only to name a few[6]. Up to date, around 48 million people worldwide suffer from dementia, the global prevalence of AD has been estimated to be ~30 million in 2015[6]. Due to a general demographic ageing worldwide, partly also as the success of improved health care, this number is expected to double or even triple until 2050, making AD a major healthcare burden[7]. Therefore, it is imperative to develop effective therapies to halt or delay disease onset or attenuate the course of disease. However, despite decades of intensive basic research and drug trial studies, only symptomatic relief in early disease stages, but no causative treatment is available up to now[8].

Symptoms

On a symptomatic level AD patients show a progressive loss of cognitive functions including memory loss and word finding difficulties, confusion with time and place, withdrawal from social activities and changes in mood and personality[6]. Thereby, the disease progresses typically slowly, starting from an early-stage mild AD to a moderate and finally severe phase. Besides these phases, 'mild cognitive impairment' (MCI) is seen as a separate diagnosis[5]. MCI patients show an impairment in cognitive functions that is above normal aging deterioration, but they are not affected in their daily lives. Furthermore, MCI patients can represent a preliminary stage of dementia, but do not necessarily develop disease. Patients in early stages start to experience memory gaps and find themselves misplacing objects or searching for the right word but they are still able to function independently. In contrast, affected people with moderate AD require a greater level of care. This middle phase is usually the longest phase lasting for years and is accompanied by personality changes, a struggle to recognize family members and the inability to learn new tasks. Finally, in the end-stage phase, patients are dependent on all-round care as even many normal physiological functions can no longer be

controlled[6]. AD is ultimately fatal, mostly due to Alzheimer's-related pneumonia as the patients become more vulnerable for infections when movements are impaired. Additionally, difficulties with swallowing lead to malnutrition and dehydration at last[6]. The clinical phase of AD comprises on average nine years, however, it represents only the final one-third of the whole disease process as first changes on a molecular level can be detected up to 20 years before the first symptoms arise[9].

Characteristic hallmarks of AD

The two characteristic hallmarks of AD are extracellular accumulations of the amyloid-β (Aβ) peptide known as amyloid plaques and fibrillar bundles of hyperphosphorylated tau protein within the cell, referred to as neurofibrillary tangles[10] (Fig. 1). These molecular changes assign AD to the disorder group of amyloidosis, characterized by depositions of normally soluble protein into insoluble, proteinaceous β-sheet-rich fibrils[11]. Although the etiology is still not yet clear, the pathology of AD is assumed to result firstly from extracellular Aβ peptide assemblies that mediate cell death by interfering with the interneuronal synaptic communication. Secondly, an impaired intraneuronal supply of nutrients due to a transport blocking caused by the tau protein is presumed to contribute to AD pathology[6]. As a consequence of these changes on a molecular level, the degeneration of neurons particularly in the basal forebrain and the limbic system including the hippocampus results in cortical atrophy and a general shrinking of brain tissue, accompanied by an enlargement of the lateral ventricles[12].

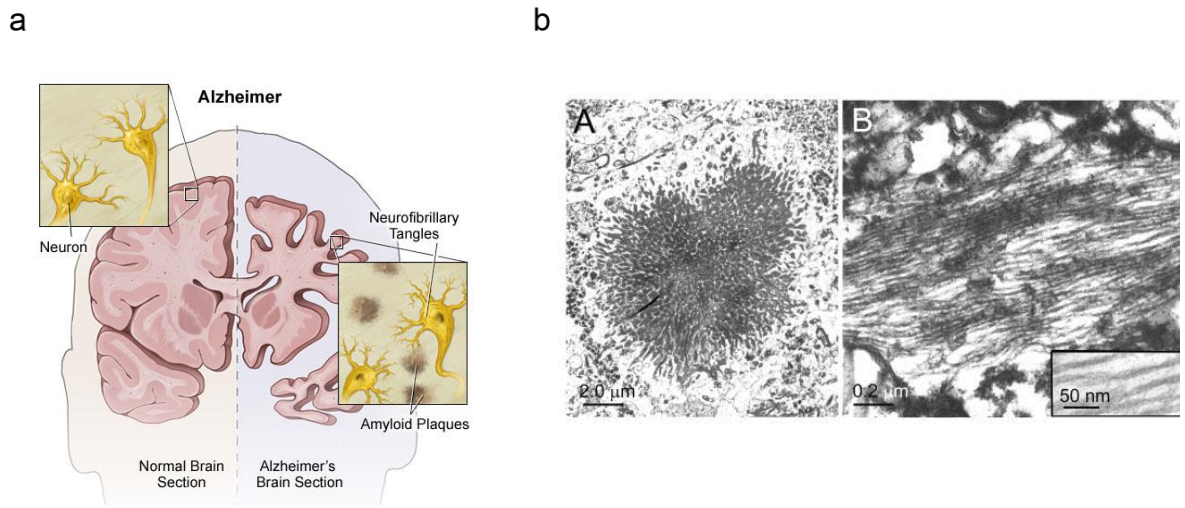

Figure 1 | Histological hallmarks of an Alzheimer's disease brain
(a) Schematic drawing of a brain section of an AD patient compared to a healthy control. AD-affected brains reveal extracellular amyloid plaques and intracellular tau tangles together with an overall atrophy of brain tissues due to neuronal cell death (Image from http://uhealthsystem.com/health-library/neuro/disorder/alzheim; 24.05.18). (b) Electron microscopical images of the pathological characteristics of a human AD brain. A) Extracellular Aβ amyloid plaque. B) Paired helical filaments of tau protein (Image from Bamburg & Bloom, 2009[10]).

Progression of AD throughout the brain

In 1991 Braak & Braak classified the AD pathology based on neuropathological changes they observed in AD patient brain autopsy samples[13]. Within this work location and density of amyloidogenic plaques were recorded leading to the first indication that Aβ plaques spread within affected patient brains following a characteristic pattern. Later studies confirmed the finding that AD-specific proteinaceous lesions and neuronal cell loss occurs gradually throughout different brain regions[14]. Figure 2 shows the three stages of AD pathology and the progression of Aβ plaque formation within the brain[15]. After initial appearance in the basal temporal and orbifrontal neocortex (mild AD), lesions appear throughout the neocortex, in the hippocampus, diencephalon and basal ganglia (moderate AD). Finally, in severe AD cases, lesions invade the brain stem and cerebellum (severe AD). Interestingly, the spreading of plaques and pathology throughout the brain seems to follow anterograde neuronal connections, meaning that synaptically connected areas develop lesions consecutively. This indicates a potential synaptic transmission of Aβ that leads to a spreading of AD pathology throughout the brain along specific neuronal networks[14].

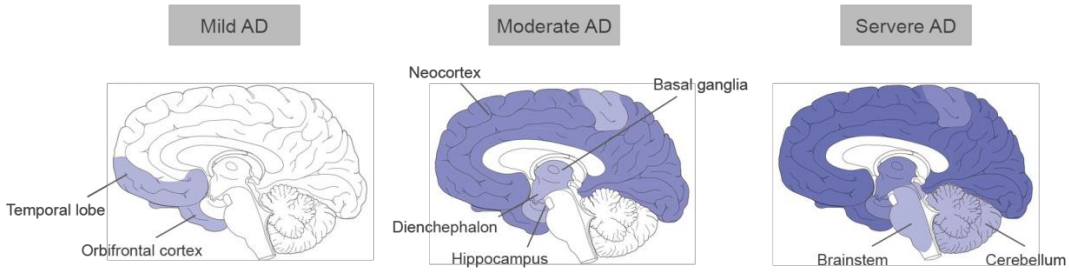

Figure 2 | Characteristic progression of specific proteinaceous lesions in AD
Aβ plaque pathology in AD patients spreads throughout the brain by following a characteristic pattern, starting from the basal temporal and orbifrontal cortex throughout the neocortex, followed by hippcampus, diencephalon and cerebellum until lesions invade the brainstem (Image adapted from Goedert, 2015[15]).

Familiar and sporadic AD

In general, two different forms of AD can be distinguished, an early-onset, hereditary familial type (FAD) and a late-onset sporadic form (SAD). FAD is characterized by an earlier onset of disease that is before the age of 65 years. It displays a faster disease progression and accounts for rare ~1 % of the AD cases[16]. It is associated with autosomal dominant mutations in the Amyloid precursor protein (*APP*) gene, presenilin-1 (*PS1*) and presenilin-2 (*PS2*) genes[17,18]. The *APP* gene encodes for the protein precursor of the Aβ peptide. Processing of the APP protein by two enzymes, the β- and y-secretase, results in release of Aβ peptide in the extracellular space. The genes *PS1* and *PS2* encode for the catalytic subunit of the y-secretase complex that mediates the last step in the generation of the Aβ peptide from its substrate APP[19,20]. By now, over 50 mutations in the *APP* gene clustering around the

secretase cleavage sites (e.g. Swedish mutation KM670/671NL, Artic mutation E693G, Florida mutation I716V, London mutation V717I) and over 200 mutations in the *PS1/2* genes could be identified to be causative for AD with most of them increasing the production of Aβ peptide[20-22].

In contrast to rare hereditary FAD, sporadic AD is the more prevalent form, accounting for ~95 % of all AD cases. With a late-onset, SAD usually develops after age 65, making age the highest risk factor[23]. The specific cause for the development of SAD is still largely unknown, but a number of genetic risk factors could be identified with genome-wide association studies (GWAS)[24,25]. However, the pure presence of any of these genetic risk factors is neither necessary nor sufficient for AD development, but rather in interaction with environmental factors, genetic predispositions become effective to cause disease. *APOEε4* represents the main risk factor and describes the ε4 allele of the Apolipoprotein E (*APOE*) gene, which is involved in cholesterol metabolism by regulating lipid homeostasis[16]. The human *APOE* gene exists in three polymorphic alleles, ε2, ε3 and ε4 with the frequency of the ε4 allele being increased up to ~40 % in AD patients[26]. APOE seems to play an important role in mediating Aβ clearance through multiple mechanisms with isoform ε4 being less effective than the other isoforms[27]. Furthermore single nucleotide polymorphisms in the neuronal sortilin-related receptor gene *SORL1* have been associated with late-onset SAD, probably due to an involvement in intracellular trafficking of the amyloid precursor protein APP[28,29]. Another example is the microglial-expressed receptor TREM2 for which a rare heterozygous missense mutation was found to be associated with a 2-4-fold increased risk of developing AD[30,31]. Recent studies indicate a potential role for TREM2 in supporting AD-induced microgliosis, a process where microglia cells accumulate and are activated due to pathological conditions[30]. Besides these genetic risk factors, also certain lifestyle factors were found to modify the development of sporadic forms of AD, including smoking, physical activity, education, social engagement, cognitive stimulation, alcohol consumption and diet[32].

Diagnosis

AD patients are diagnosed clinically predominantly by examining physical and neurological conditions as well as assessing their mental status (e.g. a Mini-mental state examination, MMSE[33]). However, a clinical diagnosis can be imprecise as observed phenotypes overlap between different forms of dementia. Therefore, a definitive AD diagnosis that confirms the clinical observations can only be made *post mortem* via histological examination[13,34].

For early diagnosis, imaging techniques, e.g. structural brain imaging via magnetic resonance imaging (MRI) or computer tomography (CT) are used to obtain information about shape and volume of brain tissue[35]. This is helpful to exclude other causes for memory deficits, e.g. due to tumors or damages from severe head trauma. Structural brain imaging also captures the shrinkage of brain tissue in general as well as in specific brain regions such as in the hippocampus, which can be an early sign of

AD. Functional imaging approaches aim to gain information about the brains functionality e.g. by visualizing the cellular glucose or oxygen consumption as it was suggested that AD brains are often associated with reduced glucose levels in brain areas that are important for memory and learning[36]. To visualize impaired glucose consumption PET scans with fluorodeoxyglucose (FDG) are performed[37]. Finally, molecular imaging techniques like positron emission tomography (PET) are used to visualize the presence of plaques by using radioactively labeled tracer molecules (e.g. Pittsburgh compound B (PIB), florbetapir F-18/Amyvid®) that bind to Aβ plaques in the brain[37,38].

In addition to imaging approaches, the analysis of biochemical marker proteins in the cerebrospinal fluid (CSF) is applied for AD diagnostics. CSF or *liquor cerebrospinalis* is the fluid circulating around the brain and spinal cord and is thus suggested to reflect the pathobiochemical changes in affected AD brains due to the direct contact with the cerebral tissue[39]. Currently, concentrations of Aβ42, total-tau (t-tau) and phosphorylated tau (p-tau) are determined from CSF samples obtained from patients via a minimally invasive procedure called lumbar puncture[40,41]. Characteristically, the concentration of both t-tau and p-tau is increased in CSF of AD patients. In contrast, AD patients have decreased levels of Aβ42 peptides, probably due to deposition of plaques in the brain[42-44]. However, a recent study in mouse models showed that during the very early phase of cerebral Aβ deposition increased Aβ40 and Aβ42 levels could be observed in CSF samples[45]. In general, the detection limit for the mentioned marker proteins is low, highlighting the importance of sensitive assays for an early detection of minimal alterations in the CSF. Additionally, severe variations between different labs were observed, likely due to differences in sample preparation and Aβ-measurement techniques[44]. Therefore, highly sensitive assays together with standardized workflows are required to be able to use CSF analysis as an early diagnostic tool for AD. Figure 3 summarizes and illustrates the different procedures described and their potential to diagnose AD at an early disease state.

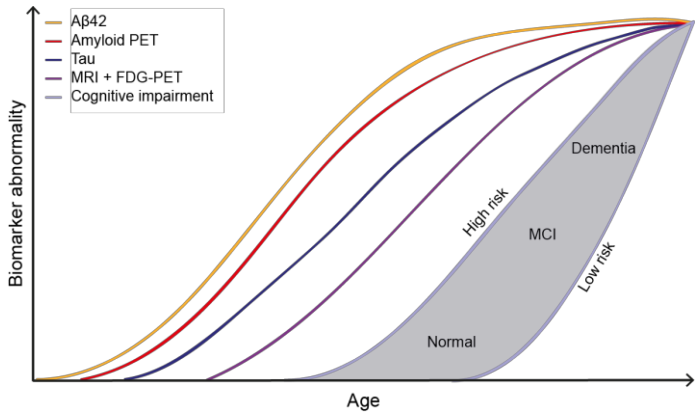

Figure 3 | Hypothetical model of dynamic biomarkers of the AD pathology
In AD patients changes of the Aβ42 concentration in the CSF can be detected first, followed by amyloid plaques via PET scans. Thereafter, altered tau levels in CSF become apparent. Finally, MRI and PET scans with fluorodeoxyglucose (FDG-PET) are able to detect alterations in AD patient brains before cognitive impairment becomes evident (Image adapted from Jack, 2003[46]).

3.2 The Amyloid-β peptide

APP processing

The Aβ peptide results from proteolytic cleavage of the amyloid precursor protein (APP), a transmembrane protein with a large extracellular domain. APP is ubiquitously expressed and not restricted to the CNS. Regarding its physiological function, APP was found to be involved in various processes including cell adhesion, axonal transport and gene transcription[47]. A vivid concept describes APP as a central molecular hub fulfilling regulatory functions of converging metabolic and regulatory pathways[47]. The processing of the APP protein can occur via two different pathways, a non-amyloidogenic and an amyloidogenic pathway (Fig. 4a). In the non-amyloidogenic pathway APP is initially cleaved by a α-secretase that cuts within the Aβ sequence. This results in formation of the soluble fragment sAPPα and the C-terminal fragment CTF83. Further processing of the CTF83 fragment by the γ-secretase finally generates the p3 and AICD (APP intracellular domain) fragments. In contrast, the amyloidogenic pathway is entered when APP is cleaved by the β-secretase BACE1 (β-site APP cleaving enzyme) at the N-terminus of the Aβ sequence, leading to the formation of the sAPPβ fragment and the C-terminal fragment CTF99. Subsequent cleavage of the CTF99 fragment by a γ-secretase finally results in the AICD fragment from which the 49-amino acid long Aβ peptide is produced by cleavage at the ε-site (Fig. 4b)[48]. Subsequently, the remaining membrane-associated fragment gets further processed at the ζ-site to generate an Aβ46 peptide. Finally, Aβ peptide is released into the extracellular lumen by the final cut at the γ-cleavage site. This cleavage site is variable, resulting in the production of amyloid-β peptides with lengths of 38, 40 or 42 amino acids[48].

Physiological roles of Aβ peptides

Before discussing the contribution of Aβ peptides to Alzheimer's pathology, it is noteworthy to mention that they might also have physiological roles in the brain. The proteolytic cleavage pathway *per se* represents a physiological process, however, it becomes pathological when production and degradation of the Aβ peptide are imbalanced[49]. For example, several lines of evidence indicate a potential role of Aβ peptides in controlling and depressing synaptic activity, thus contributing to prevent excessive glutamate release and overexcitation[49,50]. Another study suggested a role for Aβ peptides in neuronal survival as primary cultures of cortical neurons died upon inhibition of endogenous Aβ production via secretase inhibitors or after Aβ immunodepletion[51]. Interestingly, addition of Aβ peptides prevented the toxicity of secretase inhibitors in neuronal cells[51]. Finally, *Kumar et al*. presented evidence that Aβ peptides can act as antimicrobials as they showed a protective activity against fungal and bacterial infections in mouse and cell culture models of AD[52].

In the context of AD, Aβ peptides of 40 and 42 amino acids lengths were shown to be of crucial importance. Interestingly, ~90 % of APP is processed by the α-secretase via the non-amyloidogenic pathway, preventing the generation and release of Aβ peptide. The remaining ~10 % of neuronal APP is cleaved by the β-secretase BACE1 and further processing of the CTF99 fragment results in approximately 90 % of the cases in the generation of the Aβ40 peptide while only 10 % of the Aβ42 peptide is released[53]. Even though the Aβ40 peptide is much more common, the Aβ42 form shows a higher propensity to aggregate as it harbors two additional C-terminal hydrophobic amino acids (isoleucine and alanine) compared to Aβ40 (Fig. 4c) and represents the major component of Aβ plaques.

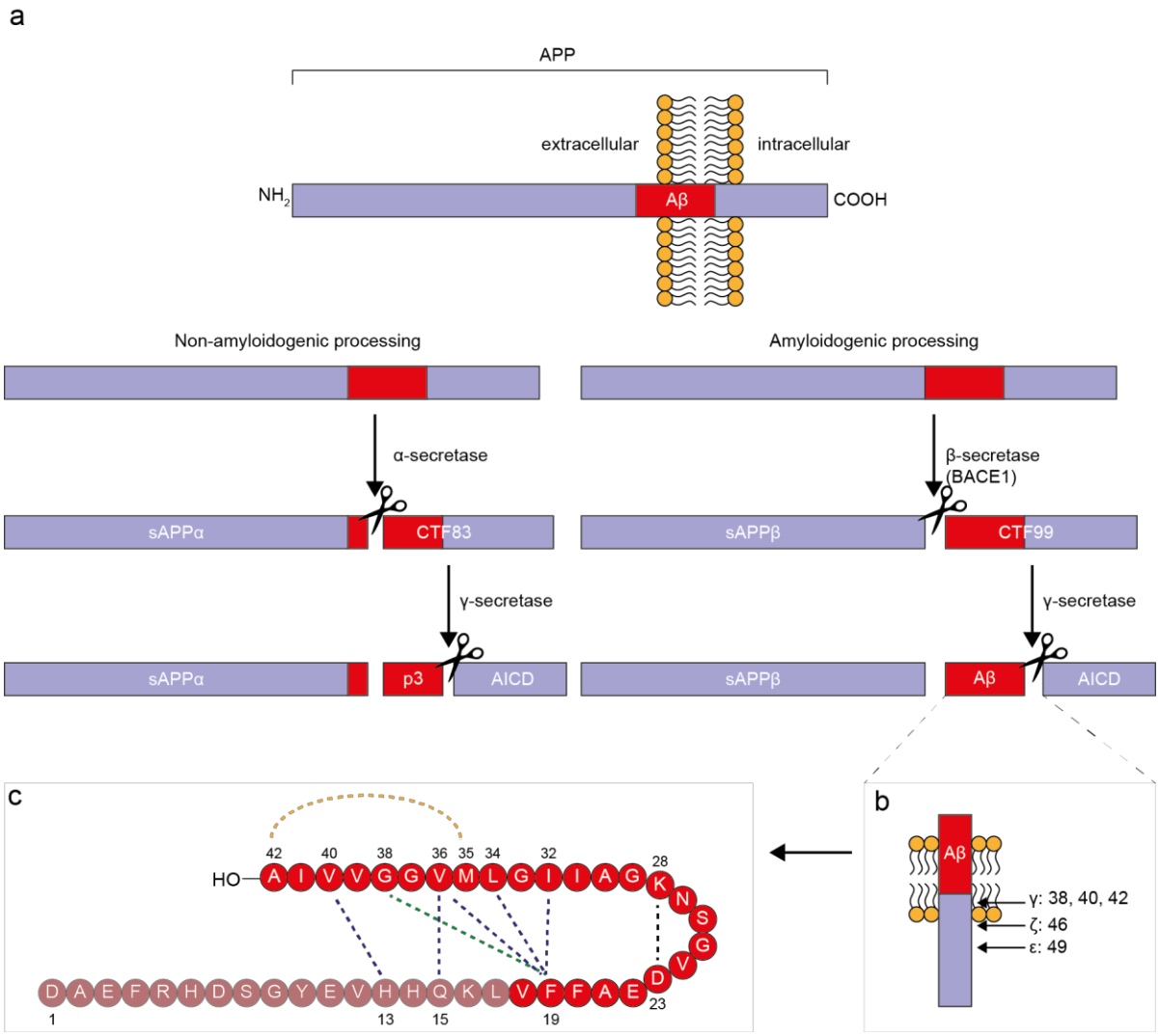

Figure 4 | Proteolytic processing pathways of the Aβ precursor protein APP
(a) Overview of the proteolytic processing of APP either via the non-amyloidogenic or the amyloidogenic pathway. While the α-secretase cuts within the Aβ sequence, the β-secretase BACE1 initiates the amyloidogenic pathway by cutting a the N-terminus of Aβ. Subsequently, processing by the γ-secretase ultimately leads to release of Aβ peptide into the extracellular space (Image adapted from Bayer & Wirths, 2008[54]). (b) Various cleavage sites of the γ-secretase. The γ-secretase complex cuts its substrate at least three times, resulting in the release of Aβ peptides of various lengths. (c) Sequence of the Aβ42 peptide and proposed intramolecular contacts (Image adapted from Ahmed, 2010[55]).

In general, the C-terminal amino acids of the Aβ peptides arise from the APP transmembrane domain and therefore are high lipophilic. Thus, release of Aβ peptides from the membrane environment into the cytosol promotes the conversion of the α-helical or random coiled Aβ structure into β-sheets, which is a prerequisite for the formation of abnormal aggregates[56,57]. NMR spectroscopy has identified specific amino acids that are involved in intramolecular contacts and the structural conversion towards β-sheet favored structures[55] (Fig. 4c). In Aβ42, residues 1-17 seem to be unstructured while between amino acids 18-42 a β-turn-β-fold structure is found[55]. Molecular hydrogen bond interactions were observed between phenylalanine 19 and glycine 38 (green dashed line) and methionine 35 and alanine 42 (orange dashed line) with a salt bridge between aspartate 23 and lysine 28 (black dashed line) that stabilizes the turn conformation.

The formation of Aβ aggregates is a highly complex process

After an intramolecular structural conversion of natively unfolded Aβ monomers into partially folded or misfolded monomers, a highly complex, multi-step aggregation process is initiated, resulting in various species that differ in size, structure and toxicity (Fig. 5). Thereby, also a distinction is made between reactions that are on-pathway to amyloid fibril formation or off-pathway, leading to various oligomeric Aβ assemblies, e.g. annular oligomers or dodecamers[58,59]. Fibrils are generated through on-pathway Aβ aggregation, where misfolded monomers first assemble into dimers and oligomeric species in a reaction that is thermodynamically unfavored. After that, the aggregation proceeds rapidly, leading to the formation of various intermediate higher molecular weight assemblies, often referred to as protofibrils. Finally, with the formation of mature Aβ fibrils, the major components of amyloid plaques, the reaction reaches saturation[60].

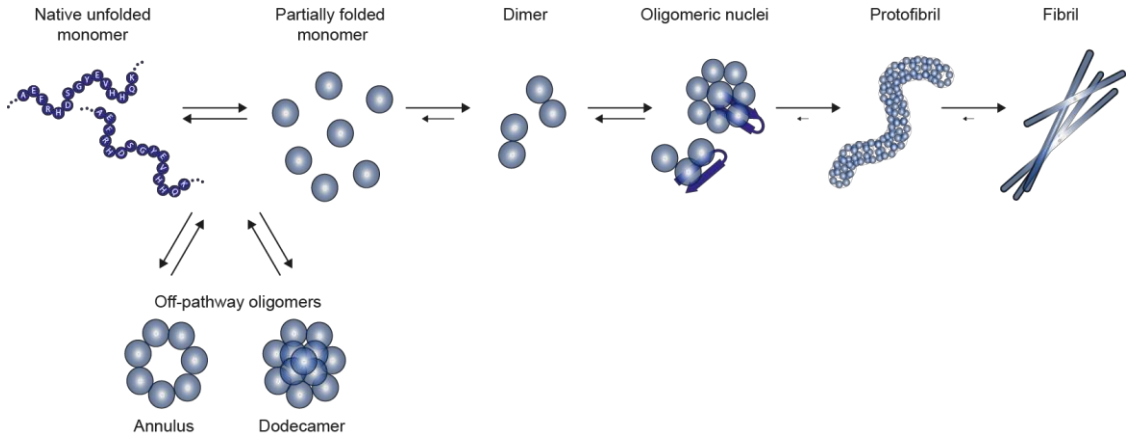

Figure 5 | Aβ aggregation is a highly complex process
Schematic overview of the Aβ aggregation process. In on-pathway aggregation reactions, native monomers undergo conformational changes and subsequently associate to form oligomeric nuclei. Subsequently, these nuclei rapidly grow into protofibrils and larger fibrilar structures until saturation is reached. Besides fibrillogenesis, also off-pathway aggregation events occur, leading to meta-stable Aβ assemblies (Image adapted from Kumar & Walter, 2011[60]).

Characterization of different Aβ species

Table 1 summarizes different Aβ species that were found *in vitro* and *in vivo* and their characteristic features. However, it should be kept in mind that the formation of distinct Aβ structures *in vitro* largely depends on the preparation and aggregation conditions of the Aβ peptide. This explains the disagreement that can be found in different studies regarding specific Aβ species and their attributed properties, especially in regard to cellular toxicity[61]. For many years, numerous researchers focused on identification of a specific Aβ species that accounts for neurotoxicity and thereby could explain the severe cell loss that is observed in AD. Such a species could further represent the crucial point of attack regarding medical treatment.

Aβ species	Characteristics and structure	Occurence	Size	Toxicity	References
Monomers	soluble amphipathic molecule; potential α-helical, random coil or β-sheet conformation		4,5 kDa		57,62-65
Dimers	hydrophobic core; resistant to SDS and Aβ-degrading enzyme IDE; alter synaptic structure and function	intracellular localization *in vivo*, in human brain extracts and *in vitro*	Ø35 nm		66-71
Trimers	potential key role as subunit of toxic oligomers; resistant to SDS and Aβ-degrading enzyme IDE; alter synaptic structure and function	observed *in vivo* in mouse models	3-50 monomers		72,73
Small oligomers	heteromorphous; mostly transient and unstable	observed *in vivo* in AD patients and mouse models and *in vitro*		toxic	72,74-80
Aβ*56	apparent dodecamer of endogenous brain Aβ; might correlate with memory loss	observed in brains of APP tg mouse line	56 kDa; 12mer	non-toxic	72,81
ADDLs (Aβ-derived diffusible ligands)	synthetic globular Aβ oligomers smaller than annuli; off-pathway and nonfibrillar; might affect neural signal-transduction pathways	observed in murine and human brain extracts and *in vitro*	17-42 kDa; 3-24mers	neurotoxic	82-87
Annular oligomer	doughnut-like structures of synthetic Aβ; off-pathway; potential role as membrane disrupting pores or ion channels	observed in cell culture and *in vitro* experiments	outer Ø ~8-12 nm; inner Ø ~2.0-2.5 nm		74,88-92
Protofibrils	short, flexible, rod-like structure; precursor of mature fibrils; β-sheet structure, Congo Red and Thioflavin T positive	observed *in vitro*	up to 200 nm in length, 8 nm in width	toxic	84,93-101
Fibrils	stable, filamentous Aβ aggregates composed of repeating Aβ units perpendicular to the fiber axis; Congo Red and Thioflavin T positive	observed in AD patients as well as in mouse models and *in vitro*	Ø7-13 nm		3,102-106
Plaques	large extracellular Aβ deposits; predominantly composed of fibrils; surrounded by dystrophic dendrites, axons, activated microglia and reactive astrocytes	observed *in vivo* in AD patients as well as in mouse models		non-toxic	62,107-109

Table 1 | Aβ species observed in various AD models, patients and *in vitro*
(Table modified from Finder & Glockshuber, 2007[110], Haass & Selkoe, 2007[48] and Benilova *et al.*, 2012[111])

Initially, the extracellular deposits of insoluble fibrillar Aβ aggregates were assumed to be responsible for the observed pathological changes in AD[112]. This might be also due to the fact that originally mainly histological studies were performed that pointed out the presence of Aβ plaques in affected AD brains[113]. However, it became apparent that neurotoxicity, disease severity and progression do not correlate with the burden of Aβ plaques and meanwhile it is even partly assumed that mature Aβ plaques comprising insoluble amyloid fibrils could serve as deposits to store smaller and potentially neurotoxic species[109,114]. Also the observation that neurotoxicity and memory impairment were detected in transgenic mice before the occurrence of plaque deposition turned the focus of research towards smaller soluble Aβ oligomers as being the culprit for neurotoxicity[78,115]. For example, it was shown that secreted SDS-stable Aβ oligomers can inhibit hippocampal long-term potentiation (LTP) *in vivo* and induce synaptic dysfunction[79,116]. In addition, toxic properties were assigned to various Aβ preparations, which include protofibrils[96,100], Aβ-derived diffusible ligands[86] and a 56-kDa Aβ species termed Aβ*56[72]. Even though many Aβ species with toxic properties were characterized, one unique toxic species has still not been identified yet. Thus, neurotoxicity in AD could also arise from the ongoing complex aggregation reaction itself that produces a heterogeneous mixture of Aβ species rather than by very specific Aβ assemblies[117].

Amyloid fold

While the monomeric Aβ peptide is largely unstructured in its native form, amyloid fibrils are highly structured. These fibrillar Aβ structures cannot only be found in deposits of affected AD patients brains or in the walls of blood vessels of the CNS such as in cerebral amyloid angiopathy (CAA) patients[118,119], but rather represent a common structural feature that is present in various amyloid diseases or amyloidosis, for example in Huntington's disease (deposition of Huntingtin protein with a polyglutamine expansion) or in Parkinson's disease (deposition of α-synuclein protein)[120]. This commonality between different proteins that do not share sequence or conformational homology suggests that the common polypeptide chain backbone is responsible for the main interactions within the amyloid fibril, mostly independent from the amino acids side chains[121].

Amyloid fibrils are unbranched and often twisted structures with 7-13 nm in diameter, but can reach micrometers in length. They are composed of rope-like twisted smaller protofilaments, usually two to six protofilaments per fibril[122] (Fig. 6a, b). X-ray diffraction patterns of amyloid fibrils displayed a cross-β-sheet pattern with the proteins in the protofilaments being organized as β-strands that run perpendicular to the fibril axis and hydrogen bonds oriented parallel along the fibril, enabling hydrogen bond stacking (Fig. 6c, d).

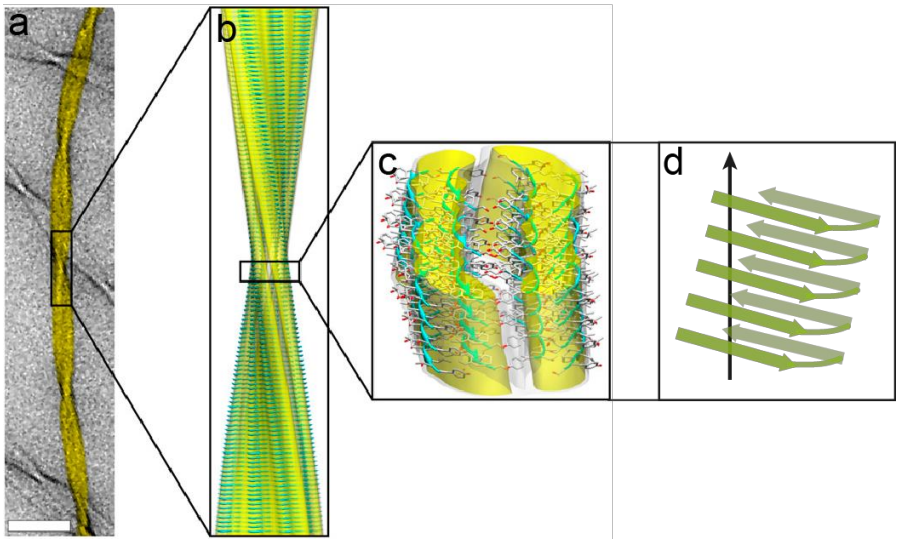

Figure 6 | Structure of an amyloid fibril

(a) Transmission electron microscopy image of an amyloid fibril formed from a transthyretin fragment (scale bar: 50 nm). (b) Atomic resolution of the fibril from *a* via *s*olid-state NMR analysis. (c) Detailed view of the amyloid fibril from *b*. Fibril surfaces are shown as electron density maps and β-sheets in ribbon representation. Oxygen, carbon and nitrogen atoms are shown in red, gray, and blue, respectively (Images a-c from Fitzpatrick *et al.*, 2013[123]). (d) Schematic ribbon representation of β-sheets of an amyloid fibril orientated perpendicular to the fibril axis.

3.3 Amyloid-β kinetic and the concept of seeding

Even though the Aβ aggregation represents a highly complex process, remarkable details of the molecular events underlying the overall aggregation kinetic could be resolved within the last decade of research. In fact, at least four microscopic processes were identified and characterized that contribute to the aggregation of the Aβ peptide as a whole (Fig. 7). Primary nucleation describes the homogeneous and spontaneous conversion of soluble monomers into misfolded oligomeric structures. This process is only dependent on the concentration of monomers and independent of existing fibrils[124]. During fibril elongation, monomers add up to the reactive ends of existing aggregates and lead to their growth, making this process dependent on the presence of monomers and fibrils[125]. Secondary nucleation events are also monomer and fibril dependent processes, where the surface of existing fibrils catalyzes the nucleation of new aggregates from monomers. Finally, fragmentation represents a process that is only fibril dependent, where the number of reactive ends is doubled by every breakage[126-129]. Those four mechanisms are currently used to describe Aβ protein aggregation[130,131]. However, it is important to note that these processes are hardly to be considered separate from each other as it is more likely that multiple processes proceed simultaneously at different rates[125,132].

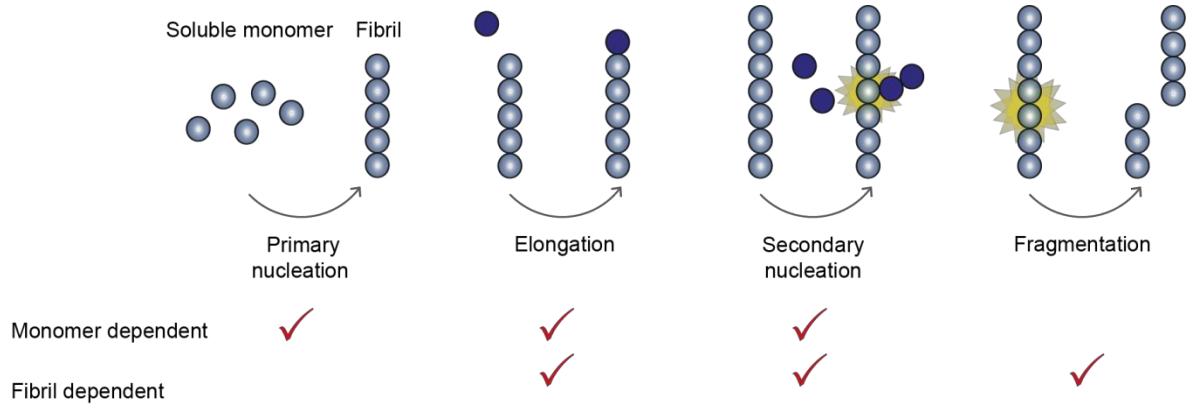

Figure 7 | Microscopic processes underlying the Aβ aggregation cascade
Primary and secondary pathways are distinguished as mechanism for the formation of new aggregates. Primary nucleation processes result in generation of new aggregates by interaction soley between monomeric forms. Addition of monomers to existing fibrils leads to their growth in elongation events. Secondary nucleation is a surface-catalyzed process from monomers on the fibril surface, while fragmentation is dependent only on the present fibril concentration (Image modified from Arosio *et al.*, 2015[125]).

The analysis of the Aβ42 aggregation kinetics with *in vitro* measurements reveals a characteristic sigmoidal curve with a lag phase, a growth phase and a final plateau phase, indicating a nucleation-dependent process of aggregate formation[130,133-135] (Fig. 8). Here, the lag phase represents the rate-limiting, thermodynamically unfavorable step. In this phase, soluble monomeric Aβ42 peptides convert into β-sheet-rich oligomeric nuclei that represent the highest-energy species in the

aggregation cascade[60,136]. Subsequently, the formed nuclei proliferate in an autocatalytic growth phase into fibrillar structures through the addition of monomers to the reactive ends of fibrils and by secondary nucleation processes. The growth of amyloid structures is thermodynamically favored, wherefore it processes rapidly, leading to the characteristic sigmoidal curve shape. Finally, the aggregation process reaches saturation in a steady state where all free monomers are mostly depleted and are integrated into fibrillar assemblies, demonstrated by the plateau phase[125]. It is noteworthy, that the lag phase cannot be defined as the required time for primary nucleation events only. In contrast, the lag phase results from a combination of both nucleation and growth processes and includes also the proliferation of primary nuclei by secondary nucleation processes up to a critical concentration[125,137].

Because of Aβ's nucleation-dependent aggregation mechanism, addition of pre-formed Aβ aggregates or oligomeric nuclei to soluble monomers can significantly shorten the lag phase, leading to an acceleration of the overall aggregation process as rate-limiting nucleation events can be bypassed[94,138,139] (Fig. 8). This process is termed seeding or seed-mediated aggregation and can be compared to crystallization mechanisms[94].

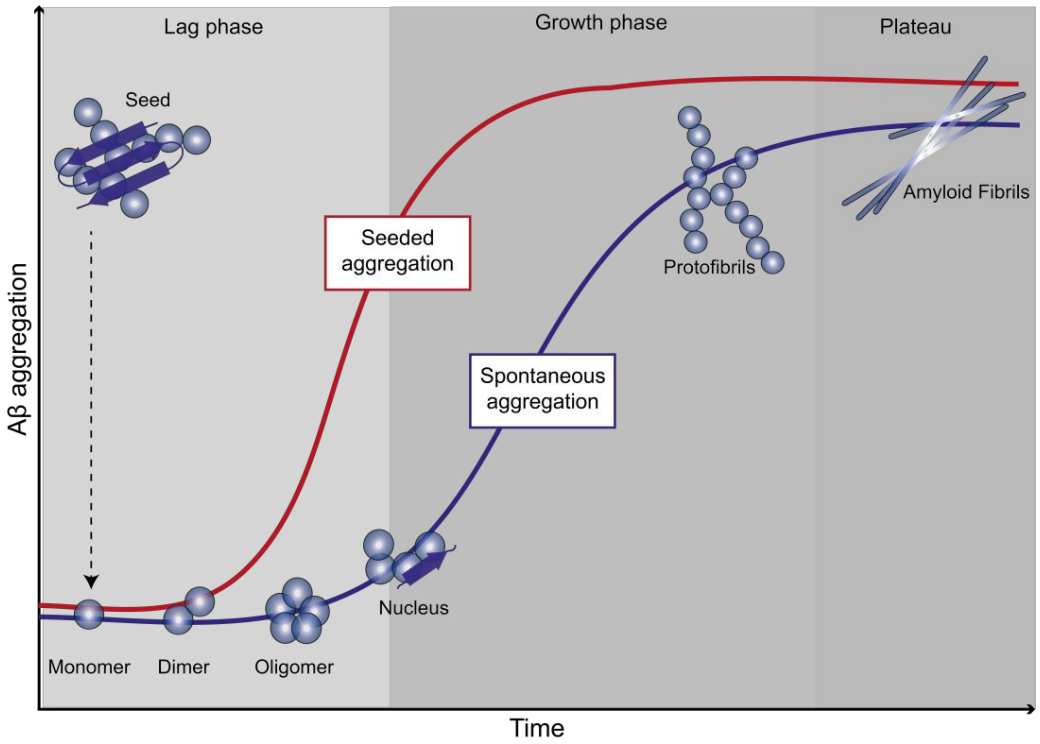

Figure 8 | Nucleation-dependent polymerization of amyloid formation and seeding
Kinetics of the Aβ peptide is presented by a characteristic sigmoidal curve due to the underlying nucleation-dependent polymerization mechanism. The lag phase represents the first and rate-limiting step within the aggregation process. Its length mainly depends on the self-assembly of monomeric species into β-sheet-rich nuclei, which proliferate in an autocatalytic growth phase until a steady state is reached in the plateau phase. Addition of pre-formed aggregates (seeds) shortens the lag phase and speeds up the whole aggregation process (Image adapted from Kuma & Walter, 2011[60]).

The *in vitro* concept of seeding gained more importance since several lines of experimental evidence indicate that Aβ42 aggregate species also *in vivo* can act as seeds. Especially due to the work of *Jucker* and *Walker* it could be shown that transgenic mice overexpressing human APP display significantly enhanced Aβ deposition when they are inoculated with pre-formed *in vitro* Aβ aggregates or brain extracts from AD transgenic mice or human AD patients[140-143]. Furthermore, it was shown that the seeding activity of brain extracts could be reduced and even abolished by immunodepleting the Aβ-reactive material using anti-Aβ antibodies, denaturation of the Aβ protein using formic acid or by immunization of the host against Aβ[144]. Another study showed that even intraperitoneal inoculation with Aβ-rich extracts induced amyloidosis in APP transgenic mouse brains. However, in this case more time was required and it was less effective than direct inoculation into the brain[145].

The concept of seeding provides a possible explanation to better understand AD pathology and the progressive deposition of aggregates throughout the brain. It was hypothesized that seeding-competent Aβ species might propagate and spread from neuron-to-neuron in the brain of affected AD patients[140,146-148]. As already mentioned earlier, AD pathology seems to spread along specific neuronal networks[13], probably via cell-to-cell contacts or synaptic transmission[149]. Various studies addressed this specific question and found e.g. that amyloid aggregates in general can get released from cells either by vesicle-mediated or lysosomal exocytosis[6,150,151]. Additionally, release of aggregates from cells could also occur passively after cell rupture of the cell membrane as a potential result of toxicity[146]. Also mechanisms of cellular aggregate uptake were studied, indicating the involvement of endocytotic processes and a breaching of the plasma membrane[146,152]. Hence, the mechanism of seeding represents a crucial component of the aggregation of the Aβ peptide in general and furthermore seems to be of significance for the progression of AD pathology throughout the brain.

3.4 Tau and the amyloid cascade hypothesis

A description of the molecular basis of AD cannot be provided without expounding the tau protein and its potential contribution to AD pathology. Tau proteins are polypeptides with high abundance in neuronal axons of the CNS and belong to the group of microtubule-associated proteins (MAPs)[153]. As a representative of MAPs, tau's main function is to stabilize microtubules within neurons, which are components of the cytoskeleton that are crucial for intracellular transport and to maintain the neuronal morphology and function[154]. Encoded by the *MAPT* gene six different isoforms of tau (between 36-45 kDa) can be produced in the human CNS due to alternative splicing. They differ mainly in the number of tubulin-binding domains (R1-R4)[154,155]. Tau is a phosphoprotein comprising 80 serine/threonine and five tyrosine phosphorylation sites. It was shown that the phosphorylation status of the protein critically influences its ability to bind to microtubules[156]. To a certain extent the tau protein is also phosphorylated in normal brain, however, in AD hyperphosphorylation leads to an at least three-fold greater load of phosphate groups[156,157]. Upon phosphorylation by kinases like GSK-3β (glycogen synthase kinase 3β), tau's affinity towards microtubules gets reduced, leading to a breakdown of microtubules and ultimately of cellular integrity[158]. Additionally, the naturally unfolded and soluble tau protein gets more aggregation-prone and self-assembles into paired helical filaments (PHF) that bundle together into neurofibrillary tangles, which, besides the Aβ plaques, are the second hallmark of AD[154] (Fig. 9). PHFs are composed of two strands of hyperphosphorylated tau filaments that are twisted around each other with a periodicity of 80 nm. Besides PHF, also straight filaments (SF) can be found within neurofibrillary tangles.

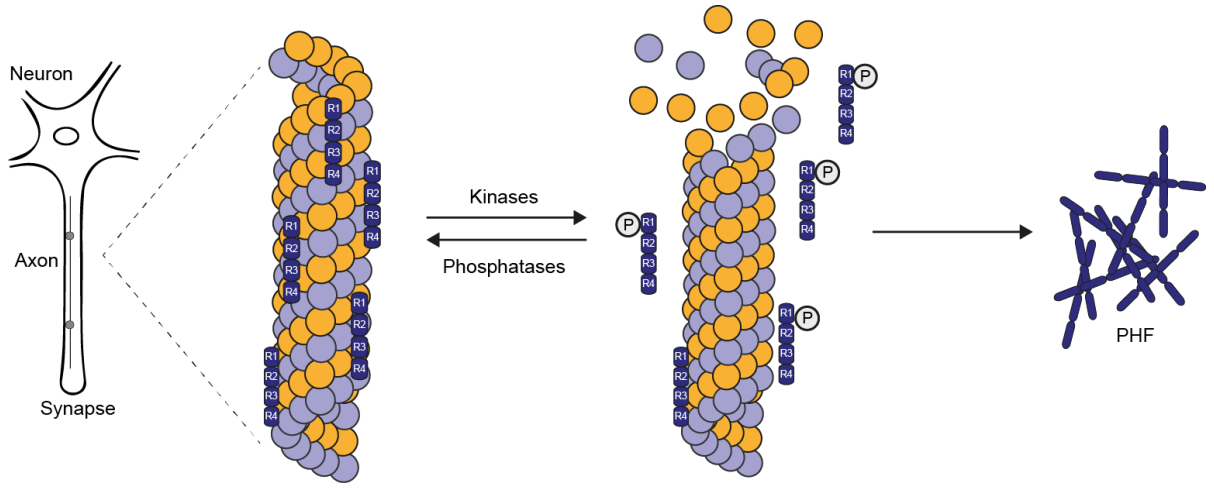

Figure 9 | Pathological alterations of tau in AD
Axonal transport is dependent on microtubles that function as tracks. They are stabilized by tau proteins, illustratrated by the tau binding domains R1-R4. In AD, tau protein detaches from microtubules upon hyper-phosphorylation caused by kinases. This leads to a breakdown of microtubules and the self-assembly of tau into paired helical filamets (PHFs) (Image adapted from Mandelkow and Mandelkow, 1998[154]).

Mutations in the *MAPT* gene were found in patients diagnosed with a form of frontotemporal dementia termed FTDP-17 (frontotemporal dementia with parkinsonism linked to chromosome 17)[159]. However, no mutations in the *MAPT* gene are known to be directly associated with AD[160-162]. The precise mechanism by which tau contributes to the AD pathology is not yet fully understood and both loss- and toxic gain-of-function mechanisms for tau aggregates have been suggested. A loss of tau protein that stabilizes microtubules directly affects their integrity, which results in an impairment of intracellular transport mechanisms and cellular structure[163-165]. Additionally, detachment of tau protein from microtubules increases the concentration of cytosolic tau which may enter the aggregation pathway. A toxic gain-of-function effect is suggested for non-filamentous tau aggregates and oligomers rather than for filaments since transgenic tauopathy mouse models show neuronal loss and memory impairment that precede detectable filamentous tau pathology[166-168].

Trying to unite the characteristic hallmarks and symptoms of AD to provide an overall hypothesis for the progression of molecular events in AD pathology, *Hardy & Higgins* proposed the amyloid cascade hypothesis in 1992[169]. Importantly, the deposition of the Aβ peptide in the brain was claimed to be the causative agent of Alzheimer's pathology and the formation of tau neurofibrillary tangles and cell loss were downstream events resulting from Aβ deposition[169]. This concept was relevant in subsequent years for the focus of AD research and was further developed since (Fig. 10).

In more detail, the amyloid cascade hypothesis claims that AD develops from an imbalance between Aβ production and clearance, leading to increased levels of aggregation-prone Aβ42 peptides[170]. This imbalance can be due to genetic mutations as observed in rare familial AD cases or, more common, the result of combined aging and environmental factors together with genetic predispositions as in sporadic AD forms. In both cases, conformational changes in soluble Aβ42 peptides lead to the formation of aggregation-prone misfolded monomers and oligomers, which induces subtle and later more severe synaptic dysfunction[48]. In parallel, aggregated Aβ42 peptides start to deposit as diffuse, non-fibrillar plaques, followed by characteristic amyloid plaque formation that trigger microglial and astrocytic activation and local inflammatory response reactions. Over time, synaptic spine loss and neuritic dystrophy occur as well as oxidative stress, which impairs neuronal ionic homeostasis[170,171]. Due to altered kinase and phosphatase activities a hyperphosphorylation of tau leads to the formation of intracellular neurofibrillary tangles that then contribute to neuronal lesions by impairing cellular transport mechanisms. Finally, a widespread dysfunction of neurons and cell death occurs, leading to progressive dementia with Aβ plaque and tau neurofibrillary tangle pathology[48,170,171].

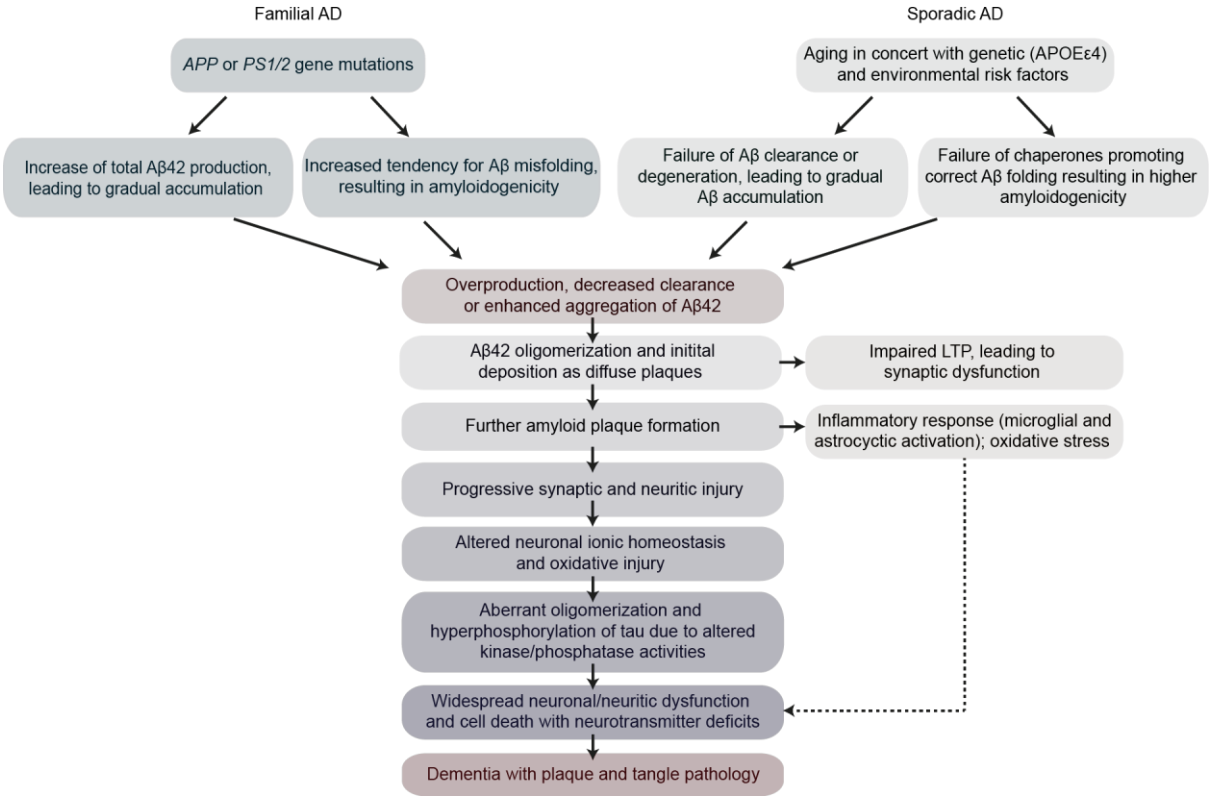

Figure 10 | The amyloid cascade hypothesis
The amyloid cascade hypothesis claims the deposition of Aβ peptide in the brain as the crucial initiating step in AD. Increased levels of aggregation-prone Aβ42 peptide assemble into neurotoxic oligomers that impair synaptic function. Additionally, aggregation into dense amyloid plaques causes inflammatory responses. In parallel, altered enzymatic activities lead to tau hyperphosphorylation and the formation of neurofibrillary tangles. Ultimately, these different molecular changes culminate in neuronal cell loss and dementia (Image adapted from Haass & Selkoe, 2007[48], Citron, 2004[171] and Blennow *et al*., 2010[170]).

Several studies supported Aβ's role to trigger tau malfunction and thereto relating the overall amyloid cascade hypothesis. For example, it could be shown in neuronal cells that Aβ induces activation of kinase GSK-3β, leading to phosphorylation of tau and its subsequent detachment from microtubules[172]. Additionally, it was suggested that Aβ might impair proteasomal degradation and thus reduce the clearance of misfolded tau. However, critical review of the amyloid cascade hypothesis based on newer data and information led to a persistent revision of the initial amyloid cascade hypothesis. Especially the observation that Aβ plaques do not correlate with the severity of AD pathology challenges the importance of Aβ deposition as the crucial initiating event in AD. Also the assumption that the intracellular formation of tau deposits is a downstream event of Aβ aggregation is questioned meanwhile[173]. For example, it was shown in neuropathological studies that tau pathology is already present in some AD patients at a very early stage and precedes amyloid pathology in general. At present, it is assumed by some researchers that Aβ aggregation is a crucial event, but runs in parallel with tau dysfunction[173,174]. However, amyloid pathology is likely to drive spreading of tau from allocortical regions throughout the cortex in AD[175] whereas tau dysfunction and paired helical

filament formation stays restricted to allocortical regions in normal age-related memory impairment[173]. Additionally soluble small molecular weight Aβ oligomers are attributed greater importance as clinical disease progression and synaptic loss correlates with levels of soluble Aβ[78]. Hence, Aβ oligomers are considered the neurotoxic agent that inhibits hippocampal LTP and thus disrupts synaptic plasticity[176].

3.5 Alzheimer's disease treatment and identification of compounds for therapeutic use

To this day, no causative treatment options are available for AD. Current medications merely seek to attenuate the disease symptoms and achieve only an overall improvement of life quality for patients. Table 2 shows an overview of five FDA (Food and Drug Administration) approved drugs that are currently available and applied to treat AD. These drugs target either the enzyme acetylcholine esterase or the NMDA (N-methyl D-aspartate) receptor, the drug Namzaric® represents a molecule that can target both proteins.

Drug name	Drug type and use	Effect mechanism
Aricept® (donepezil)	Cholinesterase inhibitor to treat symptoms of mild, moderate, and severe AD	Prevents breakdown of ACh in the brain
Razadyne® (galantamine)	Cholinesterase inhibitor to treat symptoms of mild to moderate AD	Prevents breakdown of ACh, stimulates nicotinic receptors to release more ACh in the brain
Exelon® (rivastigmine)	Cholinesterase inhibitor to treat symptoms of mild to moderate AD	Prevents breakdown ACh and butyrylcholine in the brain
Namenda® (memantine)	NMDA antagonist to treat symptoms of moderate to severe AD	Blocks the toxic effects associated with excess glutamate and regulates glutamate activation
Namzaric® (donepezil and memantine)	NMDA antagonist and cholinesterase inhibitor to treat symptoms of moderate to severe AD	Prevents breakdown of ACh in the brain, blocks the toxic effects associated with excess glutamate

Table 2 | Current medication for AD treatment
To this date, three cholinesterase inhibitors and one NMDA antagonist are available as FAD approved drugs for AD treatment, the drug Namzaric® targets both cholinesterase and NMDA receptors for the treatment of AD symptoms (Table modified from https://www.nia.nih.gov/health/how-alzheimers-disease-treated; 25.05.18).

Acetylcholine (ACh) is an important neurotransmitter in the CNS and has been implicated to be involved in many cognitive processes, such as learning and memory function[177]. In AD, predominantly ACh- producing, cholinergic neurons in the basal forebrain die, leading to a loss of ACh in the human brain[178]. By inhibiting the ACh degrading enzyme acetylcholine esterase, the local concentration of ACh can be increased at synapses[179]. In addition, glutamate is the primary excitatory neurotransmitter in the hippocampus and the neocortex. It is also of high importance for memory and learning in human brains[180]. Under resting conditions, glutamate is stored in presynaptic neurons and only a small amount of this neurotransmitter is released into the synaptic cleft. Upon excitation, e.g. due to a cognitive activation, glutamate, however, is released into the synaptic cleft where it binds to postsynaptic NMDA receptors that usually are blocked by magnesium in a voltage-dependent manner. By removal of magnesium as the result of excitatory events associated with a depolarization of the neuron, calcium ions can enter the postsynaptic neuron and trigger a new action potential to forward the excitation to downstream synapses via neurotransmitter release[181].

However, in AD the concentration of released glutamate in the synaptic cleft is consistently very high due to damaged neurons. This chronic overexposure of calcium ions leads to overexcitement of neurons, also termed excitotoxicity that is accompanied by a loss of synaptic function and ultimately causes cell death[182]. However, as already indicated the available neurotransmission modulating drugs are only capable of causing symptomatic improvement and cannot treat the underlying patho-mechanism or provide a significant delay in disease progression. Different strategies for AD therapy are explored right now, summarized in Table 3.

Strategy	Example
Modulating neurotransmission	Cholinesterase inhibitors
	NMDA receptor antagonism
Tau based therapies	Tau phosphorylation inhibition
	Stabilization of microtubles
	Blocking Tau oligomerization
	Enhancing Tau degradation
	Tau based immunotherapy
Aβ based therapies	Secretase enzymes modulation
	Amyloid transport
	Preventing amyloid aggregation
	Promoting amyloid clearance
	Amyloid based immunotherapy
Others	Modulating intracellular signaling cascades
	Reduction of oxidative stress
	Modulation of cellular calcium homeostasis
	Anti-inflammatory therapy

Table 3 | Therapeutic strategies in AD
(Table modified from Anand *et al*., 2014[178]).

One potential approach to delay the disease progression in AD is to inhibit either β- or γ-secretases in order to directly prevent the release of Aβ[183,184]. However, especially the γ-secretase is not only responsible for Aβ cleavage but also for the cleavage of the transmembrane domain of other proteins such as e.g. notch, an important receptor within the notch signaling pathway that is crucial during embryonal development as well as in adulthood in cell differentiation events[185-187]. Recently, therefore a therapeutic approach was developed that aims to modulate enzyme cleavage, leading to the release of the more benign Aβ38 isoform instead of Aβ42[188]. In immunotherapy-based approaches, specific anti-Aβ antibodies are used to interfere with the aggregation process. For example, anti-oligomer antibodies are designed to prevent the formation of potential toxic oligomeric intermediates[189]. Another example is the human monoclonal IgG1 antibody *Aducanumab* that selectively targets a conformational epitope of Aβ aggregates and does not bind to Aβ monomers[190]. It was shown to enter the brain of transgenic mouse models and to reduce the abundance of amyloid plaques in a dose-dependent manner. *Aducanumab* is currently tested in AD patients in a phase 3 clinical trial[190]. Another therapeutic approach is focused to promote the degradation of Aβ oligomers and fibrils by using amyloid-degrading enzymes (e.g. insulin-degrading enzyme IDE and neprilysin)[191]. However, it has to be considered that the precise pathomechanism of AD still remains partly unsolved, wherefore

an uncontrolled degradation of largely inert mature fibrillar structures into smaller Aβ assemblies might be highly detrimental as it would increase the concentration of potentially neurotoxic intermediate species[82,85,86,96].

A different strategy is to use small molecules to directly target amyloidogenic Aβ peptides and interfere with the aggregation process. For example, organic dyes such as Congo Red or Chrysamine G were shown to bind to β-sheet-rich amyloidogenic Aβ assemblies and to reduce the spontaneous self-assembly of Aβ peptides[192,193]. Another example is the small molecule Ro 90-7501 that was shown to selectively bind to Aβ42 fibrils and to suppress the mature fibril formation[194]. Amongst natural products, aggregation inhibiting compounds like Curcumin were found, which often contain phenolic groups that have been shown to efficiently inhibit Aβ aggregation[195-198] (Fig. 11). Within this group also the catechine EGCG ((–)-epigallocatechin-3-gallate), a component of green tea was shown to affect Aβ42 aggregation by redirecting amyloidogenic polypeptides into unstructured oligomers that are off-pathway to fibril formation[59]. Importantly, the EGCG-induced Aβ assemblies did not reveal toxic effects and were efficiently degraded in mammalian cells[199].

Recent studies identified stilbenes, also termed styrylbenzenes as potent binders of amyloid aggregates and modulators of the amyloidogenic aggregation *in vitro*[200]. Development of stilbenes as amyloid aggregation targeting small molecules started with the compound Chrysamine G, a bis-diazo benzene and compounds that are related to Curcumin[201-203] (Fig. 11). Chrysamine G is a well-known fluorescent probe for histological amyloid stainings and was used as a starting compound for small molecules that are currently in clinical applications[203]. In general, the development of therapeutic drugs for the CNS is particularly challenging since the brain is protected by the blood brain barrier (BBB), a highly selective layer of endothelial cells that separates the extracellular fluid in the CNS from circulating blood[204]. To overcome this hindrance, drugs need to meet certain prerequisites. The *Lipinski rule of five* covers criteria to determine the potential absorption of compounds after preoral application[205]. Among other things, the rule includes a molecular weight of the compound of less than 500 kDa as well as a high lipophilicity to enable the passage of cell membranes. The *Lipinski* criteria are meanwhile widely used to assess the overall drug-likeness of a compound[206]. Further development of Chrysamine G led to synthesis of compound BSB, which features greater membrane permeability due to its reduced size, while at the same time preserves the fluorescent amyloid-binding property of Chrysamine G[207]. It was shown that BSB detects Aβ plaques with high sensitivity in AD brain sections and is capable to enter cultured cells where it specifically binds to intracellular Aβ aggregates[207]. Subsequently, the compounds methoxy-X04 and K114 were developed as derivatives from BSB, bearing even higher lipophilicity due to the absence of acidic groups[208-212]. Methoxy-X04 was shown to feature a high *in vitro* binding affinity for Aβ fibrils and to stain Aβ plaques in *post mortem* sections of AD brains. Additionally, due to its blood brain permeability ^{11}C-labeled methoxy-X04 has been used as

a PET amyloid-imaging agent for human studies[208]. Finally, K114 has been described as a binder of amyloid fibrillar structures. It also functions as an aggregation inhibitor *in vitro* as well as in transgenic APPPS1 AD mice[209-212]. In summary, using small molecules to directly target the Aβ aggregation process represents a valuable approach, even though, the exact mechanism of action as well as the molecular targets remains mostly unclear for many compounds.

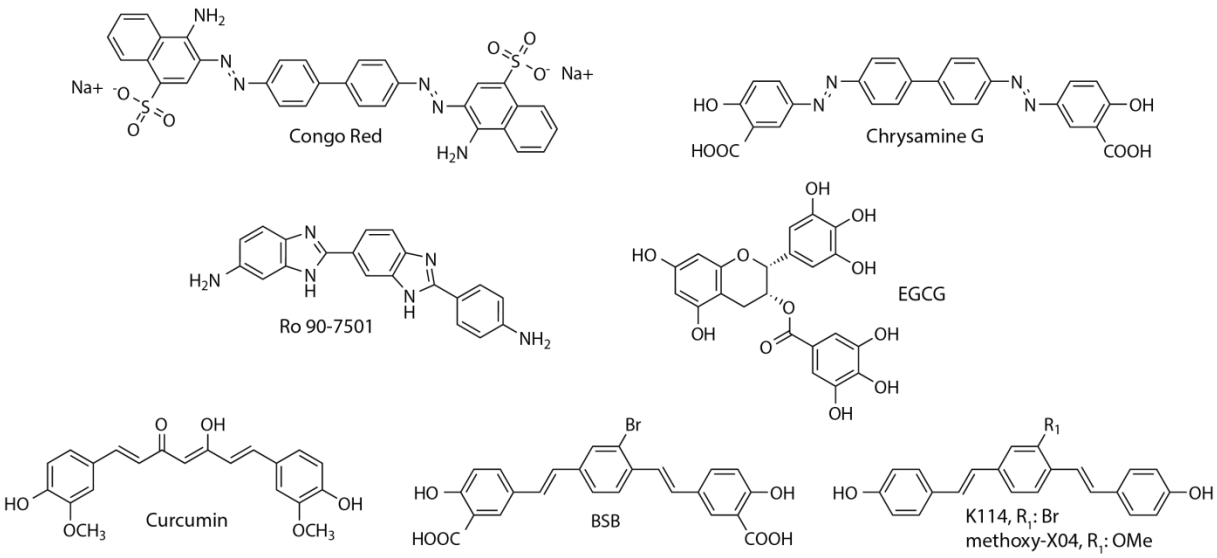

Figure 11 | Amyloid aggregate binders and modulators of the amyloidogenic aggregation process
Structures of Congo Red, Chrysamine G, Ro 90-7501, EGCG, Curcumin, BSB, K114 and methoxy-X04.

Especially challenging is the identification and design of small molecules that target specifically seed-mediated aggregation events. Since the assembly of fibrils in seeded aggregation reactions occurs more rapidly than in spontaneous reactions, seed-mediated aggregation can be seen as a more aggressive process. Given the high importance of seeding-competent Aβ species for AD pathology and their relevance in disease progression, systematic studies addressing this question are highly relevant. Potentially, only a subgroup of already known amyloid targeting compounds is capable of preventing or delaying seed-mediated Aβ42 aggregation reactions *in vitro*. However, their identification could be a promising therapeutic strategy, as they would target an early step in the aggregation process and thereby might halt aggregate formation as well as disease progression.

3.6 Methods for the analysis of Amyloid-β aggregation

For the characterization of different Aβ species and aggregate assemblies a whole set of biochemical methods is available. For the analysis of the molecular weight and the size of a particular Aβ species polyacrylamid gel electrophoresis (PAGE) can be used[213,214]. Here, either native (NativePAGE) or denaturating conditions (SDS-PAGE) can be applied, where in the latter disulfide bonds in protein complexes are broken by reducing agents such as DTT (Dithiothreitol) or β-mercaptoethanol. Furthermore, secondary structures are denaturated by SDS (sodium dedoecyl sulfate), which disrupts non-covalent bonds in proteins[215]. Another useful method is dynamic light scattering (DLS), which allows the determination of the size distribution profile of polymers in solutions[216]. Here, the size of particles is measured by referring it to the random motion of particles in solution, known as Brownian motion. Size-exclusion chromatography (SEC) represents another useful tool for the separation of various Aβ assemblies regarding their size, either as an analytical approach to determine the Aβ size distribution or as a preparative strategy to enrich for Aβ assemblies with a specific size. Finally, analytical ultracentrifugation can be used to separate molecules from each other regarding their sedimentation coefficient.

To gain information about a species' morphology, high-resolution microscopy like electron microscopy (EM) or atomic force microscopy (AFM) can be performed[217,218]. For the determination of structural conformations e.g. of secondary and tertiary structures circular dichroism (CD) is a valuable method[219].

Furthermore, antibody-based immunodetection methods can be used to specifically target Aβ-isoforms or conformations using e.g. Sandwich ELISAs[220]. Sequence- or conformation-specific Aβ antibodies can further be equipped with a fluorescence tag, which enables fluorescence/Förster resonance energy transfer (FRET) studies[221]. FRET measurements are useful to analyze protein-protein interactions and could thus be utilized to elucidate interacting proteins that bind to the Aβ peptide.

To be able to capture the whole aggregation process in a time-resolved manner, spectroscopic techniques are commonly used for kinetic investigations. Turbidity assays at ~400 nm wavelength measure an increase in turbidity over time, which reflects the formation of fibrillar aggregates[222]. However, smaller Aβ assemblies such as protofibrils cannot be detected, which prevents the assay from a more precise kinetic application for the Aβ peptide[100,139]. Therefore, fluorescent amyloid binding dyes are usually used to follow the aggregation process with Congo Red (CR) and Thioflavin T (ThT) being the most common ones. Both dyes change their fluorescence properties upon binding to cross-β-sheet-rich structures of amyloid proteins such as Aβ, α-synuclein and huntingtin[223].

Congo Red is a diazo dye and mainly applied for histological staining of tissues samples to detect cross-β-sheet-rich amyloids[224]. Upon amyloid binding, it undergoes a shift in its absorption maximum

from 490 to 540 nm and exhibits a characteristic green birefringence under polarized light[225]. Its application in *in vitro* aggregation studies is feasible, but limited since studies revealed a potential interference of the dye with the Aβ aggregation process[226-228].

The benzothiazol dye ThT is a fluorescent amyloid binding dye that displays a strong enhancement in its fluorescence accompanied with a shift in its excitation (from 385 to 450 nm) and emission maximum (from 445 to 480 nm) upon binding to β-sheet-rich amyloid[229] (Fig. 12a, b). Similar to CR, ThT is well suited for histological applications to identify the presence of amyloid in tissue samples[230]. Additionally, ThT is widely used in *in vitro* aggregation assays based on its increase in fluorescence when it binds to β-sheet-rich structures that are associated with amyloid proliferation (Fig. 12c). However, the ThT assay is not well suitable for the screening of small molecules that influence the Aβ aggregation process, as the dye can interfere with compounds in a competitive binding reaction. Especially when added in a molar excess the ThT signal can be biased in the presence of compounds and false-positive hit compounds could be detected[231,232]. Furthermore, ThT assays are indirect aggregate measurement techniques with the increase in the fluorescence signal being mediated by binding of a dye to secondary structure elements of a protein.

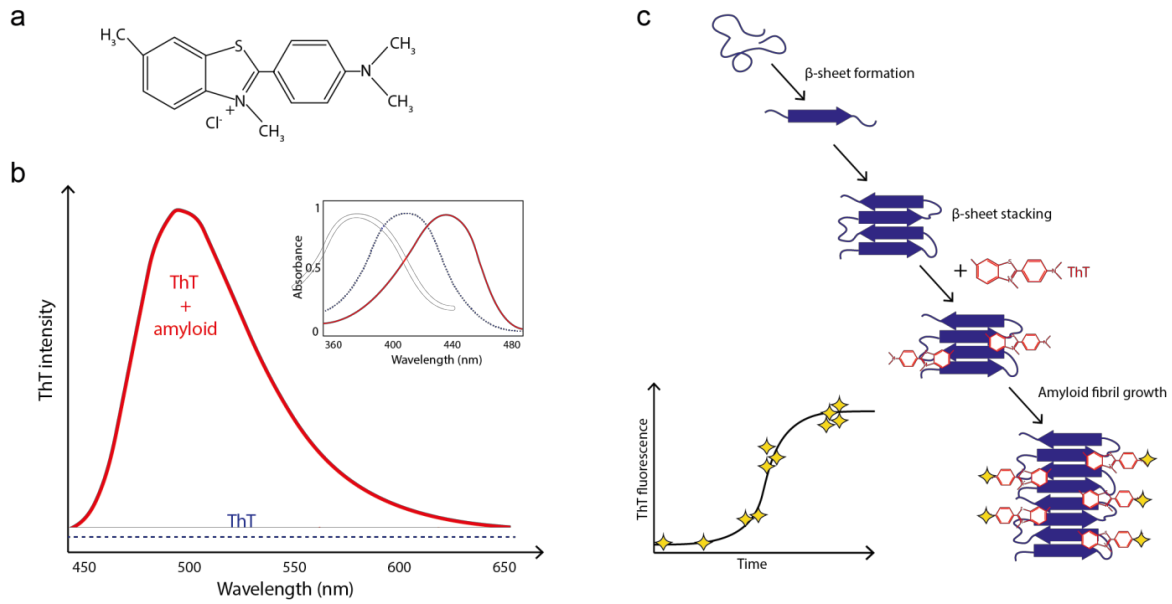

Figure 12 | Thioflavin T assay for the detection of β-sheet-rich amyloid structures
(a) Molecular structure of Thioflavin T (ThT). (b) Upon amyloid binding, ThT displays a strong enhancement in its fluorescence together with a characteristic red shift in its emission spectrum (Image adapted from Singh *et al.*, 2015[233]). (c) The ThT assay can be used to quantify protein aggregation *in vitro* in a time-resolved manner.

While there are plenty of biochemical methods available to analyze size, morphology and structure of Aβ aggregate structures, there is a strong need for alternative techniques to follow the Aβ aggregation process in a time-resolved manner. It is important to exclude potential competitive binding effects associated with the analyzed compounds.

3.7 Fluorescence polarization

Theoretical background

A potential alternative method to monitor the Aβ aggregation process in a time-resolved manner are fluorescence polarization-based assays. In the following, the theoretical background of this phenomenon will be discussed as it will be used for the subsequent assay establishment.

A fluorophore is a molecule that emits light after excitation. The average time laps between excitation and emission is characteristic for each fluorescent molecule and is referred to as the fluorescence lifetime of the fluorophore (τ)[234]. Driven by Brownian movements, which describe the steady tumbling of molecules in solutions, every fluorophore rotates around its own axis with a specific speed, referred to as the rotational relaxation time (ρ). More precisely, the rotational relaxation time is defined as the time it takes for a molecule to rotate through an approximate 68.5° angle after excitation[235,236]. This speed is dependent on its size, the temperature and the viscosity of the surrounding solution[237]. If fluorescent molecules are irradiated with linear planar polarized light, fluorophores whose absorption dipoles are roughly aligned with the direction of the electric field vectors of the excitation light are preferentially excited. Assuming that the fluorescence lifetime of the excited fluorophore is longer than its rotational relaxation time, the orientation of the molecules will randomize in solution during the process of emission, leading to a depolarization of the light emitted by the fluorophore. However, if fluorophores stay aligned or do only marginally rotate during the process of emission, they emit light in the same plane as the polarized excitation light. This dependency of polarization of emitted fluorescent light from the rotational relaxation time (ρ) of the fluorophore in relation to the lifetime (τ) of its excited state is termed fluorescence polarization and was described first by Francis Perrin in 1926[236,238] (*Equation 1*). P_0 represents the intrinsic polarization of the fluorophore observed in the absence of rotational diffusion, τ its fluorescence lifetime.

$$\left(\frac{1}{P}-\frac{1}{3}\right)=\left(\frac{1}{P_0}-\frac{1}{3}\right)\left(1+\frac{3\tau}{\rho}\right) \qquad \textit{(Equation 1)}$$

With a constant fluorescence lifetime the polarization is proportional to the rotational relaxation time of a fluorophore, which itself is dependent on viscosity (η) and temperature (T) of the solution, further from the constant value of the general gas constant (R) and the molecular volume (V) (*Equation 2*).

$$P \sim rotational\ relaxation\ time = \frac{3\eta V}{RT} \qquad \textit{(Equation 2)}$$

Thus, in an environment of constant temperature and viscosity, this altered fluorophore mobility can be directly correlated to a change in molecular volume[239].

Experimental setup

The experimental setup to measure fluorescence polarization is shown in Figure 13. A vertical polarizer allows the isolation of a single electric field vector from excitation light resulting in linear polarized light. A sample containing the fluorescence probe, here exemplarily depicted as a cuvette, is excited with the linear polarized light and fluorophores within the vertical plane are able to fully absorb it. The resulting emission of polarized fluorescence is then detected by use of a second mobile polarizer that is positioned parallel (vertical; $I_{\parallel}$) (Fig. 13a) and perpendicular (horizontal; $I_{\perp}$) to the vertical polarizer (Fig. 13b)[240]. The ratio of difference and sum of the parallel and perpendicular measured intensities results in the fluorescence polarization value and is calculated as follows[241]:

$$P = \frac{I_{\parallel} - I_{\perp}}{I_{\parallel} + I_{\perp}} \qquad \textit{(Equation 3)}$$

Equation 3 further displays that the polarization values are independent of the fluorophores' concentration and intensity.

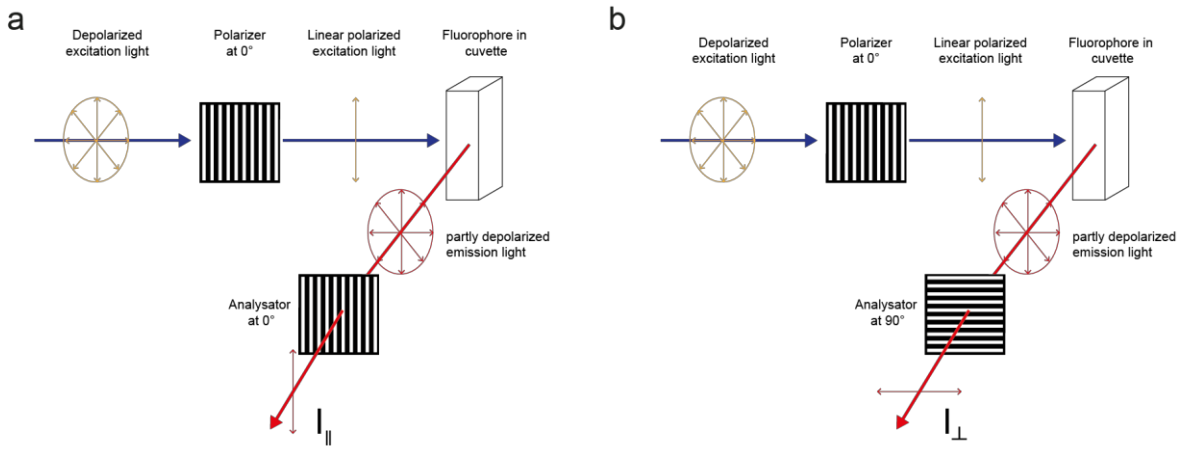

Figure 13 | Schematic diagram for the measurement of fluorescence polarization
(a) By use of a vertical polarizer, linear polarized light is produced from depolarized excitation light. The polarized light is absorbed and emitted by those fluorophores within the sample that are oriented in the same vertical plane as the excitation light. By detection of the emission in vertical and (b) horizontal direction, the polarization value can be determined on the basis of measured vertical ($I_{\parallel}$) and horizontal ($I_{\perp}$) intensities. (Image adapted from Serdyuk *et al*., 2007[241])

Fluorescence anisotropy (r) is another value that can be found to describe the same phenomenon. Even though the calculation of anisotropy is slightly different (*Equation 4*), the physical informational content of both values is identical and the use of the terms 'polarization' or 'anisotropy' are due to practical considerations or custom[242,243]. For example in the field of clinical chemistry predominantly the polarization function is used, whereas usage of the anisotropy function dominates in biophysics and biochemistry fields[243]. Besides, polarization and anisotropy can easily be converted into each other[244] (*Equation 5 and 6*).

$$r = \frac{I_{\parallel} - I_{\perp}}{I_{\parallel} + 2I_{\perp}} \qquad \textit{(Equation 4)}$$

$$P = \frac{3r}{(2 + r)} \qquad \textit{(Equation 5)}$$

$$r = \frac{2P}{(3 - P)} \qquad \textit{(Equation 6)}$$

Summarized, the fluorescence polarization (FP) value is calculated by two successive fluorescence intensity measurements differing in the mutual orientation of the polarizing filters. By processing both data sets the extent of how much the fluorophore has changed orientation in the time span between excitation and emission can be measured.

The relation between measured vertical and horizontal intensities and the resulting polarization values can be seen in Figure 14, exemplarily shown for a binding reaction were a small labeled fluorophore gets incorporated into bigger complexes over time. At time point zero of this reaction, the excited fluorophore features a fast rotation with an accompanied stochastic distribution of its electric field vectors and a depolarization of the light ($I_{\parallel} - I_{\perp} = 0$; blue line). As soon as the difference between vertical and horizontal intensities increases ($I_{\parallel} - I_{\perp} > 0$; blue line) the incorporation into a bigger complex occurs. Simultaneously, the sum of vertical and horizontal intensities decreases over time due to the incorporation ($I_{\parallel} + I_{\perp}$; red line). Calculation of the polarization values according to *Equation 3* results then in a sigmoidal curve shape where the inflection point represents the point of intersection of ($I_{\parallel} - I_{\perp}$) and ($I_{\parallel} + I_{\perp}$) from Figure 14a (Fig. 14b). The FP value is a dimensionless number, but mostly indicated as millipolarization units (mP)[245].

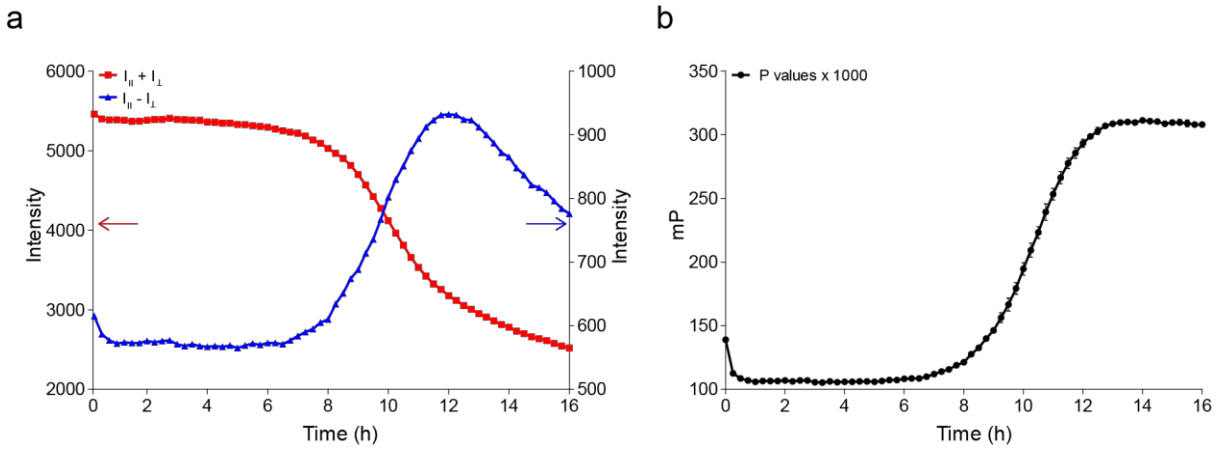

Figure 14 | Correlation between vertical and horizontal intensities and polarization values
(a) Sum of $I_{\parallel}$ and $I_{\perp}$ decreases over time due to incorporation of the tracer into aggregates. Simultaneously, the difference between both measured intensities ($I_{\parallel} - I_{\perp}$) increases, indicating incorporation of the tracer into bigger assemblies. (b) Calculation of the polarization values according *Equation 3* results in a sigmoidal curve shape where the inflection point represents the point of intersection of ($I_{\parallel} - I_{\perp}$) and ($I_{\parallel} + I_{\perp}$) in *a*.

It is noteworthy to mention, that the resulting polarization values represent the weighted average of all individual fluorophore molecules that are each orientated differently. Finally, it is the ratio of free unbound tracer to bound or incorporated tracer as demonstrated in the example above (Fig. 14) that is pivotal for the resulting polarization values. *Equation 7* shows this regularity of the polarization values of a mixture of molecules described by Weber[246,247] with P_i being the polarization value of each fluorophore species and F_i their fractional fluorescence intensity.

$$\left(\frac{1}{P}-\frac{1}{3}\right)^{-1}=\sum_{i=n}^{n}F_i\left(\frac{1}{P_i}-\frac{1}{3}\right)^{-1} \qquad \textit{(Equation 7)}$$

As a consequence of the weighted average the ideal concentration of a fluorophore needs to be determined prior to any experiment, since excess fluorophores that remain unbound lower the total signal height.

Application of fluorescence polarization

The principle of fluorescence polarization has been used for a variety of applications, all of them are based on changes in rotation and mobility of a fluorescently labeled molecule due to a change in molecular weight. This includes direct binding assays, e.g. binding of a fluorescent ligand to a receptor[248], antibody-antigen reactions[239,249] and DNA-protein binding[250], competitive binding assays, enzyme assays as well as degradation assays that are accompanied with a size reduction[242]. Applications of the fluorescence polarization principle on the Aβ peptide include up to now only a degradation assay with proteases[251] and approaches to determine binding affinities to e.g. fibrinogen[252] and an indol[124] derivative. Interestingly, *Allsop et al.* showed the first attempt to apply fluorescence anisotropy for the detection of aggregated Aβ species[253].

To allow a transfer of the fluorescence polarization principle to an experimental application, appropriate tracer molecules have to be used, which are typically generated by linking a fluorescent dye to a reactive derivative of the analyte[244]. The fluorescent tracer molecule needs to meet certain requirements. First of all, the linkage of the fluorophore to the ligand protein needs to be short and rigid to prevent propeller effects where, despite binding of tracer to the interaction partner, only little increase in polarization values would be detectable[239]. However, the linker should not be too short, as this might interfere with the binding of the tracer. Second, the difference between the initial polarization value and the maximal detectable value should be high enough to be able to detect changes in polarization, presupposing a fluorescent tracer molecule with a low molecular weight. Finally, the fluorescence lifetime of the fluorophore is a decisive factor that limits the detectable

molecular weight since changes in polarization values depend on the rotation of the fluorophore related to its fluorescence lifetime. Figure 15 describes the relationship between polarization values and the molecular weight of four different fluorophores with distinct lifetimes[242]. For example, with the frequently used tracer dye fluorescein, which has a fluorescence lifetime of 4 ns, changes in the molecular weight of up to ~100 kDa can be detected by fluorescence polarization. By use of fluorophores with longer life times, interactions with higher molecular weight molecules can be followed.

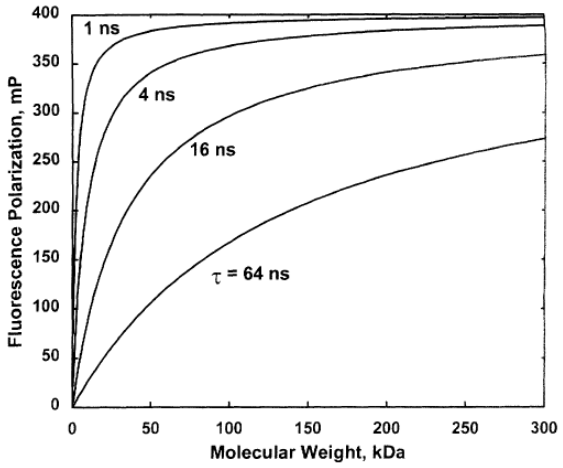

Figure 15 | Correlation between fluorescence lifetime and detectable molecular weight
The detectable molecular weight is dependent on the fluorescence lifetime of the used fluorophore (Image from Owicki, 2000[242]).

Advantages of fluorescence polarization

The advantages of using fluorescence polarization (FP) in experimental applications are numerous. First, FP measurements do not affect the sample and allow a direct and nearly instantaneous measurement[245]. Contrary to other homogeneous fluorescence techniques like energy transfer measurements (FRET), that presupposes two labeled interaction partner, no multiple labeling is necessary and low-affinity interactions can be measured in real-time without radioactive ligands[235]. Second, since a separation of the bound and free species is not required equilibrium and kinetic analysis can be easily performed[239,245]. This further enables to use fluorescence polarization based approaches in e.g. high-throughput screenings for drug discovery.

4.

Aim of the study

4. Aim of the study

In-depth understanding of the molecular processes underlying the aggregation of soluble Aβ42 monomers into fibrillar assemblies in AD requires sensible and reliable techniques to capture the kinetic profile of the aggregation. Therefore, the aim of this study was to establish a new assay to monitor the aggregation process of Aβ42 in a time-resolved manner based on fluorescence polarization. Following, the assay should be used to characterize the properties of seeding-competent aggregate species *in vitro* and *in vivo*. For the latter, a method needs to get established to extract Aβ aggregate species from biosamples and allow their subsequent analysis regarding a potential to accelerate the spontaneous Aβ42 aggregation reaction. The method is then ought to be applied to transgenic AD mouse samples as well as human brain and CSF samples. Finally, the assay should be used to identify small molecules that target specifically disease-relevant seeding-competent Aβ42 aggregate species. By systematic structure-activity relationship studies crucial structural requirements of a compound to mediate aggregation inhibiting effects are ought to be evaluated and the mechanism of action of potential hit compounds will be assessed.

5.

Results

5.1

Establishment of a fluorescence polarization-based Aβ42 aggregation assay

5.1 Establishment of a fluorescence polarization-based Aβ42 aggregation assay

Until now, monitoring of the amyloid-β aggregation process in a time-resolved manner was dependent on the utilization of the Thioflavin T (ThT) assay. This is, as already mentioned, a spectroscopic technique based on an absorbance spectrum shift of the benzothiazol dye ThT accompanied with increased fluorescence intensity upon binding to β-sheet-rich amyloid structures. The ThT assay is routinely used to monitor amyloidogenic fibril formation *in vitro*[254] and is well suited for histological applications[230]. However, it exhibits a weakness when being used to screen for small molecules and compounds that influence the Aβ aggregation process as the dye can interfere with the screened compounds in a competitive binding reaction. Aiming to provide an alternative and reliable method to monitor the Aβ aggregation independently of high concentrations of binding dyes, the first part of the project was focused on the establishment of a new Aβ42 aggregation assay by taking advantage of the fluorescence polarization principle.

5.1.1 Demonstration of characteristic properties of fluorescence polarization

The dependency of fluorescence polarization on the molecular volume and, associated with that, the molecular weight was already discussed in the introduction by consulting *Equation 2*. To verify this correlation experimentally various proteins of different molecular weights were initially N-terminally labeled with the fluorophore FAM (5-Carboxyfluorescein): ^{FAM}Aβ42: 4.5 kDa; ^{FAM}Ribonuclease A: 13.7 kDa; ^{FAM}Carbonic Anhydrase: 29 kDa; ^{FAM}BSA: 66 kDa; ^{FAM}Apoferritin: 433 kDa. Measurement of the FP values of these proteins resulted in a clear increase of FP with increasing molecular weight, starting from ^{FAM}Aβ42 (67 mP) to ^{FAM}BSA (~156 mP) (Fig. 16). However, the polarization signal curve reached saturation and curve fitting suggested that ^{FAM}Apoferritin (~210 mP) does not run within the detectable dynamic range. As already mentioned, the maximal achievable signal height is limited by the fluorescence lifetime of the fluorophore. Therefore, these results are in agreement with published literature, suggesting that with FAM's fluorescence lifetime of ~4 ns the dynamic range is expected to be restricted to a molecular weight of 50-100 kDa of soluble, folded proteins (Fig. 15)[242].

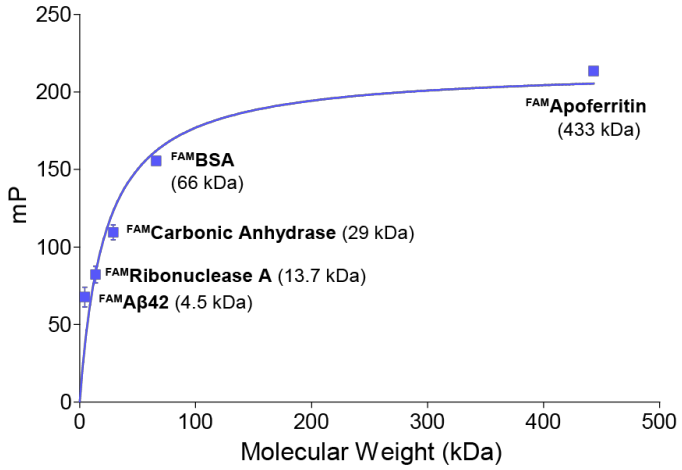

Figure 16 | Dependency of fluorescence polarization from molecular weight
Analysis of FAM-labeled proteins of various sizes reveals an increase of polarization values with increasing molecular weight.

5.1.2 Model for a fluorescence polarization-based Aβ aggregation assay

On the basis of *Equation 2* and confirmed by the obtained first results, the general feasibility of using a fluorophore-labeled Aβ42 monomer as a tracer to follow the aggregation of Aβ42 peptides over time was anticipated in an environment of constant viscosity. A small amount of a fluorescently-labeled Aβ42 monomers (^{FAM}Aβ42) was ought to be used as a tracer (Fig. 17). As a monomer this tracer would be highly mobile and able to rotate fast in relation to the fluorescence lifetime of the fluorophore. However, it can be assumed that throughout the aggregation process the tracer would get incorporated into growing Aβ42 assemblies resulting in a decrease in rotation. The decelerated tracer mobility due to an increasing molecular weight could then be monitored by an increase of polarization when maintaining constant viscosity and temperature.

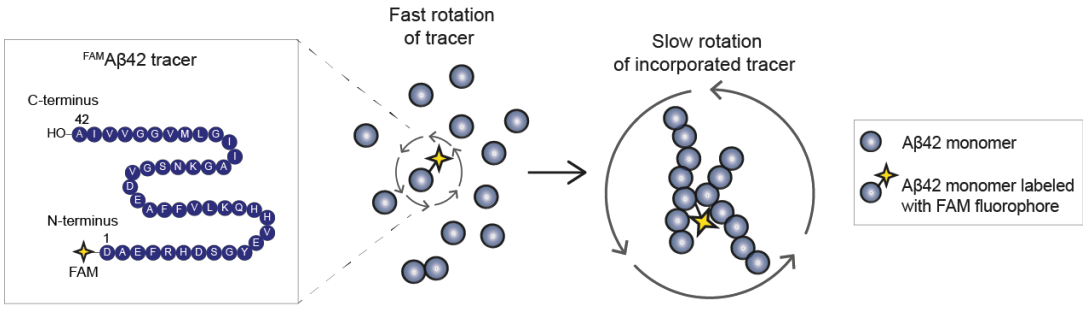

Figure 17 | Model for a fluorescence polarization-based Aβ42 aggregation assay (Aβ42-FP assay)
N-terminally fluorophore-labeled Aβ42 monomer constitutes a fluorescent tracer molecule (^{FAM}Aβ42). Due to its small size, the tracer alone rotates fast in relation to the fluorescence lifetime of the fluorophore. Upon incorporation of the tracer into bigger aggregates the rotation is slowed down as a result of an increasing molecular weight.

5.1.3 Establishment of assay conditions

Basic conditions for the Aβ42-FP assay were already established in our lab within the diploma thesis of Lydia Brusendorf[255] (e.g. assessment of assay buffer and concentrations of Aβ42 monomers and tracer). Different conditions were systematically tested and optimized to ensure maximal signal readout with concurrently minimal material consumption.

Initially, two different dyes conjugated to Aβ42 monomers were tested as potential tracer molecules, ^{HiLyte}Aβ42 (Fluor 488-labeled) and ^{FAM}Aβ42 (5-Carboxyfluorescein-labeled). In both cases 10 µM Aβ42 monomers were mixed with different tracer concentrations (0.5 %, 1 % and 2 %) and the FP values were measured. It has to be noted that only four high-performance LEDs (light emitting diode) for fluorescence polarization measurements were available within the plated reader device (LED 1: 470 nm; LED 2: 530 nm; LED 3: 590 nm; LED 4: 635 nm)[256]. LED 1 was used and FP was measured at 470/528 nm as it suited best to the wavelengths of HiLyte (488/528 nm) and FAM (492/518 nm). Figure 18a shows that in principal ^{HiLyte}Aβ42 can be used as a tracer molecule as an increase of polarization could be detected throughout the aggregation process. However, the signal increase was only ~Δ70 mP with 2 % tracer. In comparison, the use of Aβ42 monomer labeled with FAM as a tracer revealed a characteristic sigmoidal aggregation profile (Fig. 18b). Aiming for a maximal signal range between the starting position in the lag phase and final values at the plateau phase different ^{FAM}Aβ42 tracer concentrations (0.5 %, 1 % and 2 %) were tested. The concentration of the tracer needs to be high enough to get incorporated, cause an FP signal and thereby detect many emerging aggregates. Since the resulting FP values represent the weighted average of bound and free tracer, the use of a high tracer concentration could lower detectable changes in FP values. Furthermore, FAM is a known inhibitor of the Aβ aggregation[222] and would delay the aggregation reaction at too high concentrations. After testing different tracer concentrations, 0.5 % of ^{FAM}Aβ42 (0.05 µM) was chosen as the concentration for routine applications as it resulted in a signal increase of ~170 mP. Increasing the concentrations of the tracer up to 2 % did not strongly affect the aggregation process, but in the presence of 2 % tracer the slope of the curve in the exponential phase leveled out. Additionally, also the plateau height was reduced, demonstrating the impact of potentially unbound tracer molecules.

With regard to a minimal material consumption different Aβ42 monomer concentrations (5, 10, 20 µM) were tested (Fig. 18c). Use of 5 µM Aβ42 monomers incubated with 0.5 % ^{FAM}Aβ42 did not lead to a characteristic sigmoidal aggregation curve, which was indeed observed with 20 µM Aβ42. Here, the lag phase was quite short and potential seeding effects might not be properly distinguishable. Therefore, using 10 µM Aβ42 together with 0.5 % ^{FAM}Aβ42 (0.05 µM) for the

aggregation process revealed the ideal compromise to monitor spontaneous and seed-mediated Aβ42 aggregation *in vitro*.

Since the formation of Aβ42 aggregates is also dependent on the ion content of the buffer[55], two different assay buffers were tested (Fig. 18d): PBS (Phosphate-buffered saline) and LSB (low salt buffer). The application of PBS resulted in a fast Aβ42 aggregation with a very short lag phase due to the higher ion content. In contrast, the low salt buffer LSB revealed a longer lag phase, allowing a better resolution of the potential seeding with FP assays.

Two other major properties of the ^{FAM}Aβ42 tracer had to be investigated. First of all, the tracer needs to be stable over time to allow time-resolved measurements and second the observed increase of FP needs to result from specific interactions between ^{FAM}Aβ42 tracer molecules and non-labeled monomers. Therefore, it was tested whether Aβ42 monomers associate with free FAM molecules and result in a time-dependent increase of the FP signal (Fig. 18e). The reaction of 0.05 µM ^{FAM}Aβ42 with 10 µM Aβ42 monomers again resulted in a rise of FP values (up to 250 mP) due to the incorporation of the tracer into the growing aggregates. In comparison, addition of 0.05 µM FAM to 10 µM Aβ42 monomers did not cause an increase of FP, indicating that the Aβ42 peptides in the FAM-labeled tracer molecules are critical for the interaction with unlabeled Aβ42 monomers. Additionally, it was demonstrated that the fluorescence intensity of the tracer stays stable over the measured time period.

After examination of different assay conditions the final setup for the ^{FAM}Aβ42/Aβ42 co-polymerization assay was determined (Fig. 18f). 0.05 µM ^{FAM}Aβ42 together with 10 µM Aβ42 monomers (^{FAM}Aβ42/Aβ42) in LSB buffer proved to be the optimal conditions to obtain sigmoidal aggregation profiles with a lag phase between 5-8 h depending on the Aβ42 monomer preparations. Accordingly, a plateau was reached after ~10 h. The measurement took place in cycles of 15 min for a minimum of 14 h. Within the first 30 minutes of measurement a decrease in FP values could be observed due to temperature effects and equilibration of the assay plate at 37°C. As a control 0.05 µM ^{FAM}Aβ42 alone showed a consistent low signal.

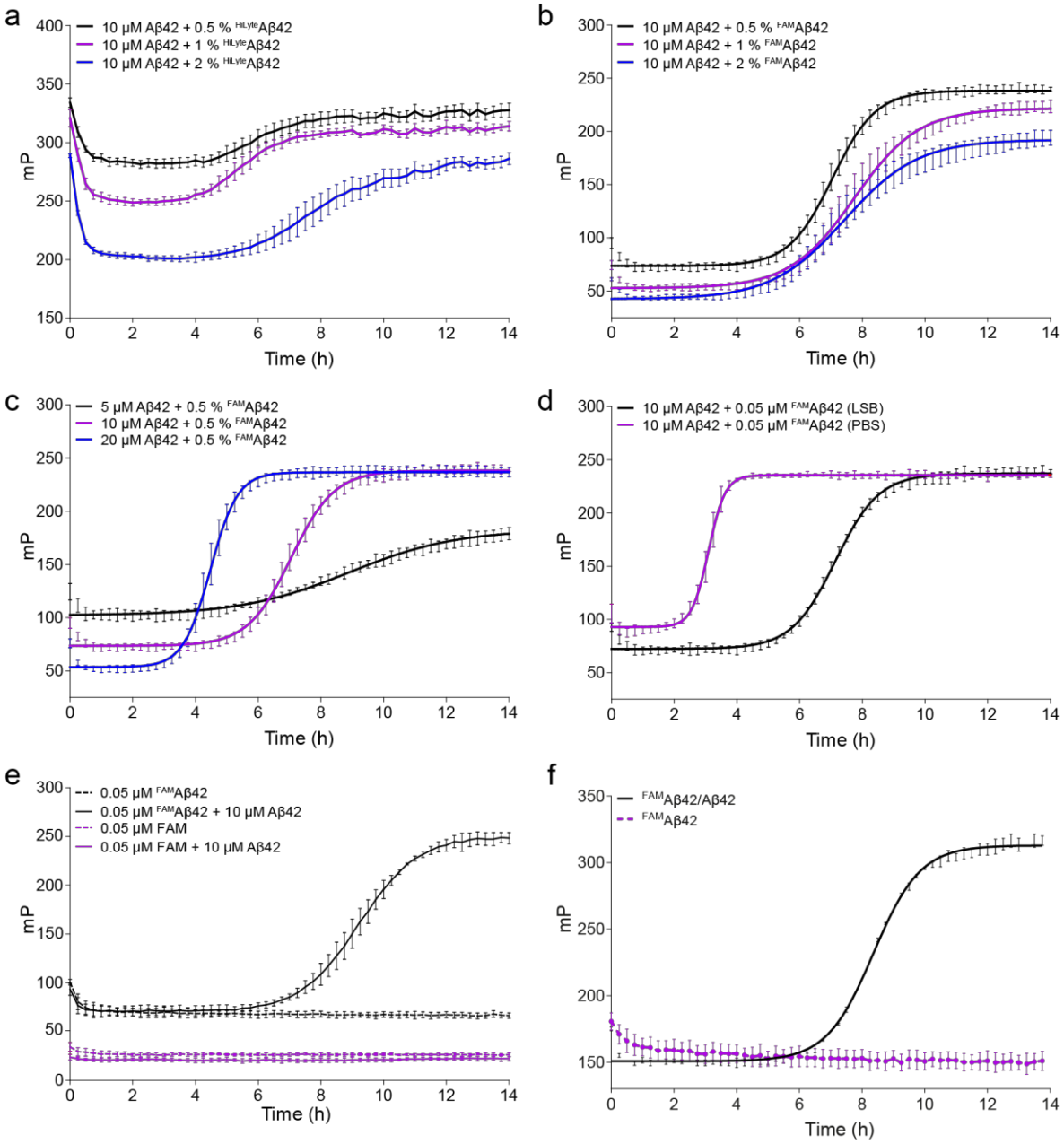

Figure 18 | Establishment of the assay conditions for the Aβ42-FP assay

(a) Using HiLyteAβ42 as a candidate tracer for the Aβ42-FP assay reveals only a small signal range. (b) Aggregation of 10 µM Aβ42 monomers with different concentrations of FAMAβ42 peptides (0.5, 1 and 2 %) as a tracer. Signal ranges with different tracer concentrations are similar and reveal a characteristic sigmoidal curve. With 2 % tracer the sigmoidal curve gets flat. (c) Aggregation of different Aβ42 monomer concentrations (5, 10 and 20 µM) with 0.5 % FAMAβ42 tracer peptides. Aggregation with 10 µM Aβ42 monomers leads to a sigmoidal growth curve with a reasonable long lag phase. (d) Aggregation of 10 µM Aβ42 monomers in phosphate-buffered saline (PBS) or low salt buffer (LSB). Aggregation in PBS proceeds faster than in LSB as represented by a very short lag phase. (e) Specificity and stability of FAMAβ42 tracer over time. The signal height obtained with FAMAβ42 molecules is stable over 15 h. The increase of FP values is specific due to an interaction of FAMAβ42 and unlabeled Aβ42 monomers and not caused by unspecific binding of FAM molecules to Aβ42 peptides. (f) Final assay conditions for the Aβ42 fluorescence polarization assay. 10 µM Aβ42 monomers are mixed with 0.05 µM FAMAβ42 tracer, which gets incorporated in growing aggregates. The resulting increase in molecular weight leads to heigher FP values, demonstrated by the characteristic sigmoidal curve shape of the Aβ42 aggregation process.

Additionally, the technical set up in the iControl software of the Tecan plate reader device was optimized. For instance, the software program was supplied with an incubation step in a parking position between the cycles of the kinetic measurement every 15 minutes. The incubation was then performed at the heating position to ensure proper temperature distribution for 13 minutes. After that the plate was relocated to the measurement head just shortly before the actual measurement. Considering that temperature highly effects the aggregation of the Aβ42 peptides, this reduced variations in temperature during the measurement. Furthermore, the G-factor as well as the Z-position were determined for a maximal signal outcome. The G-Factor is a device-specific factor that compensates for differences in optical components between the parallel and the perpendicular measurements and must be determined for any used device individually[256]. It can be examined for the wavelength of the fluorophore by measuring a sample with a known polarization value (e.g. 1 nM fluorescein as reference against 10 mM NaOH as blank). The Z-Position represents the height of the measurement head above the microplate. It was determined by using 1 nM fluorescein measured at various positions within the 384-well plate (100 µl/well) to examine uniformity within the plate.

	G-Factor	Z-Position
Tecan1000	1.19	26000
Tecan1000Pro	1.16	23530

Table 4 | Determination of the G-Factor and the Z-Position for the used Tecan plate readers

5.1.4 Characterization of the Aβ42-FP assay

In theory, it is expected that due to the low concentration of ^{FAM}Aβ42 tracer it gets completely incorporated into Aβ42 aggregates within the aggregation process. Additionally, the tracer could also bind to existing and pre-formed aggregates. To address this question, 0.05 µM ^{FAM}Aβ42 was directly added to Aβ42 monomers or to pre-formed Aβ42 aggregates (Fig. 19a). Addition of tracer to Aβ42 monomers resulted in the expected sigmoidal curve progression, starting with low FP values and reaching a plateau after 8 h. In contrast, FP was already at a high value when the tracer (^{FAM}Aβ42) was added to pre-formed Aβ42 aggregates and FP was immediately measured. This indicates that the tracer is also able to directly bind to pre-formed aggregates. However, the reached plateau was lower compared to the aggregation reaction starting with Aβ42 monomers in the 384-well plate. It has to be noted that the pre-formed aggregates originated from a different aggregation reaction where 10 µM Aβ42 monomers were incubated in Eppendorf tubes for 24 h (37°C, 300 rpm). Thus, Aβ42 aggregates of different size and quality might have been formed there and would thus explain the lower plateau.
To further validate that ^{FAM}Aβ42 peptides indeed are bound to Aβ42 aggregates and to ensure that this does not impair the fibril formation process, immunoelectron microscopy (IEM) studies with the

aggregation end products (t = 15 h) with and without FAM-tracer were performed (Fig. 19b). The tracer was detected using an anti-FITC primary antibody (mouse) and subsequent incubation with 12 nm anti-mouse gold particles. Indeed, the presence of incorporated ^{FAM}Aβ42 molecules (indicated with arrows) could be detected. Furthermore, the observed morphology of the ^{FAM}Aβ42/Aβ42 fibrils was comparable to the Aβ42 aggregates, indicating that the tracer does not influence the fibril formation process.

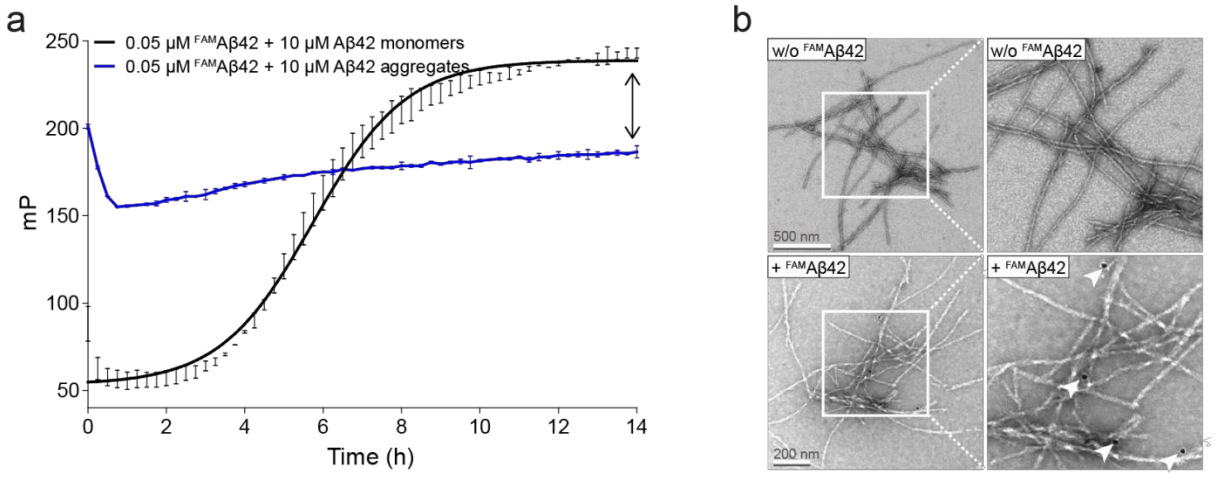

Figure 19 | Direct binding of ^{FAM}Aβ42 tracer molecules to pre-formed Aβ42 aggregates
(a) Incubation of 10 µM Aβ42 monomers or pre-formed Aβ42 aggregates (20 µM, 24 h, 37°C, 300 rpm) with 0.05 µM ^{FAM}Aβ42. The tracer seems to directly bind to pre-formed aggregates demonstrated by means of high polarization values at t = 0 h. (b) Immunoelectron microscopy (IEM) of ^{FAM}Aβ42/ Aβ42 aggregation products. IEM images of 10 µM Aβ42 monomers with or without 0.05 µM ^{FAM}Aβ42 after 15 h labeled with primary anti-FITC antibody and secondary 12 nm anti-mouse gold particle. Gold particles are indicated by arrow heads and represent bound tracer moleucles at fibrillar Aβ42 aggregates. Aβ42 aggregates without tracer feature a comparable fibrillar morphology.

To characterize the ^{FAM}Aβ42/Aβ42 co-polymerization assay in a more comprehensive manner, a time-resolved analysis was performed (Fig. 20). Therefore, a standard aggregation reaction (10 µM Aβ42 + 0.05 µM ^{FAM}Aβ42) was performed and samples were taken at different time points and analyzed regarding molecular size and morphology of the corresponding Aβ42 species at the given time points (Fig. 20a). Figure 20b shows the atomic force microscopy (AFM) analysis of the time points t = 0 h and t = 14 h. At the very beginning (t = 0 h) only monomeric or small oligomeric Aβ42 species are detected. The plateau was reached after 14 h, corresponding to long fibrillar Aβ42 aggregates. Analysis of samples by NativePAGE shows that in the lag phase (between 0-6 h) the amount of monomeric Aβ42 steadily decreases, accompanied by a simultaneous increase in lower molecular weight assemblies (LMWAs) ranging from 100-400 kDa (Fig. 20c). After 8 h, the exponential phase starts. This phase is dominated by the time-dependent formation of large Aβ42 aggregates that are stuck in the pockets of the gel.

Next, to compare the Aβ42-FP assay with the routinely used ThT assay the aggregation of 10 µM Aβ42 was simultaneously monitored with both methods (10 µM Aβ42 + 0.05 µM ^{FAM}Aβ42 for measurement of FP; 10 µM Aβ42 + 5 µM ThT for measurement of fluorescence intensity at 440/485 nm) (Fig. 20d). Thereby, a concentration of 5 µM ThT was necessary to obtain a reproducible signal to noise ratio. Both measurement types revealed comparable aggregation profiles with a sigmoidal curve progression. However, with the FP assay in comparison to the ThT assay a longer lag phase (~2 h) was observed. This could be due to the fact that the incorporation of FAM-labeled Aβ42 peptides into Aβ42 fibrils slows down polymerization[222]. However, it may also be that the relatively high concentration of ThT (5 µM) in the reaction stimulates spontaneous Aβ42 nucleation. Still, the increase in polarization values over time correlates with the formation of β-sheet-rich Aβ assemblies throughout the course of aggregation.

Finally, the samples were analyzed on dot blot assays (DB) using the protofibril-specific anti-Aβ antibody 352. This is a monoclonal anti-Aβ antibody that was raised against pre-formed, seeding-competent fibrillar and protofibrillar Aβ42 aggregates (Fig. 20e). In comparison, the sequence-specific monoclonal antibody 6E10 is shown which features reactivity to amino acid residue 1-16 of the Aβ peptide and thus recognizes both higher molecular weight Aβ42 aggregates as well as monomers in dot blot assays. DB analysis revealed that the first 352-reactive species are formed after 6 h, indicating the presence of the first fibrillar oligomers at the transition of the lag phase to the growth phase (Fig. 20f, g). Taken together, time-resolved analysis of the Aβ42-FP assay indicates that the assay is capable to follow the aggregation reaction of the Aβ42 peptide displayed by the sigmoidal curve progression. During the lag phase 352-reactive, β-sheet-rich structures seem to form, which then lead to an increase in polarization values in the subsequent growth phase. The final plateau phase represents high β-sheet-rich Aβ assemblies with fibrillar morphology; it is reached when the ratio of bound to unbound FAM-tracer is maximal.

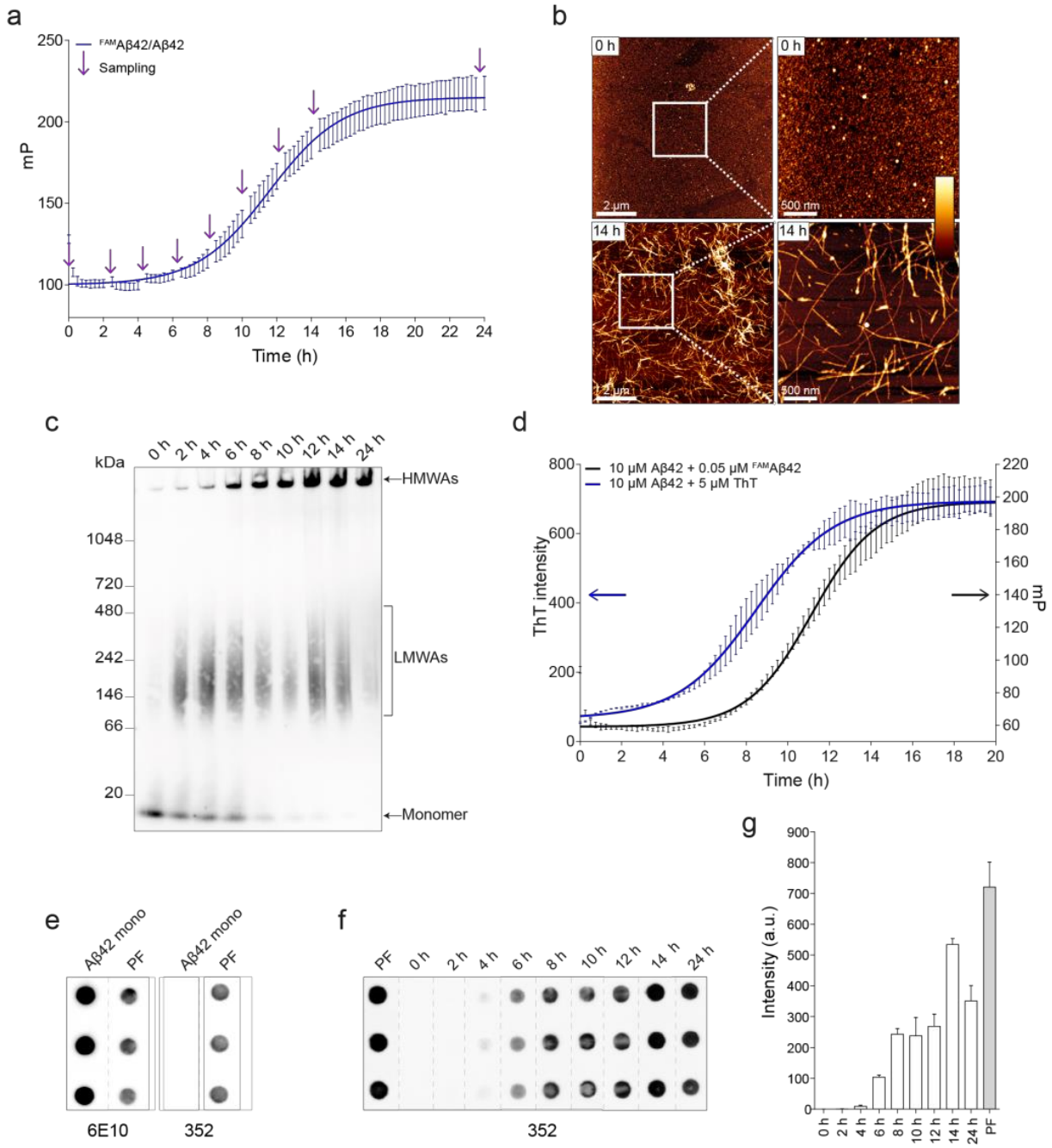

Figure 20 | Time-resolved analysis of FAMAβ42/Aβ42 co-aggregation in FP assays

(a) Time-resolved Aβ42-FP assay. Samples were taken at the indicated time-points (arrow heads). (b) AFM analysis of t = 0 h and t = 14 h. Left: 10 x 10 µm, scale bar: 2 µm; right: 3 x 3 µm; scale bar: 500 nm; color gradient 0 h: 0-5 nm height; color gradient 14 h: 0-10 nm height. (c) Analysis of samples taken from *a* with NativePAGE (6E10) indicates that the assay captures an increase of large Aβ42 structures. (d) Simultaneous analysis of 10 µM Aβ42 aggregation with Aβ42-FP and ThT assays. Both assays reveal similar kinetic Aβ42 aggregation profiles. (e) Characterization of 6E10 and 352 antibodies using dot blot assays. The conformation-specific antibody 352 detects only pre-formed fibrillar assemblies (protofibrils, PF), whereas the sequence-specific antibody 6E10 also comprises reactivitiy for Aβ42 monomers (Aβ42 mono). (f) Analysis of samples taken from *a* with dot blot assays (100 ng; detection with 352). The 352 antibody captures the formation of fibrillar oligomers during the transition of the lag phase into the growth phase. (g) Quantification of dot blot assay from *f*. (Data were partly modified from Nicole Groenke).

5.1.5 Applicability of the Aβ42-FP assay for the detection of seeding effects

The FP assay is ought to be used not only to monitor and detect spontaneous Aβ42 aggregation, but also to evaluate the potential seeding activity of biological samples. Hence, the assay needs to reliably detect seeds and their shortening of the lag phase with high sensitivity. Therefore, pre-formed fibrillar Aβ42 assemblies (protofibrils, PF) prepared form synthetic peptides were utilized as *in vitro* seeds in a proof of principle experiment. These species are predominantly small, fibrillar and β-sheet-rich Aβ42 assemblies as observed by AFM and ThT fluorescence intensity measurements (Fig. 21a, b). However, analysis on a native gel indicates that the preparation of PFs always consists of a mixture of various sized structures, ranging in size between 60-500 kDa. Furthermore, it also contains bigger assemblies that remain stuck in the gel pocket (Fig. 21c).

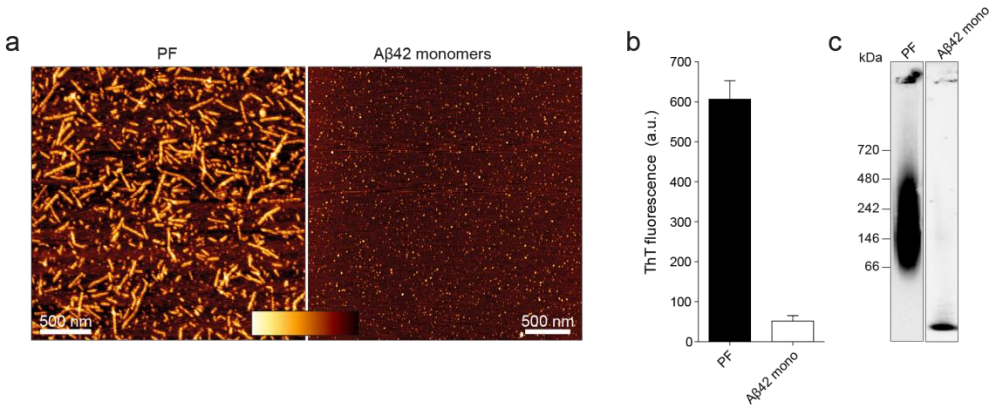

Figure 21 | Characterization of protofibrils as seeds
(a) Analysis of pre-formed protofibrils (PF) and Aβ42 monomers by AFM; 3 x 3 µm, scale bar: 500 nm, color gradient indicates 0-10 nm height for PF and 0-5 nm height for Aβ42 monomers. (b) ThT assay of pre-formed PFs and Aβ42 monomers (4.5 µM) with ThT (20 µM) measured in arbitrary units (a.u.). (c) Analysis of pre-formed PFs and Aβ42 monomers (mono) by NativePAGE (detection with 6E10) reveals the presence of a mixture of various sized structures.

Right from the start different concentrations (5-200 nM, monomer equivalent) of PFs were added as seeds to a standard FP assay (10 µM Aβ42 + 0.05 µM ^{FAM}Aβ42) (Fig. 22a). Through addition of these pre-formed Aβ42 aggregate seeds the lag phase in FP assay was shortened in a concentration-dependent manner, confirming previous data that the spontaneous Aβ42 aggregation can be seeded with pre-formed aggregates[136]. For quantification of the seeding activity the data were first subjected to nonlinear curve fitting. Then, the inflection point (IP) was determined for each aggregation profile, describing the time point where the half-maximal FP intensity is reached (t_{50}) (Fig. 22b). Finally, the t_{50} values were determined for the non-seeded (control) and the seeded (sample) ^{FAM}Aβ42/Aβ42 aggregation reactions and subtracted from each other to obtain the seeding activity of the sample ($\triangle t_{50} = t_{50}ctrl - t_{50}sample$). Quantification of the seeding activities of PFs shows that a concentration of ~50 nM results in a significantly reduced lag phase. In contrast, Aβ42 monomers at the highest tested concentration (200 nM) did not show any seeding activity (Fig. 22c).

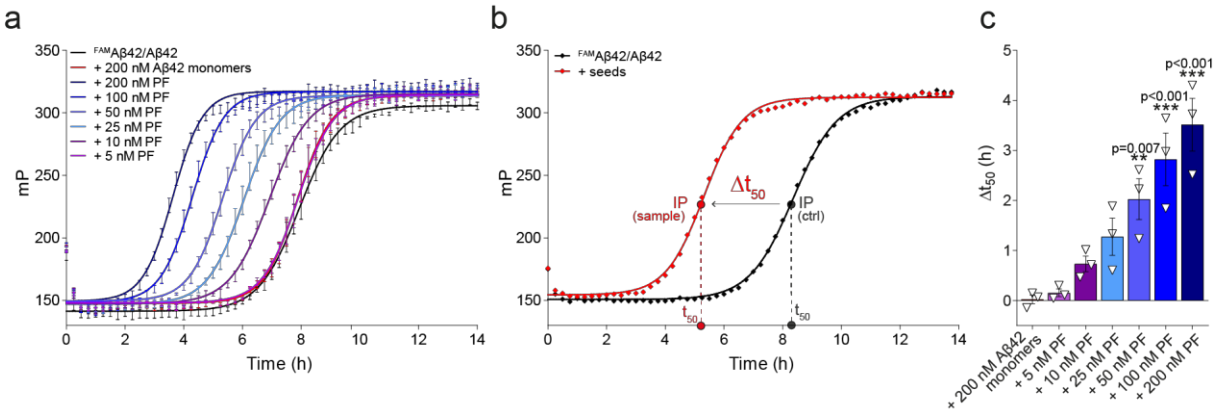

Figure 22 | Applicability of Aβ42-FP assay for the detection of seeding effects
(a) Protofibrils (PFs) induce a concentration-dependent acceleration of the ^{FAM}Aβ42/Aβ42 co-aggregation. (b) Quantification of the seeding effects on ^{FAM}Aβ42/Aβ42 co-aggregation analyzed in FP assays. To calculate the seeding activity of a sample ($\triangle t_{50}$), the calculated t_{50} value of the sample was substracted from the t_{50} value of the unseeded control. (c) Quantification of concentration-dependent seeding effects from three independent experiments. Data are mean ± SEM (n = 3) and individual values are presented as triangles. Statistical significance is referred to seeding with 200 nM Aβ42 monomers and was assessed by one-way ANOVA followed by Dunnett's multiple comparison post hoc test.

The seeding effects mediated by PFs were also used to determine the sensitivity of the assay. As already mentioned, PF preparations comprise as mixture of species (Fig. 21c), making it difficult to clearly define the molecular weight of PFs and with that a precise estimation of detection limit of the Aβ42-FP assay. However, the average molecular weight of the low molecular weight smear can be estimated to ~200 kDa. With a molecular weight of one Aβ42 monomer unit of 4.5 kDa, the ~200 kDa species would represent an aggregate species consisting of ~44 monomers. Since a minimum concentration of PFs of 50 nM was sufficient to obtain a reproducible shortening of the lag phase (Fig. 22), the detection limit of the Aβ42-FP assay was calculated to be ~11 fmol.

Since one objective of the project was to apply the Aβ42-FP assay for the detection of seeding-competent Aβ42 aggregate species in biological samples, the detection limit and sensitivity of the assay can be a restraining factor. Therefore efforts were undertaken to optimize the assay sensitivity. Measurements of kinetic profiles comprise repetitive measurement cycles, here every 15 minutes. Thereby it is recommended to subject the samples to a short shaking period before each measurement to prevent the aggregates from sedimentation and rather keep the material in solution. Since it has been shown previously that duration and intensity of shaking can significantly accelerate the aggregation process and the seeded conversation of the prion protein into aggregates[257,258], various shaking conditions were systematically tested (linear and orbital shaking; shaking duration: 5 sec, 30 sec, 1 min; shaking amplitude: 2, 4 and 6 mm). Since no significant improvement of sensitivity could be detected with an extended shaking step before each FP measurement (*data not shown*), a shaking condition of 5 sec with an amplitude of 2 mm was used in standard FP measurements.

It was shown in several studies that the Aβ peptide can interact with other misfolded proteins such as α-synuclein and IAPP (islet amyloid polypeptide)[259-263]. Thus, these amyloidogenic proteins could potentially also accelerate the Aβ42 aggregation process in a cross-seeding reaction, leading to false-positive results when analyzing e.g. complex biosamples. To analyze if the assay exclusively responds to Aβ42 aggregate species or reacts also to other aggregate forms, such as fibrillar α-synuclein or IAPP aggregates[264,265], such structures were produced under standard conditions and added as seeds (200 nM) to the established Aβ42-FP assay (Fig. 23). The fibrillar morphology of the prepared α-synuclein and IAPP aggregates was confirmed by AFM (Fig. 23a). In contrast to PFs obtained from Aβ42 monomers that clearly accelerated the Aβ42 aggregation reaction, neither IAPP nor α-synuclein aggregates influenced the polymerization process (Fig. 23b, c). Thus, these results indicate that the Aβ42-FP assay is template-specific and specifically responds to Aβ42 aggregate structures.

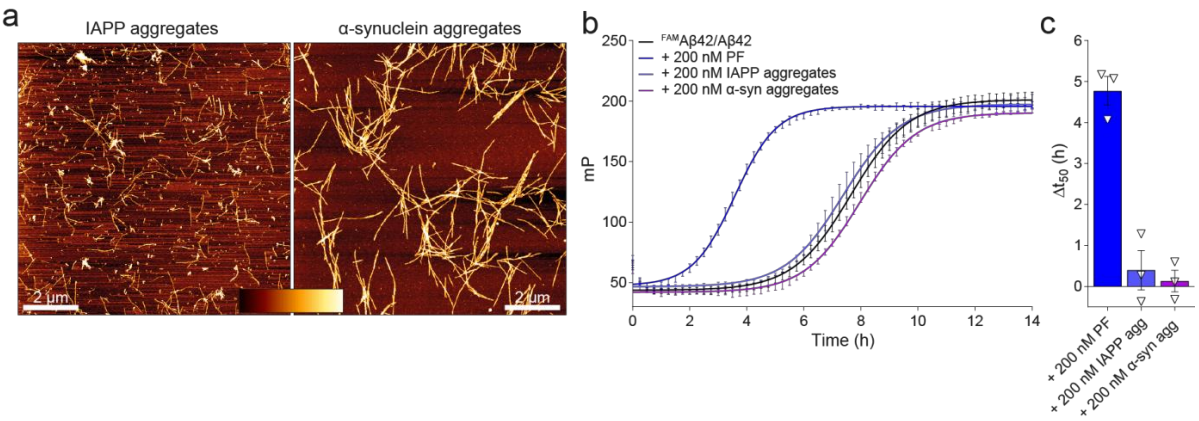

Figure 23 | Template-specificity of the Aβ42-FP assay
(a) AFM images from IAPP and α-synuclein aggregates demonstrate fibrillar aggregate structures; 10 x 10 µm, scale bar: 2 µm, color gradient indicates 0-5 nm height for IAPP and 0-10 nm height for α-synuclein. (b) The Aβ42-FP assay shows a high specificity for Aβ42 aggregate seeds (PF) as IAPP or α-synuclein aggregates do not accelerate the FAMAβ42/Aβ42 co-polymerization. (c) Quantification of seeding activity from three independent experiments; data are mean ± SEM (n = 3) and individual values are presented as triangles. Agg, aggreagtes.

5.1.6 Applicability of the Aβ42-FP assay for the detection aggregation inhibiting compounds

Next, it was assessed whether the Aβ42-FP assay is capable of detecting the effects of compounds on FAMAβ42/Aβ42 co-aggregation and thus would provide a suitable tool to screen for aggregation inhibiting small molecules. Therefore, known amyloid-binding molecules were utilized and their effects on the FAMAβ42/Aβ42 co-aggregation process were analyzed using the Aβ42-FP assay (Fig. 24). Previous studies already demonstrated the influence of (-)-epigallocatechin gallate (EGCG) on the Aβ42 aggregation pathway by redirecting the polypeptides into non-amyloid spherical aggregates and preventing amyloid-β fibrillogenesis[59]. Congo Red is widely used as a histological dye for amyloid detection and has previously also been described to inhibit amyloid fibril formation[266]. Finally, the

bis-diazo benzene dye Chrysamine G was initially developed as a cell permeable derivative of Congo Red and is a well-known probe for fibrillar aggregates. It also was previously found to act as an amyloid aggregation inhibitor. The compounds were added at sub-stoichiometric ratios to Aβ42 monomers (1 µM compound/10 µM Aβ42 monomers) and their effects were analyzed with the standard ^{FAM}Aβ42/Aβ42 co-polymerization assay. All three tested compounds significantly decreased the Aβ42 aggregation process by extending the lag phase with EGCG showing the most potent effect ($\triangle t_{50}i$ = 6.2) (Fig. 24a, c). To calculate the inhibitory effect of a compound ($\triangle t_{50}i$) the curves were subjected to non-linear curve fitting to obtain inflections points (IPs) and t_{50} values for all curves as described earlier. Following, the t_{50} value obtained from the inflection point of the Aβ42 control reaction was subtracted from the compound-treated t_{50} value ($\triangle t_{50}i = t_{50}sample - t_{50}ctrl$) (Fig. 24b). Interestingly, also the plateau heights were significantly decreased (Fig. 24a). This could reflect the formation of different aggregate structures in presence of the compounds featuring different binding properties that ultimately lead to higher amounts of unbound tracer molecules. In summary, these results indicate that the Aβ42-FP assay is suitable to detect the inhibitory effects of small molecules on spontaneous Aβ42 aggregation.

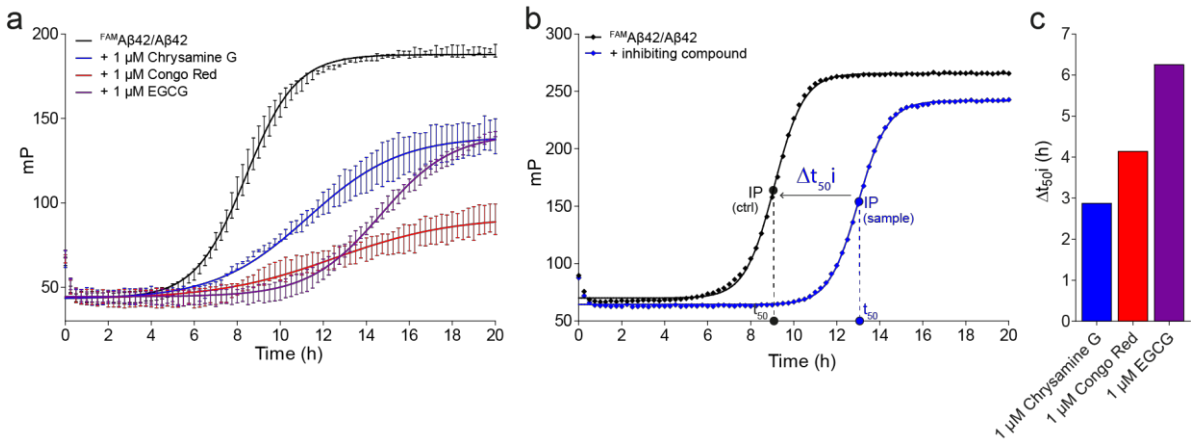

Figure 24 | Applicability of Aβ42-FP assay for the detection of aggregation inhibiting compounds
(a) Aβ42-FP analysis of the known amyloid aggregation inhibitors Chrysamine G, Congo Red and EGCG reveal an inhibiting effect of all tested compounds. (b) Scheme for the quantification of compound inhibiting effects. To calculate an inhibitory compound effect ($\triangle t_{50}i$), the t_{50} value of the spontaneous Aβ42 control reaction was substracted from t_{50} values of the sample. (c) Quantifaction of inhibitory compound effects from *a*.

5.1.7 Reproducibility of the Aβ42-FP assay

To evaluate the overall reproducibility and quality of the Aβ42-FP assay, the aggregation profiles of all cavities of a 384-well plate were analyzed (Fig. 25). Therefore, the standard ^{FAM}Aβ42/Aβ42 reaction (10 µM Aβ42 + 0.05 µM ^{FAM}Aβ42) was added to all 384 cavities of one plate and their resulting FP values were compared to each other (Fig. 25a). 93.5 % of the cavities showed a comparable result and in only ~6.5 % of the cavities a variation in lag phase and/or intensity was

observed after 20 h. To further exclude position-specific effects of the plate, the measured signal intensities were mapped to the plate and presented as a heat map (Fig. 25b). This illustration shows that a few specific wells in the plate are responsible for the altered signal intensities. For the assessment of the assay quality the Z-value was determined in four independent experiments. The Z-value reflects the dynamic range as well as the data variation associated with the signal measurements[267]. Thus, the Z-value is a statistical measure to assess the assay quality and to benchmark compound screening assays[267]. Figure 25c shows the signal intensities of the monomeric state (μ_{mono}) during the lag phase in comparison to the signal of the plateau phase of the aggregated form (μ_{agg}) from four independent experiments. The Z-factor was calculated using the following equation (μ: mean; SD: standard deviation; agg: Aβ42aggregated state; mono: Aβ42monomeric state):

$$Z = \frac{1 - \left(3SD_{agg} + 3SD_{mono}\right)}{\mu_{agg} - \mu_{mono}}$$

Z-values ranging between 0.87 and 0.93 were found within these four independent experiments (Fig. 25d), indicating that the established assay is indeed highly robust and reproducible. As literature esteems Z-values >0.5 as acceptable for high-throughput screening[267], the established FP assay has a high-quality standard.

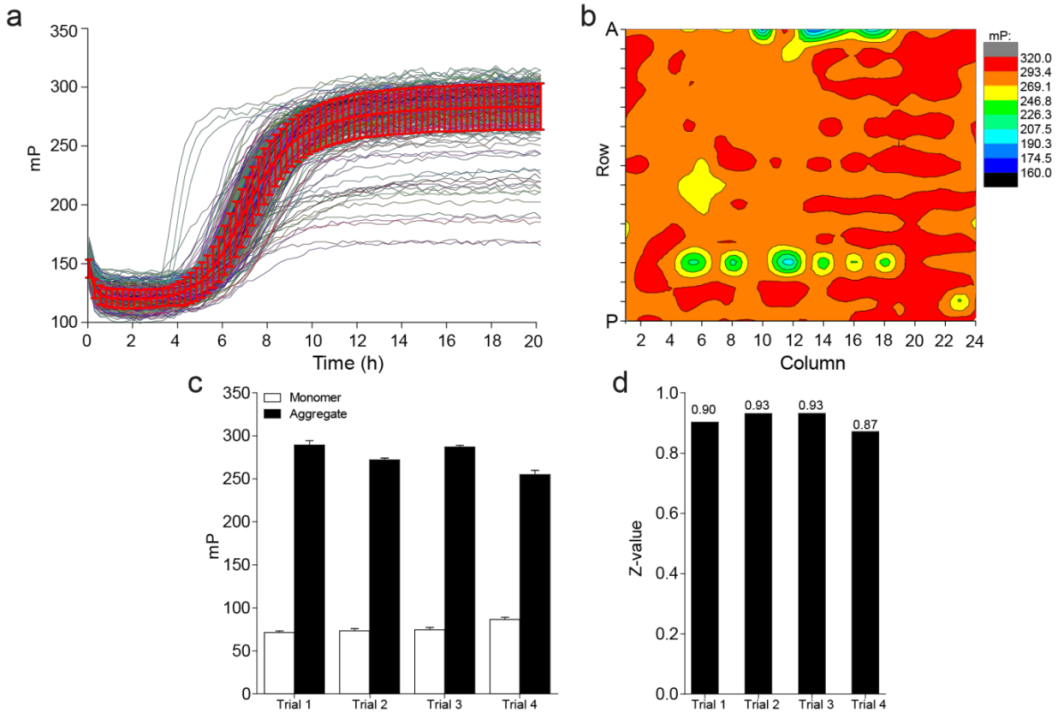

Figure 25 | Homogeneity of the fluorescence polarization values over a 384-well plate
(a) FP profiles of all cavities in a 384-well microtiter plate were obtained from a standard ^{FAM}Aβ42/Aβ42 reaction (10 μM Aβ42 monomers + 0.05 μM ^{FAM}Aβ42). 94 % of the data show very similar results. (b) Signal intensities after 20 h of all cavities shown in a heat map. The large area of the 384-well plate shows comparable FP signals. (c) Signal intensities of four independent experiments before and after aggregation are shown. (d) Calculated Z-values are depicted and indicate a high assay quality (Data were obtained from Nicole Groenke).

5.1.8 Assessment of intra-plate variations of FP-based Aβ42 aggregation profiles

Despite assessing the homogeneity of the FP assay in 384-well microtiter plates at the beginning of the project (Fig. 25), deviations of the obtained signals within one plate, e.g. shifts from left to right, were observed throughout the project probably due to variations in the manufacturing process of the microtiter plates. Figure 26a shows the FP values of the same Aβ42 peptide measured in three different rows of a 384-well plate (row 2, 12 and 22). Comparing the measured FP values in row 2 and 22 revealed that the lengths of the lag phases differed by ~2 h. Especially critical was the fact that accordingly seeded aggregation kinetics did not show the same shift and quantification of the $\triangle t_{50}$ values led to a difference of ~1.5h ($\triangle t_{50}(2) = 2.8$ h; $\triangle t_{50}(22) = 4.6$ h). Earlier experiments already showed that the addition of 200 nM PFs to Aβ42 aggregation reactions results in a maximum seeding effect in Aβ42-FP assays that cannot be resolved further (*data not shown*). Therefore, while strong seeding effects were unaffected from plate conditions, the investigation of spontaneous Aβ42 aggregation can be strongly influenced by intraplate differences (e.g. differences in the quality of individual wells).

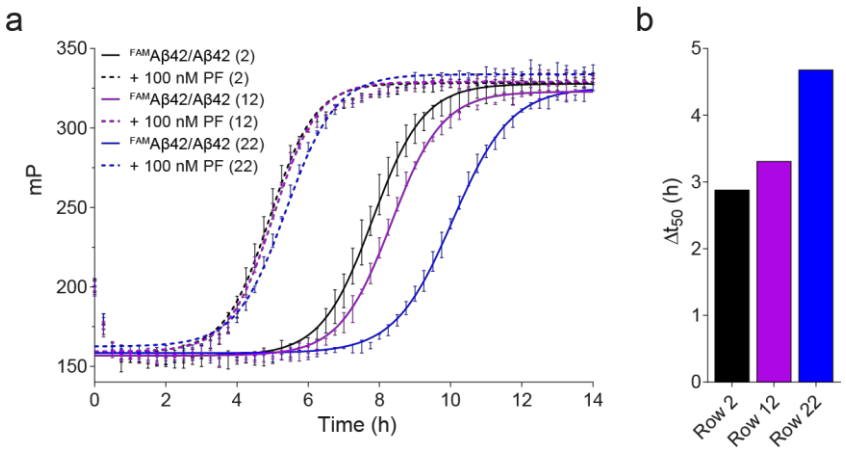

Figure 26 | Intra-plate deviations influence the outcome of aggregate measurements in Aβ42-FP assays
(a) Intra-plate deviations of the measured FP values were observed with a shift from left to right, affecting rather the spontaneous Aβ42 aggregation process than the seed-mediated formation of aggregates. (b) Quantification of seeding activity of PF seeds (100 nM) from *a* revealed a deviation of ~2 h between the three rows.

Considering that the assay is ought to be applied for the analysis of biological samples such obscure deviations in FP values would be a major concern, if controls are only investigated at one defined position in the assay plate. Therefore, it was analyzed if potential microplate-related deviations can be compensated when not only one, but several unseeded Aβ42 control samples are distributed over the microplate. Then, the seeding effect of a respective sample can be referred to the unseeded control that is in very close proximity to the analyzed samples. Figure 27a shows the plate layout with PF seeds (samples 1-9) depicted in blue and the surrounding Aβ42 monomer controls in grey. Analyzing all nine samples together, significant deviations between the nine seeded reactions could be

observed, but also within the Aβ42 monomer controls (Fig. 27b). However, when analyzing each sample individually and in regard to the nearby Aβ42 monomers controls these deviations were mainly abolished, illustrated exemplarily with samples 1 and 3 (Fig. 27c). The average standard deviation between the seeding activities of all nine samples was 7.3 % and the maximal deviation 13.2 %, indicating that the results are comparable and the obtained FP values from different samples can be compared on a plate (Fig. 27d).

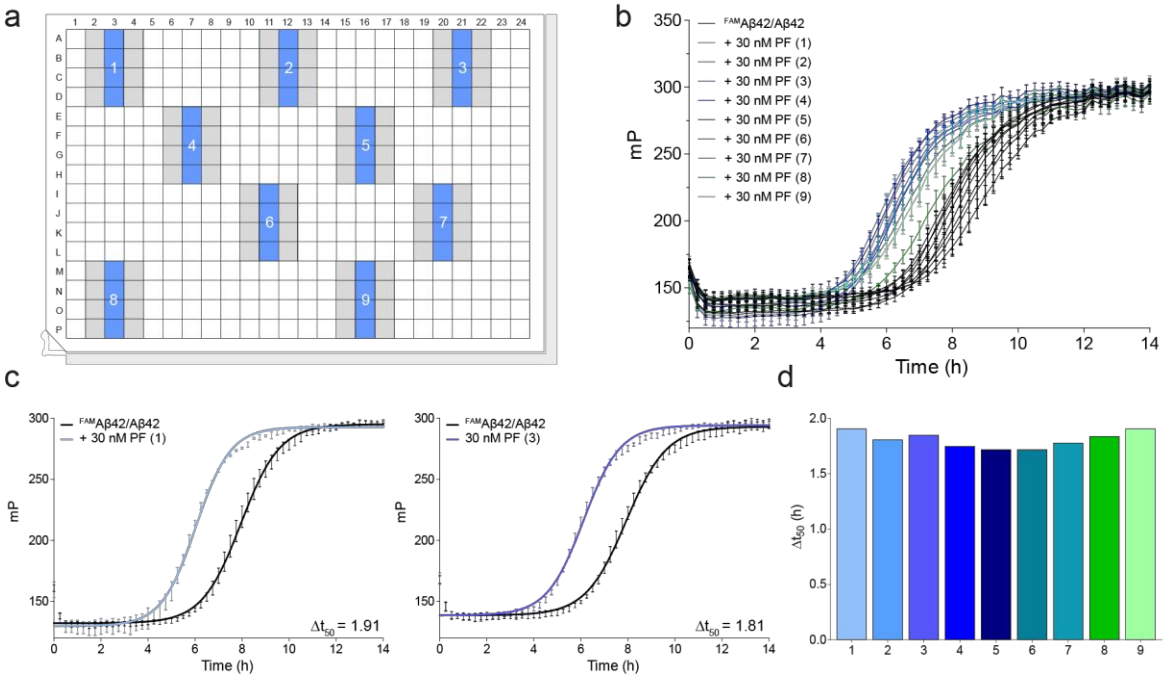

Figure 27 | Reproducibility of measured FP seeding activity within a 384-well microtiter plate
(a) 30 nM PFs as seeds were distributed over the plate (blue, 1-9) and the seeding activity was determined in relation to nearby positioned non-seeded reactions (Aβ42 monomer controls, grey). (b) The Aβ42-FP assay shows deviations between the nine analyzed samples. (c) Analysis of each individual sample in relation to the appropriate controls (Aβ42 monomers; non-seeded reactions, exemplarily shown for two samples). (d) Quantification of the seeding effects of all nine samples. The average $\triangle t_{50}$ values differ by ~7.3 %.

Since the observed intraplate deviations are critical for the final interpretation of the generated FP data, different 384-well plates form various distributors were tested and systematic FP measurements were performed. In principle, only black plates were tested since they absorb light and reduce background signals which make them superior over white plates for fluorescence measurements. Furthermore, due to the fact that Aβ42 peptides are very hydrophobic and stick to surfaces[268], only plates with non-binding surfaces were assessed in Aβ42-FP assays. Systematic analysis of plates from different providers showed that the 384-well plates from Greiner proved to be most suitable to analyze Aβ42 aggregation by FP assays. Furthermore, using appropriate numbers of control samples on each plate is critical for a proper data analysis and reduces the risk of false-positive results with FP assays.

Besides the intra-experimental variations due to the use of microplates, additional deviations appeared that could be traced back to the Aβ42 peptide itself. Synthetic Aβ42 peptides purchased from different suppliers are generally subjected to a highly standardized protocol for the preparation of non-aggregated monomers prior to their use in FP aggregation assays. Pretreatment with HFIP (1,1,1,3,3,3-Hexafluoro-2-propanol) was supposed to ensure a monomerization of the peptide as it induces α-helical conformations and thus prevents aggregation based on β-sheet formation, which is a prerequisite for aggregate formation[269-271]. Subsequently, by lyophilization the solvent was removed and the peptide could be stored dry in its monomeric form in single aliquots. However, despite highly standardized conditions differences in the aggregation profiles could be observed with different Aβ42 preparations. The impact of different peptide preparations on the FP output became apparent by comparing the slopes of the exponential phase and the durations of the lag phase from multiple independent experiments. Usually the onset of Aβ42 aggregation occurred after ~5-8 h in standard FP-assays. Figure 28a shows the standard ^{FAM}Aβ42/Aβ42 co-polymerization reaction of three independent experiments (Experiment 1-3) using three different Aβ42 preparations. These studies indicate that the onset of aggregation significantly varies from experiment to experiment (IP1: 6.8 h; IP2: 10.9 h; IP3: 14.2h). Since these results are most likely due to batch to batch variability, it was important to investigate whether the aggregation profiles of seeded polymerization reactions are equally affected. To address this question, the inflections points (IPs) obtained with standard ^{FAM}Aβ42/Aβ42 aggregation reactions were systematically compared to seeded reactions (plus addition of 100 nM PF seeds). Analysis of nine independent experiments were plotted against each other and revealed a linear correlation between the IP values obtained from seeded and non-seeded reactions. This indicates that the results from different aggregation experiments can be compared with each other

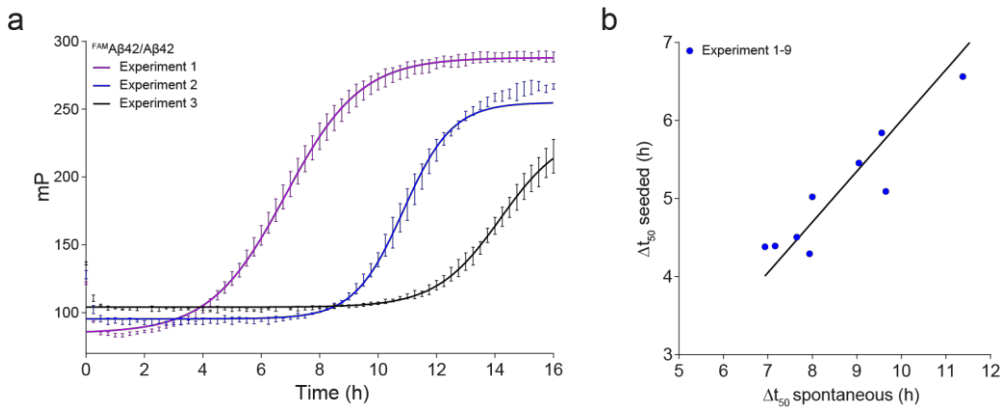

Figure 28 | Differences in Aβ42 peptide preparations influence the outcome of FP-based aggregation assays
(a) Comparison of aggregation profiles of standard ^{FAM}Aβ42/Aβ42 co-polymerization (10 µM Aβ42 + 0.05 µM ^{FAM}Aβ42) assays of three independent experiments (experimentes 1-3). The lag phase can differ strongly, when different Aβ42 peptide batches are applied in Aβ42 FP assays. (b) Comparison of t_{50} values obtained from spontaneous and seeded (addition of 100 nM PFs) ^{FAM}Aβ42/Aβ42 co-aggregation reactions. In total, nine independnet experiments were systematically analyzed. The data indicate that the effect of seeds are independent from the observed onset of ^{FAM}Aβ42/Aβ42 aggregation .

In summary, in this study a FP-based one-step, cell-free Aβ42 aggregation assay (Aβ42-FP assay) could be established to monitor spontaneous and seed-mediated Aβ42 aggregation *in vitro* in a time-resolved manner. Plane polarized light is used to excite a fluorescent molecule (Fig. 29). Then, the fluorophore emits photons in the same plane if it is not tumbling, making the fluorescence polarization value of the fluorophore directly proportional to its rotational relaxation[239]. Provided that the temperature and viscosity of the system are held constant, the polarization values can be directly correlated to the molecular volume of a molecule as smaller molecules have a higher mobility than bigger ones. Small amounts of a FAM (5-Carboxyfluorescein)-labeled Aβ42 monomers are used as tracer molecules (^{FAM}Aβ42) to follow the aggregation process. Initially, only low FP values are obtained because tracer molecules are highly mobile and light gets emitted in various planes of oscillation. Under defined aggregation conditions the fluorescently-labeled Aβ42-tracer molecules (0.05 µM) interact with unlabeled Aβ42 monomers (10 µM) leading to the formation of larger fibrillar Aβ42 aggregates. The increase of the molecular volume of the growing aggregates leads to a decreased mobility that can be followed by an enhancement of polarization as the polarized light is predominantly emitted in the excitation plane. The assay can be performed in a 384-well format and is suitable for high-throughput applications. Of particular importance is that the assay can be performed in presence and absence of pre-formed Aβ42 seeds, meaning that besides spontaneous also seed-mediated Aβ42 aggregation processes can be systematically investigated.

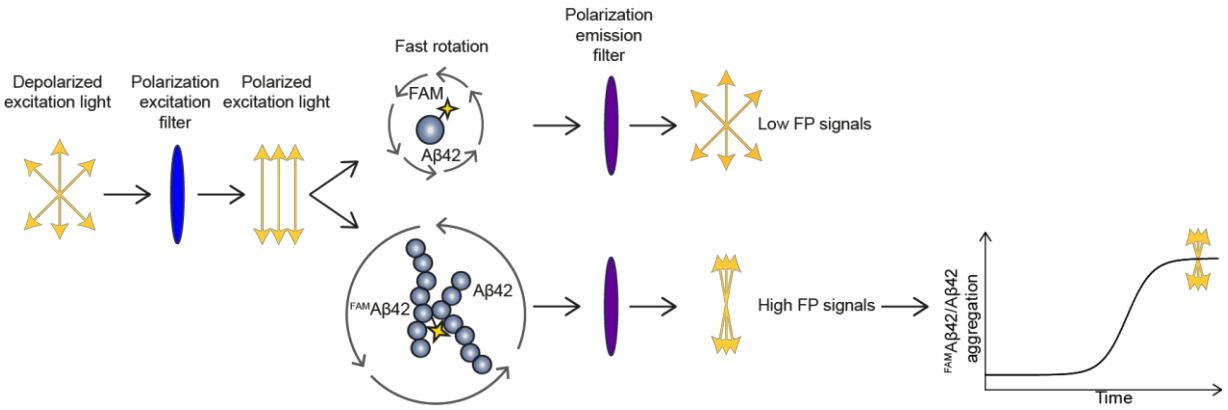

Figure 29 | Principle of the fluorescence polarization-based Aβ42 aggregation assay (Aβ42-FP assay)
Schematic of the fluorescence polarization (FP)-based ^{FAM}Aβ42/Aβ42 co-polymerization assay. The rate of tumbling of the fluorescent tracer ^{FAM}Aβ42 decreases upon co-aggregation with unlabeled Aβ42 molecules. This phenomen leads to a time-dependent increase of the FP signal.

5.2

Characterization of seeding-competent Aβ42 species in vitro

5.2 Characterization of seeding-competent Aβ42 species *in vitro*

Prior to the detection of potential seeding-competent Aβ aggregate species in biological samples, I first performed investigations with pre-formed synthetic Aβ42 aggregates in order to study their activities in Aβ42-FP assays and to characterize their biochemical and structural properties.

5.2.1 Time-resolved analysis of Aβ42 aggregation

A time-resolved analysis of an *in vitro* Aβ42 aggregation reaction was performed where 20 µM Aβ42 monomers were aggregated in an Eppendorf tube (37°C, 300 rpm) and aliquots were taken every hour for 8 h from the starting point (t = 0 h). A final sample was taken after 24 h, representing the end point of the aggregation process. The Aβ42 aggregate species spontaneously formed over time were then analyzed regarding their seeding activity, morphology, β-sheet content and molecular size using established assays. Thereby, information about the biochemical and biophysical properties of Aβ42 seeds and their specific activities and molecular features can be gained.

Analysis of samples from the different time points as seeds (50 nM Aβ42) in the established Aβ42-FP assay revealed that the Aβ42 peptides at time point t = 0 h (corresponding to monomers) are not able to seed ^{FAM}Aβ42/Aβ42 co-aggregation in FP assays (Fig. 30a, b). But already after 1 h a slight seeding effect was observed that increased further over time. Interestingly, after 5 h the maximum seeding activity was reached, indicating that this activity is independent of the size of the spontaneously formed Aβ42 fibrils, which grow constantly in their size within the next hours. This is also in agreement with a time-dependent increase of the ThT signal, which indicates the formation of β-sheet-rich, fibrillar Aβ42 aggregates (Fig. 30c). Thus, after 5 h most seeding-competent Aβ42 aggregates seemed to have formed and a further increase in ThT reactivity does not correlate with seeding activity. The prepared samples were also analyzed by SDS/NativePAGE and immunoblotting to study the molecular size of the spontaneously formed Aβ42 aggregates (Fig. 30d, e). Both blots show a progressive increase of high molecular weight assemblies (HMWAs) and even bigger aggregates over 24 h, concomitantly with a steady decrease of Aβ42 monomers (~4.5 kDa). Gel electrophoresis under denaturating conditions shows that after 3 h SDS-stable aggregates are formed that are stuck in the gel pockets (Fig. 30d). Between 2-5 h a prominent smear of HMWAs can be detected above 720 kDa on native gels (Fig. 30e). After 6 h most of these structures seem to have aggregated into bigger species that are stuck in the gel pockets under native conditions. Together, these investigations suggest that higher seeding activity can mainly be assigned to bigger and fully aggregated Aβ42 peptides than to low and high molecular weight species. Morphological analysis by AFM showed that at the starting point at t = 0 h only monomeric or small oligomeric species can be detected (Fig. 30f).

After 2 h, the first small fibrillary structures start to form that grow larger over time until after 24 h very big clusters of aggregated Aβ42 fibrils are detectable. For final dot blot analysis the protofibril-specific antibody 352 was used. Figure 30g shows that the first protofibrillar structures are detectable after 2 h and that after ~5 h the aggregation process seems to have reached saturation. Thus, the quantified 352-reactivity seems to correlate well with the observed increase in seeding activity.

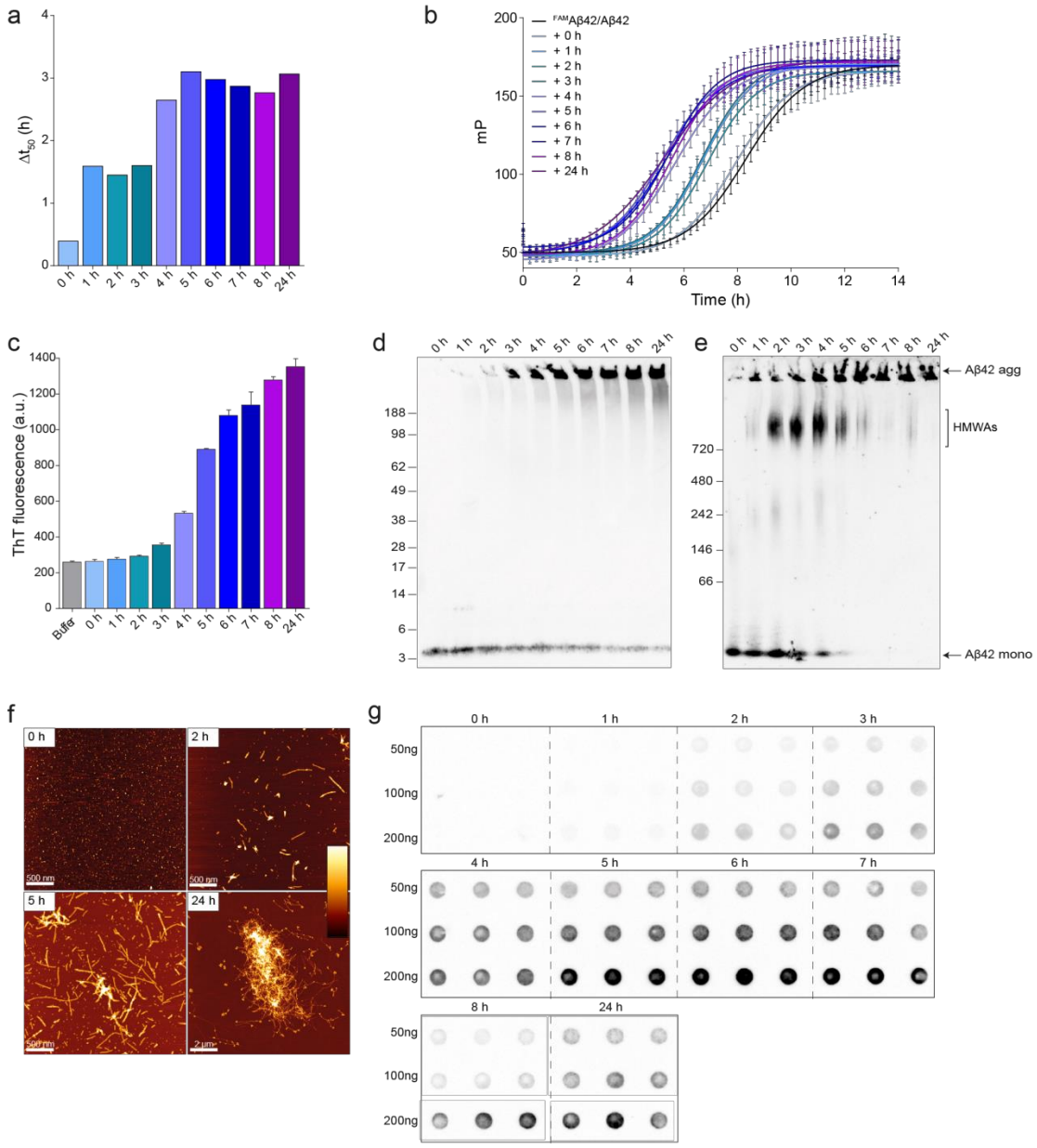

Figure 30 | Time-resolved analysis of aggregation-prone Aβ42 monomers *in vitro*
Aggregation of 20 µM Aβ42 monomers (37°C, 300 rpm) and analysis of different time points. (a, b) For the analysis of the seeding activity 50 nM of prepared aggregates were used as seeds in a standard ^{FAM}Aβ42/Aβ42 co-polymerization assay. The seeding activity increases with time whereby a maximum seems to be reached after 5 h. (c) The β-sheet content of spontaneously formed aggregation products (4.5 µM) was measured using a ThT fluorescence assay (20 µM) in arbitrary units (a.u.). (d) SDS-PAGE and immunoblotting, detection with 6E10. (e) NativePAGE and immunoblotting, detection with 6E10. (f) Analysis of Aβ42 aggregates (10 µM) by AFM; 0 h, 2 h and 5 h: 3 x 3 µm, scale bar: 500 nm; 24 h: 10 x 10 µm, scale bar: 2 µm; color gradient represents 0-10 nm height. (g) Dot blot, detection with 352.

5.2.2 Impact of sonication on the activity of seeding-competent Aβ42 structures

Based on literature addressing amyloid fibril formation[272] and prion-related research[94], it was assumed that seeding-competent Aβ structures must comprise reactive binding sites, probably similar to aggregation nuclei that build up within the normal Aβ aggregation process. *Soto et al.* have reported the PMCA (protein misfolding cyclic amplification) method[258,273] which allows the detection of prion aggregates with high sensitivity by amplifying the aggregates via sonication. The sonication step breaks down large aggregates into smaller fragments to multiply the number of reactive units.

Considering a nucleation-dependent polymerization mechanism[130,133-135] and that the number of active seeds increases upon sonication, I asked whether the seeding activity of Aβ42 aggregates formed after an incubation period of 24 h can be further increased by a sonication step. The 24 h aggregates were subjected to two different sonication methods: sonication for 5 seconds was performed with a single tip sonicator, while for the longer 5 min sonication a water bath was used. Figure 31a, b show the result of the Aβ42-FP assay of a spontaneous ^{FAM}Aβ42/Aβ42 aggregation reaction that was seeded with 50 nM of sonicated seeds. Sonication with both methods significantly increased the seeding activity of Aβ42 aggregates whereby longer sonication in the water bath was even more efficient. Analysis of the β-sheet content of the sonicated aggregates with the ThT assay (Fig. 31c) showed that the amount of ThT-reactive β-sheets decreases, a result which is in line with Figure 30c that already showed that higher β-sheet content does not correlate with higher seeding activity.

Being interested in the morphology of the sonicated and more seeding-competent Aβ42 species, atomic force microscopy was performed (Fig. 31d). As expected, the 24 h aggregates showed long fibrillar Aβ42 assemblies. Sonication for 5 sec or 5 min, respectively led to a steady fragmentation of these fibrils and the formation of smaller species. Interestingly, these smaller structures did not show single fibrillar fragments but more compact, bulkier assemblies. Western blot analysis with a 6E10 antibody under native conditions showed that in comparison to the untreated 24 h aggregates, both sonicated samples contained higher amounts of HMWAs (Fig. 31g). This demonstrates that bigger aggregates indeed were fragmented into smaller Aβ42 species via the sonication step. Dot blot analysis with the 352 antibody revealed no difference between controls and sonicated aggregates, indicating that the antibody reactivity remains conserved even after subjection to ultrasound (Fig. 31e). Additionally, the three samples were also analyzed with a filter retardation assay under denaturating conditions (Fig. 31f). By addition of SDS and DTT to the samples and boiling at 95°C only heat- and SDS-resistant aggregates that are bigger than 0.2 µm can be detected as they do not pass the membrane pores[274,275]. Whereas the 24 h aggregates are too big to pass the pores and remain on the membrane, the 5 sec sonicated species were able to pass to a certain extent. In contrast, no 6E10 signal could be detected with the samples that were sonicated for 5 min. This indicates that under this

sonication conditions Aβ42 aggregates are fragmented efficiently, resulting in the formation of structures that are too small to be retained on the membrane.

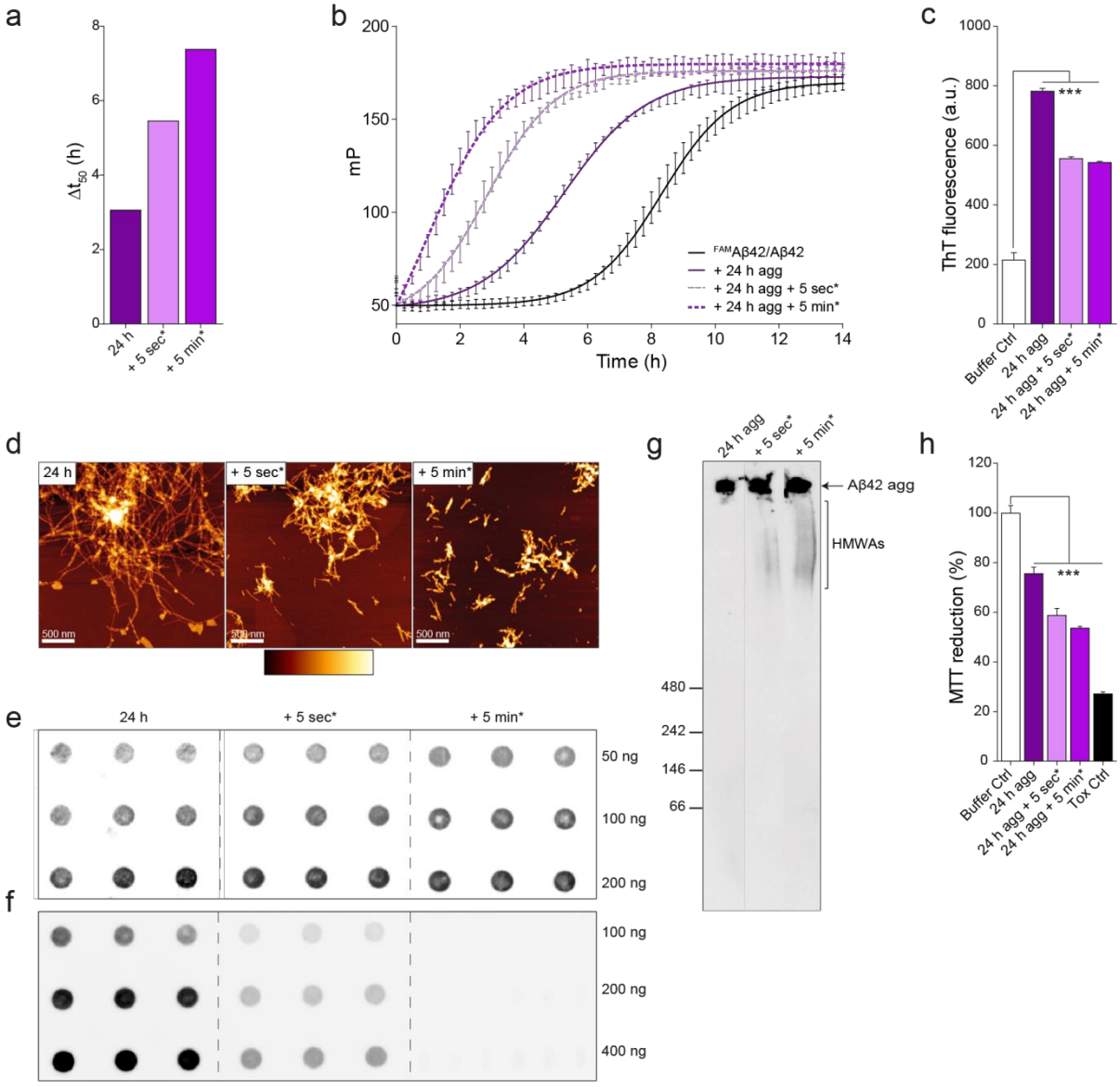

Figure 31 | Sonication increases the seeding activity of fibrillar Aβ42 aggregates
(a,b) 50 nM Aβ42 peptides after aggregation for 24 h (24 h agg) with or without sonication (5 sec or 5 min; indicated by asterisks) were added to standard ^{FAM}Aβ42/Aβ42 co-polymerization assays. The seeding activity of sonicated aggregates was higher compared to untreated Aβ42 aggregates. (c) ThT-signal of highly seeding-competent sonicated Aβ42 aggregates decreases compared to unsonicated control aggegates (4.5 µM Aβ42 samples, 20 mM ThT; measured in arbitrary units, a.u.). Statistical significance was assessed by one-way ANOVA followed by Dunnett's multiple comparison post hoc test. ***, p≤0.001. (d) AFM analysis of Aβ42 peptides (10 µM) aggregated for 24 h with or without subsequent sonication; 3 x 3 µm, scale bar: 500 nm, color gradient represents 0-20 nm height. (e) Dot blot, detection with 352. (f) Denaturating FRA, detection with 6E10. (g) NativePAGE and immunoblotting, detection with 6E10. (h) Treatment of PC12 cells with untreated or sonicated Aβ42 aggregates and measurement of metabolic activity using a MTT assay. Aβ42 peptides aggregated for 24 h reveal a significant effect on cellular metabolic activity that increases further after sonication. Values represent percentage of buffer control. 0.05 % Triton X-100 were used as toxicity control. Statistical significance was assessed by one-way ANOVA followed by Dunnett's multiple comparison post hoc test. ***, p≤0.001.

My analysis revealed the presence of HMWAs and even bigger Aβ42 aggregates in sonicated samples (Fig. 31g). Thus, it can be hypothesized that besides fragmentation into small structures also some bigger aggregates remain that can still be detected by NativePAGE. However, these aggregates do not seem to be SDS stable as they cannot be detected on a denaturating filter. Finally, the Aβ42 peptides that are present after aggregation for 24 h as well as the sonicated samples were added to PC12 cells to investigate whether this treatment influences the viability or metabolic activity of cells. PC12 cells are derived from a pheochromocytoma of the rat adrenal medulla. They exhibit a neuronal like phenotype and thus represent a suitable cellular model to investigate neurodegenerative disorders[276,277]. The effect of the Aβ42 species on the cellular metabolic activity was analyzed using the MTT assay[278-280]. This is a colorimetric assay to assess cell metabolic changes. It is based on the conversion of the tetrazolium salt MTT (3-(4,5-dimethylthiazol-2-yl)-2,5-diphenyltetrazolium bromide) into a formazan product in living cells only. The formazan concentration is then determined by optical density measurement at 570 nm with a microtiter plate reader. For the MTT assay cells were treated with 50 nM Aβ42 species and incubated for 72 h. The 24 h aggregates reduced the MTT signal by ~30 %. Sonication of these aggregates led to a changed metabolism in PC12 cells up to 60 %, indicating that seeding activity can be correlated with impaired metabolic activity (Fig. 31h).

In summary, a time-resolved analysis of Aβ42 aggregation was performed to gain information about the spontaneous formation of seeding-competent Aβ42 aggregate species *in vitro*. Based on the collected data it can be hypothesized that highly seeding-competent Aβ42 aggregates are higher molecular weight structures as HMWAs and fully aggregated Aβ42 species seem to account for seeding capacity, rather than very small assemblies. Interestingly, early Aβ42 assemblies that did not show an increase in ThT-fluorescence already revealed seeding activity to a certain extent. This could be due to the fact that the ThT assay is not sensitive enough to detect small conformational changes before stable β-sheet-rich structures are formed. The monoclonal antibody 352 that was specifically raised against fibrillar structures and does not detect monomeric Aβ42 peptides proved to be capable to detect seeding-competent Aβ42 assemblies and thus represents a suitable tool to detect seeds. Sonication of Aβ42 aggregates further increased their seeding activity, probably by providing more reactive binding sites that trigger the Aβ42 nucleation process. AFM analysis, NativePAGE and filter analysis demonstrated that the sonication step generates not only one specific species but rather leads to a mixture of aggregate assemblies. Most interestingly, the higher seeding-competence was accompanied by an increased metabolic impairment in cell-based assays.

5.3

Detection of Aβ seeding activity in Alzheimer's disease biosamples

5.3 Detection of Aβ seeding activity in Alzheimer's disease biosamples

After successful establishment of the FP-based Aβ42 aggregation assay and its application to quantify the activity of synthetic Aβ42 seeds, I used the assay to detect seeding-competent Aβ aggregates in disease-relevant biological samples.

5.3.1 Analysis of applicability of the Aβ42-FP assay for the detection of seeding-competent Aβ species in transgenic AD mouse brains

5.3.1.1 AD mice model

Transgenic (tg) AD mouse brains were used for proof-of-principle experiments and method optimization. Within this project three different AD mouse models (5xFAD, APPPS1 and APP23) were used and are ought to be discussed briefly.

The **5xFAD** mouse model is a widely used AD model as it develops a severe amyloid pathology with an early disease phenotype[281]. It is a double transgenic human APPPS1 mouse model that co-expresses five AD mutations: mutant human APP with Swedish (KM670/671NL), Florida (I716V) and London (V717I) mutations and mutant human PSEN1 with the M146L and L286V mutations. Both transgenes are regulated by elements of the mouse Thy1 promoter to drive overexpression in the brain. The Swedish mutation leads to higher levels of total Aβ, the presence of the other four mutations increases the production of Aβ42. This leads to an accumulation of high levels of intraneuronal Aβ42 (~1.5 month) and thus early onset of plaque deposition (~2 month). Amyloid plaques can be found first in the subiculum and layer 5 of the cortex before spreading throughout the hippocampus and cortex by 6 months of age. 5xFAD mice also display gliosis (~2 month) and synapse degeneration (~4 month) followed by neuronal loss and deficits in spatial learning (~4-5 months)[282]. *Oakley et al.* also reported the development of age-dependent synaptic degeneration indicated by the reduction of synaptic markers[282].

Another commonly used AD mouse model is the **APPPS1** model[283]. It contains the human transgenes for *APP* and *PSEN1*, but harbors only two mutations (APP: Swedish KM670/671NL; PSEN1: L166P), both under the control of the Thy1 promoter. The expression of the human *APP* transgene is approximately 3-fold higher than endogenous murine APP. Aβ plaque deposition starts at 6 weeks of age in the neocortex and 3-4 months of age in the hippocampus[284]. A global neuronal loss is not observed in APPPS1 mice, but in contrast to the 5xFAD model that reveals no tau pathology at all, phosphorylated tau-positive neuritic processes have been observed near Congo Red-positive amyloid deposits[284,285]. Regarding cognitional and behavioral phenotypes, deficits in spatial learning and

memory in the Morris water maze were reported at ~7 months as well as an impaired reversal learning of a food-rewarded four-arm spatial maze task at 8 months[284,286].

Finally, a characteristic feature of the APP23 AD mouse model is that the mutant human APP protein with the Swedish mutation is ~7-fold overexpressed in the brain[287]. Again, a Thy-1 promoter is used to drive expression of the transgene in this model[288]. APP23 mice display extensive β-amyloid pathology with congophillic, dense-core amyloid plaques first appearing at 6 months and increasing in number and size with age[289]. In the vicinity of the plaques, activated microglia, astrocytes and dystrophic neurites containing hyperphosphorylated tau can be detected[290,291]. Neuronal loss has been reported in the CA1 region of the hippocampus[292]. The cognitive impairment exhibits spatial memory defects in the Morris Water maze at 3 months and progresses with age[293,294].

To analyze whether seeding-competent Aβ species can be detected in AD tg mice using the Aβ42-FP assay, mouse brains were collected at different age and homogenized. The detailed preparation of mouse brain lysates can be found in the methods section. Briefly, frozen tissue was homogenized in ice cold RIPA buffer. The homogenate was centrifuged at low speed (1,500 x g) to remove cell debris and the supernatant was transferred to a new tube. The low-speed centrifugation reduced the risk of losing Aβ aggregates into the pellet as Aβ fibrils are usually only precipitated at higher centrifugation speed (>14,000 x g)[295]. For the sake of completeness, the pellet fraction was also analyzed in a trial experiment. Since the analysis of the pellet fraction delivered no satisfactory and reproducible results (*data not shown*), likely due to the disruptive cellular debris, in the following work the supernatant fraction was exclusively investigated.

At first, different homogenization buffers were tested in this project. For example, homogenization in pure ice-cold PBS was performed as described by *Jucker* and colleagues[296]. However, addition of detergents (SDS, Triton or NP40) to the homogenization buffer increases the release of Aβ peptides that are located in membrane-enclosed compartments. Even though literature suggests that in the brain Aβ aggregates primarily reside in a detergent-insoluble compartment[297], there have been several studies that demonstrated the presence of Aβ peptides in distinct intracellular compartments[298-301]. For testing homogenization buffers human AD and control (Ctrl) brain tissues were used and homogenized in three different buffers (PBS, RIPA or HEPES buffer) under otherwise equal conditions. Then, the homogenates were analyzed on a dot blot to quantify the total amount of Aβ peptides. Figure 32 shows the results of the dot blot analysis using the antibodies 6E10 and 4G8 for immuno-detection. 6E10 was already introduced earlier and recognizes N-terminal amino acids in the Aβ peptide. The monoclonal anti-Aβ antibody 4G8 specifically targets the amino acids 17-24 in the Aβ

peptide. Both antibodies clearly show that the highest amounts of Aβ peptides are extracted from AD brain tissues when they are homogenized with RIPA buffer.

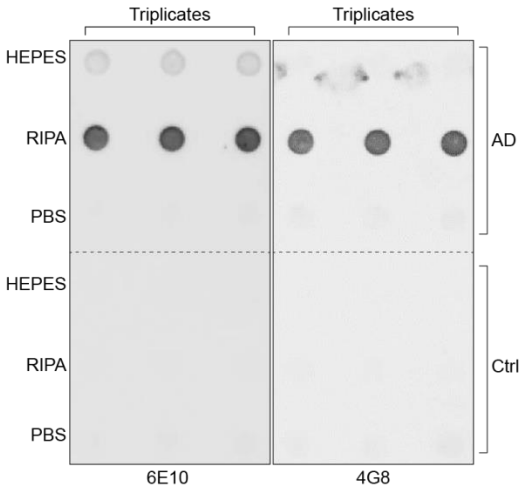

Figure 32 | Detection of Aβ antibody reactivity in brain samples after homogenization with different buffers
Dot blot analysis with 6E10 or 4G8 antibodies of an AD and a Ctrl human brain sample (supernatant) homogenized in HEPES, RIPA or PBS buffers, respectively. The highest Aβ signals were obtained after homogenization of tissues with RIPA buffer.

In summary, homogenization of brain samples was systematically optimized regarding homogenization buffer and preparation protocols to enable a maximal release of Aβ aggregate species. Additionally, it is important to take into account that the treatment with detergents should not affect the stability of Aβ aggregates since amyloid fibrils usually are SDS resistant structures[302].

5.3.1.2 Analysis of mouse brain homogenates in Aβ42-FP assays

First, I tested whether the prepared supernatant fractions from mouse brain tissues can directly be analyzed regarding their seeding activity with Aβ42-FP assays. However, proof-of-concept experiments revealed that already the use of pure RIPA homogenization buffer tremendously impairs the normal FP measurements. Especially the detergent Triton-X100 seemed to accelerate the ^{FAM}Aβ42/Aβ42 aggregation process dramatically even at relatively low concentrations (Fig. 33a). In general, I found that the detergent Triton promotes the solubility of the Aβ42 monomers. However, the triton concentration of 0.01 % (w/v) is close to its critical micelle concentration above which micelles are formed spontaneously[303]. Thus, it seems possible that in FP assays the Aβ42-tracer gets enclosed into Triton micelles, leading to an acceleration of the ^{FAM}Aβ42/Aβ42 aggregation process. Dilution series with Triton revealed that a final assay concentration of 0.001 % would be tolerable for FP measurements (Fig. 33a). Therefore, a new homogenization buffer (HB) based on low salt FP-assay buffer (LSB) and 0.5 % Triton was established. A subsequent 1:500 dilution of the buffer led to a final

concentration of 0.001 % Triton in the assay plates (Fig. 33b). Following, the total protein concentration used in the assay that is not disturbing the readout had to be evaluated. Therefore, a wildtype (wt) mouse brain homogenate was produced in HB buffer and tested for its effects on FP in the established Aβ42-FP assay. It was observed that protein concentrations higher than 2.5 ng decelerate the ^{FAM}Aβ42/Aβ42 aggregation process (Fig. 33c). Hence, after establishing these vital conditions 2.5 ng of wt and tg APPPS1 mouse brain homogenates were assessed for seeding activity in the ^{FAM}Aβ42/Aβ42co-polymerization assay (Fig. 33d). Unfortunately, seeding activity could not be detected in any of the tested brain samples. This result was not completely unexpected as my earlier experiments already indicated that a sufficient amount of detergents in the homogenization buffer is crucial to release Aβ aggregates from membranes or other compartments.

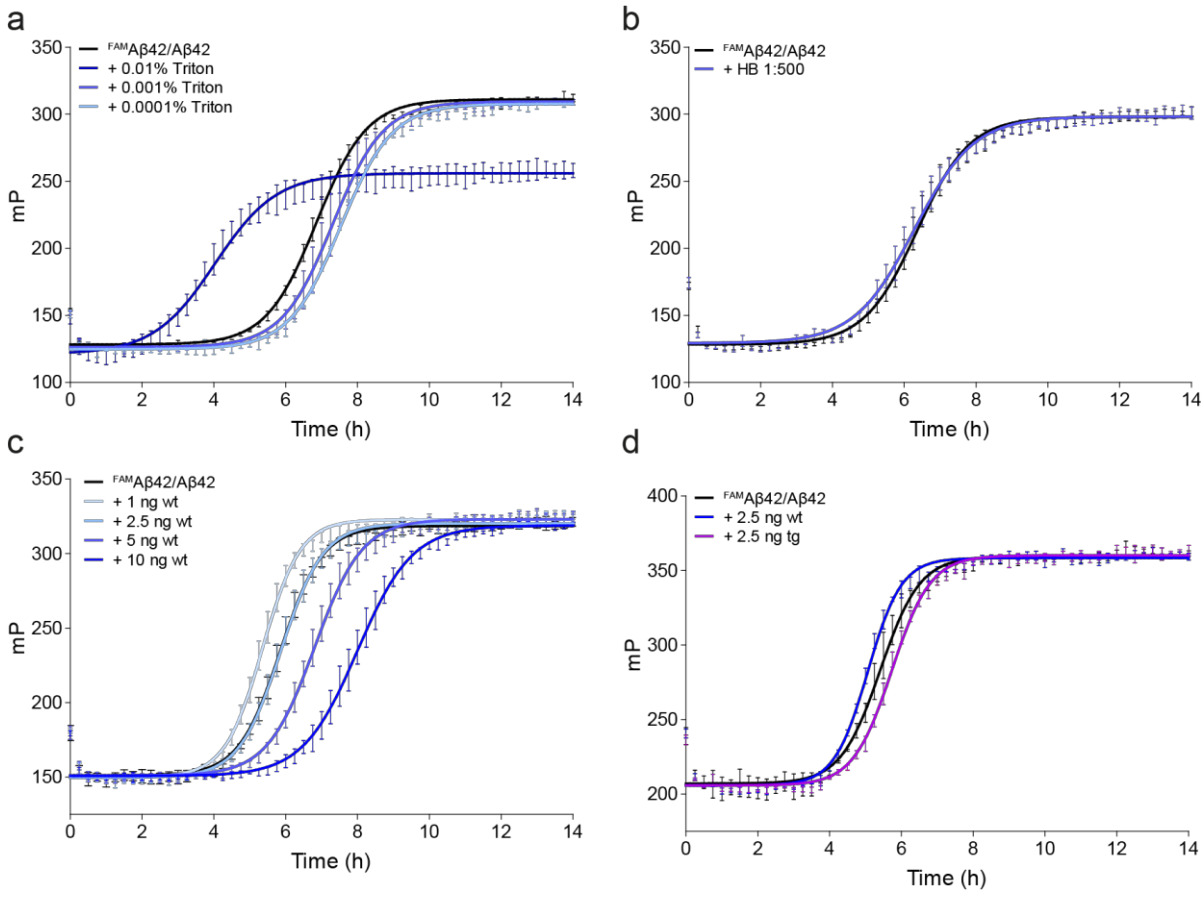

Figure 33 | Optimization of homogenization buffer conditions for the analysis of brain lysates in ^{FAM}Aβ42/Aβ42 assays

(a) Influence of Triton on ^{FAM}Aβ42/Aβ42 aggregation reactions. (b) Optimized homogenization buffer (HB) with 0.5 % Triton did not influence the Aβ aggregation measurement. (c) Influence of protein concentration on Aβ aggregation in Aβ42-FP assays. The addition of 2.5 ng of wt protein shows no effect in ^{FAM}Aβ42/Aβ42 aggregation. (d) Addition of 2.5 ng wt or tg protein extracts do not influence the ^{FAM}Aβ42/Aβ42 aggregation kinetics.

5.3.1.3 Method setup for the extraction of Aβ aggregates from mouse brain samples

Trying to combine both, the necessity of a detergent-rich homogenization buffer for the release of Aβ peptides from intracellular compartments with the incompatibility of the Aβ42-FP assay to detergents, a procedure was established to extract Aβ aggregates directly from biosamples by application of an immunoprecipitation method.

Immunoprecipitation (IP) describes a technique to precipitate a protein antigen out of solution by use of an antibody with specificity for that particular antigen. By applying such a method specific proteins can be isolated and concentrated from a sample comprising a mixture of different proteins, for example from a crude lysate. As Aβ specific antibodies, the antibodies 6E10 and 352 were used. Additionally, an IgG1 antibody was used as an isotype control in all IP experiments as 6E10 and 352 both belong to the IgG1 antibody family. Again, 6E10 detects both monomers and higher molecular weight Aβ42 aggregates. The protofibril-specific antibody 352 was chosen as it might exclusively enrich seeding-competent Aβ assemblies from biosamples. To ensure that 352-reactive Aβ species can be detected in transgenic mouse brain homogenates, a dot blot assay with an AD brain homogenate (APPPS1, 22 mo) and the 352 antibody was performed (Fig. 34a). Indeed, a strong 352-reactive antibody signal was detected on dot blots, indicating that protofibrillar Aβ aggregates are detectable in mouse brains.

Besides the specific antibodies, the IP technique requires a solid-phase substrate where the antibodies can get immobilized (Fig. 34b). For this, superparamagnetic microbeads (dynabeads, uniform, 2.8 µm) were used. As these beads comprise recombinant protein G (~17 kDa) covalently coupled to their surface, any IgG antibody can be bound to their surface via the Fc-region[304]. In the next step, the supernatant fraction prepared from brain homogenate was added to the antibody-coated beads and incubated for at least 30 min at room temperature or overnight at 4°C while rotating to allow proper mixing and binding. By placing the tube on a magnet afterwards the beads and potentially bound Aβ aggregates can be enriched.

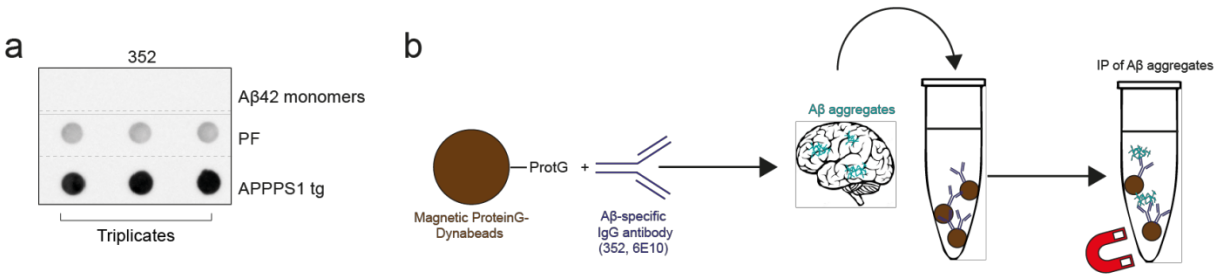

Figure 34 | Enrichment of Aβ aggregates from AD transgenic APPPS1 mouse brain extracts via IP
(a) Dot blot assays (100 ng) of a transgenic mouse homogenate (tg APPPS1, 22 mo) reveals the presence of 352-reactive species. (b) Scheme for the IP of Aβ aggregates from transgenic mouse brain homogenate. Aβ-specific IgG antibodies are bound to magentic dynabeads via their Fc-region. Addition of brain homogenates from tg AD mice allows the extraction of Aβ aggregates from the lysate by use of a magnet.

This direct capture method was used in all standard IP experiments. In preliminary tests the antibody/bead ratio was determined to cover the maximal binding capacity of the beads. Furthermore, also the antibody/lysate ratio was systematically tested to achieve a maximum yield (*data not shown*). As a result, the use of 4 µg antibody bound to 1.5 mg ProteinG dynabeads proved to be sufficient for immunoprecipitation of Aβ species from 0.25 mg brain homogenate from AD transgenic mice.

Two further optimization steps were performed within the method development process. First, after binding of the antibodies to the magnetic dynabeads, a saturation step was included to block residual binding sites on the surface of microbeads and prevent background signals. For that a commercially available protein-free blocking buffer was used and incubated for 30 min at room temperature under rotating conditions with the antibody-bound beads. Second, after immunoprecipitating the aggregate species from the lysate, the beads were washed first with an attenuated RIPA buffer containing fewer detergents (0.01 % SDS, 0.05 % Sodium deoxycholat, 0.1 % Triton). This prevented the release of bound aggregate species due to high detergent concentrations in the wash buffer. Subsequently, two washing steps with low salt buffer (LSB) followed to exchange the buffer for FP analysis.

Using the IP approach has several advantages. First, after isolation of the Aβ aggregate species sufficient washing steps can be performed to remove all FP assay disturbing detergents from the Aβ aggregates. Second, the IP approach enables an enrichment of the target analyte from the crude protein homogenate. Finally, the establishment of an isolation protocol should also facilitate further characterization of the seeding-competent aggregate species e.g. regarding morphology or toxicity.

After establishment of all these conditions an APPPS1 transgenic mouse brain (22 mo) and an age-matched wildtype control brain were utilized for proof-of-principle IP experiments (Fig. 35). The samples containing magnetic protein G beads with bound immunoprecipitated Aβ aggregate species were boiled with 4x SDS-PAGE sample buffer for 5 min and then loaded onto an SDS gel followed by Western blotting. Western blot analysis showed neither the presence of Aβ42 monomers (~4.5 kDa) nor of Aβ aggregates in the gel pockets when the wildtype mouse brain was assessed. Solely a signal for the heavy (HC; ~50 kDa) and the light chains (LC; ~23 kDa) of the antibodies used for the IP can be detected on the blots. In contrast, in the transgenic mouse brain extracts Aβ42 monomers as well as Aβ aggregates in the gel pockets were detectable (input 10 %). At a size ~87 kDa a double band indicating human APP was detected (upper band: glycosylated APP, lower band: immature non-glycosylated APP[284]), which is expressed in tg but not in wt mice. With both antibodies (352 and 6E10) aggregated Aβ peptides were detected in the gel pockets (IP) whereas only a low background signal can be seen with the isotype control antibody IgG1. The flow-through fractions (FT) showed almost no remaining aggregated material compared to the input, confirming that an optimal antibody/lysate

ratio was chosen earlier. The wash fractions (Wash) show that especially in case of the 352-IP some aggregates were lost during the washing step. This supports the hypothesis that washing under too harsh conditions may decrease the amount of Aβ aggregates bound to beads.

Taken together, this first experiment demonstrated the general feasibility of an IP approach for the extraction of Aβ aggregate species from transgenic AD mouse brains.

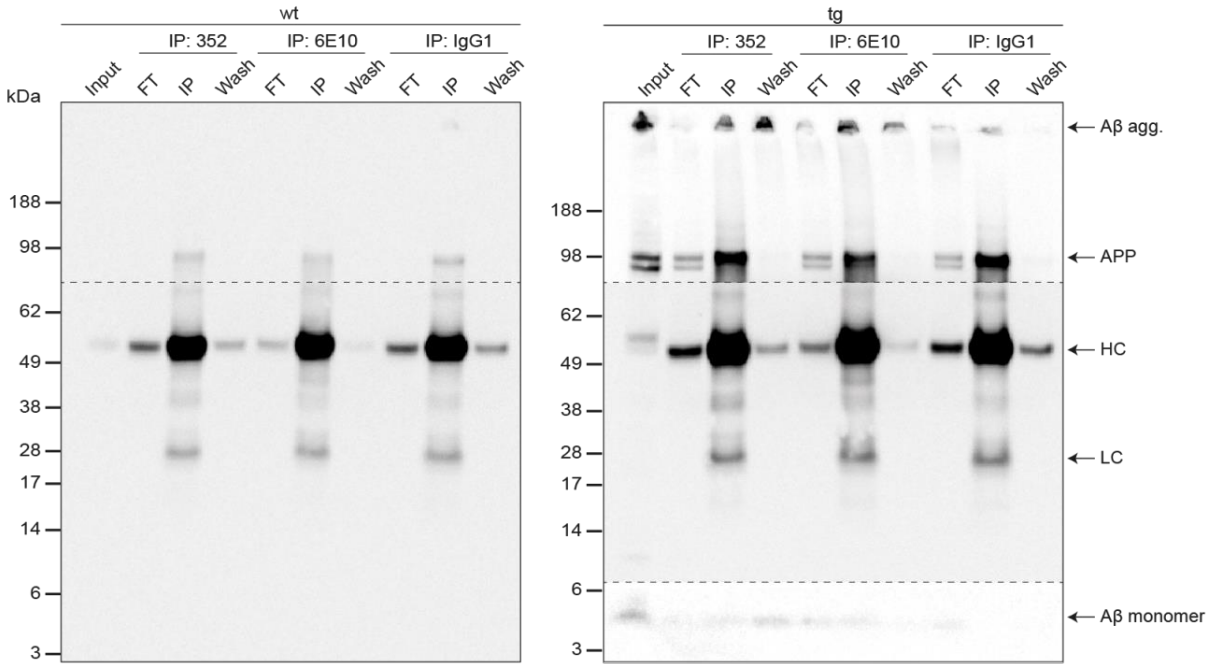

Figure 35 | Analysis of immunoprecipitates prepared from APPPS1 mouse brain extracts by Western blotting
For immunodetection of Aβ the monoclonal anti-Aβ antibody 6E10 was used. Brain homogenate used for IP was loaded on the gel (Input, 10 %) as well as flow-through (FT) and wash fraction (Wash). High molecular weight Aβ aggregate species were enriched from transgenic brain homogenates with the Aβ-specific antibodies but neither from the wildtype homogenates nor by using the control antibody IgG1. For better visualization of aggregates and monomers parts of the blot were longer exposed during development (indictad by dashed lines).

5.3.1.4 Establishment of a protocol for the release of Aβ seeds from antibody beads

After immunoisolation the enriched Aβ aggregates are still bound to the antibodies that have initially been coupled to dynabeads. For a further analysis of these species regarding their seeding activity with Aβ42-FP assays, they need to be eluted from the beads. Even though boiling in SDS-buffer can elute the aggregate species from the beads and allows their detection on Western blots, this is not a suitable strategy for the analysis of aggregate structures in FP assays because detergents like SDS impair ^{FAM}Aβ42/Aβ42 co-aggregation.

Thinking about other methods that would allow the elution of extracted aggregates without having to use harsh denaturating conditions, methods that would mechanically remove the aggregates from the beads were considered. Hence, the dynabeads with the extracted material were subjected either to vigorous vortexing in presence of glass beads or to ultrasound with a sonicator bath. Both methods

should enable the breakage of Aβ aggregates into smaller fragments and thereby release them from the beads into the supernatant. A fragmentation of the extracted aggregates would also offer the advantage of amplifying their number, which might increase seeding activity in FP assays[258,273]. Success of both methods was verified again by Western blotting (Fig. 36). In more detail the two tested methods contained:

1. IP*1: Addition of 1 glass beads (2 mm), vortexing 5 x 1 min
2. IP*2: Sonication for 15 min in a sonicator bath

Figure 36 shows a Western blot after IP of a transgenic 22-month-old APPPS1 mouse homogenate with the standard antibodies. The input as well as the IP with 352 or 6E10 antibody shows again that Aβ aggregates are stuck in the gel pockets. However, such a result was not obtained with the IgG1 control antibody. The use of glass beads and vigorous vortexing of the aggregate-bound dynabeads resulted in a slight reduction of the aggregates in the gel pockets. In comparison, sonication for 15 min in a sonicator bath caused an efficient release of the Aβ aggregate species from the dynabeads, as no Aβ signal could be detected in the gel pockets any more. This experiment indicates that sonication in a water bath is a powerful strategy to release Aβ aggregates from beads.

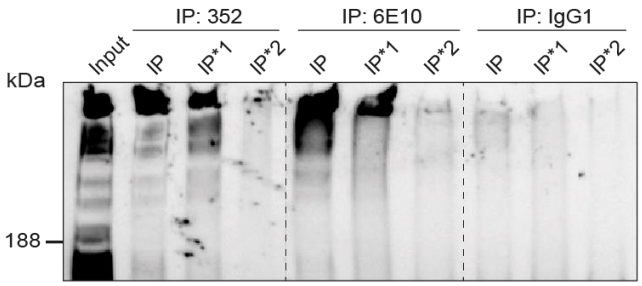

Figure 36 | Release of Aβ seeds from dynabeads after IP
Extracted Aβ aggregate species bound to magnetic dynabeads were subjected to two different methods to release Aβ aggregates into the supernatant. Addition of glass beads and vigorous vorexting (IP*1) resulted only in a slight decrease of the aggregates that are stuck in the gel pockets. In contrast, sonication (IP*2) significantly decreased the amount of Aβ aggregates in the gel pockets.

5.3.2 Detection of Aβ seeding activity in brains of transgenic Alzheimer's disease mice

5.3.2.1 Proof of principle

After optimization of all necessary parameters for the IP and the release of seeds from dynabeads, both methods were applied for the detection of seeding-competent Aβ aggregate species in biosamples (Fig. 37a). First, brain hemispheres of AD and wildtype control mice were homogenized in RIPA buffer. In standard assays, 0.25 mg of the brain homogenate (supernatant) was used for the

IPs with the Aβ-specific antibodies 352 and 6E10 or the isotype control antibody IgG1. All antibodies were bound to magnetic ProteinG dynabeads. After isolation of Aβ aggregates from the brain lysates, the potential seeding-competent Aβ species were removed from the beads by sonication. Finally, the enriched seeds were added to ^{FAM}Aβ42/Aβ42 co-polymerization assays (10µl/well) to assess their seeding activities.

Indeed, I found that both the 6E10- and the 352-reactive Aβ species revealed a significant seeding activity as they potently decreased the lag phase of spontaneous ^{FAM}Aβ42/Aβ42 co-polymerization in the FP assay by ~2.5 h (Fig. 37b and c). The seeding-efficiency of the 6E10- and 352 isolated species exhibited the same effect in this experiment while the isotype control antibody IgG1 did not show any acceleration of the aggregation process. Also, seeds prepared from age-matched wildtype mice did only slightly promote the Aβ42 aggregation in FP assays.

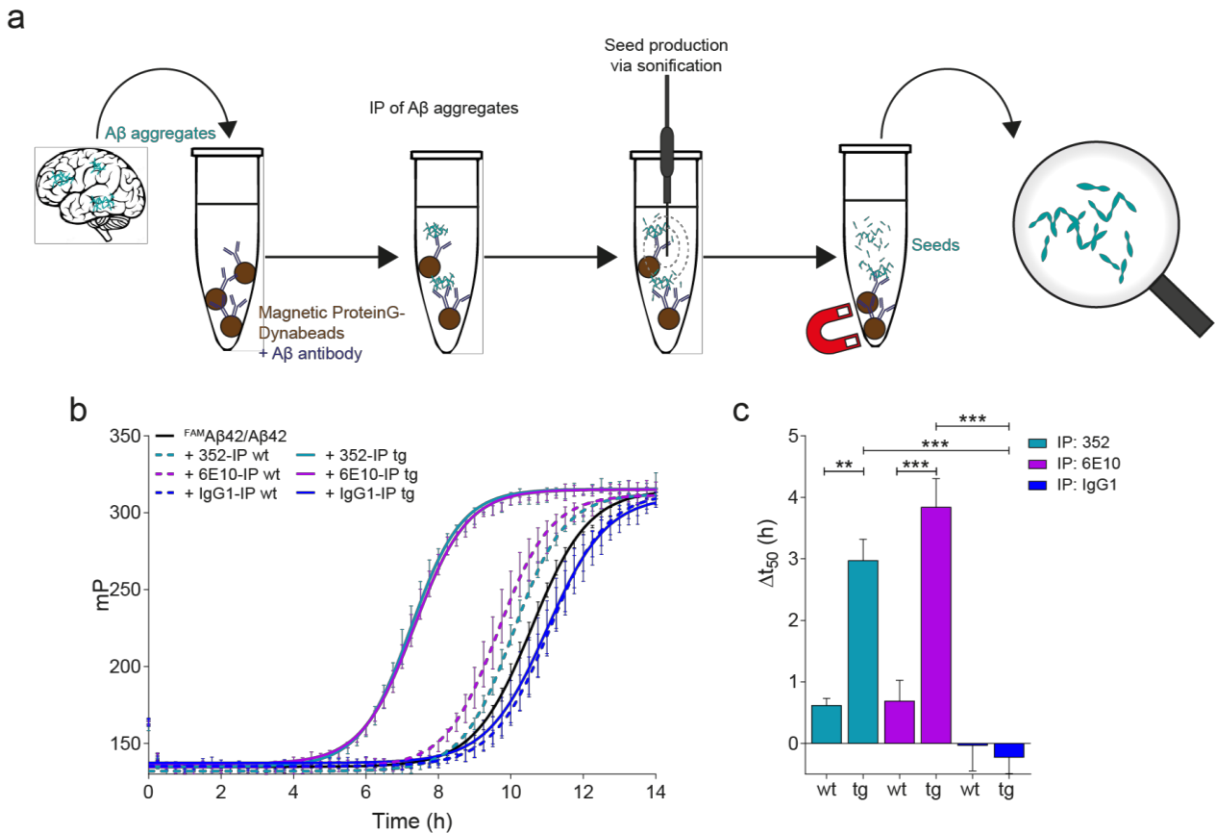

Figure 37 | Enrichment of seeding-competent Aβ aggregate species from transgenic AD mouse brain
(a) Schematic representation of the workflow for the enrichment of seeding-competent Aβ assemblies from mouse brain homogenates by immunoprecipitation (IP) experiments. Aβ-specific antibodies bound to magentic beads enable the isolation of Aβ aggregates from tg mouse brain homogenate. Subsequent sonication of bound aggregates leads to a fragmenation and smaller assemblies that can be further analyzed. (b) Aβ42-FP analysis of extracted Aβ aggregate species isolated from APPPS1 tg brain homogenates with Aβ specific antibodies (352, 6E10) reveal seeding activity in comparison to age-matched wt control. Shown is one representative experiment (mean ± SD of quadruplicates). (c) Quantification of seeding effects. Data are mean ± SEM (n = 3) and statistical significance was assessed by one-way ANOVA followed by Bonferroni multiple comparison post hoc test. **, p≤0.01; ***, p≤0.001.

As part of the standardization, the step of seed release was subjected to a more precise examination. Using a sonicator water bath for seeds release might come with deviations between different samples as they are floating around in floating tube racks on the water surface and thus might get exposed to different hot spots within the sonication time. Hence, the force that is applied to different samples might vary due to their position in the water bath. To obtain more precise results for all tested samples, two alternative sonicator devices were tested. First, a single sonicator tip was used and directly compared to the performance of the water bath sonicator. 6E10-reactive Aβ aggregate species extracted from transgenic APPPS1 mouse brain (22 mo) were prepared and sonicated either 15 min in the water bath or with the single tip device for different durations (10 sec up to 1 min) and under various conditions (continuous and intermitted pulsing; intensities ranging from 20 % to 60 %). Tip sonication for 30 sec with 20 % intensity proved to be most efficient and seemed to amount to water bath sonication efficiency when compared in an Aβ42-FP assay (Fig. 38a). By use of a single tip, deviations in operating ultrasound force can be diminished as any sample would be processed separately. To be able to handle more samples simultaneously without a large time delay between the different samples, use of an 8-tip attachment was also tested. For this experiment 6E10-reactive aggregates bound to dynabeads were transferred to a non-binding 96-well plate in a total volume of 100 µl per well. Examining homogeneity between the 8 tips revealed a good comparability (Fig. 38b), but the observed seeding effect was smaller than with the single tip when using the same duration and intensity for sonication as the power is distributed over 8 entities. Again, systematic testing of different conditions and intensities resulted in using 1 min sonication with 60 % intensity to achieve good efficiency with the 8-tip attachment. Longer sonication duration (1min instead of 30 sec) helped to enhance the seed release, but a further increase up to 2 min diminished the efficiency again (Fig. 38c). Thus, applying too harsh sonication conditions for the release of seeds can be counterproductive as the applied power is likely to also release antibody fragments from beads together with the aggregates. These antibody fragments could then impair the FP measurement in ^{FAM}Aβ42/Aβ42 co-polymerization assays. Therefore, a systematic evaluation of the precise sonication conditions was crucial to ensure maximal fragmentation of immunoprecipitated Aβ aggregates.

Additionally to the FP readout also a denaturating filter assay was performed in order to assess the size and SDS-stability of the released Aβ aggregates (Fig. 38d, e). It can clearly be seen that the SDS-stable Aβ aggregates after IP almost completely get fragmented into smaller species with all methods as they cannot be detected on the cellulose acetate membrane anymore. Sonication with the 8-tip attachment proved not only to be the most handy and precise method, but also the most efficient tool for the release of seeds. Together, it could be shown that through the combination of the IP method with the sonication assay Aβ aggregates with seeding activity can be efficiently enriched from AD transgenic mouse brains.

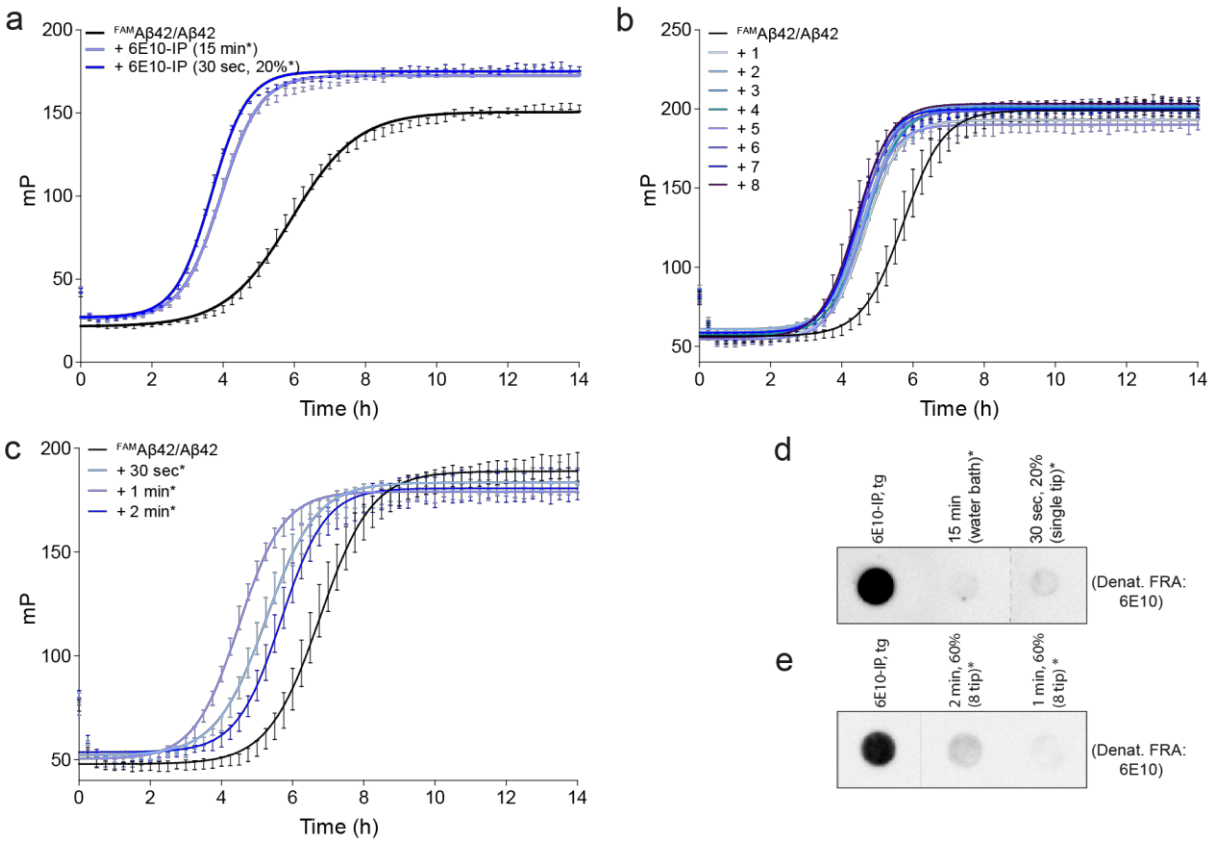

Figure 38 | Comparison of sonicator devices for optimizing seed release from extracted Aβ material
(a) 6E10-reactive Aβ species extracted from tg mouse brain was sonicated using a water bath for 15 min (15 min*) or utilitzing a sonicator tip for 30 sec at 20 % intensity (30 sec, 20 %*). Analysis of obtained seeds in Aβ42-FP assays revealed that both methods efficiently realease seeds. (b) Use of an 8-tip attachment allows the simultaneous sonication of 8 samples with similar output. (c) For the 8-tip appartus a sonication duration of 1 min at 60 % seems to provide the optimal setup to obtain seeding-competent Aβ species. (d) Analysis of dynabeads before and after seed release (indicated with asterisk) on a denaturating filter. Using the 6E10 antibody for detection reveals a high load of SDS-stable aggregates after IP. Sonication for 30 sec with a single tip reveals the same efficiency as sonication with the water bath to shred extracted aggregates into smaller species. (e) Seeds release with an 8-tip attachment for 1 min (60 %) shows the highest effiency to transform extracted Aβ aggregates into smaller fragments.

5.3.2.2 Concentration-dependent and time-dependent analysis of seeding activity

Next, the extracted Aβ seeds were used in different dilutions to determine concentration-dependency of the seeding activity. Figure 39 shows the result for the transgenic 6E10 and 352-seeds (concentrated, 1:5, 1:10 and 1:50). A concentration-dependent decrease of the seeding activities was observed with higher dilutions. Interestingly, in this used mouse brain (APPP21, 18 mo) the seeding efficiency differed with the 6E10 and 352 antibody used for IP. It is conceivable that the two antibodies enrich different amounts of seeds and that different aggregate types are present amongst individual animals that are detected with the 6E10 and 352 antibodies.

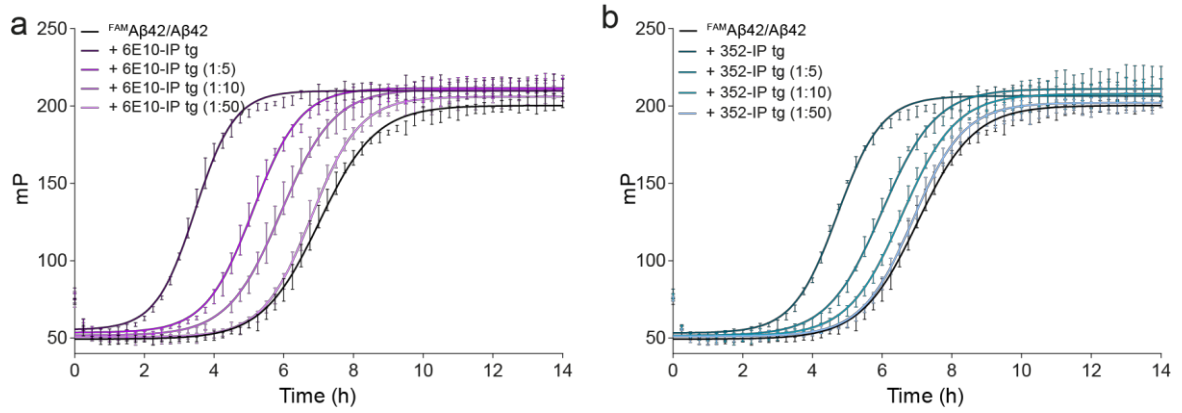

Figure 39 | Concentration-dependent seeding with tg mouse seeds
(a) Addition of 6E10-reactive or (b) 352-reactive seeds enriched from tg mouse brain homogenates (APPPS1, 18 mo) accelerate the spontaneous ^{FAM}Aβ42/Aβ42 co-polymerization in a concentration-dependent manner.

Since the amount of Aβ plaques increases with age, it was analyzed whether age influences the detection of seeding-competent Aβ aggregates in transgenic AD mouse brains. Therefore, mice of two different AD models were analyzed at different ages (Fig. 40). Analysis of immunoprecipitates from brains of 5xFAD transgenic mice with an age of 1, 2 and 5 month revealed that in brains of 1- and 2-month-old mice no Aβ seeding activity is detectable, while in brains of 5-month-old mice seeding activity could be observed (Fig. 40a). Additionally, analysis of immunoprecipitates prepared from brains of APPPS1 transgenic mice (4, 6 and 9 month) revealed that in this model, Aβ seeding activity can be detected with an age of 9 month (Fig. 40b). Since the 5xFAD mouse model with its five different AD mutations represents a much more aggressive model with a more severe and earlier phenotype, the earlier detection of Aβ seeding activity in this mouse model compared to APPPS1 transgenic mice is plausible.

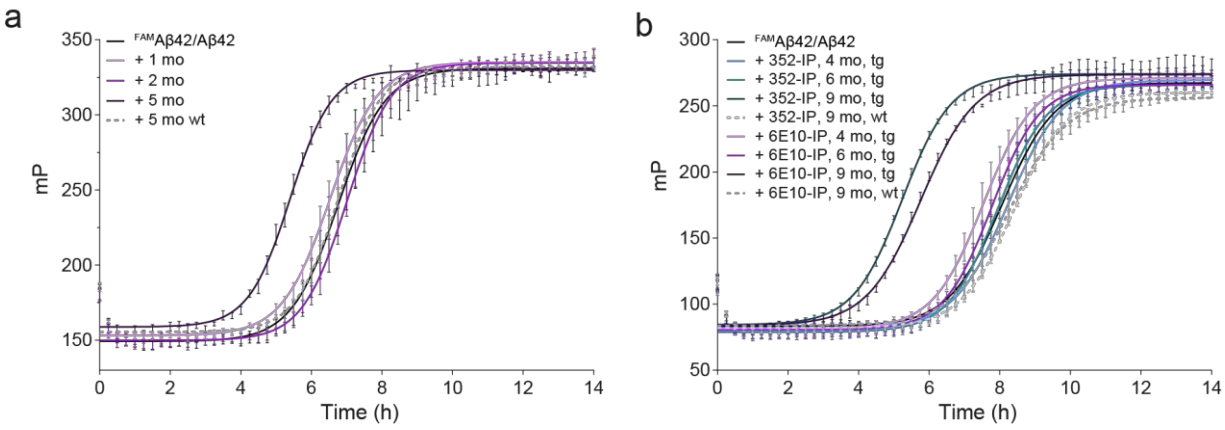

Figure 40 | Detection of seeding-competent Aβ aggregate species in different aged transgenic mice
(a) Analysis of 5xFAD mice of different age (1, 2, 5 mo) regarding their seeding activity with Aβ42-FP assay after IP with 6E10 antibody reveals that seeding-competent Aβ species are detectable in brains of 5-month-old mice. (b) Analysis of APPPS1 mice of different age (4, 6, 9 mo) regarding their seeding activity with ^{FAM}Aβ42/Aβ42 co-polymerization assay after IP with 6E10 or 352 antibody demonstrates that seeding-competent Aβ aggregate species can be detected at 9 month of age.

5.3.2.3 Characterization of seeds

The release of Aβ seeds from dynabeads by sonication has the advantage that the enriched structures can be further analyzed with biochemical and imaging methods. Besides assessing their seeding potential, also morphology and other characteristic features can be evaluated. Therefore, I first tried to characterize the seeding-competent material prepared from an APPPS1 tg mouse with an age of 18 month. Dot blot and denaturating filter assays confirmed that the enriched seeds are 6E10-reactive Aβ peptides (Fig. 41a) and that they are SDS-stable structures (Fig. 41b). Analysis by SDS-PAGE/NativePAGE and immunoblotting revealed that the 352- and 6E10-reactive seeds are higher molecular weight aggregates (Fig. 41c, d).

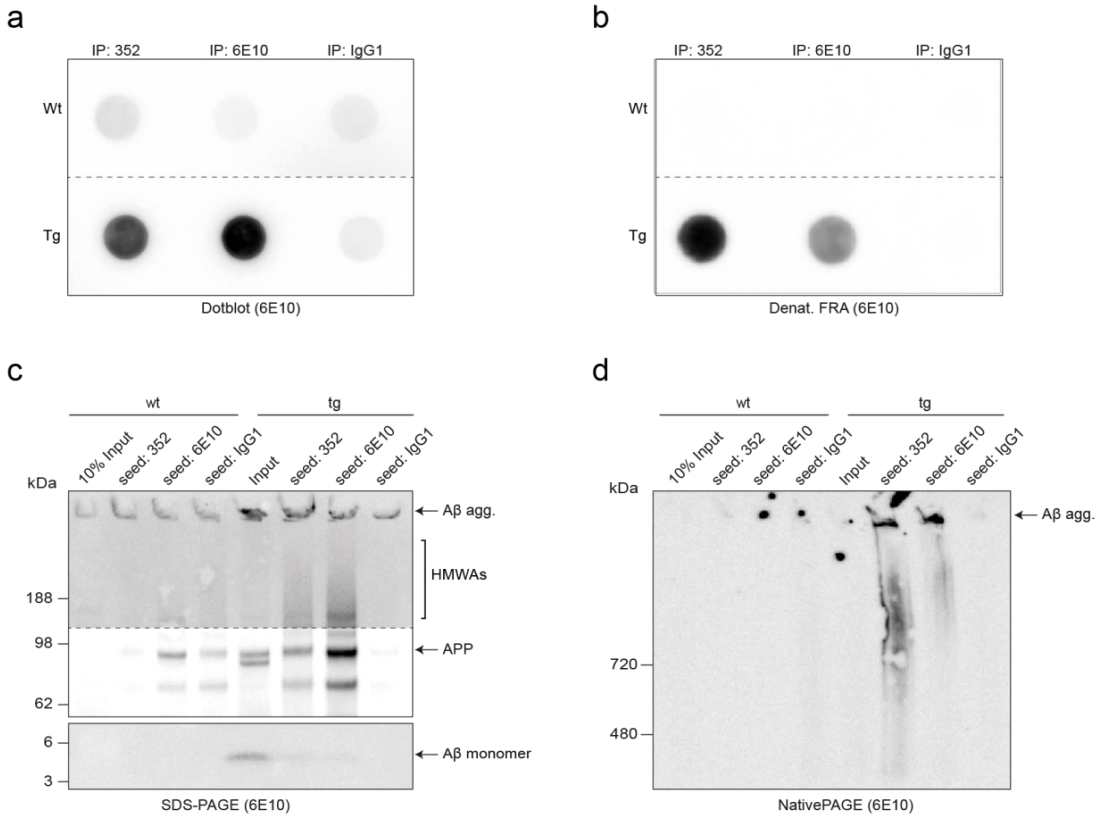

Figure 41 | Characterization of IP enriched seeding-competent Aβ species
Analysis of released seeds after IP from mouse brain lysates using (a) Dot blots, (b) denat. FRAs, (c) SDS-PAGE and (d) NativePAGE. All membranes were developed using the 6E10 antibody. For better visualization of aggregates and Aβ monomers parts of the blot were longer exposed during development (indicated by dashed lines).

To further elucidate the morphology of the prepared seeding-competent Aβ aggregates, both atomic force microscopy (AFM) and immunoelectron microscopy (IEM) were performed. Figure 42a shows AFM images from 352- and 6E10-reactive seeds prepared from the tg APPPS1 lysate, revealing Aβ species with a complex fibrillar structure. IEM images of 6E10-reactive seeds confirm these data as

small fibrillar structures with diameters of ~12 nm and lengths ~90 nm can be readily detected (Fig. 42b). These structures were also detected with the 6E10 antibody and a gold-labeled secondary antibody (12 nm). AFM and IEM analysis of control samples from wt seeds or IgG1-reactive tg seeds did not reveal specific fibrillar structures (Supplementary Fig. S1).

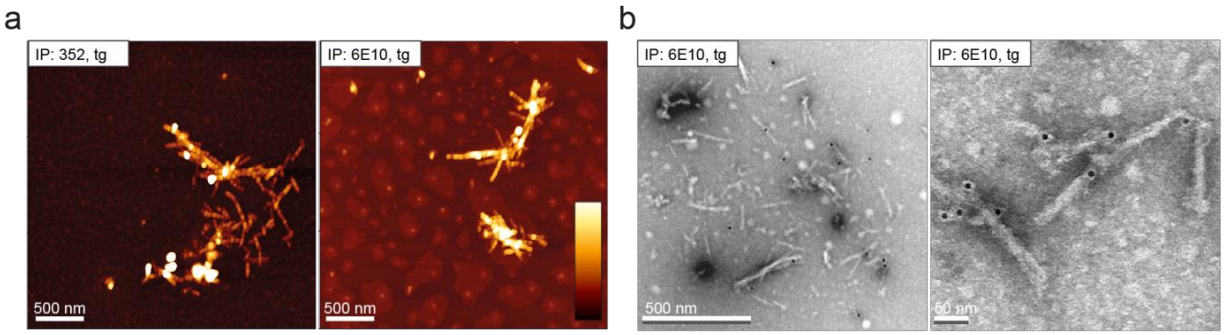

Figure 42 | Characterization of extracted Aβ seeds with high-resolution imaging methods
(a) AFM images of tg 352- or 6E10-reactive mouse seeds; 3 x 3 µm, scale bar: 500 nm, color gradient represents 0-10 nm height. (b) Immunoelectron microsocpy of tg 6E10-reactive species labeled with primary 6E10 antibody and a secondary antibody with a 12 nm gold particle; left scale bar: 500 nm, right scale bar: 50 nm.

5.3.2.4 Aβ aggregates prepared from mouse brains cause a cellular metabolic impairment

Recently, increasing efforts were made to correlate seeding activity of aggregates with toxicity to better explain the AD pathology. Since the enriched Aβ seeds are potential disease-relevant aggregates, I assessed their toxicity in PC12 cells using the established MTT assay[276,277]. MTT reduction was monitored after an incubation period of 24 or 48 h. As already mentioned earlier, the colorimetric MTT assay detects absorbance changes at 570 nm due to a conversion of a tetrazolium salt into a formazan product by living cells. Previously, the increase of formazan signals upon Aβ treatment was interpreted as an indication of cell death. However, meanwhile it is assumed that a reduced MTT signal is not an indication for toxicity but rather a marker for impaired mitochondrial metabolism, which can lead to cell death in the long term[305,306]. Strikingly, I found that the material that was enriched with the antibodies 352 or 6E10 from wildtype mouse brains homogenates or from AD transgenic brains with the isotype control antibody IgG1 did not cause MTT reduction in PC12 cells. In contrast, a significant concentration-dependent effect was detected with material that was enriched with the antibodies 352 and 6E10 from AD transgenic brain (Fig. 43a, b). This indicates that the enriched seeding-competent, fibrillar Aβ aggregates are proteotoxic structures that lead to mitochondrial dysfunction in PC12 cells. Together these studies indicate that the enriched Aβ aggregate species, which possess seeding activity, are likely disease relevant proteotoxic structures that impair the mitochondrial metabolism of neuronal-like cells.

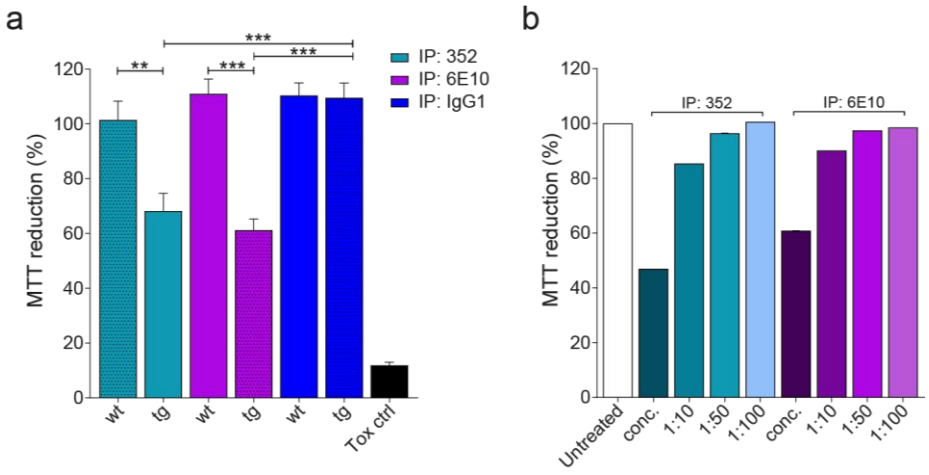

Figure 43 | Antibody-enriched Aβ seeds lead to metabolic impairment in a PC12 cell model
(a) Influence of prepared Aβ seeds on the metabolism of PC12 cells assessed with MTT assay. The extracted 352- and 6E10-reactive Aβ seeds significantly reduce the turnover of a tetrazolium salt into a formazan product, indicating an impairment of mitochondrial function. Values represent percentage of buffer control. 0.05 % Triton X-100 were used as toxicity control. Statistical significance was assessed by one-way ANOVA followed by Bonferroni multiple comparison post hoc test. **, p≤0.01; ***, p≤0.001. (b) Concentration-dependet effect of 352 and 6E10-tg seeds on PC12 cells.

5.3.2.5 Analysis of APP23 mice extracts

In addition to samples prepared from 5xFAD and APPPS1 transgenic mice, also samples from APP23 transgenic mice were biochemically characterized and tested for their seeding activity. Brain extracts of two different 7-month-old APP23 mice, (1) and (2), were first analyzed with dot blot assays using the 6E10 and 352 antibodies (Fig. 44a). Standard homogenization of brain samples in the *Jucker* lab is performed with 10 % (w/v) sterile PBS via vortexing and sonication for 3 x 5 seconds. Afterwards the extract was centrifuged at 3,000 × g for 5 minutes[144,307]. According to a personal statement of a member of the *Jucker* lab, the seeding activity of brain extracts prepared from 7-month-old APP23 transgenic mice was very low in *in vivo* seeding assays where the extract is intracerebrally injected into young, pre-depositing APP23 transgenic mice and the induction of Aβ deposition in different brain regions analyzed via histological stainings[296].

Therefore, I analyzed if the IP approach would allow a concentration of seeding-competent Aβ aggregate species from such extracts. However, my analysis revealed that no seeding activity is detectable in brain extracts prepared from 7-month-old APP23 mice (Fig. 44b). In contrast, analysis of another PBS extract from a pool of 30-month-old APP23 mice with known *in vivo* seeding activity (injection of 2.5 µl extract after 1:1000 dilution leads to 50 % affected mice showing seeding activity in *in vivo* assays after 6 month; personal statement) showed a striking seeding effect in the Aβ42-FP assay after IP with the 6E10 antibody and a moderate effect with the 352 antibody (Fig. 44c). In this brain extract also high molecular weight Aβ aggregate species were detected with Western blotting (Fig. 44d), confirming the results with the FP assays.

Since it was shown earlier that the presence of detergents in the homogenization buffer might be crucial for the maximal release of Aβ aggregate species, the detergents as being used in the RIPA buffer were subsequently added to the PBS extracts and incubated for 30 min while rotating. Indeed, the seeding effect for the 6E10 and 352-enriched Aβ species was enhanced (Fig. 44c, dashed lines), highlighting the already discussed necessity of detergents in the homogenization buffer.

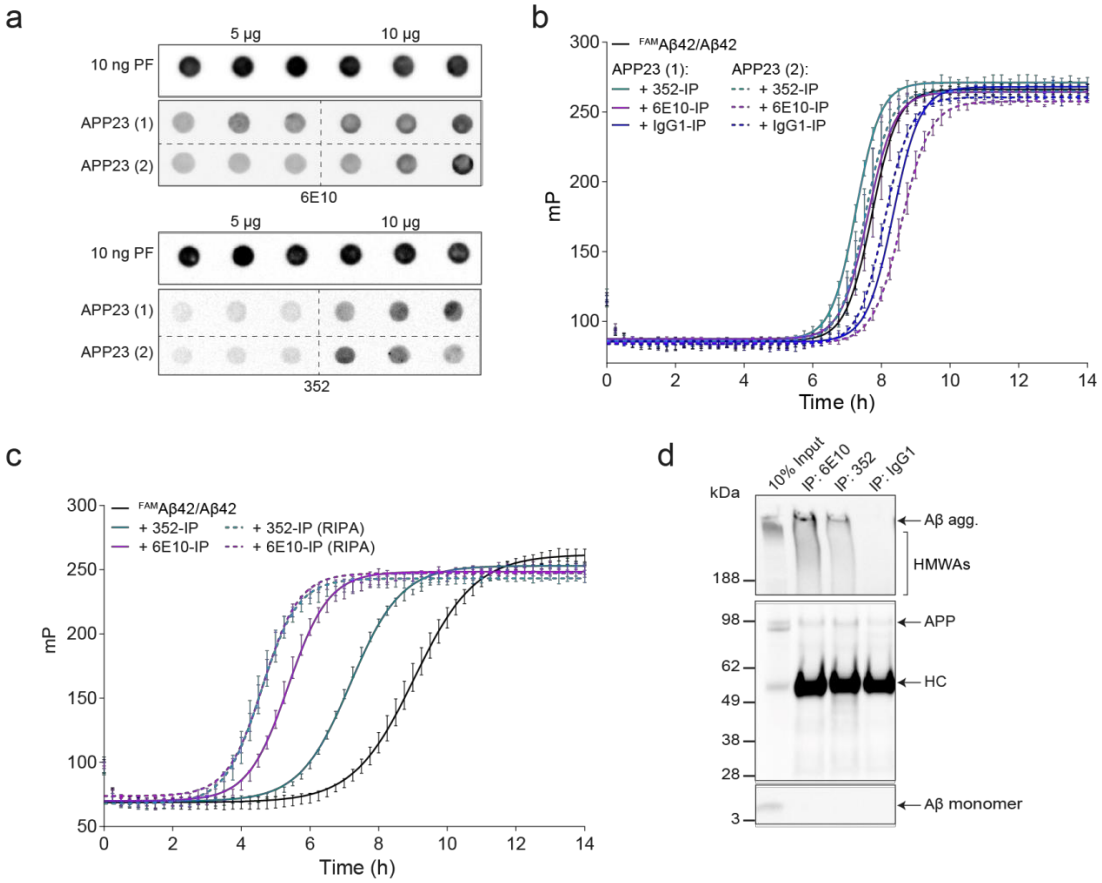

Figure 44 | Analysis of APP23 PBS extracts
(a) Dot blot analysis of APP23 PBS extracts revealed the presence of 6E10- and 352-reactive Aβ material. (b) Use of PBS extracts from two different 7-month-old APP23 mice, (1) and (2), for the IP with 352 and 6E10 antibody did not reveal any detectable seeding activity in the Aβ42-FP assay. (c) Analysis of *in vivo* seeding-rich PBS pool in ^{FAM}Aβ42/Aβ42 co-polymerization assay reveals a high seeding activity of 6E10-reactive species. The seeding activity of the 352-reactive species can be increased upon supplementation with RIPA detergents (dashed line). (d) Western blot of *in vivo* seeding-rich PBS pool shows the enrichment of high molecular weight assemblies after IP with 352 and 6E10 antibody.

5.3.2.6 Proteinase K digestion

My experiments indicate that the presence of detergents in protein homogenates promote the extraction of seeding-relevant Aβ species from biosamples. However, literature indicates that detergents and especially SDS (Sodium dodecyl sulphate) has the potential to induce amyloid formation in cell-free assays[308,309]. Therefore, I analyzed whether the observed increased seeding

effect might be due to SDS or if the detergent rather enables antibody binding to target Aβ aggregate species in a crude homogenate.

As an alternative approach that works without SDS, digestion with the enzyme proteinase K (PK) was tested. Proteinase K is a subtilisin-related serine protease with both endo- and exoproteolytic activity that hydrolyzes a variety of peptide bonds. Thus, it was conceivable that treatment with PK would digest the majority of proteins in a crude brain homogenate, except seeding-competent Aβ aggregates as they were shown to be PK-resistant[296]. Additionally, a recent publication also suggested that the sensitivity of a different seeding assay could be increased upon PK treatment of protein homogenates[136]. Therefore, a brain hemisphere of a 22-month-old APPPS1 transgenic mouse was homogenized in a standard RIPA buffer (sample 1) or a RIPA base buffer (50 mM Tris, pH 7.5, 10 mM NaCl) without any detergents, but supplemented with PK (w/w ratio of total protein concentration in the sample: 1:500; sample 2). After incubation for 2 h at 25°C PK activity was stopped with a protease inhibitor mix (4x PK concentration; 30 min at 4°C, rotating). A third sample was homogenized like sample 2 but detergents from standard RIPA buffer (1 % SDS, 0.5 % Sodium deoxycholat, 1 % Triton) were added afterwards (sample 3). Next, IPs and FP assays were performed under standard conditions. For reasons of simplicity, Figure 45a shows the result with the 352 antibody only, however, the same results were obtained when using the 6E10 antibody for IP (*data not shown*). All three approaches revealed significant and comparable seeding effects, when the 352-reactive immunoprecipitates were analyzed in FP assays. The finding that a high seeding activity was obtained in samples that were treated with PK rules out a potential artificial result due to SDS treatment and further confirms the hypothesis that the surface of Aβ aggregate species needs to be exposed in order to promote seeding.

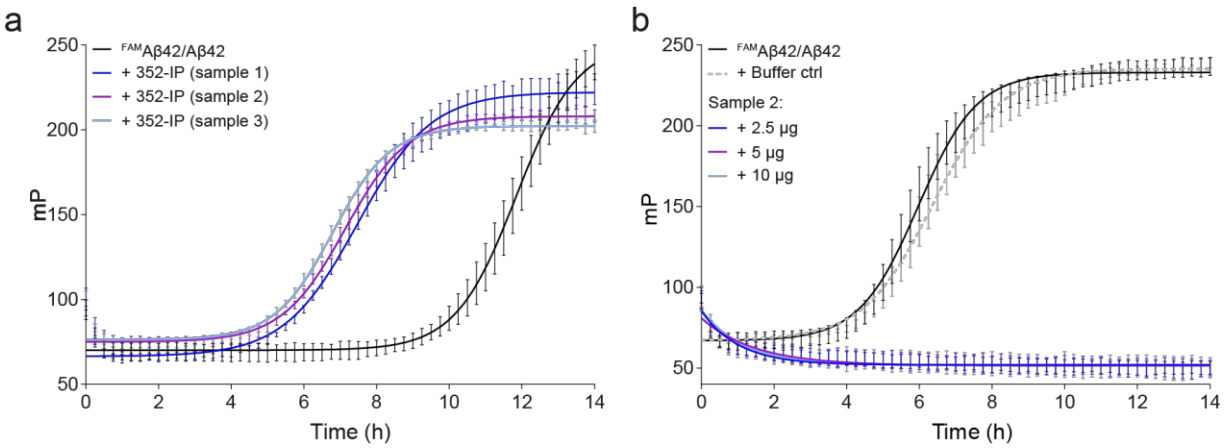

Figure 45 | Treatment of detergent-free crude brain homogenate with Proteinase K
(a) Treatment of SDS-free brain lysate with Proteinase K (PK, sample 1) reveals the same seeding activity after IP with the 352 antibody in ^{FAM}Aβ42/Aβ42 assays as 352-enriched Aβ seeds from homogenates prepared with detergent-rich RIPA buffer (sample 2). (b) Direct utilization of PK-treated brain extracts without preceding IP inhibits the ^{FAM}Aβ42/Aβ42 co-polymerization in FP assays.

Additionally, the PK-digested homogenate without supplemented RIPA detergents (sample 2) was added to a standard ^{FAM}Aβ42/Aβ42 co-polymerization assay in different concentrations without preceding IP as these samples should not interfere with the FP measurement due to the lacking detergents (Fig. 45b). However, under these conditions an inhibition of the ^{FAM}Aβ42/Aβ42 co-aggregation was observed. This could be due to the partially digested proteins and membrane components that are present in the crude brain homogenate. In summary, these studies further support the relevance of the established IP procedure, which enriches Aβ seeds and reduces the abundance of interfering components that are present in crude lysates.

5.3.3 Analysis of human Alzheimer's disease brain samples with FP assays

5.3.3.1 Proof of principle

After successful establishment of the workflow for the enrichment of seeding-competent Aβ aggregate species from transgenic mouse brains, the method was ought to be applied to human brain samples. In general, the analysis of human brain samples can be more challenging than the investigation of transgenic mouse brains. It has to be considered that the Aβ plaque load can already differ enormously within a group of e.g. 5xFAD transgenic mice that were bred on the same genetic background and kept under the same conditions (e.g. food, housing), thus with standardized and controlled environmental factors. Human patients, however, might exhibit tremendous differences in their lifestyle and additionally might not have suffered from a severe phenotype as transgenic mice that bear multiple AD related mutations. Furthermore, the limitation of patient brain material might make the adjustment of experimental parameters for the establishment of new methods very difficult. As a proof of principle experiment, I applied the established immunoprecipitation technique to enrich Aβ aggregates from AD patient brains. Human brain samples were obtained from the Newcastle Brain Bank. In total, eight brain samples (4 AD patient samples, 4 Ctrl brain samples) were analyzed, but only one AD patient sample (AD9) showed Aβ aggregates already in the input fraction that could be enriched by use of the 352 antibody in comparison to control patients. Figure 46a shows a Western blot analysis of the IPs from this AD patient (AD9) and a representative control patient (Ctrl19). Sample AD9 was from a 68-year-old male AD patient with a Braak VI phenotype, the control brain sample (Ctrl19) was from a 67-year-old person that did not show any AD-related changes in the *post mortem* brain (Braak 0). Braak staging helps to classify the severity of an AD phenotype and disease progression due to the observed tau neurofibrillary tangle distribution in affected brains[13,310]. Even though Braak stages reflect more the tau neurofibrillary tangle phenotype, a Braak VI stage depicts the end stage of AD progression. It thus can be assumed that also the amyloid plaque deposition is already

high. However, the enrichment of Aβ aggregates from the AD9 patient brain was only successful when I used 2 mg of brain lysate for the IP experiment. In comparison, 0.25 mg brain lysate was sufficient to enrich Aβ aggregates from APPPS1 or 5xFAD transgenic mice (Fig. 37, 39 and 40). Interestingly, TEM analysis revealed that the immunoprecipitated Aβ aggregates from the patient brain also have typical fibrillar morphology (Fig. 46b, 352-IP AD brain). For TEM analysis, the IP-enriched material was fixed with glutaraldehyde and embedded in epoxy resin. Subsequently, ultrathin sections were prepared and contrasted with uranyl acetate. In contrast to the fibrillar species enriched from the AD9 patient, only unspecific material could be enriched from the control patient (352-IP Ctrl brain). Since suchlike structures (black arrowheads) also occurred with a beads only control (Beads), this is likely to represent unspecific background signals. Together, these first experiments indicated that IPs from human AD brain homogenates are possible and fibrillar potentially disease-relevant Aβ structures can be successfully enriched.

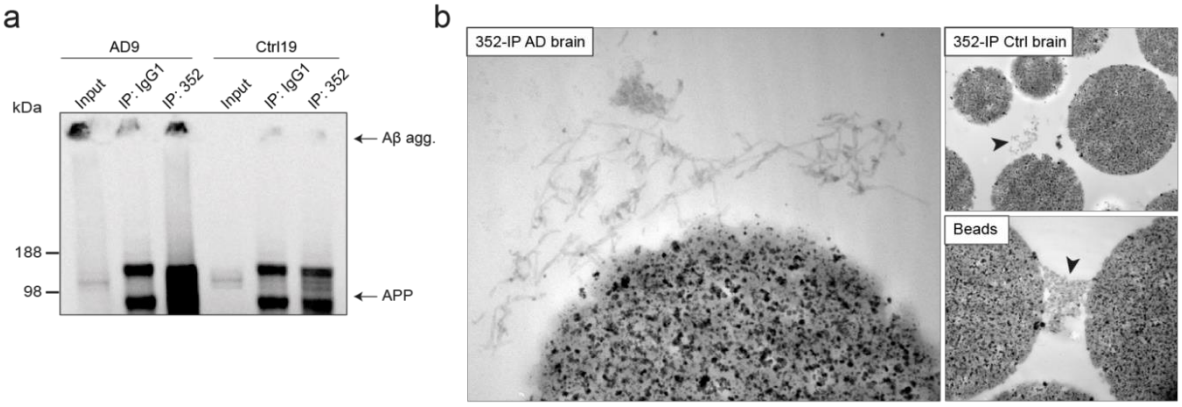

Figure 46 | Enrichment of Aβ aggregates from human brain samples
(a) Western blot analysis after IPs from an AD (AD9) and a control patient (Ctrl19) brain with 352 and IgG1 (control) antibodies. (b) TEM of immunoprecipitated 352-reactive Aβ aggregate species from patient AD9 and Ctrl19. After IP with 352 antibody the magnetic dynabeads together with the extracted Aβ material were fixed in glutaraldehyd and embedded in epoxy resin before ultrathin sections were prepared and contrasted with uranyl acetate. Extracted Aβ material form an AD patient reveals fibrillar structures. TEM analysis of samples enriched from a control brain reveals only unspecific material that was also enriched with beads alone.

5.3.3.2 Analysis of human brain samples with native filter assays and FP-based seeding assays

Since a higher amount of brain lysates was necessary for immunoprecipitation from human samples and the number of samples further limited, initially, native filter assays were performed from available samples with the 6E10 and the 352 antibodies to specifically select patients with a high amount of Aβ aggregates (Fig. 47a, b). For this, a human brain sample set consisting of 10 AD patients and 10 control samples from Newcastle Brain Bank with various diagnosed Braak stages was analyzed. Almost no signal could be detected in any patient sample when using the 352 antibody for development of the membrane. The 352 antibody was raised against synthetic protofibrils and even

though reliable results could be achieved with this antibody in transgenic mouse brains, the antibody might not be suitable to detect Aβ aggregate species in human brain samples. Analysis with the 6E10 antibody showed that high signals could be detected in almost as many AD (4, 5, 8) as control samples (16, 17, 18). Two AD (4, 8) and control samples (11, 15) were consciously chosen as representatives of each group to perform IP experiments. For the IP analysis the 6E10 antibody was used that successfully detects Aβ aggregates in filter assays. Western blot analysis revealed that no higher molecular weight Aβ aggregates could be enriched from brain homogenates by the IP experiments (Fig. 47c). Furthermore, no significant seeding activity was detectable when the antibody-enriched immunoprecipitates were analyzed in FP assays (Fig. 47d). This indicates that the IP method needs to be further improved to efficiently enrich seeding-competent Aβ aggregates from AD patient brain extracts.

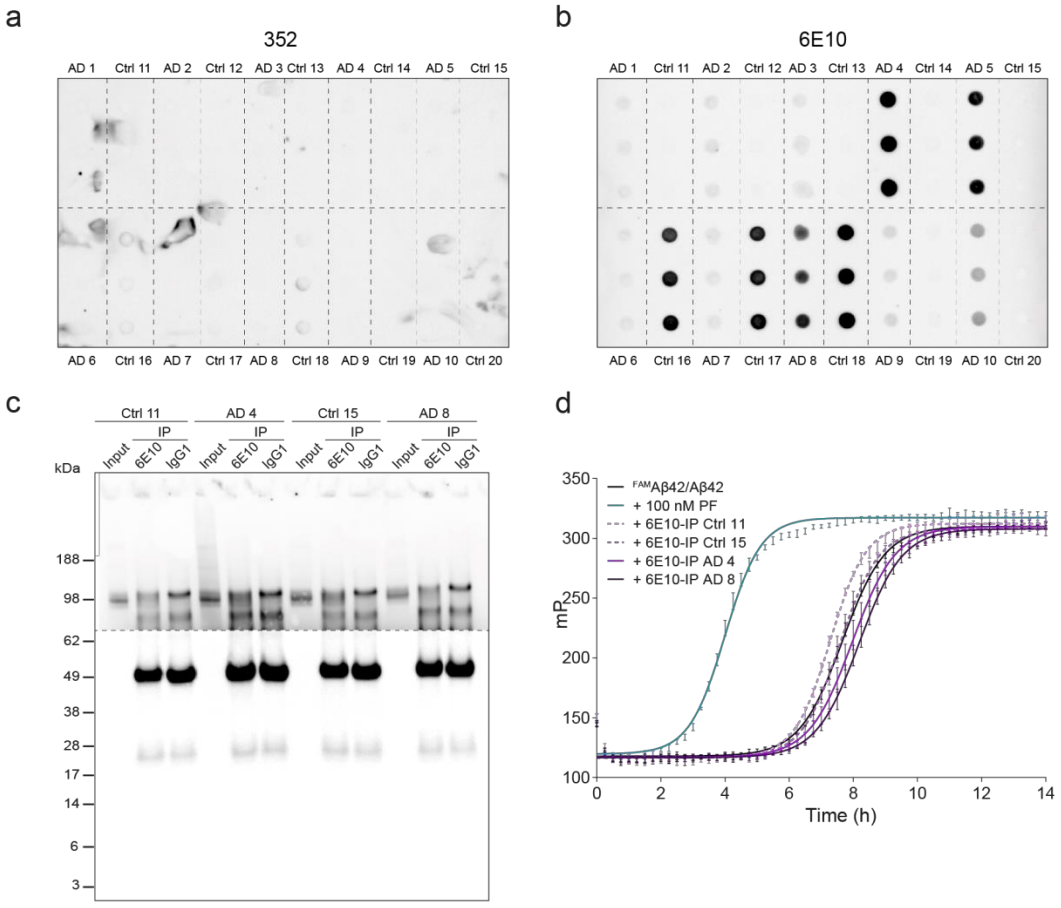

Figure 47 | Analysis of selected human brain samples with native FRAs, SDS-PAGE and immunoblotting and FP-based seeding assays

(a) Native FRA from 10 AD patient and 10 healthy control samples (20 µg) immunodetected with 352 or (b) 6E10, respectively. (c) Western blot analysis (detection with 6E10) after IP with 6E10 and IgG1 (control) antibodies from selected AD samples (4, 8) and control samples (11, 15) using 2 mg lysate. For better visualization of Aβ material in the gel pockets the upper part of the blot was longer exposed during development (indictad by dashed lines). (d) Analysis of seeding-activity from enriched 6E10-reactive material revealed no seeding effect for any AD sample with the ^{FAM}Aβ42/Aβ42 co-polymerization assay.

5.3.4 Analysis of human Alzheimer's disease CSF samples with FP assays

Recent studies suggest that small soluble Aβ oligomers rather than large fibrillar aggregates may lead to neuronal degradation in AD[311-313]. It therefore would be reasonable to investigate earlier time points of disease progression and to assess whether seeding-competent Aβ assemblies are detectable with the established methods. Therefore, I next focused on samples of human cerebrospinal fluid (CSF) to obtain higher sample numbers and to investigate earlier stages of disease. As already mentioned CSF is in direct contact with the cerebral tissue and thus represents an accessible biosample that can be obtained from patients via a minimal-invasive procedure. Additionally, analysis of CSF has the benefit that potentially very early biomarkers for diagnosis can be identified. Furthermore, misfolded Aβ aggregates isolated from the CSF of AD patients have recently been shown to be seeding-competent structures that accelerate the polymerization of monomeric Aβ[258]. Therefore, the experimental setup of IP and seed release by sonication was applied to human CSF samples by undertaking a systematic study of a larger patient cohort. By correlating the Aβ seeding activity of analyzed CSF samples with neuropsychiatric behavioral tests potentially novel insights into AD pathogenesis can be gained. Still, as already described earlier, it had to be considered that Aβ42 levels are usually decreased in AD patients[42-44] which would not be favorable for the IP approach. But due to a recent publication[45] where it was shown that within a very early phase of AD progression Aβ levels are increased, I postulated that through IPs with specific Aβ antibodies such as 352 small seeding-competent fibrillar oligomers could be detected in CSF samples.
All CSF samples were kindly provided by PD Dr. Oliver Peters (Klinik für Psychiatrie und Psychotherapie Charité, Berlin). Information about the used samples and sample preparation can be found in the material and methods section. The concentrations of Tau, Aβ42, Aβ40 as well as the ratios of Aβ40/Aβ42 and tTau/Aβ42 were determined for all samples. Additionally, the mental status of each patient was assessed leading to the indicated diagnosis.

5.3.4.1 Optimization for the analysis of CSF samples

Before the analysis of CSF samples was carried out, the IP method was examined regarding possible optimization steps. First, I assessed the total protein concentration of CSF samples by BCA measurements in order to use the same protein amounts for IPs. However, since this method delivered unsatisfactory and unreliable results (*data not shown*), I generally used the same volumes for IP experiments (0.5 ml per antibody per IP), a common approach used in several other studies too[314-317]. Second, instead of performing washing steps with RIPA wash buffer, an artificial CSF (ACSF)[318] solution was prepared to maintain physiological conditions. Finally, CSF samples were supplemented with 0.05 % Tween as a recent publication by *Toombs et al.* showed that this detergent

reduces variability in CSF Aβ42 measurements that were otherwise caused by protein-tube surface interaction[319].

Three CSF samples were used for a first proof of principle experiment to evaluate if Aβ aggregates can be enriched from human CSF samples. Therefore, samples from two diagnosed AD patients (#5 and #14) suffering from moderate dementia and mild cognitive impairments (MCI), respectively were used. As a control, CSF from a 42-year-old individual diagnosed with anxiety disorder, but without any cognitive deficits was used (#15). Table 5 shows the available biomarker levels for the three samples. Numbers highlighted in red display critical values that indicate an AD diagnosis. For Aβ42 levels a concentration <600 pg/ml suggests the presence of an amyloid metabolic disorder, furthermore an Aβ42/Aβ40 ratio <0.065 pg/ml is considered noticeable. A tau concentration >350 pg/ml is an indicator of a neurodegenerative disease (age-dependent; >300 pg/ml for patients younger than 60 years, >450 pg/ml for patients older than 80 years) but were not further taken into account in this study.

#	Age	Diagnose	hTau (pg/ml)	Aβ42 (pg/ml)	Aβ40 (pg/ml)	Ratio Aβ40/Aβ42	Ratio tTau/Aβ42
5	75	Moderate AD, meningioma, remitted after surgery	655	208	3770	0,055	3,154
14	76	Mild cognitive impairment, neurodegenerative disorder	769	630	14230	0,044	1,221
15	42	Anxiety disorder without cognitive deficits	119	391	5452	0,072	0,305

Table 5 | Diagnosis of CSF samples

The IP experiments were performed using the 352 and 6E10 antibodies and the IgG1 antibody as a control. Figure 48 shows a Western blot analysis of the three CSF samples after IP. In case of the IP with the 352 antibody high molecular weight Aβ structures could be detected in the gel pockets of patient #14, suggesting that seeding-competent aggregates are present in CSF samples of AD patients. In comparison, with the 6E10 and IgG1 antibodies a clear enrichment of high molecular weight Aβ aggregates was not observed.

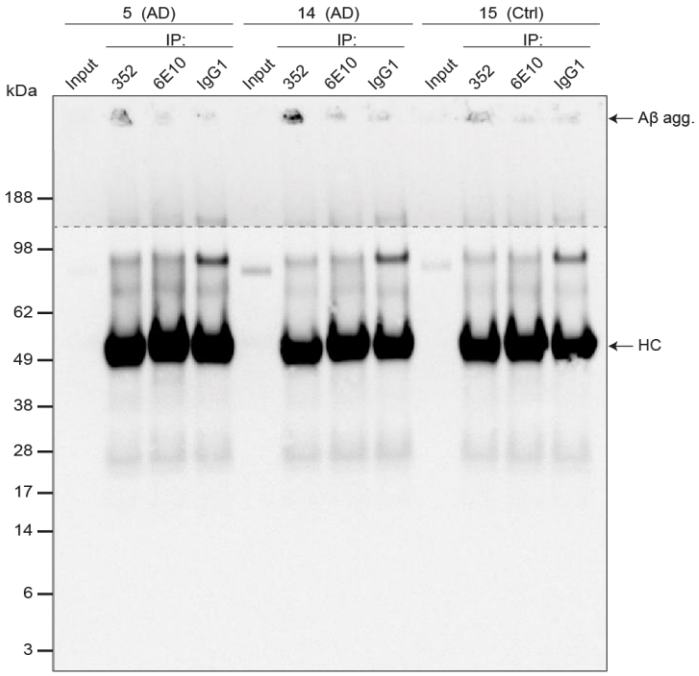

Figure 48 | IP of Aβ aggregates from human CSF samples with Aβ-specific antibodies
Western Blot analysis (detection with 6E10) of a denaturating SDS gel. The protofibril-specific antibody 352 as well as the 6E10 antibody were used to immunopurify Aβ aggregate species from human CSF samples (0.5 ml). IgG1 was used as an isotype control antibody. For better visualization of Aβ aggregates the upper part of the blot was longer exposed during development (indictad by dashed lines).

The CSF contains endogenous immunoglobulins[320], which could prevent a successful IP of Aβ aggregates when ProteinG dynabeads are used. Thus, it was tried to pre-clear the CSF from endogenous antibodies before use in IP experiments. For the pre-clearing step 0.5 ml CSF was added to 1.5 mg ProteinG dynabeads and incubated for 30 min while rotating. Following, the supernatant was removed and IPs with antibodies were performed as described earlier. For this experiment CSF from one diagnosed AD patient (#32) and one control sample (#36) was used. The IPs again were performed with 352, 6E10 and IgG1 antibodies. Table 6 shows the biomarker analysis of the used samples.

#	Age	Diagnose	hTau (pg/ml)	Aβ42 (pg/ml)	Aβ40 (pg/ml)	Ratio Aβ40/Aβ42	Ratio tTau/Aβ42
32	84	Mild dementia, AD type; depressive episode	649	165	4963	0,033	3,939
36	53	Depressive episode with cognitive deficits	84	417	3959	0,105	0,201

Table 6 | Diagnosis of CSF samples

In general, no difference could be observed between immunoglobulin-depleted (IP*) and untreated CSF samples (IP) (Fig. 49a, b). The lag phase after addition of CSF seeds from the AD patient (#32) was slightly reduced (Fig. 49a), but also with the control antibody IgG1. In general, no significant difference could be detected between AD and control patient sample.

Additionally, it was tested if the CSF samples could be analyzed even without an IP experiment since the samples do not contain disturbing detergents and thus could theoretically be analyzed without further treatment. Therefore, artificial CSF (ACSF) was used again to determine the necessary dilution that would not interfere with the measurements in Aβ42-FP assays. Figure 49c shows that addition of undiluted ACSF affects the curve progression of the Aβ aggregation, whereas a dilution of 1:500 did not. Subsequently, the CSF samples, naïve as well as pre-cleared (*) from patient #32 and Ctrl #36 were added in the appropriate dilution (1:500) to a standard ^{FAM}Aβ42/Aβ42 assays (Fig. 49d). Unexpectedly, addition of all CSF samples led to deceleration of the aggregation process with a delay of the lag phase. Even if an artificial CSF solution was already used to adjust the salt content of the buffer control, obviously other impairing components of naïve CSF samples play an important role. A potential capacity of CSF to inhibit Aβ fibril formation was already shown in earlier studies where lipoproteins like apolipoprotein E were hold responsible for the inhibitory effects[321]. Thus, it is important to note that the enrichment of Aβ aggregates from CSF by an IP step is critical for their analysis in Aβ42-FP assays.

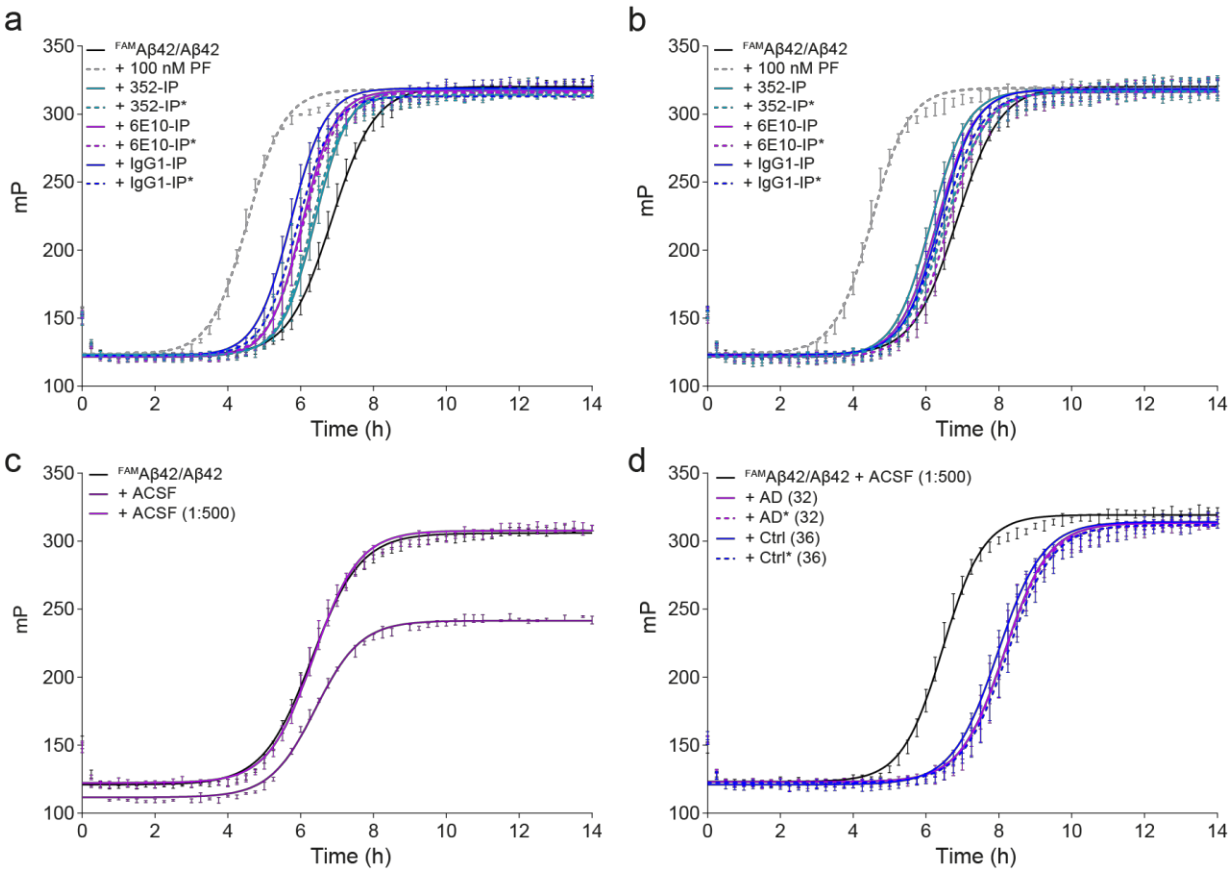

Figure 49 | Pre-clearing of CSF samples and ^{FAM}Aβ42/Aβ42 analysis of CSF samples without IP
(a) Analysis of pre-cleared CSF (IP*) in comparison to untreated CSF after IP from an AD patient (#32) and (b) Ctrl sample (#36) regarding seeding activity using the ^{FAM}Aβ42/Aβ42 co-polymerization assay. (c) Assessment of ACSF dilution that is not affecting the Aβ42-FP measurement. (d) Aβ42-FP assay analysis of CSF samples without IP after dilution (1:500).

Since it was shown that the presence of detergents in the homogenization buffer is crucial to enable a detection of seeding-competent Aβ structures in transgenic mice brains (Fig. 32), it was tested if CSF samples would also benefit from supplementing with detergents. Therefore, CSF from an AD patient (#32) and a control (#36) was supplemented with SDS, Sodium deoxycholate and Triton to ensure final concentrations similar to the RIPA buffer used for mouse brain homogenization. Following, IP was performed using the 6E10 antibody, seeds were released and analyzed with Aβ42-FP assay under standard conditions. A slight seeding effect could be detected for AD samples #32, but also for the control #36 (Fig. 50a). However, no difference could be detected between detergent-treated and untreated samples. Therefore, for following analysis CSF samples were not supplemented with detergents to keep the liquor in naïve condition.

Finally, in the course of optimization it was tested, if an extension of the IP step could help to maximize the outcome of detectable seeding effects from CSF samples. For transgenic mice brain samples, 30 min at room temperature revealed to be sufficient for the binding of lysate to antibody-coupled beads. Additionally, IP overnight for 16 h at 4°C was tested, using CSF from a moderate dementia AD sample (#35). Indeed, prolongation of the binding time resulted in a detectable seeding effect for the tested CSF sample after IP with the 6E10 antibody (Fig. 50b).

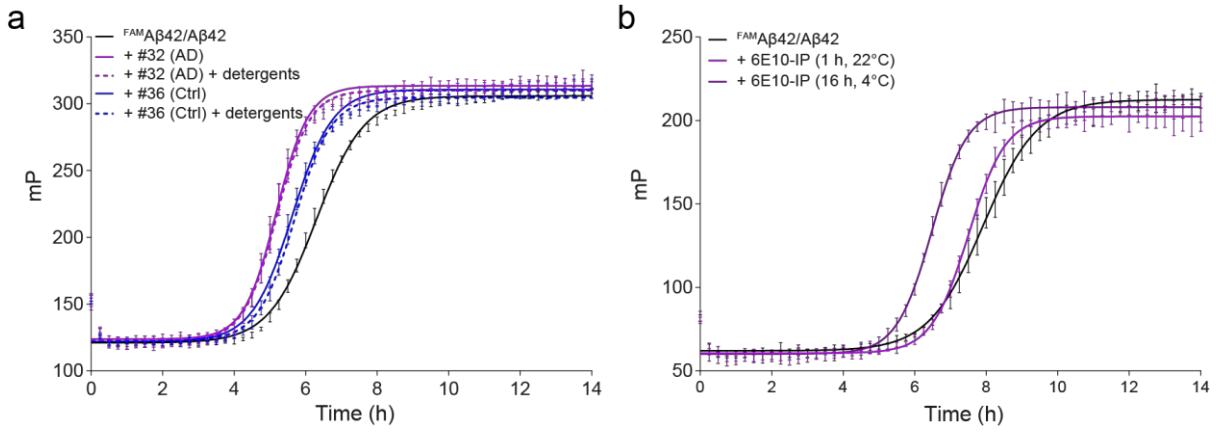

Figure 50 | Addition of detergents and optimization of IP incubation time
(a) Supplementation of CSF samples with detergents (0.1 % SDS, 0.5 % Sodium deoxycholat, 1 % Triton) during IP and before analysis regarding seeding activity using the ^{FAM}Aβ42/Aβ42 co-polymerization assay. Addition of detergents does not improve the detection of seeding-competent structures in Aβ42-FP assays. (b) Test of different incubation times for the IP. Prolongation of IP incubation time up to 16 h at 4°C enables to detect seeding effects with ^{FAM}Aβ42/Aβ42 aggregation assays from an analyzed AD patient CSF sample (#35).

5.3.4.2 Analysis of human CSF samples

After performing preliminary experiments, a highly standardized protocol was established for the analysis of a larger cohort of CSF samples. Working with CSF samples requires standardized procedures as the inter- and intra-lab variability is very high[44]. Therefore, I tried to stick to the

established experimental setup starting from the thawing process of the samples on ice, execution of the IP experiments and the final seed release step. In total, 36 CSF samples were analyzed, comprising patients with mild cognitive impairment (MCI), mild and moderate AD diagnosis. Unfortunately, no liquor samples from completely healthy individuals were available that could function as proper controls. Instead, patients with a depressive episode or unknown etiology had to serve as controls. The liquor samples were obtained via lumbar puncture and directly frozen without centrifugation to avoid possible precipitation of aggregates. All analyzed CSF samples and their biomarker evaluation can be found in the *Material* and *Supplementary information* section. Table 7 and Figure 51 show four selected samples where a seeding effect of 6E10- and 352-reactive seeds in comparison to the IgG1 control could be observed. The strongest seeding effect with 6E10- and 352-reactive seeds was obtained with a CSF sample from patient #30, a 71-year-old individual suffering from mild cognitive impairment, most likely from the AD type (Fig. 51a). This patient represents a classical AD patient with all three biomarkers clearly being affected. Addition of these seeds led to a shortening of the lag phase of ~2 h (352: Δt_{50} = 1.7 h; 6E10: Δt_{50} = 1.9 h). Analysis of CSF from sample #68, a 75-year-old patient diagnosed with MCI, most likely with a vascular etiology also revealed a significant decrease in the lag phase of ~2h (Fig. 52b; Δt_{50} = 1.8 h) with the 352-reactive seeds and of ~1 h (Δt_{50} = 0.8 h) with 6E10-reactive seeds (Fig. 51b). This patient is not diagnosed as a classical AD patient as the cause of his impaired brain function is due to the vascular system, probably initiated by a cerebral infarction. Patients #72 and #78 also revealed a seeding effect with 352- and 6E10-reactive seeds with an average shortening of the lag phase of ~1 h (Fig. 51c, d). Patient #72 was not diagnosed as an AD patient as the clinical findings were unremarkable and he performed well at MMSE tests despite very conspicuous biomarkers (*personal statement from Oliver Peters*). Regardless, his brain showed a light atrophy and he suffered from various strokes during lifetime. These two patients were not yet diagnosed as AD patients, but rather classified as 'depressive episode with measurable cognitive deficits'. Thus, they might progress in the future into AD.

#	Age	Diagnose	hTau (pg/ml)	Aβ42 (pg/ml)	Aβ40 (pg/ml)	Ratio Aβ40/Aβ42	Ratio tTau/Aβ42
30	71	Mild dementia, AD type	559	166	3371	0,049	3,360
68	75	Mild cognitive impairment, vascular etiology	396	888	7636	0,116	0,446
72	79	Depressive episode with cognitive deficits, vascular encephalopathy	1024	343	7139	0,048	2,988
78	79	Depressive episode with cognitive deficits	147	779	7495	0,104	0,189

Table 7 | Diagnosis of positive CSF samples

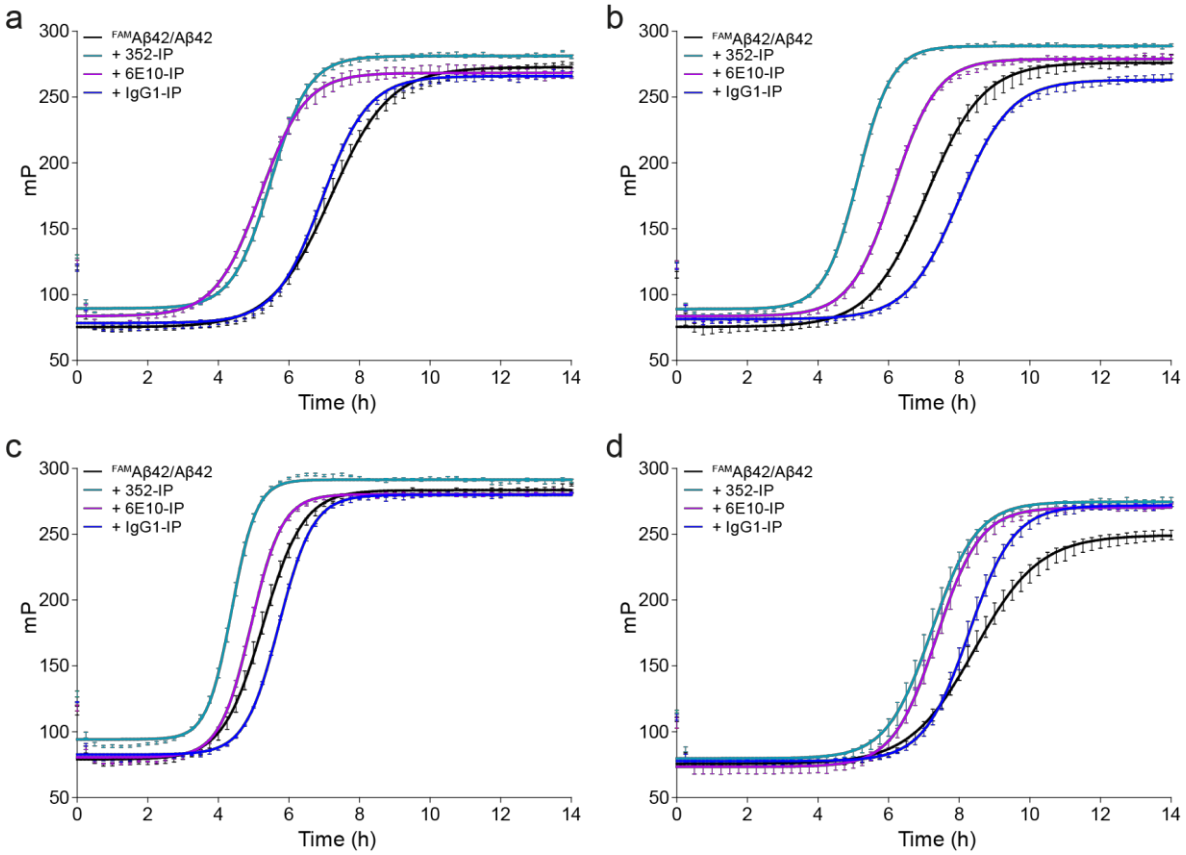

Figure 51 | Analysis of human CSF samples with the ^{FAM}Aβ42/Aβ42 co-polymerization assays
Aβ42-FP analysis reveals seeding activity in four selected CSF samples. (a) #30: Mild dementia; (b) #68: MCI; (c) #72: Depressive episode with cognitive deficits (d) #78: Depressive episode with cognitive deficitis.

However, a conclusive interpretation of the generated data was difficult due to several reasons. First, a lack of samples from definite healthy individual made it difficult to assess the results since there was no opportunity to compare the obtained curves from the Aβ42-FP assays with data from AD patients and healthy controls. Therefore, only single experiments could be analyzed by comparing the enriched Aβ-specific seeds with the IgG1 control seeds. Second, during the execution of the experiments at a certain point an inhibition of the ^{FAM}Aβ42/Aβ42 co-polymerization through the applied antibodies was observed (Supplementary Fig. 2 and 3). These results were unexpected since an inhibition of the aggregation never occurred before when performing IPs with material from transgenic mouse brains. Finally, the differences between 352- and 6E10-reactive seeds were partly quite big (Supplementary Fig. 2 and 3; e.g. samples 26, 29, 73). Even though the 352 antibody detects exclusively aggregated Aβ assemblies, the sequence-specific antibody 6E10 also should be able to detect Aβ aggregates. However, especially the 352-enriched seeds frequently inhibited the spontaneous ^{FAM}Aβ42/Aβ42 co-aggregation reaction, an effect that could not be fully explained.

It was assessed whether the applied sonication step for the release of seeds from the dynabeads might be too harsh leading to a release of antibodies, which might finally interfere with the FP-based

seeding assay. To address this question, an IP was again performed from a CSF sample (#20) resulting in a clear inhibition of the ^{FAM}Aβ42/Aβ42 co-aggregation process by the 352 antibody only (Fig. 52a). However, simultaneous seeds released from antibody-coupled beads without a sample, but only with ACSF buffer as a control did not influence the aggregation kinetic (Fig. 52b). Thus, a technical impairment due to antibody fragmentation during the seed release step could be ruled out.

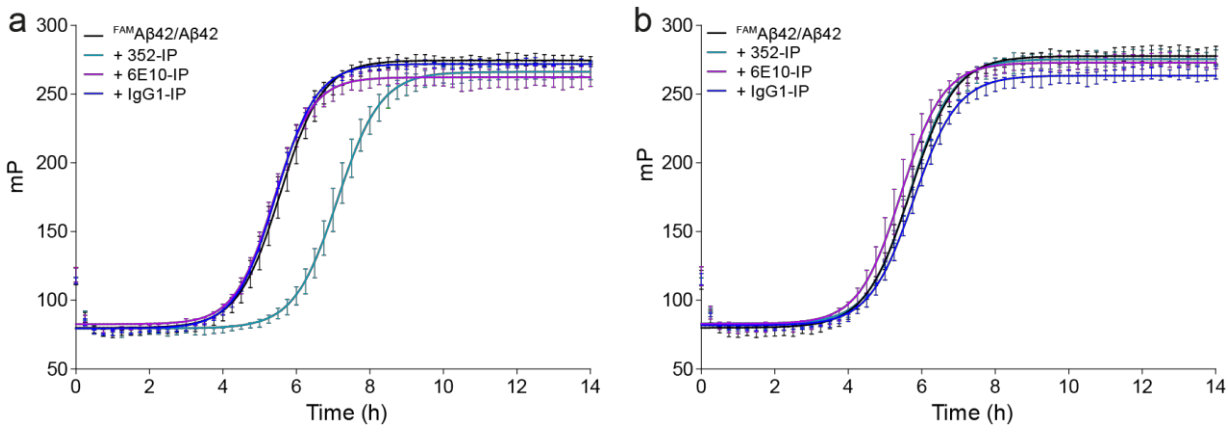

Figure 52 | Test of a possible inhibition of ^{FAM}Aβ42/Aβ42 FP measurements by antibody fragments
(a) Aβ42-FP analysis of seeds extracted from a CSF sample (#20) reveales an inhibiting effect by the 352-reactive seeds only. (b) Simultaneous seeds release in a buffer only control does not affect the ^{FAM}Aβ42/Aβ42 aggregation kinetic.

Summarized, the established workflow for the immunoprecipitation of Aβ aggregates and their subsequent release for quantification of seeding activity was applied for the analysis of human CSF samples from AD patients. Even though a first proof-of-principle experiment indicated the general feasibility of this approach for the detection of Aβ seeds in CSF, only 4 of 36 tested samples showed a clear seeding effect in FP assay. However, it seems that further optimizations and method development steps are necessary to finally establish a procedure that can be applied for the systematic detection of Aβ seeds in CSF samples.

5.4

Structure-activity relationship analysis for small molecules targeting seed-mediated Aβ42 aggregation

5.4 Structure-activity relationship analysis for small molecules targeting seed-mediated Aβ42 aggregation[1]

After application of the FP-based Aβ42 aggregation assay for the detection of potential disease-relevant Aβ seeds in biosamples, I assessed whether the assay could provide a suitable method to screen for aggregation inhibiting small molecules. Within the assay development phase the effects of the known aggregation-inhibiting compounds EGCG, Congo Red and Chrysamine G were already analyzed in a proof of principle experiment (Fig. 24). All three compounds delayed the ^{FAM}Aβ42/Aβ42 co-aggregation process, confirming the general applicability of the assay to screen for compounds that affect aggregation. Furthermore, it was ought to be examined if compounds might function differently on spontaneous and seed-mediated aggregation reactions and, if so, whether small molecules can be identified that specifically target seed-induced Aβ aggregation. Finally, by performing structure-activity relationship studies I aimed to elucidate specific structural requirements that are critical to directly target seed-mediated Aβ42 aggregation.

5.4.1 The effect of structurally related amyloid binders on Aβ42 aggregation in FP assays

The two well-known amyloid-binding small molecules methoxy-X04 and K114 were consulted and their effects on the Aβ42 aggregation reaction were analyzed in Aβ42-FP assays. The compounds were both shown to be fluorescent dyes and to bind to fibrillar amyloid structures[208-212]. Both compounds feature the same bis-styrylbenzene scaffold structure comprising three aromatic benzene rings; the two terminal rings are hydroxylated at position *2*. However, they differ at position *2* in the central benzene ring where methoxy-X04 is substituted with a methoxy group, while K114 contains a bromine residue (Fig. 53a). Because previous investigations indicate that the self-assembly of monomers into nuclei is rare and energetically unfavorable[130], it was hypothesized that substoichiometric compound concentrations should be sufficient to perturb this specific process. Therefore, 1 µM of compound were added to a standard ^{FAM}Aβ42/Aβ42 co-aggregation reaction (10 µM Aβ42 + 0.05 µM ^{FAM}Aβ42) and their effect on the spontaneous and seed-mediated aggregation was analyzed with Aβ42-FP assays (Fig. 53b-d). The spontaneous ^{FAM}Aβ42/Aβ42 aggregation showed a lag phase of ~6 h and was significantly extended by addition of both compounds (Fig. 53b, d). Quantification of the compounds inhibitory effects revealed $\triangle t_{50}i$ values of ~2.9 h and 2.4 h for the compounds methoxy-X04 and K114, respectively, indicating that both compounds delay spontaneous ^{FAM}Aβ42/Aβ42 aggregation with similar potency.

[1]The text and figures under section 5.4 have been reused with modification from the manuscript: Diez, L. *et al.* Structure-based discovery of amyloid-β nucleation modulators using a fluorescence polarization-based aggregation assay (2018) *(manuscript submitted).*

Following, the effects of the compounds (1 µM) on seeded ^{FAM}Aβ42/Aβ42 co-aggregation was analyzed. In these reactions ^{FAM}Aβ42/Aβ42 co-aggregation was stimulated by the addition of PFs (0.1 µM) as seeds. As expected the seeded aggregation was significantly accelerated with a lag phase of ~2 h (Fig. 53c). Interestingly, methoxy-X04 showed only a weak effect in delaying the seed-mediated ^{FAM}Aβ42/Aβ42 aggregation reaction ($\triangle t_{50}i$ ~0.6 h), while K114 was very potent ($\triangle t_{50}i$ ~4.1 h), highlighting a potential importance of the bromine substituent at position *2* of the middle ring to target seed-mediated Aβ42 aggregation.

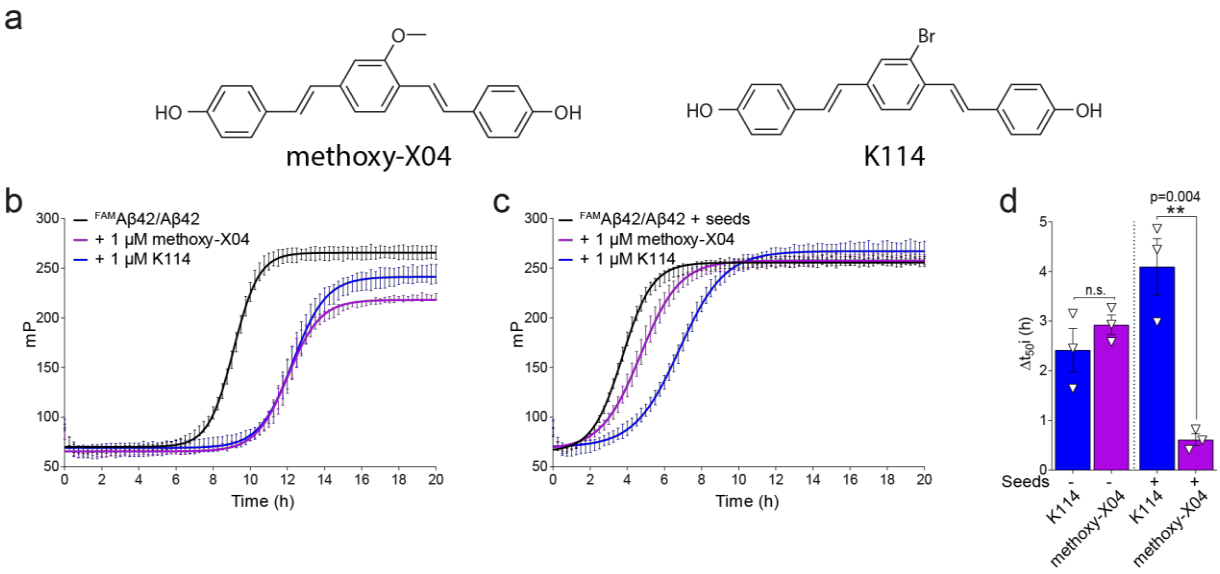

Figure 53 | Effects of the small molecules K114 and methoxy-X04 on both spontaneous and seed-mediated ^{FAM}Aβ42/Aβ42 co-polymerization

(a) Structures of the tested small molecules methoxy-X04 and K114. (b, c) Effects of the compounds methoxy-X04 and K114 (1 µM) on the spontaneous (b) and seeded (c) co-aggregation in standard ^{FAM}Aβ42/Aβ42 co-polymerization (10 µM Aβ42 + 0.05 µM ^{FAM}Aβ42) assays. In seeded reactions pre-formed, β-sheet-rich fibrillar assemblies (0.1 µM, monomer equivalent) were added. Representative experiments (mean ± SD of quadruplicates) are shown. (d) Quantification of compound effects ($\triangle t_{50}i$ values) on spontaneous *b* and seeded *c* ^{FAM}Aβ42/Aβ42 co-polymerization in FP assays. Data are mean ± SEM (n = 3); individual values are presented as triangles. Statistical significance was assessed by unpaired t-test, two-tailed. **, p≤0.01.

In general, these data suggested that the Aβ42-FP assay is capable of detecting compound inhibitory effects on both spontaneous and seed-mediated ^{FAM}Aβ42/Aβ42 co-aggregation. Furthermore, it could be seen that a compound can have different effects and efficiencies on spontaneous and on seed-induced Aβ42 polymerization as these two aggregation types underlie a different composition of microscopic processes. Finally, these experiments implied that only small changes in molecular structure can make a difference in a compounds mechanism of action to affect Aβ42 peptide aggregation and that these changes can be detected using the Aβ42-FP assay.

5.4.2 Synthesis of K114 derivatives for structure-activity relationship studies

Intrigued by these observations, I focussed on compound K114 as the starting compound since it showed the strongest effect on both the spontaneous and the seed-mediated ^{FAM}Aβ42/Aβ42 co-aggregation. A focused library of derivatives was designed aiming to identify chemical components that are crucial not only to inhibit spontaneous polymerization, but also seed-induced ^{FAM}Aβ42/Aβ42 aggregation. Summarized, four components and their structure-activity relationship regarding Aβ42 aggregation inhibition were of interest in this study, color-coded in Figure 54.

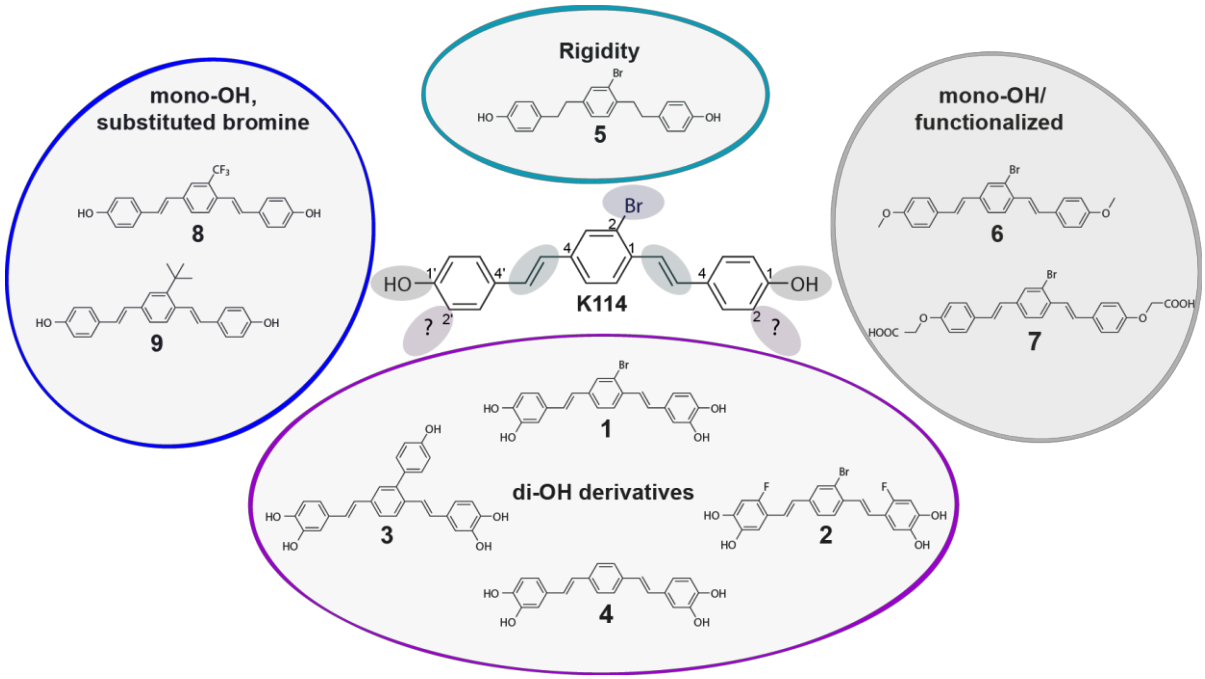

Figure 54 | Structures of synthesized K114 derivatives for compound testing in FP assays
The color code indicates groups of compounds with potentially related functionalities on Aβ42 aggregation in FP assays. Color code explanation: turquoise: compound with less rigidity due to single bond; grey: compounds with functionalized terminal hydroxyl groups; purple: compounds with di-hydroxylation at the outer aromatic rings, with or without central bromine substitution; blue: compound with mono-hydroxylation at the outer aromatic rings, with substitution of central bromine residue.

First, it was hypothesized that a certain degree of rigidity is essential to ensure that the compound can interact with the Aβ42 assemblies, leading to design of compound **5** featuring a less rigid, but flexible single bond with 4 freely rotating sp^3-hybridized carbons. Second, the impact of the electronegative bromine residue at position *2* of the middle benzene ring was assessed. Therefore compounds **8** and **9** were synthesized where the bromine was substituted with a trifluoromethyl or tert-butyl residue, respectively. It was hypothesized that this substituent with its electronegative quality is essential to mediate inhibitory effects on particularly the seed-mediated aggregation as methoxy-X04 with a lack of bromine showed an impaired inhibitory activity as described earlier (Fig. 53c, d). Third, the impact of the terminal hydroxyl groups was supposed to be analyzed, realized by compounds **6** and **7** that

carry terminal modifications, namely a methoxylation and an ethanoic acid functionalization. Finally, it was anticipated that introduction of an additional terminal hydroxyl group would further increase the compounds inhibitory effect on the ^{FAM}Aβ42/Aβ42 co-polymerization reaction, leading to synthesis of compound **1**. Compounds **3** and **4** were designed as di-hydroxyl-styryl molecules with substitution of the central bromine residue. Finally, Compound **2** was equipped with additional fluorine atoms at position *6* in the terminal benzene rings to further test electron-withdrawing effects in the terminal styryl systems.

A detailed description of the compound synthesis can be found in the supplementary information section (Supplementary Fig. S4). Briefly, K114 was re-synthesized in accordance to recent publications[209,210]. All central in position *2* substituted compounds were synthesized based on 2-bromo-1,4-bis(bromomethyl)benzene (**11**). Via Arbuzov reaction tetraethyl 2-bromo-1,4-phenylene-diphosphonate (**10**) was synthesized and further coupled in a Horner-Wadsworth-Emmons (HWE) reaction with methoxy substituted benzaldehydes to afford bis-styrylbenzenes **1a, 2a, 4a** and **6**. Direct deprotection of these intermediated compounds led to final compounds **1**, **2**, **4** and **K114**. Bromine substitution by Suzuki coupling of intermediate compound **1a** led to compound **3.** Methoxylated compound **6** was used to perform copper- and nickel-mediated cross-coupling reactions to insert a trifluoromethyl (**8**) and tert-butyl (**9**) residue. Compound **5** was produced from **6** by silane-TFA reduction and the phenoxyacetic acid derivative **7** was obtained from K114. In total, a focused compound library of K114 and nine derivatives was synthesized that was available for analysis regarding their aggregation-inhibiting effects in Aβ42-FP assays (Table 8).

	Trivial name / Code (IUPAC Nomenclature)	Structure	Purity	Yield
K114:	4-[(E)-2-{3-bromo-4-[(E)-2-(4-hydroxy-phenyl)ethenyl]phenyl}ethenyl]phenol	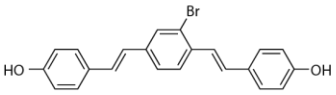	90%	29%
1	4-[(E)-2-{3-bromo-4-[(E)-2-(3,4-di-hydroxy-phenyl)-ethenyl]phenyl}ethenyl]benzene-1,2-diol	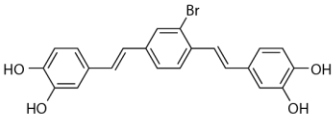	95%	32.9%
2	4-[(E)-2-{2-bromo-4-[(E)-2-(2-fluoro-4,5-di-hydroxyphenyl)ethenyl]phenyl}ethenyl] -5-fluorobenzene-1,2-diol	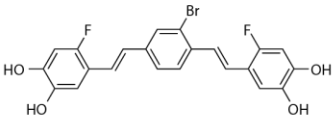	95%	58%
3	4-[(E)-2-{4-[(E)-2-(3,4-dihydroxyphenyl) ethenyl]-3-(4-hydroxyphenyl)phenyl}ethenyl] benzene-1,2-diol	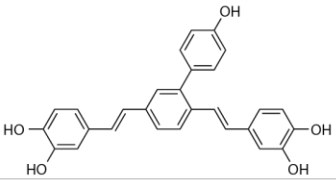	91%	38%
4	4-[(E)-2-{4-[(E)-2-(3,4- dihydroxyphenyl) ethenyl]phenyl}ethenyl]benzene-1,2- diol	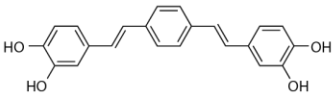	95%	50.6%
5	4-(2-{3-bromo-4-[2-(4-hydroxyphenyl) ethyl]phenyl}ethyl)phenol	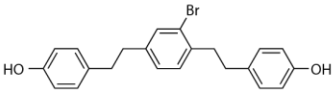	92%	81%
6	2-Bromo-1,4-bis-[(E)-2-(4-methoxy-phenyl)-vinyl]-benzene	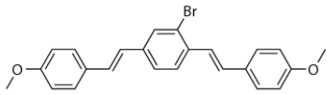	95%	95%
7	[4-((E)-2-{3-Bromo-4-[(E)-2-(4-carboxymethoxy-phenyl)-vinyl]-phenyl}-vinyl)-phenoxy]-acetic acid	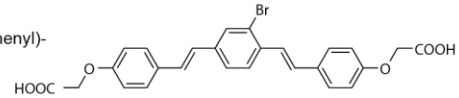	95%	39%
8	4-[(E)-2-{4-[(E)-2-(4-hydroxyphenyl)ethenyl]-3-(trifluoromethyl)phenyl}ethenyl]phenol	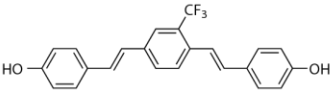	95%	47%
9	4-[(E)-2-{3-tert-butyl-4-[(E)-2-(4-hydroxy-phenyl)ethenyl]phenyl}ethenyl]phenol	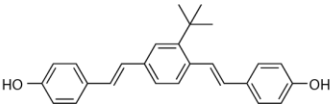	90%	45%

Table 8 | Structure and purities of newly synthesized K114 derivatives

5.4.3 Effect of K114 derivatives on seeded and spontaneous ^{FAM}Aβ42/Aβ42 co-polymerization

To analyze the effects of K114 derivatives on seed-mediated and spontaneous ^{FAM}Aβ42/Aβ42 co-aggregation, the compounds were added in a sub-stoichiometric concentration (1 µM) to standard ^{FAM}Aβ42/Aβ42 reactions (10 µM Aβ42 + 0.05 µM ^{FAM}Aβ42) with or without PF seeds (0.1 µM). Figure 55a displays one representative result of the FP analysis showing compound effects on seeded aggregation reactions. Figure 55b shows the impact of small molecules on spontaneous ^{FAM}Aβ42/Aβ42 co-aggregation. The quantification of the compound effects from four biological replicates is shown in Figure 56.

At first, the impact of K114 derivatives on seed-mediated aggregations was assessed as such reactions are more selective for compound testing compared to spontaneous reactions, because the nucleation rate gets increased through the addition of pre-formed Aβ42 seeds. The seed-mediated ^{FAM}Aβ42/Aβ42 aggregation revealed a lag phase of ~2 h (Fig. 55a; black).

Direct comparison of **K114** to its hydrogenated derivative compound **5** revealed the importance of a certain degree of structural rigidity to mediate inhibitory effects as this compound showed no activity in FP assays. Thus, an increase in flexibility seems to decrease the activity of a small molecule as it might entail too many degrees of freedom. This result fits to previous observations, where it was shown that linker flexibility dramatically influences the inhibitory activity of curcumin in amyloid polymerization assays[322].

By comparing **K114** with compounds **8** and **9**, where the central bromine residue was substituted by a trifluoromethyl or tert-butyl residue, respectively, it became evident that the bromine residue indeed seems to increase the potency to target seed-mediated ^{FAM}Aβ42/Aβ42 aggregation as it was already observed for methoxy-X04 (Fig. 53). The bromine residues features high electronegativity and is polarizable, thus could contribute to van der Waals forces with the Aβ42 peptide. This impact is also strengthened by the fact that the compound **9**, whose tert-butyl residue represents a bioisoster of bromine regarding spatial expansion but is not electronegative, was less efficient in inhibiting seed-mediated Aβ42 aggregation in FP assays. Thus, the qualities of electronegativity and polarizability seem to contribute to the aggregation delaying effect of K114 derivatives. Trifluoromethyl compound **8** features a strongly electronegative residue comparable to bromine, but spatially extended. However, it was not capable to strongly delay the seeded aggregation. This indicates that the good polarizability of the bromine residue seems to be a pivotal property of K114 to target seed-mediated aggregation via van der Waals binding.

Next, the two terminally modified, namely methoxylated and ethanoic acid functionalized compounds **6** and **7** showed basically no effect on delaying the lag phase, demonstrating the necessity of a free

hydroxyl group to mediate the aggregation inhibitory properties. The free terminal hydroxyl groups are most likely involved in the formation of hydrogen bonds with the Aβ42 peptide, that could form with various residues e.g. amines or with secondary structure elements like β-sheets in pre-aggregated seeds.

Finally, all four compounds with two terminal hydroxyl groups (**1-4**) were able to efficiently delay seeded Aβ42 aggregation, indicating that the higher number of free hydroxyl groups improves compound activity. It can be postulated that two terminal hydroxyl groups at each outer benzene ring simply increase the likelihood of a favorable orientation to form hydrogen bonds with the Aβ42 interaction partner. Compound **1**, which can be described as the di-hydroxylated version of K114 proved to be the most potent delayer of seed-mediated Aβ42 aggregation in FP assays. Interestingly, compared to compound **4** that also comprises four terminal hydroxyl groups, but lacks a functional group at position *2*, the impact of the central bromine residue does not come into effect here. It can be postulated, that the effect of the di-hydroxylation exceeds the effect of the bromine residue as observed earlier. In line with that, also compound **3** with a para-hydroxy phenyl group instead of a bromine residue at position *2* showed a comparable effect as compound **1**. Finally compound **2** with additional fluorine atoms at position *2* of the terminal aromatic rings showed a similar effect, indicating that electron-withdrawing effects in the terminal styryl systems seem to be negligible here.

The impact of all compounds on the spontaneous ^{FAM}Aβ42/Aβ42 co-aggregation was also analyzed (Fig. 55b; black). In general, the effects of all compounds were stronger on the spontaneous aggregation as almost all compound delayed the lag phase over 1 h (Fig. 56b; dashed line). In seeded aggregations only **K114** and the four di-hydroxylated derivatives (**1-4**) were able to decelerate the process efficiently, demonstrating the more rapid progress of seed-mediated aggregation. Apart from that, the effects of all compounds were comparable to their effects on seeded aggregations. There, the non-rigid compound **5**, the terminal modified compounds **6** and **7** and the mono-hydroxylated compounds with bromine substitution (**8**, **9**) were also less potent in delaying the lag phase compared to **K114**. Again, the di-hydroxylated compounds **1-4** revealed a significant effect on delaying the aggregation process. Here, the central bromine residue at position *2* further seemed to increase the compounds potency as observed when directly comparing compound **1** and **4**.

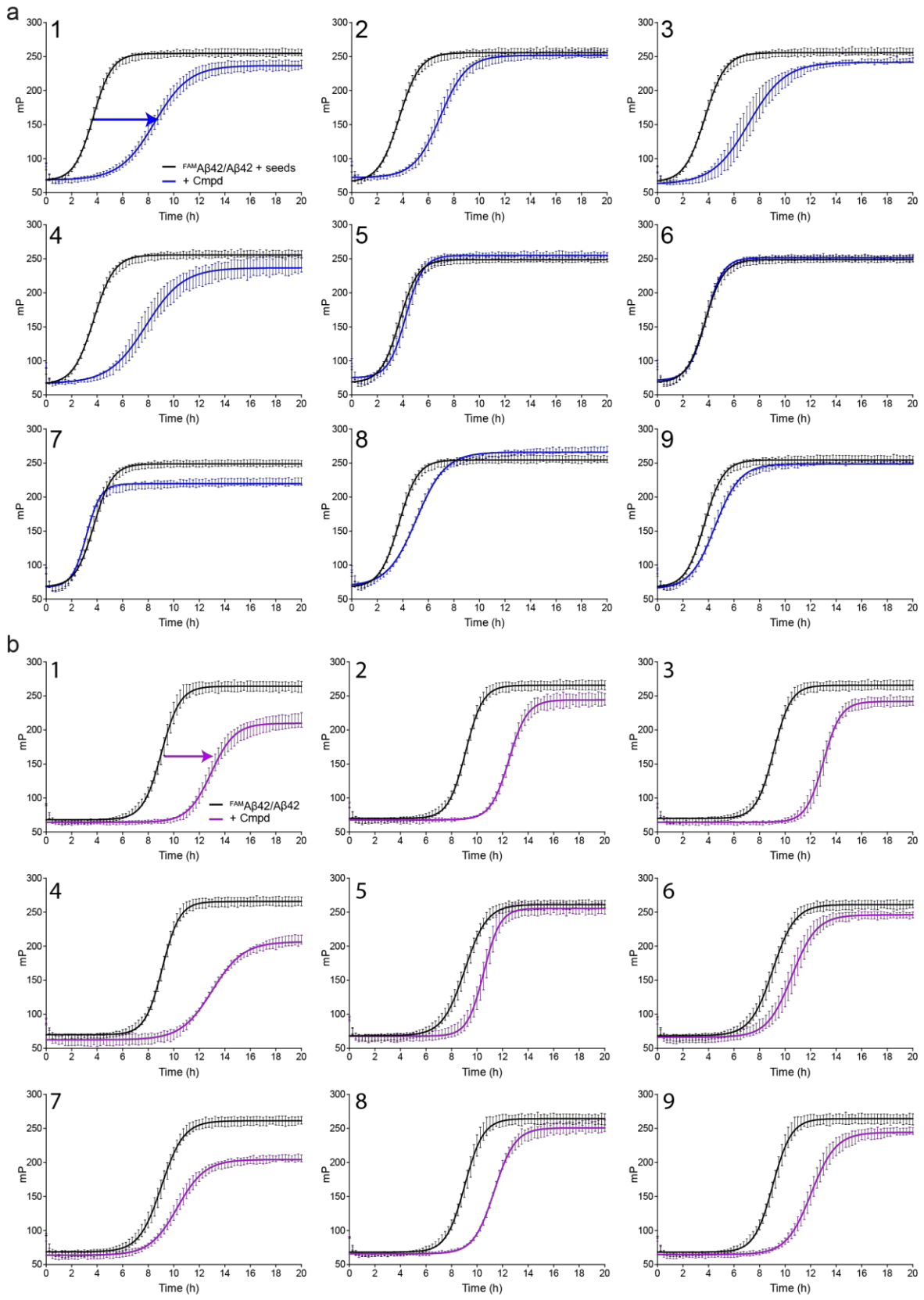

Figure 55 | Effects of K114 derivatives on seed-mediated and spontaneous ^{FAM}Aβ42/Aβ42 co-polymerization
(a) Effects of small molecules (1 µM) on seed-mediated co-polymerization of ^{FAM}Aβ42 (0.05 µM) and Aβ42 (10 µM) with PF seeds (0.1 µM) in FP assays. The colors blue and black indicate compound-treated and untreated reactions, respectively. (b) Effects of small molecules (1 µM) on spontaneous of ^{FAM}Aβ42/Aβ42 co-aggregation. The colors purple and black indicate compound-treated and untreated reactions, respectively. Shown is one representative experiment (mean ± SD of quadruplicates).

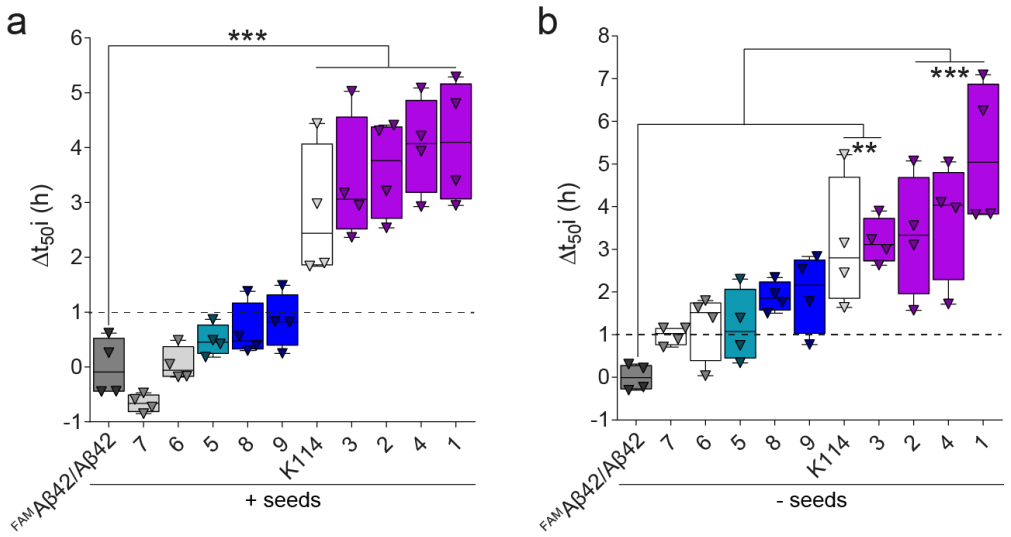

Figure 56 | Quantification of compound effects on ^{FAM}Aβ42/Aβ42 co-aggregation in FP assays
(a, b) Quantification of inhibiting effects of K114 derivatives on seeded (a) or spontaneous (b) ^{FAM}Aβ42/Aβ42 co-aggregation. Data are mean ± SEM (n = 4) and individual values are presented as triangles (Box-and-whiskers plots: center line, median; box limits, upper and lower quartiles; whiskers, maximum and minimum). Statistical significance is referred to seeded (a) or spontaneous (b) ^{FAM}Aβ42/Aβ42 aggregation, respectively without compound and was assessed by one-way ANOVA followed by Dunnett's multiple comparison post hoc test. **, p≤0.01; ***, p≤0.001.

Summarized, this small focused compound screen of the known amyloid-binder K114 and structurally related compounds revealed that the Aβ42-FP assay is a valuable tool not only to screen aggregation inhibiting compounds, but also to resolve the contribution of single functional groups and substructures and thus to allow structure-activity relationship studies. It could be shown that a high aggregation inhibitory activity is directly linked to molecular rigidity, terminal o*rtho*-dihydroxylated phenyl residues and the presence of a central substituent, preferentially a bromine residue. With its good polarizability this halogen residue might contribute to dipole induced interactions with the Aβ peptide to mediate the observed aggregation inhibiting activity. Second, it was demonstrated that seed-induced aggregation indeed is more aggressive than spontaneous aggregation. Thus, highly proficient compounds are needed to interfere with seeded aggregation. Finally, o*rtho*-dihydroxylated *bis*-stilben **1**, in the following referred to as **LT1**, was found to be the most potent delayer of both spontaneous and seed-mediate Aβ42 aggregation in FP assays.

5.4.4 Characterization of LT1's effect on Aβ42 aggregation

Prior to further analysis regarding LT1's potential mechanism of action, the solubility of the compound was assessed. It is known that certain compounds can mediate inhibitory effects by acting as colloidal inhibitors that self-assemble and thereby nonspecifically and physically sequester proteins[323,324]. To ensure that LT1 is soluble at the tested concentrations, its solubility was assessed by gradually increasing its concentration (0.01 µM - 30 µM) in aqueous solution while measuring the absorbance at 700 nm. An increase in turbidity upon a critical concentration could then be correlated to the compounds insolubility. At a concentration of ~8 µM a steep increase in absorbance could be observed, indicating that above that concentration LT1 has a high tendency to self-aggregate and to form compound precipitates (Fig. 57). Therefore, in all further Aβ42 aggregation experiments a maximum concentration of 5 µM LT1 was applied in order to avoid unspecific compound effects

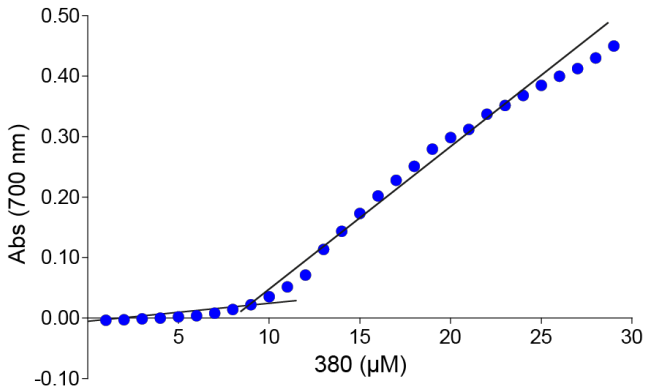

Figure 57 |Solubility of LT1
LT1 solubility was assessed by measuring its absorption at different concentrations in an aqueous solution at 700 nm. Upon 8 µM, LT1 seems to self-assemble as the turbidity increases due to the compound's insolubilty.

Next, the effects of LT1 on spontaneous and seed-mediated ^{FAM}Aβ42/Aβ42 co-aggregation in a concentration-dependent manner was assessed and the IC_{50} values were determined (Fig. 58). LT1 (0.01 - 5 µM) was added to standard FP reactions (10 µM Aβ42 + 0.05 µM ^{FAM}Aβ42 +/- 0.1 µM PF seeds) and its impact on Aβ42 aggregation systematically analyzed. In both experimental paradigms the lag phase was extended in a concentration-dependent manner, supporting the hypothesis that LT1 acts as a potent Aβ nucleation modulator and perturbs early events in the amyloid polymerization cascade.

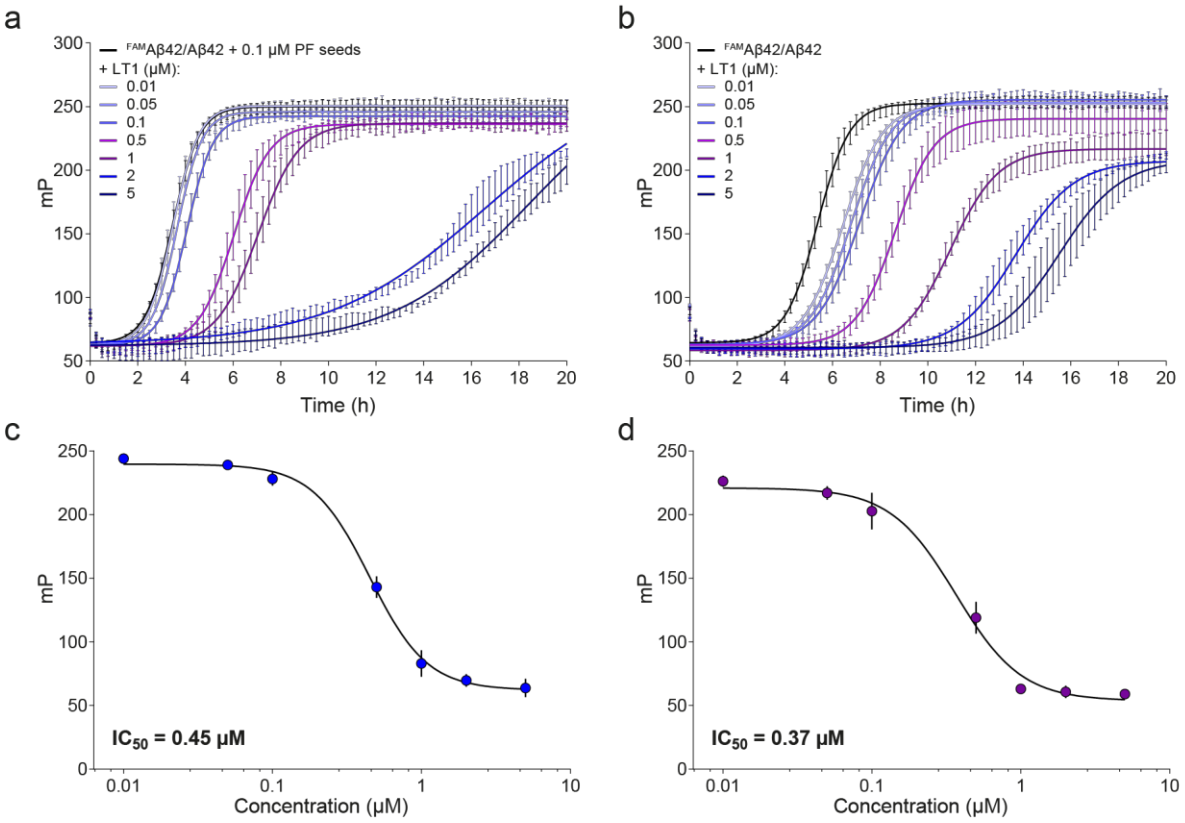

Figure 58 | Concentration-dependent inhibition of Aβ42 aggregation by LT1 treatment
(a, b) Effects of different concentrations of LT1 (0.01 - 5 µM) on seeded (0.1 µM PF seeds) (a) or spontaneous (b) standard FP-based assays (10 µM Aβ42 + 0.05 µM ^{FAM}Aβ42). Average values were derived from quadruplicates of each sample in one experiment (mean ± SD of quadruplicates). (c, d) Determination of LT1's IC_{50} value for seeded (c) or spontaneous (d) ^{FAM}Aβ42/Aβ42 aggregation. IC_{50} values were calculated from aggregation profiles shown in *a* at 5.5 h (c) and from aggregation profiles shown in *b* at 8 h (d).

To better understand how LT1 delays the lag phase and thereby the whole Aβ42 aggregation process, the ^{FAM}Aβ42/Aβ42 aggregate species from FP assays, that were formed in the presence or the absence of compound (1 µM) were analyzed. Thereby, two different time points (t = 6 h and t = 20 h) were examined (Fig. 59a). The Aβ species being present after 6 h of aggregation represents and intermediate of the aggregation reaction and a sample was taken at the transition from the lag phase to the growth phase. At time point t = 20 h the ^{FAM}Aβ42/Aβ42 reaction has reached the plateau and the taken sample represents the end point of the FP-based aggregation reaction.

First, the samples were analyzed using both SDS- and native PAGE and subsequent immunoblotting. Analysis of the 6 h sample on a denaturating SDS gel shows a higher concentration of Aβ42 monomers and less bigger aggregates stuck in the gel pockets in presence of the compound (Fig. 59b). Interestingly, the low molecular weight assemblies (LMWAs) ranging between 50-100 kDa that are already present in the 6 h sample get more prominent with the end point aggregates after 20 h of aggregation, indicating that this species is a normal on-pathway Aβ42 assembly that seems to be withheld by the compound. These results could also be confirmed with analysis under native

conditions where in LT1-treated samples low molecular weight assemblies (LMWAs) with a size of ~100-250 kDa are detectable after 20 h, supporting the hypothesis that the compound targets transiently formed Aβ42 oligomers and delays their conversion into HMWAs (Fig. 59c). Together, these results substantiate the results obtained with FP assays (Fig. 55 and 56), indicating that a substoichiometric concentration of LT1 can delay amyloid polymerization, but does not prevent the self-assembly of Aβ42 into aggregates. Following, the 6 h and 20 h samples were analyzed on a denaturating filter assay, revealing that at both time points the Aβ42 assemblies formed in presence of compound are less SDS-stable structures (Fig. 59d, e).

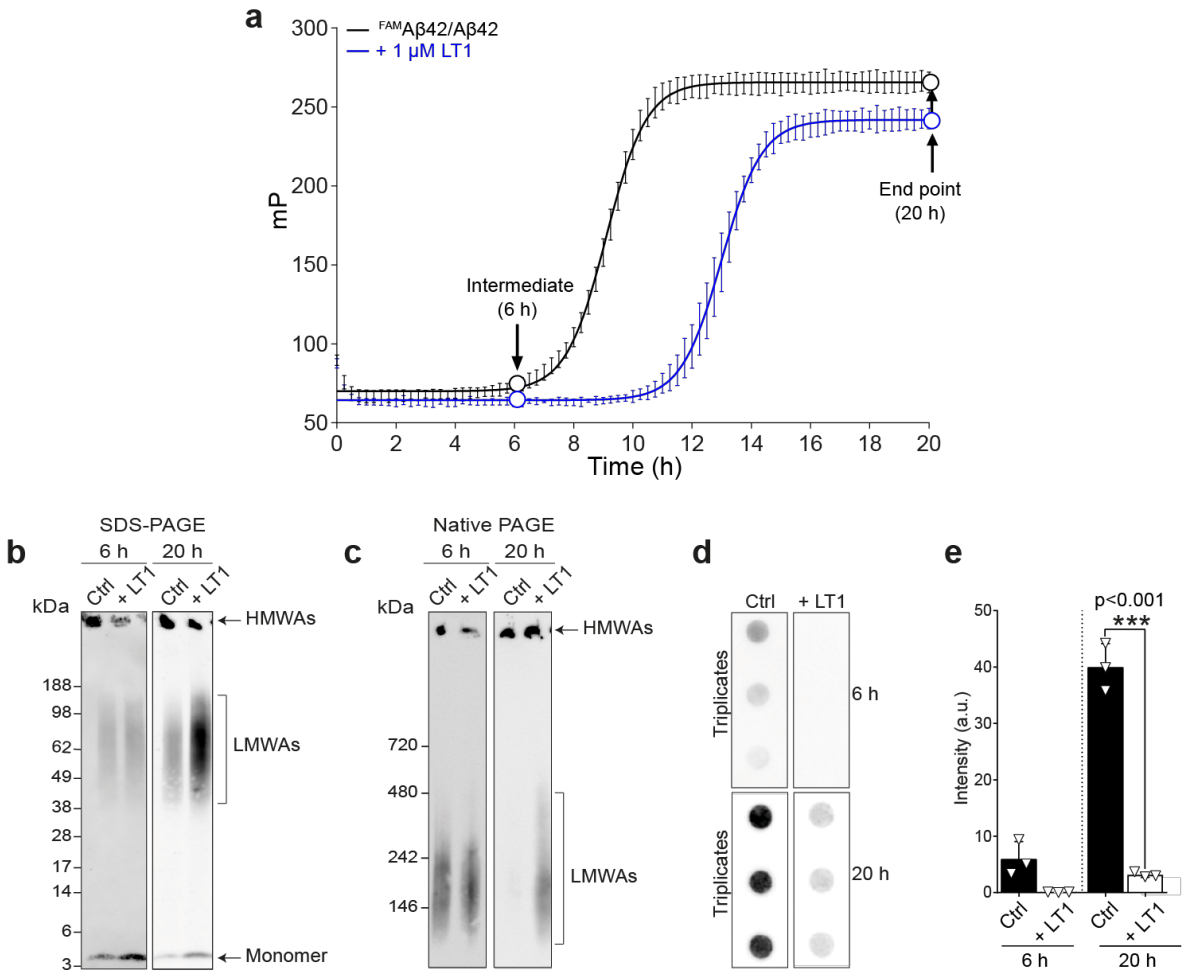

Figure 59 | Characterization of LT1's *in vitro* mechanism of action

(a) Increase of FP over time in LT1-treated (1 µM) and untreated ^{FAM}Aβ42 (0.05 µM) and Aβ42 (10 µM) co-aggregation assays. At indicated time points samples were taken for the investigation of co-aggregates with biochemical assays. (b, c) Analysis of spontaneously formed ^{FAM}Aβ42 (0.05 µM) and Aβ42 (10 µM) co-aggregates in the presence (1 µM) and absence of LT1 (Ctrl) by SDS-PAGE and immunoblotting (b) and native PAGE and immunoblotting (c). For immunodetection the monoclonal anti-Aβ antibody 6E10 was applied. HMWAs, high molecular weight ^{FAM}Aβ42/Aβ42 assemblies; LMWAs, low molecular weight ^{FAM}Aβ42/Aβ42 assemblies. (d) Analysis of spontaneously formed ^{FAM}Aβ42 (0.05 µM) and Aβ42 (10 µM) co-aggregates in the presence (1 µM) and absence of LT1 (Ctrl) by denaturing filter retardation assay. Aggregates retained in filter membranes were detected using the anti-Aβ antibody 6E10. (e) Quantification of 6E10 immunoreactivity of triplicate samples shown in *d*. Data are mean ± SD; individual values are presented as triangles. Statistical significance was assessed by unpaired t-test, two-tailed. ***, p≤0.001.

It can be hypothesized that this effect might be due to an incorporation of LT1 molecules into Aβ42 fibrils. Previous studies already suggested that amyloid-binding small molecules may alter the stability of Aβ42 fibrils when they are added to reactions at early time points and are incorporated into fibrillar structures[325].

Finally, the effect of LT1 on Aβ42 fibril formation was also analyzed by AFM. In untreated control samples multiple long Aβ42 fibrils with an average height of ~4.7 nm could be detected after 6 h (Fig. 60; Supplementary Fig. S5), indicating that first fibrillar structures are already formed during the lag phase in the amyloid polymerization cascade. In comparison, fewer Aβ42 fibrils with an average height of ~3 nm were detectable in LT1-treated samples, indicating that compound treatment alters the thickness of spontaneously formed amyloid fibrils. However, no obvious effect of LT1 on fibril formation was observed when aggregation reactions were analyzed after 20 h (Fig. 60), confirming the initial results that substoichiometric compound concentrations do not prevent aggregate assembly. By impression the LT1-treated fibrils of both time points also seemed to be longer, the longitudinal growth, however, was difficult to quantify.

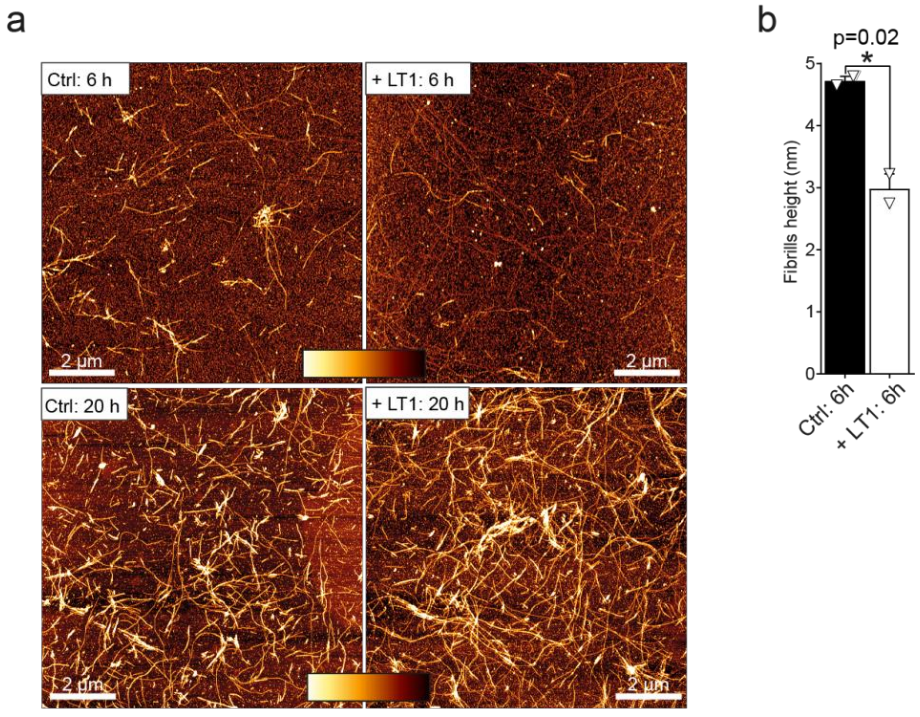

Figure 60 | LT1 decreases thickness of spontaneously formed ^{FAM}Aβ42/Aβ42 fibrils
(a) AFM images of compound-treated and untreated samples analyzed in *Fig.59a*. 10 x 10 µm, scale bar: 2 µm, color gradients indicate heights between 0-10 and 0-8 nm for 6 and 20 h samples, respectively. (b) Quantification of fibril heights in samples taken after 6 h. The height of Aβ42 fibrils (n = 8) was quantified in two independent experiments (10 x 10 µm images). Data are mean ± SEM (n = 2); individual values are presented as triangles. Statistical significance was assessed by unpaired t-test, two-tailed. *, p≤0.05.

5.4.5 LT1's auto-fluorescence can be utilized to monitor Aβ42 fibrillogenesis

Previous studies have demonstrated that the fluorescence of the LT1 precursor molecule K114 can be applied to measure amyloid aggregation in cell-free assays[210]. Therefore, I assessed whether the interaction with Aβ42 peptides influences the fluorometric properties of LT1. To address this, LT1 (5 µM) was incubated either with 10 µM soluble, unstructured Aβ42 monomers or pre-formed β-sheet-rich fibrillar aggregates for 5 min and emission spectra (between 400 and 680 nm) were generated using a constant excitation wavelength of 380 nm. An emission peak with a maximum wavelength of ~450 nm was detectable with both monomers and fibrillar Aβ42 aggregates, but with higher intensity with the latter (Fig. 61). Additionally, a second emission peak appeared with fibrillar Aβ42 assemblies only, indicating that the compound similar to K114 can be applied as a reporter molecule to monitor the spontaneous formation of β-sheet-rich, fibrillar structures in complex polymerization reactions.

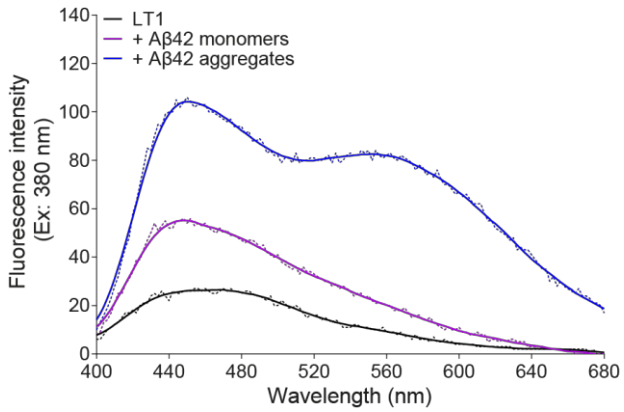

Figure 61 | Fluorescence spectrum of LT1 in presence of Aβ42 monomer or aggregates
Fluorescence spectra of LT1 (10 µM) in the presence of Aβ42 monomers (10 µM) or pre-formed aggregates (10 µM, monomer equivalent). Fluorescence was measured at a constant excitation wavelength of 380 nm and varying the emission wavelength at 2 nm intervals between 400 and 680 nm. The fluorescence of LT1 is increased in the presence of Aβ42 aggregates and a second emission peak with the maximum at ~560 nm arises. Dashed lines display unfitted curves.

Following, it was investigated whether the fluorescence of LT1 can be used to monitor the time-dependent formation Aβ42 fibrils in a microtiter plate assay. Therefore, Aβ42 monomers (10 µM) were incubated with LT1 (5 µM) at 37°C and fluorescence emission at 560 nm was monitored over time. Indeed, a sigmoidal curve progression after a lag phase of ~6 h could be observed, confirming the compounds utility as a reporter molecule to monitor the spontaneous amyloid fibril formation (Fig. 62a, blue). Simultaneously, Aβ42 monomers (10 µM) were incubated with ThT (5 µM) and fluorescence was quantified at 485 nm in a control aggregation reaction (Fig. 62a, black). The kinetic profile of the aggregation was comparable with both reporter dyes. However, the onset of

aggregation was delayed for ~2 h with LT1 in comparison to ThT measurements, supporting initial results obtained with FP assays that LT1 extends the lag phase in the aggregation process.

Finally, it was analyzed whether Aβ42 fibrils formed in the presence of LT1 and ThT possess similar seeding activities. Therefore, samples were taken from the aggregation reaction after 18 h (Fig. 62a) and added as seeds to standard ^{FAM}Aβ42/Aβ42 aggregation reactions (100 nM corresponding to monomer) to assess their seeding activity. It could be seen that Aβ42 fibrils taken from ThT assays potently shortened the lag phase in FP assays (Fig. 62b; $\triangle t_{50}$ = 5.1 h), demonstrating that they are highly seeding-competent structures. In contrast, LT1-aggregates showed a clear reduction of seeding activity ($\triangle t_{50}$ = 1.8 h), supporting the hypothesis that LT1 treatment leads to formation of Aβ42 fibrils with impaired seeding activity. It had to be ensured that the reduction of seeding was not due to residual compound in the sample obtained from LT1-aggregation reactions. Therefore, samples taken from ThT Aβ42 aggregation assay after 18 h were incubated with 50 nM LT1 and added to FP assays. This concentration of LT1 corresponds to the compound concentration that is present in the FP assays after addition of LT1/Aβ42 aggregates (100 nM). However, I found that LT1-treated and untreated ThT/Aβ42 aggregates (100 nM) display comparable seeding activities in FP assays, suggesting that the observed reduced seeding activity of LT1/Aβ42 aggregates is not due to the small amount of residual free compound in the sample

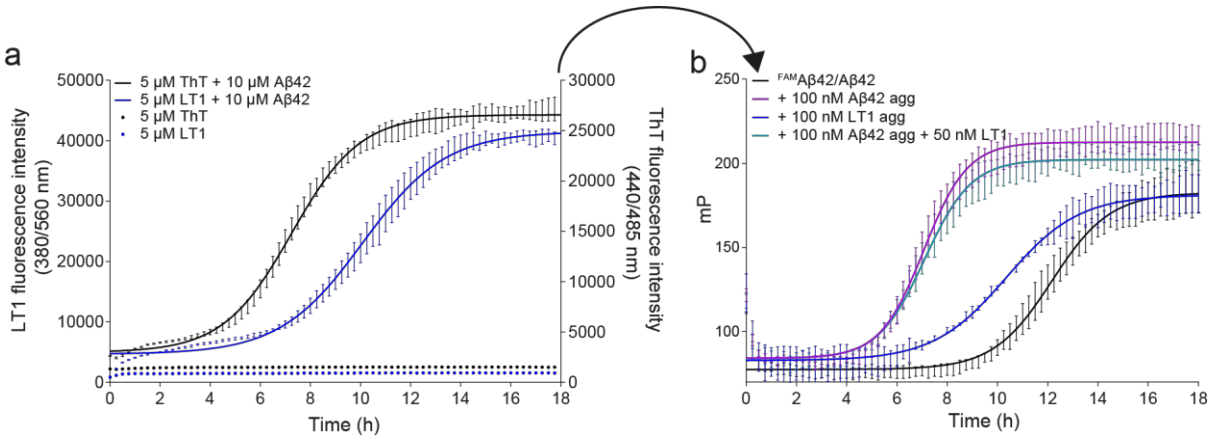

Figure 62 | LT1's auto-fluorescence can be utilized to monitor Aβ42 aggregation and LT1-treated Aβ42 assemblies show a reduced seeding activity in FP assays

(a) Measurement of ThT (5 µM) and LT1 (5 µM) fluorescence intensities over time in spontaneous Aβ42 (10 µM) polymerization reactions. Samples were incubated in microtiter plates at 37°C. Fluorescence emission of ThT and LT1 was measured at 485 and 560 nm, respectively. Measurements were performed in quadruplicates. Average values of one experiment are shown (mean ± SD). (b) LT1 treatment leads to the formation Aβ42 aggregates with low seeding activities in FP-based ^{FAM}Aβ42/Aβ42 co-polymerization assays. Samples were taken from ThT and LT1 Aβ42 polymerization reactions in *a* after 18 h and added as seeds (100 nM) to ^{FAM}Aβ42/Aβ42 co-polymerization reactions. FP intensities were quantified over time in microtiter plates. In control experiments, samples taken after 18 h from ThT/Aβ42 (100 nM) polymerization reactions additionally treated with LT1 (50 nM) were also analyzed in FP assays.

5.4.6 Detection of intracellular Aβ42 aggregates using LT1 fluorescence

After the investigation of the fluorometric properties of LT1 *in vitro*, I also analyzed whether LT1 can be used to detect Aβ aggregates in cells. This experiment was also motivated by the fact that LT1's precursor K114 is capable of detecting amyloid lesions in brain tissue[210]. For the intracellular detection of Aβ42 aggregates first unlabeled and fluorescently labeled Aβ42 aggregates were prepared by incubating 20 µM Aβ42 peptides with or without 5 % ^{TAMRA}Aβ42 peptides (Aβ42 N-terminally labeled with 5-Carboxytetramethyl-rhodamine) in LSB for 18 h at 37°C with constant agitation. Following, the aggregates were sonicated (6 x 10 sec at 20 % intensity) using a Sonic Dismembrator Ultrasonic Processor with a single tip to allow a better uptake of the aggregates into cells. SH-EP cells were then treated with 600 nM Aβ42 aggregates (unlabeled or labeled) via direct infusion into the cell culture medium for 6 h. To ensure removal of surface-bound aggregates, cells were washed with PBS, trypsinized and seeded into 96-well cell culture plates. After attachment of cells for 2 h, LT1 was added to the cells for a final concentration of 0.5 µM or 1 µM, respectively and LT1 fluorescence was measured after 1 h using a Tecan Spark plate reader that provides temperature and CO_2 control (37°C, 5 % (v/v) CO_2). As observed for *in vitro* aggregates, the fluorescence intensity of LT1 significantly increased in presence of both labeled or unlabeled Aβ42 aggregates in a concentration dependent manner, allowing the detection of intracellular Aβ42 aggregates (Fig. 63a).

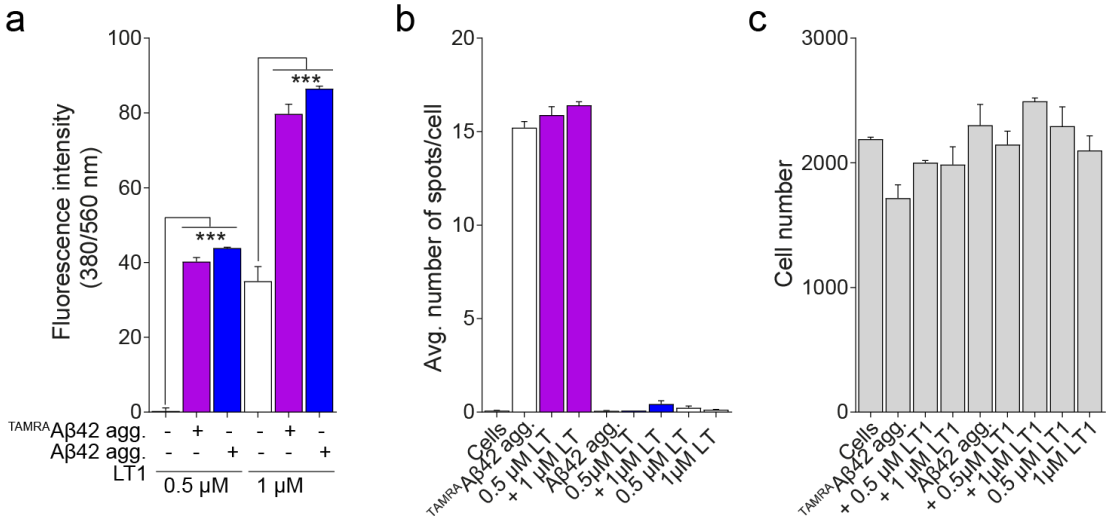

Figure 63 | Detection of intracellular Aβ42 aggregates using LT1 fluorescence
(a) SH-EP cells were treated with 0.6 µM TAMRA-labeled or unlabeled Aβ42 aggregates for 6 h. After internalizaton of aggregates, cells were treated with LT1 (0.5 µM or 1 µM) and LT1 fluorescence was measured after 1 h. In presence of both labeled or unlabeled Aβ42 aggregates, LT1's autofluorescene significantly increases in a concentration-dependent manner. Data are mean ± SD from triplicates. Statistical significance was assessed by one-way ANOVA followed by Dunnett's multiple comparison post hoc test. ***, p≤0.001. (b) The prescence of intracellular ^{TAMRA}Aβ42 aggregates was validated using an automated microscope. The average number of spots per cell shows a signal for ^{TAMRA}Aβ42 treated cells (mean ± SD from triplicates). (c) Similar cell numbers were measured by detecting the Hoechst fluorescence signal (mean ± SD from triplicates).

Use of TAMRA-labeled aggregates allowed to verify the presence of intracellular Aβ aggregates by using a Cellomics ArrayScan High-Content System device. After LT1 fluorescence measurement cells were fixed with PFA and stained with Hoechst before images with Cellomics were acquired and an automated data analysis was performed using the ArrayScan VTI software. For quantification, individual cells were detected via Hoechst fluorescent signals (Ex/Em: 350/461 nm) and the average number of TAMRA spots per cell (Ex/Em: 544/572 nm) was obtained from technical triplicates to obtain the aggregate load per cell (Fig. 63b). Unlabeled Aβ aggregates were used simultaneously to exclude cross-excitation between TAMRA and LT1 as their excitation/emission wavelength are in very close proximity (TAMRA: 544/572 nm; LT1: 380/560 nm). Hoechst staining showed that the cell number per well was similar for all tested samples (Fig. 63c).

Additionally, HiLyte-labeled aggregates (5 % ^{HiLyte}Aβ42, Aβ42 N-terminally labeled with HiLyte Fluor™488) were prepared and cells treated with aggregates as described earlier. In this case, however, cells were seeded on cover slips for co-localization experiments. Also, cells were treated with 5 µM LT1 for 3 h before being PFA-fixed and prepared for confocal microscopy. HiLyte and LT1 fluorescent images were acquired at excitation wavelengths of 488 and 380 nm, respectively and co-localization analysis of fluorescent puncta was performed. Figure 65 shows ^{HiLyte}Aβ42 aggregates as green puncta inside the cell, LT1 fluorescence is presented in magenta (Fig. 64). Correlating the fluorescence intensity along a selected section (white arrow) reveals a co-localization between HiLyte and LT1 fluorescence signal (Pearson's r = 0.756).

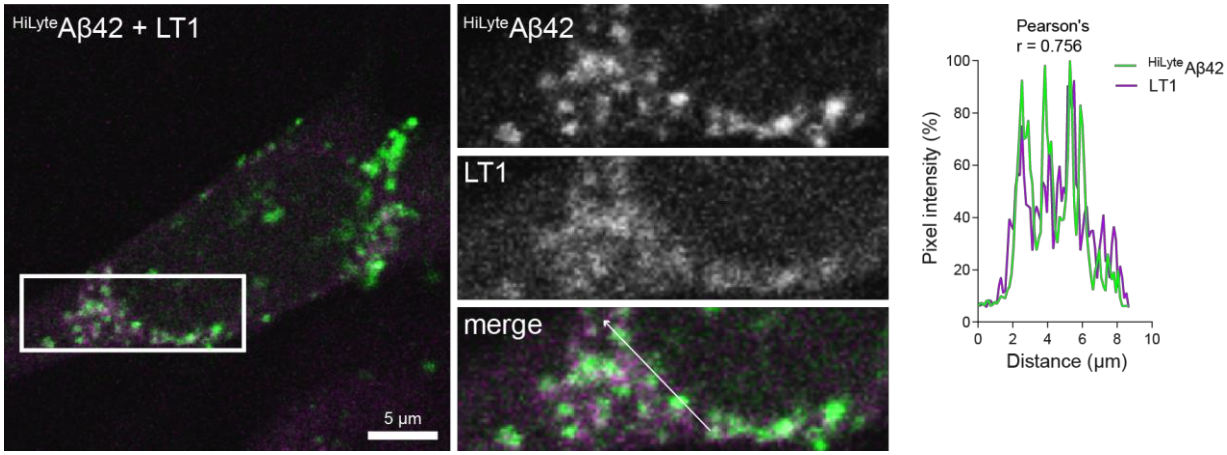

Figure 64 | Co-localization of LT1 and HiLyte-labeled Aβ42 aggregates in SH-EP cells
Confocal microscopy reveals that LT1 partly co-localizes with Aβ42 aggregates. SH-EP cells were treated with ^{HiLyte}Aβ42 aggregates (0.6 µM) and stained with LT1 (5 µM) for 3 h before PFA fixation. HiLyte and LT1 fluorescence intensities were quantified along the white arrow in the merged image. Fluorescent signals clearly overlap at several locations indicating that LT1 binds to Aβ42 aggregates. One representative image is shown with co-localization analysis using Pearson's correlation coefficient. Scale bar: 5 µm.

Summarized, the fluorometric properties of LT1 enable a detection of intracellular Aβ aggregates as the fluorescence intensity of LT1 significantly increases upon interaction with β-sheet-rich aggregate structures. Furthermore, using LT1's auto-fluorescence a co-localization with intracellular Aβ42 aggregates can be observed.

5.4.7 LT1 decreases the seeding activity of Aβ aggregates prepared from AD transgenic mice

After assessing LT1's capacity to delay seed-mediated Aβ42 aggregation *in vitro*, it was tested if the compound can also target potentially disease-relevant Aβ seeds isolated from AD transgenic mouse brains. Besides LT1 also compound 6 was tested as a control as this compound with its terminal methoxylation did not affect the activity of *in vitro* seeds in Aβ42-FP assays (Fig. 55, 56). Indeed, the compound LT1 was capable of attenuating the seeding effect of transgenic mouse seeds and delayed the aggregation in FP assays in a concentration-dependent manner. In comparison, no significant effect was observed for compound 6 (Fig. 65a, b). Together, these results proved the capacity of hit compound LT1 to target potentially disease-relevant Aβ aggregates extracted from AD transgenic mouse brain.

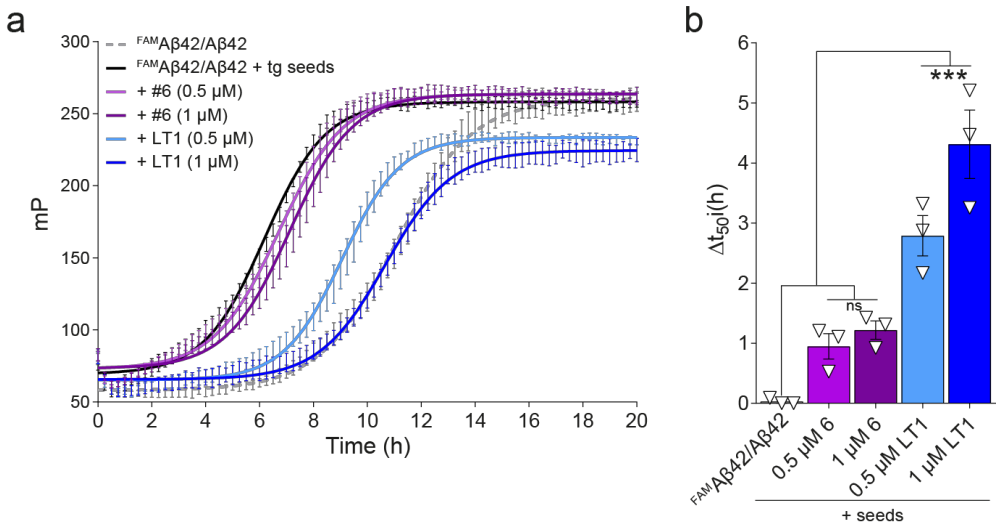

Figure 65 | LT1 decreases the activity of disease-relevant Aβ seeds prepared from tg AD mouse brain
(a) Effects of compounds LT1 and 6 on the seeding activity of Aβ species extracted from tg mouse brain with Aβ-specific 6E10 antibody in a concentration-dependent manner. FP assays were performed in quadruplicates. Shown is one representative experiment (mean ± SD). (b) Quantification of compound effects on the seeding effect of mouse seeds from three independent experiments. Data are mean ± SEM (n = 3) and individual values are presented as triangles. Statistical significance was assessed by one-way ANOVA followed by Dunnett's multiple comparison post hoc test. ***, p≤0.001.

For any further experiments regarding a potential *in vivo* application of LT1, a requirement would be the capability of LT1 to cross the blood-brain barrier. To address this question the compound concentration was measured in crude brain extracts by RP18-HPLC after oral administration of 20 mg/kg at three different time points (0.5, 1 and 4 h), with samples being collected at each time point from three mice. After 30 min, LT1 could be detected in mouse brain homogenates (Fig. 66), indicating that the compound can cross the blood-brain barrier even though the concentration again decreased after 1 h.

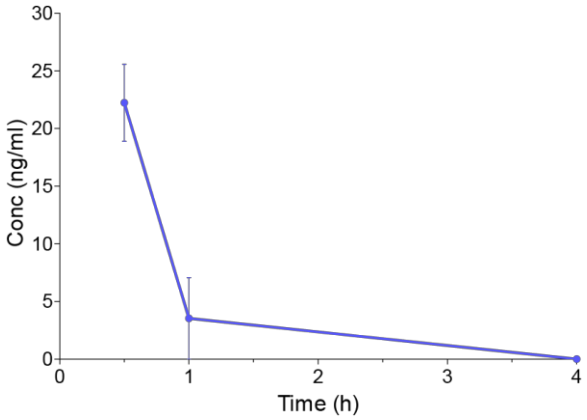

Figure 66 | Assessment of LT1 concentration in mouse brains (blood-brain barrier study)
The pharmacokinetic evaluation of LT1 including assessment of brain penetration after oral application was done by Pharmacelsus (Saarbrücken, Germany). Concentrations of LT1 were determined in brain samples from male C57BL/6N mice after oral administration of 20 mg/kg (vehicle: 1 % methyl cellulose in water; application volume: 10 ml/kg) at three different time points (0.5, 1 and 4 h). For each time-point, samples were collected from three mice.

6.

Discussion

6. Discussion

With estimated 30 million affected people worldwide and development of a new AD case every 66 seconds in the US, Alzheimer's disease remains one of the biggest challenges of the 21st century[6]. Many years have passed between Alois Alzheimer's report of distinctive plaques and neurofibrillary tangles found in the *post mortem* brain of patient Auguste Deter who suffered from cognitive impairment and confusion in 1906[1] until the identification of amyloid-β as the primary component of plaques in Alzheimer's patient brain tissue (1985)[312,326]. However, with this discovery the era of modern AD research began[312]. By the time when genetic mutations in the Aβ precursor gene *APP* were discovered and could be linked to AD pathology the significance of the Aβ peptide for this devastating neurodegenerative disorder was undisputed (1992)[17,18,327]. Now, 2018 many pieces of the puzzle have been found and a lot has been accomplished in the field of basic AD research, all with the aim of finding a causative treatment to prevent and overcome the disease. However, drug trial studies of potential effective drugs keep failing, most likely because the disease has not been understood in detail yet. Thus, I think it is very important to gain more profound understanding of the Aβ peptide itself and its highly complex multi-step aggregation mechanism that leads from soluble peptides into fibrillar aggregates that ultimately deposit in the brain of AD patients. Sensitive and reliable assays are therefore required to monitor the Aβ aggregation process in a time-resolved manner that will help to understand what initiates the aggregation reaction and causes an acceleration of this abnormal process. Only when a potential and pivotal target in the whole aggregation process is found, the search for effective drugs that are able to intervene with the pursued targets becomes promising.

In this work, the establishment of a new one-step cell-free assay to monitor the Aβ42 aggregation process was shown utilizing the principle of fluorescence polarization, termed Aβ42-FP or ^{FAM}Aβ42/Aβ42 co-polymerization assay (*Chapter 5.1*). The assay was used to analyze the potential of biological samples from Alzheimer's patients or AD transgenic mice to accelerate the spontaneous Aβ42 aggregation by providing seeding-competent Aβ structures, constituting a highly disease-relevant process (*Chapter 5.3*). Furthermore, the assay was shown to be useful not only for the screening of small molecule Aβ42 aggregation inhibitors, but also to conduct systematical structure-activity relationship studies leading to the identification of crucial structural moieties of a potent compound. Therefore, the bis-styrylbenzene molecule K114 was consulted and newly synthesized derivatives were analyzed regarding their potential to target specifically the seed-mediated Aβ42 aggregation process (*Chapter 5.4*). It could be shown that introduction of an additional terminal hydroxyl group at both terminal aromatic benzene rings improved the capacity of the compound to

inhibit seed-mediated Aβ42 aggregation, represented by the hit compound LT1. Finally, LT1's mechanism of action of inhibiting the Aβ42 aggregation process was further analyzed.
The benefit of the Aβ42-FP assay, advantages, limitations and further assay developments are going to be discussed in the following. Furthermore, based on *in vitro* analysis of seeding-competent structures (*Chapter 5.2*) it is ought to define more precisely what biochemical and structural properties might contribute to the capacity of an Aβ species to seed the aggregation process. The application of the assay as a potential tool for early AD diagnosis and as a compound screening technique shall be examined. Conclusively, a mechanism of action is proposed for compound LT1 based on the obtained results to explain its aggregation-inhibiting capacities.

6.1 Development of a fluorescence polarization based-assay as a new method to monitor Aβ42 aggregation

Here, for the establishment of an Aβ42 aggregation assay the fluorescence polarization principle was utilized. Up to date, FP is widely used for receptor-ligand binding or immunoassays[239,248,249]. Previously, the FP principle has been applied to monitor the fibrillogenesis of α-synuclein in a time-dependent manner[328]. However, using FP to monitor the time-resolved aggregation of the Aβ42 peptide together with an application for the detection of seeding-competent Aβ structures was not described before. Literature research merely revealed the existence of patents using the FP principle for the investigation of Aβ aggregation, but no follow-up literature showed their application[329-331].

From a practical point of view the Aβ42-FP assay is an easy to perform one-step assay. Unlike e.g. FRET measurements that require double labeling of the interaction partners, FP analysis manages with only one single fluorescently labeled molecule and also no radioisotopes are used. FP analysis provides a direct and nearly instantaneous measurement of a tracer's bound/free ratio and a separation of bound and unbound fraction is not required, thereby true equilibrium analysis can be performed. Furthermore, the FP measurement does not affect the sample, allowing further analysis with various other methods for validation afterwards. Another advantage is that only low tracer concentrations are required. This minimizes potential interactions or competitive binding with compounds, thus making it superior over e.g. the ThT assay and highly suitable for compound screens. Subsequent data evaluation comes in handy as the FP values can be easily calculated based on the measured vertical and horizontal intensities by consulting *Equation 3*.

Assessment of the FP assay's quality revealed a good homogeneity within a whole 384-well plate in initial evaluation experiments. Additionally, Z-value determination in four independent experiments indicated high-throughput suitability for the Aβ42-FP assay (Fig. 25). However, throughout the project partly severe variations in Aβ42's aggregation behavior could be observed. This was never seen in such detail with other methods as they rather focuse on a specific Aβ species at a certain time point than displaying the whole kinetic aggregation profile. Due to the Aβ42-FP assay's high sensitivity those variations were detected promptly. By systemic analysis of this issue two culprits could be identified. First, working with Aβ42 peptides requires a highly standardized procedure and protocols, because variations could be observed upon using different peptide batches. As already mentioned, synthetic Aβ42 peptide was purchased and subjected to a pretreatment with HFIP (1,1,1,3,3,3-Hexafluoro-2-propanol) to ensure a monomerization of the peptide. It is critical to ensure that the monomeric peptide solutions used for FP assays remain seed-free for all time-resolved aggregation studies. Subsequent lyophilization of the solvent was also performed under highly standardized conditions as this reaction is influenced by temperature and humidity. Since it was shown by *Ryan et al*.[332] that pretreatment with HFIP might not result in a solution that is completely aggregate free, also NH_4OH was tested as an alternative monomerization pretreatment. However, pretreatment experiments with NH_4OH performed in our lab did not lead to satisfactory results (*data not shown*). Therefore, the protocol for Aβ42 pretreatment with HFIP was consistently optimized throughout this project until a reliable protocol for the Aβ42 monomerization was established. Nevertheless, despite high standardization and accuracy variations of Aβ's aggregation propensity could still be observed that could be due to inherent deviations of the Aβ peptide. *Zagorski et al.* addressed the many methodological and chemical factors affecting the inherent quality of synthetic Aβ peptide, and, for those reasons, referring to it as 'the peptide from hell'[271]. One major problem seems to be minor impurities and mixed peptide assemblies as the result of time- and concentration-dependent aggregation of the Aβ42 peptide in the acetonitrile-water solution during the HPLC purification[333]. Furthermore other variables such as metal impurities, salts and partial racemization that might appear during peptide synthesis might affect the synthetic Aβ42 peptides from the very beginning. Just from the first look at a newly purchased peptide batch differences could be observed e.g. electrostatic charge or consistency of the pure peptide, indicating variations in the remaining water content from synthesis. Inherent quality deviations of synthetic Aβ peptide are difficult to address. However, analysis of the aggregation behavior with FP assays promptly revealed if the peptide aliquot was error-prone by means of the resulting curve profile. Such experiments were then not taken into further account in order to prevent potential false-positive results. Furthermore, and most importantly for this study, it was ensured that a longer aggregation duration was accompanied by an accordingly longer lag phase for seeded reactions (Fig. 28). This allowed comparing different experiments with

distinct aggregation profiles since always the △-values from spontaneous and seeded inflection points were calculated. Secondly, as already indicated in the results part, also variations of the same Aβ42 peptide aliquot within one 384-well plate could be observed (Fig. 26). This was an unexpected finding and should strengthen the awareness of potential occurring deviations in consumables as well. However, this discrepancy was resolved by distributing Aβ42 controls in close proximity to the analyzed sample and always referring a sample's seeding or inhibiting effect to the close by Aβ42 control (Fig. 27).

General limitations of using fluorescence polarization for the establishment of aggregation assays arise when bigger molecules are ought to be analyzed. With a molecular weight of ~4.5 kDa the Aβ42 monomer represents a quite small molecule and thus relatively large changes in molecular volume from monomers to the final still measurable aggregate can occur as the difference of FP values between free and bound tracer is high enough. However, the assay principle is not readily transferable to any other amyloidogenic protein when it has a high molecular weight. For example, when using fluorescently labeled tau protein with ~45-60 kDa depending on the isoform as a tracer, the initial FP value would already be high. Instead, crucial fragments of the full-length protein could be used to establish a comparable aggregation assay. In case of the tau protein this could be the K18 fragment that contains the tubulin-binding domains R1-R4 and is known to be aggregation-prone[334]. Another option to enable the analysis of binding and interaction between higher molecular proteins would be the utilization of fluorophores with a longer lifetime to shift the upper signal limit upwards. However, in reality the number of suitable alternative fluorophores is modest and further limited by the availability of appropriate excitations filters provided by the plate readers. For example, using Lanthanides like Europium with a fluorescence lifetime of ~1 ms would indeed allow analysis of high molecular weight assemblies, but cannot be put into praxis due to its cage like molecular structure that would not be compatible with the current assay readout.

As already stated, the maximal measurable signal is limited by the fluorescence lifetime of the fluorophore as the FP values are proportional to the rotational relaxation time of the fluorophore. The used fluorophore FAM has a fluorescence lifetime of ~4 ns, leading to a detectable molecular weight difference of ~70 kDa based on literature and our own results (Fig. 16). In case of Aβ42, a detectable increase in molecular weight of up to 70 kDa would not allow detection beyond a 15-meric Aβ assembly. However, analysis with other methods such as NativePAGE and AFM clearly revealed the presence of bigger Aβ42 aggregates at the end point of the FP measurement when the plateau is reached (Fig. 20). To explain this discrepancy, it first of all has to be considered that the fluorescence lifetime of a fluorophore is assessed by analyzing one fluorophore-labeled protein on its own. It can be postulated that the size limitation (up to a 15-meric Aβ species) would indeed come into effect if the

labeled tracer would be the starting point from where the increase into bigger aggregates evolves. However, this scenario might not represent the experimental conditions, especially considering the highly complex aggregation process found with the Aβ42 peptide. In contrast, it is presumed that the labeled tracer acts in the same way as unlabeled monomers, thus the likelihood of the tracer being the starting point for the aggregation reaction is low. It is stochastically distributed and gets incorporated in various growing aggregates some time during the course of aggregation. Therefore, it is crucial to always consider the total population of tracer and unlabeled monomers and to appreciate that the final FP values result from the weighted average of bound and unbound tracer ratio. Thus, it can be argued that the fluorescence lifetime of the tracer does not limit the overall measurable molecular size of Aβ42 aggregates in this assay and solely the ratio of bound and free tracer molecules matters and indicates the progress of aggregation. Thereby, the inflection point displays the time point where half of the tracer can be found in its free and unbound form and the other half is incorporated into bigger assemblies. When the plateau signal is reached the tracer is maximally bound, but this does not deliver information about the size and morphology of the Aβ42 species present in the reaction, requiring additional methods to address these questions.

Interestingly, when using aggregation inhibiting compounds not only a delay in the lag phase, but also a lower plateau was observed occasionally (Fig. 24). This could indicate the formation of a different amount of aggregates, although it could be expected that a high concentration of smaller assemblies and a smaller amount of bigger aggregates would result in the same FP values if the tracer is maximally bound. Therefore, it is more likely that the reduced plateau observed in presence of particular aggregation inhibiting compounds reflects the formation of different species with distinct binding properties on the surface, leading to a higher amount of residual unbound tracer that lowers the maximal signal height. This could then be an indicator to take a closer look at the morphology of the formed aggregates.

One limitation of the Aβ42-FP assay arose when biosamples e.g. brain homogenates were ought to be analyzed directly as the FP assay features a high sensitivity. Especially detergents like Triton X-100 and SDS, that represent crucial components of an effective homogenization buffer, affected the measurements (Fig. 33). Therefore, a buffer exchange to provide a suitable environment for FP measurement is required. This limitation was overcome by establishing an alternative method and using IPs for the isolation of Aβ aggregate species and thereby enriching and purifying the analyte. Besides, the use of non-polar polystyrene adsorbent beads (BioBeads) for the removal of detergents from a solution can provide an alternative[335-337]. These beads offer a high surface area that is capable to adsorb organic and non-polar substances with a molecular weight <2,000 g/mol. Thus, I tried to remove disturbing detergents from homogenization buffer before analysis with FP assay (*data not*

shown). However, this approach was not successful in this project, but may be helpful in other assay applications. Additionally, the presence of various different proteins and lipids in crude brain homogenates could evolve in unspecific binding of the tracer or Aβ42 monomers to other protein components, leading to an impairment of the kinetic measurement. Thus, extracting the protein of interest, here Aβ42, from crude homogenate represents a valuable technique to both enrich and purify the analyte for the following analysis.

Optimal adjustment of Aβ42 monomer and FAM-tracer concentrations and assay buffer provided the standard Aβ42-FP assay to analyze both seeding and aggregation inhibiting effects of compounds. Therefore, it was especially important to obtain a reasonable long lag phase to detect seeding effects as these lead to a shortening of the lag phase. By accelerating the Aβ42 aggregation with different concentrations of pre-formed PF seeds a detection limit of ~11 fmol could be determined. As already mentioned, the PF assemblies always comprise a mixture of different sized species. Assuming a higher average molecular weight (Ø 600 kDa) or determining the detection limit with a different batch of PFs could then easily increase the detection limit up to 3.7 fmol. Interestingly, *Salvadores et al.* showed at detection limit of ~3 fmol by using a protein misfolding cyclic amplification (PMCA) assay[258]. This assay is based on the ThT readout whereby the sensitivity of the assay was significantly increased by preforming shaking conditions to amplify seeding-competent Aβ species. However, attempts to increase the sensitivity of the Aβ42-FP assay by enhanced shaking did not result in a lower detection limit.

By addition of increasing concentrations of PF seeds it was observed that addition of 200 nM seeds resulted in the maximal detectable seeding effect and addition of higher concentrations of seeds did not shorten the lag phase further. The same effect could also be observed with e.g. ThT readout and is simply owed to the nucleation-dependent aggregation mechanism of the Aβ peptide. Even after addition of a very high concentration of pre-aggregated seeds to monomeric Aβ peptide a certain amount of time is needed for the monomeric species to bind to those seeds up to a critical concentration that can be detected by any kinetic readout.

Summarized, the Aβ42-FP assay constitutes a new method to monitor the aggregation process with the capability to detect both seeding and compound inhibiting effects. Thereby, it features a high sensitivity and is most suited for high-throughput compound screens as a potential interference and competition of compound and detection dye is excluded.

6.2 What accounts for seeding-capacity?

Even though the concept of seeding is known for almost 20 years, there are still gaps of knowledge when it comes to the actual biochemical and structural properties of seeding-competent Aβ species. Additionally, there are always differences due to the preparation of the seeds and if the question is addressed from an *in vitro* or *in vivo* point of view. For example, it could be shown that only fibrillar structures larger than 200 nm can function as seeds but not oligomeric species[132]. Other groups define seeds based on their biological effect, which is to induce Aβ deposition in mice. The group of *Mathias Jucker* has shown that very potent Aβ seeds exist at the earliest stages of deposition and can be found in the 100,000 x g supernatant[296,338]. This suggests that very small species can seed efficiently, although, these Aβ fractions could include protofibrils or even fibrils too. At this point, it has to be accepted that Aβ seeds can encompass a number of different sizes and shapes, from small, soluble, protease-sensitive aggregates to large, insoluble, protease-resistant fibrils. My own results revealed that seeding-competent Aβ species indeed feature a fibrillar structure. This could be shown both from seeds prepared by aggregation of synthetic peptides (Fig. 30) as well as from seeds prepared by immunoprecipitation from transgenic mice (Fig. 42). Interestingly, the most seeding-competent species *in vitro* were prepared via sonication from bigger aggregates and rather displayed a compact and bulky morphology (Fig. 31). It is supposed that fragmentation of bigger aggregates into smaller species increases the number of reactive binding sites from where the aggregation can proceed. Results obtained from time-resolved analysis of Aβ aggregation further showed that already after 1 h of aggregation seeding-competent structures are formed and that these species do not have a high β-sheet content (Fig. 30), probably because the ThT assay is not sensitive enough to reflect small changes in secondary structure. Summarized, a reactive Aβ seed can be defined as an assembly with a critical size that features reactive binding sites on its surface, probably due to β-sheet-rich structures that enable intermolecular interactions (Fig. 67). The minimal size, however, is not known and also smaller assemblies without measurable ThT-reactivity feature a certain seeding activity. Based on data from our lab, a dimer is not sufficient to achieve seeding effects, but everything bigger than this might be able to act as a seed.

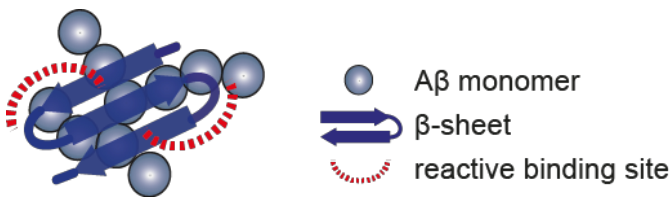

Figure 67 | Model of a seeding-competent Aβ species
A seeding-competent Aβ species can be described as an Aβ assembly of a critical size that comprises reactive binding sites on its surface, probably due to β-sheet-rich structures that enable intermolecular interactions.

Research effort was put into the identification of a specific Aβ species that accounts for the neurotoxic effects in AD, which leads to neuronal degradation and cell death, causing the neuronal deficits observed in AD. Soluble Aβ oligomers in general and ADDLs (Aβ-derived diffusible ligands) or protofibrils[96,339] in particular were in the focus of attention. But the presence of a mixture of various Aβ species in affected patient brains makes it difficult to ascribe the observed neurotoxicity to one particular Aβ species[312]. Interestingly, a previous study by *Jan et al.* linked Aβ-induced toxicity to the ongoing nucleated polymerization process rather than to a distinct Aβ species[117]. In their study they show that crude Aβ42 preparations that contain monomeric as well as heterogeneous mixtures of oligomeric Aβ species exert higher toxicity than purified Aβ species. Furthermore, it was demonstrated that after selective degradation of Aβ monomers the polymerization process is slowed down which is accompanied by reduced toxicity. It cannot be excluded that sonication of fully aggregated Aβ42 assemblies generates a specific neurotoxic Aβ42 species. But based on the observed data that show the presence of miscellaneous Aβ42 assemblies, it is more likely that the toxic effects are indeed caused by the ongoing nucleated polymerization process that occurs after adding a mixture of different species to the cell culture medium.

6.3 Applicability and limitations of the Aβ42-FP assay for the analysis of seeding activity in biosamples

When trying to use the established Aβ42-FP assay for the detection of small amounts of seeding-competent Aβ42 aggregate species in biosamples, it became obvious that a direct analysis of e.g. brain homogenates was not possible due to the interference of detergents in the homogenization buffer. However, establishment of an alternative homogenization buffer with only a small amount of Triton and subsequent dilution to a non-interfering final concentration in the FP assay did not allow distinction between wildtype and transgenic AD mice (Fig. 33). Dot blot analysis further supported the hypothesis that especially SDS seems to be an important component of the homogenization buffer to release Aβ peptides that are located in membrane-bound compartments and enable epitope accessibility (Fig. 32). It had to be excluded, that SDS artificially induces amyloid formation as suggested from recent publications[308,309]. By using a homogenization buffer with proteinase K (PK) other interfering proteins were digested, leaving PK-resistant Aβ fibrils that were accessible for the Aβ-specific antibodies used for IP (Fig. 45). Indeed, homogenization in a buffer without SDS but PK revealed the same seeding effect as SDS-based homogenization, confirming the necessity of either detergents or PK in the homogenization buffer to make Aβ aggregates available from intracellular compartments or to modify epitope accessibility.

Thus, instead of directly applying biosamples to the Aβ42-FP assay to assess their potential to seed spontaneous Aβ42 aggregation, a workflow was set up to initially extract and isolate Aβ assemblies from biosamples (Fig. 37). Immunoprecipitation is a standard technique and could be transferred to various other proteins as it only requires a specific antibody. Success of the extraction could be verified by Western blotting, however, the amount of extracted aggregates that were enriched was difficult to quantify and thus immunoblotting served more as a semi-quantitative verification method. Using immunoprecipitation of a protein from e.g. crude brain homogenate comes with the advantage that this step comprises both enrichment of the protein of interest and losing potentially interfering cellular components. Thus, after releasing the extracted species from the beads with sonication it became possible to further analyze an almost pure protein sample with various methods. Especially, it was possible to add the enriched aggregates to cells and thereby directly assess their effect on viability without adding other cellular components that might disturb the cellular homoeostasis.

It can be argued that the release of seeds from extracted Aβ aggregates represents an artificial step and does not reflect the conformation and nature of naïve Aβ aggregates that are present in e.g. AD affected brains. Various other methods were tested to release the extracted aggregate species from the beads after IP. For example, elution with guanidine hydrochloride was tested (*data not shown*).

However, utilization of such strong denaturating molecules is more likely to induce artificial modifications of the protein of interest. Using sonication to release extracted aggregates from beads seemed to be closer to the naïve aggregate conformation and additionally also enabled the amplification of reactive seeding-competent fragments. The success of sonication was verified by both Western blotting as well as filter retardation analysis that both confirmed that sonication is capable of fragmenting bigger aggregate species into small assemblies that are not retained in the gel pockets and cannot be detected on the 0.2 µm filter under denaturating conditions (Fig. 36 and 38). Appropriate conditions for the seeds release were systematically evaluated and especially the comparability between different samples that were subjected to sonication was emphasized (Fig. 38). The most reproducible results were achieved by using an 8-tip attachment that allowed simultaneous and even sonication of eight samples.

6.3.1 Analysis of mouse brain samples

Application of the experimental setup to mouse brain samples allowed the reliable differentiation between AD transgenic and control wildtype mice with three different mouse models in a concentration-dependent manner and by using two different Aβ-specific antibodies (Fig. 37 and 39). Whereas the 6E10 antibody detects both Aβ monomers and aggregate species, the 352 is reactive for protofibrillar structures only. Preceding *in vitro* analysis also indicated that 352-reactivity correlates well with seeding activity (Fig. 30), highlighting its potential to specifically target and extract seeding-competent Aβ assemblies from biosamples. In general, no significant difference could be observed between 6E10- and 352-reactive species in mouse brain samples. A potential application of the Aβ42-FP assay as an early detection method to quantify minute amounts of seeding-competent Aβ species in biosamples was confronted with limitations when analyzing transgenic mice brain samples of different age. Using the 5xFAD mouse model, no seeding effect could be detected before 5 months of age (Fig. 40). The model is reported to rapidly develop severe amyloid pathology with the first amyloid deposits being found with 2 months in the subiculum and layer 5 of the cortex[281]. By 6 month of age, however, Aβ plaques were shown to spread throughout the hippocampus and cortex. Compared to this data, the Aβ42-FP assay would still allow earlier detection of Aβ deposition if equating deposition of Aβ plaques with seeding activity. However, analysis of different aged APPPS1 mice did not reveal a seeding effect with mice younger than 9 months. Even though this model with only two mutations represents a weaker AD model compared to 5xFAD mice, Aβ deposition in cortex still starts at around 3-4 months in cortex. However, it has to be stated that from the younger mice only one animal per age could be analyzed and that even in transgenic mouse models severe variations of the phenotype can occur. Mouse brains with other ages (e.g. 3 and 4 month for FAD and 7 and 8 month for APPPS1) were not available. Furthermore, whole hemispheres

or cortex were used for the homogenization and analyzed regarding seeding activity. However, it is conceivable that by use of e.g. only hippocampal tissue that is known to be particularly vulnerable to AD and shows Aβ plaque deposits at about 3-4 months in APPPS1 mice[283], an earlier detection could be possible in this mouse model too.

Characterization of seeding-competent Aβ species prepared from transgenic mouse brains revealed that these seeds encompassed mainly fibrillar structures (Fig. 41). Furthermore, analysis with denaturating filter analysis showed the existence of SDS-stable assemblies (Fig. 41). Finally, analysis with MTT assays revealed that in the presence of 6E10- and 352-reactive seeds from transgenic mice brain the mitochondrial metabolism of PC12 cells was impaired, leading to a reduced signal (Fig. 43). The correlation between seeding activity of disease-relevant aggregates and impairment of cellular integrity is striking and was not reported yet. However, if one precise fraction of the produced seeds or rather the ongoing aggregation mechanism encouraged by the presence of seeds can be held responsible for the observed effect in cells has to be investigated in more detail.

6.3.2 Analysis of human brain and CSF samples

The application of the method for the analysis of human brain samples seemed to be possible in first proof of principle experiments. Aβ aggregates could be extracted via IP with the 352 antibody compared to the control antibody IgG1 as seen on Western blots (Fig. 46). By using transmission electron microscopy even fibrillar aggregates extracted from an AD brain lysate could be found attached to the antibody-dynabeads (Fig. 46). However, validation of the presence of Aβ peptides via immunogold-labeling was difficult due to an unspecific binding of a biotinylated 6E10 biotin antibody that was ought to be used for secondary streptavidin-gold detection (*data not shown*). Additional experiments with tosyl-activated beads (binding to amino or sulfhydryl groups in the protein of interest) instead of Protein G-dynabeads did not reveal satisfactory results either (*data not shown*). However, compared to control samples (e.g. beads only) where unspecific background signals could be observed, the 352-immunoprecipitated material from an AD patient revealed a clear fibrillar morphology, strongly indicating that indeed Aβ fibrils have been isolated. But subsequent analysis of various human AD brain samples did not reveal an acceleration of the Aβ42 aggregation in FP-based assays (Fig. 47). Furthermore, analysis of 10 AD and 10 control brain samples with native FRAs and the 6E10 antibody for aggregate detection did show inconclusive results (Fig. 47). A certain variance between different human samples is likely, but the number of diagnosed healthy controls with a significant 6E10-positive Aβ load together with the comparable small number of diagnosed patients without 6E10 reactivity made it difficult to assess the data properly. Detection with the 352 antibody revealed basically no signal and thus no 352-reactive Aβ species in any of the analyzed samples

(Fig. 47). As already mentioned, this antibody was raised against synthetic protofibrils and worked well and specific in all *in vitro* experiments, thus its high sensitivity in *in vitro* assays is unquestionable. Furthermore, the antibody was capable to detect seeding-competent Aβ42 aggregates in three different transgenic mouse lines. It can be assumed that the amount and variety of Aβ assemblies is especially high in transgenic mice that are challenged with different AD-related mutations, increasing the likelihood of the 352 antibody to capture the relevant species. However, Aβ aggregates are very polymorphic and their abundance can be very different in human brain samples. Many publications try to unveil the three-dimensional molecular structure of amyloid fibrils[104,106,340-343]. Using solid-state NMR and EM *Lu et. al* strikingly demonstrated that human brain-derived Aβ fibrils from two different patients already revealed distinct fibrils with a single predominant structure[344]. Together, it is not completely surprising that an *in vitro* optimized antibody is not necessarily also well suited for the detection of human material as the *in vivo* situation in human brains is different from the *in vitro* environment. I still propose that the method *per se* should be capable of detecting seeding-competent aggregate species in human brain samples, if sufficient brain material of a specific patient with a high Aβ plaque load could be used. The conditions for the IP could then further be optimized regarding the used homogenate concentration for IP and the duration of the IP step. The already mentioned antibody *Aducanumab* could represent an alternative antibody to be used for IP experiments. It is a fully human antibody that targets a conformation-specific fibrillar form of Aβ and was already reactive in patients in clinical trials[190].

The limited number of human brain samples made it difficult to statistically assess the results from the analysis of human brain. Using human CSF samples instead allowed analysis of more samples that also covered a broader range of diagnosis. *Salvadores et al*. recently reported the detection of seeding-competent Aβ aggregates isolated from the CSF of AD patients[258]. Therefore, a potential application of the Aβ42-FP assay with CSF samples was evaluated. It can be argued that a detection of Aβ42 aggregates in CSF samples is even less likely than the detection in human brain as it is reported that the Aβ42 levels in CSF are usually decreased in AD patients. However, it was recently shown that within a very early phase of AD progression Aβ levels are even increased, probably just right before the deposition of Aβ in the brain starts[45]. In an ideal setting, this would be the optimal time point to detect the increased amounts of Aβ aggregates in the CSF in a pre-diagnostic and minimal-invasive examination and to start treatment with a potential therapeutic drug immediately upon diagnosis. In general, the approach to enrich minute amounts of Aβ peptide from the CSF via IPs seemed to be useful. Even though the 352 antibody did not seem to function efficiently in human brain samples, it was still utilized in initial experiments with CSF samples as these samples have a completely different protein composition. It was still conceivable that the 352 antibody specifically detects small seeding-competent fibrillar oligomers from CSF samples.

In general, analysis of CSF samples was challenging due to various reasons. Even though the number of available samples was higher compared to the rare AD brain samples, the volume of each sample was limited to maximal 2 ml. When using 0.5 ml per antibody for the IP, it was in most cases not possible to repeat experiments when using two Aβ-specific antibodies and the IgG1 control antibody to assess the correctness and reproducibility of the results. Furthermore, since CSF is obtained via lumbar puncture, which is a minimal-invasive, but certainly painful procedure, only liquor from more or less neurological affected patients was available and control CSF from healthy individuals was missing. This is why samples from patients that were diagnosed with depression had to serve as controls. However, it was shown that depression can precede AD and it was furthermore described to be a risk factor for AD development[345]. Additionally, it was shown that experiments with CSF can be error-prone due to deviations in proper handling and storage of the samples. In a quality control study from *Mattson et al*. the levels of Aβ42, t-Tau and p-Tau were detected using e.g. enzyme-linked immunosorbent assays (ELISA)[44]. However, severe variations between different labs were observed with an overall variability between 20-30 % for most assays and samples (standard deviation × 100 divided by the mean)[44]. Even though a highly standardized workflow was established for the analysis of CSF samples in this project, a potential impairment of the obtained results due to e.g. storage or the time point of sample freezing could not fully be excluded.

CSF samples could theoretically be analyzed in FP-based assays without further homogenization and IP pretreatment, as disturbing detergents are lacking in this protein sample. However, even the use of CSF samples in a 1:500 dilution delayed the lag phase for all tested samples (Fig. 49). Obviously single components (e.g. apolipoprotein E) in the CSF or the sum of multiple proteins impaired the FP measurement and strengthened once more the necessity of using IP approaches prior to time-resolved measurements with Aβ42-FP assays. First initial experiments to extract Aβ aggregates from CSF samples looked promising as Aβ aggregates could be enriched from the CSF of an MCI patient (Fig. 48). Analysis of 36 samples revealed four samples were a seeding effect of 6E10, 352 or both antibodies could be observed (Fig. 51). However, these data were difficult to interpret as they differed regarding their biomarker levels and the assessed mental state status. A follow-up analysis of these four samples would be very interesting. Finally, increasing the volume of CSF for the IP (2 ml instead of 0.5 ml) led to a precipitation of the dynabeads (*data not shown*), probably due to a cross-linking of the antibody-dynabeads with endogenous protein in CSF samples. When trying to pre-clear the CSF samples form endogenous protein before the IP with Aβ-specific antibodies, the Aβ peptides, however, seem to get lost. Summarized, the application of the Aβ42-FP assay for the detection of seeding-competent Aβ assemblies both in human brain and CSF samples is challenging and requires

extensive on-going optimization and analysis. However, a large collection of biosamples would have to be available to be able to better classify the results.

6.4 Applicability of the Aβ42-FP assay for compound screening and structure-activity relationship studies[2]

Besides a potential application for early detection of seeding-competent Aβ species in biosamples, the Aβ42-FP assay was finally applied for the identification of small molecules that interfere with the aggregation process. Identification of compounds that specifically inhibit the formation of self-propagating amyloid fibrils may help to clarify their role in the pathogenesis of neurodegenerative diseases[346], the crucial first step preceding any drug development endeavors. In most previous studies inhibitors of amyloid polymerization were identified with dye-based aggregation detection methods, in particular the ThT assay[347,348]. Chemical compounds that target amyloidogenic peptides and slow down polymerization are detected in ThT assays because they delay or inhibit the time-dependent appearance of the ThT fluorescence signal[347]. However, a decrease in ThT fluorescence assumed to result from an inhibition of aggregation can simply be due to a competitive binding of the tested small molecule to the ThT-binding site on amyloid aggregates[349,350]. This leads to the necessity of comprehensive validation with dye-independent secondary assays such as ion mobility mass spectrometry[323] or filter retardation assays[275]. These circumstances could partly explain why up to date only a few studies with a convincing structure-activity relationship analysis for known amyloid-targeting compounds have been reported[351,352].

Due to the high-throughput capability of the ^{FAM}Aβ42/Aβ42 co-polymerization assay, it was also applied by colleagues for bigger compound screens in our lab. Thereby ~2,300 compounds were initially screened comprising both FDA approved molecules as well as natural products. After validation with independent assays, Sclerotiorin (SCL), a natural product primarily isolated from *Penicillium* species, could be identified as a promising hit compound (*manuscript in preparation*). Further investigations revealed that SCL delays Aβ42 aggregation by directly binding to unstructured monomeric Aβ42 peptides, thereby stabilizing their soluble state and preventing their conversion into β-sheet-rich structures. Compound treatment leads to the formation of amorphous Aβ42 structures with reduced seeding activity and a decreased cellular uptake.

Additionally, the small molecule DO1 (4-((4-nitrophenyl)diazenyl)-N-phenylaniline) could be identified as an Aβ42 aggregation modifier using the ^{FAM}Aβ42/Aβ42 co-polymerization assay (*manuscript under*

[2]Parts of the discussion in section 6.4 and 6.5 are based on the manuscript: Diez, L. *et al.* Structure-based discovery of amyloid-β nucleation modulators using a fluorescence polarization-based aggregation assay (2018) *(manuscript submitted).*

revision). It could be shown that DO1 is able to disrupt pre-formed fibrillar assemblies of synthetic Aβ42 peptides and reduces the size and abundance of diffuse Aβ plaques in brains of 5xFAD transgenic mice. Furthermore, in these AD mice a decrease of neuroinflammation-related gene expression changes was observed upon DO1 treatment. Finally, improved nesting behavior was observed upon treatment with the compound, supporting the rational to target self-propagating Aβ structures with small molecules as a valid therapeutic strategy.

Using the two known amyloid binders methoxy-X04 and K114 not only the general applicability of the Aβ42-FP assay for the detection of aggregation modulating compounds was shown, but also the potential usage of the assay to dissolve more subtle differences between a compound's structure and the relation to its activity (Fig. 53). Furthermore, it could be shown that a compound can entail different activities depending on its effect on a spontaneous or seed-induced aggregation reaction. Synthesis of K114 derivatives allowed conducting more precise structure-activity relationship studies to identify crucial structural requirements in Aβ aggregation modifying small molecules (Fig. 54). The necessity of a rigid basic structure could clearly be shown by compound **5**. Also, the importance of terminal hydroxyl groups was definite and demonstrated by terminally modified compounds **6** and **7**. It can be assumed that the terminal hydroxyl groups exist in their protonated form and thus are available for hydrogen bond formation with residues of the Aβ42 peptide. Further addition of a second hydroxyl group at each terminal benzene ring clearly improved the compounds' effectiveness (compounds **1-4**). The stronger effect of additional hydroxyl groups is probably due to a stronger binding or a better alignment of the small molecule on the surface of Aβ42 peptides. Also, addition of a third hydroxyl group at one or both terminal benzene rings is conceivable to further increase LT1's efficacy. A well characterized example for this is the polyphenolic molecule EGCG that efficiently delays the Aβ42 aggregation reaction by directly binding to the unfolded polypeptides and promoting their conversion into off-pathway oligomers[59]. In another systematic study *Masuda et al.* investigated the effect of small molecule inhibitors, *inter alia* on Aβ assembly[353]. A direct comparison between the compounds kaempferol, quercetin and myricetin that share the same basic structure and differ only in the number of hydroxyl groups at the terminal benzene ring demonstrated the increasing efficiency by means of decreasing IC_{50} values (8, 5, 0.9 µM)[353]. Additionally, also the substitution of other positions (e.g. *ortho, meta, para*) and asymmetrical OH-substitution at both terminal benzene rings could be tested. Furthermore, the hydroxyl groups could also be substituted with bioisosteres, chemical substituents featuring similar physical or chemical properties (e.g. SH, NH_2, NH_2-CH_3)[354,355]. Especially the substitution and introduction of amines could enhance LT1's binding to Aβ peptides as it enables further hydrogen bond interactions with the backbone of the Aβ peptide as shown for the compound RS-0406 containing secondary amines or other heterocyclic molecules[356-358]. In this way the

effectiveness of LT1 could be improved without making significant changes in the bis-strylbenzene basic structure. Additionally, also the bromine residue at position *2* in the central benzene ring could systematically be substituted with e.g. other halogens like fluoride, chloride and iodine. With these results in hand a better assessment of the impact of electronegativity, polarizability and spatial extension could be made if a tendency (F > Cl > Br > I) could be observed. A third plausible modification to enhance LT1's efficacy is to increase the rigidity of the structure by fusing ring systems like benzothiazole, benzoxazole or benzodiazole that still mimic the central styrene structure[354].

To optimize the general drug-likeness of the compound, its relatively low solubility upon a concentration of 8 µM (Fig. 57) could be addressed and the solubility increased by introduction of heterocyclic ring structures. By substituting one carbon atom with nitrogen, sulfur or oxygen the polarity and water solubility of a structure can be increased[355]. More efficiently, also permanently charged groups could be inserted, e.g. nitrogen cations introduced by N-alkylation or positively charged oxonium ions like pyrylium or furanium salts. Another common modification to increase a compound's solubility is the introduction of sulfite anions, which could be realized at position *2* at the central benzene ring instead of the bromine residue.

Finally, modifications to increase LT1's fluorescence properties could be performed. In this project, LT1's auto-fluorescence was already used to detect intracellular Aβ42 aggregates both by fluorescence intensity measurements at 380/560 nm and in co-localization experiments using HiLyte488-labeled Aβ42 aggregates (Fig. 63 and 64). In general, the auto-fluorescent small molecule LT1 is an aromatic compound with a double bond system and an extended π-electronic system. When being excited with light the compound molecule absorbs the energy and electrons are promoted from a low energy singlet ground state (S_0) into a singlet excited state (S_1 or S_2). With the return of the excited molecule to the ground state, photons of lower energy are emitted, corresponding to a longer wavelength than the absorbed photon. The fluorescence properties could now be optimized by shifting absorption and emission towards higher wavelengths by taking advantage of the highly conjugated aromatic system. With the terminal hydroxyl group as an electron donor on one side of the molecule and the additional asymmetrical introduction of an electron acceptor (e.g. NO_2, SO_2NMe_2 or CN as an electron withdrawing group)[359] on the opposite side, a so called 'push–pull' mechanism could become effective. With this strategy the conjugated π-electronic system over the entire length of the compound would be maximally exploited.

To further investigate LT1's capability as a potential new amyloid dye it could be applied to sections of transgenic or human brain samples to perform immunohistochemical stainings. Comparing the staining pattern with the ones of commonly used amyloid dyes like Congo Red and also structurally related dyes like e.g. K114 and methoxy-X04, the specificity and reactivity of LT1 could be determined.

In additional experiments LT1 could also be applied to transgenic AD mice orally, intracerebrally or intraperitoneally and its binding to Aβ42 assemblies could be monitored using multiphoton microscopy through a cranial window. Such an implant allows optical access to a larger area of the cortex of awake mice even over longer periods of time and can be replaced or removed as required[360]. For this approach methoxy-X04 was already used. After intraperitoneal injection in AD transgenic mice the real-time deposition of cerebrovascular Aβ in arterial walls in CAA could be visualized[361].
With a positive outcome, that is specific binding to amyloid plaques or smaller aggregate structures in the brain, a development towards a PET tracer could then also be considered. For a potential PET tracer application the general prerequisite of blood-brain barrier permeability would be met and LT1's short residence time of ~1 h in the brain would then even be advantageous. For PET scans LT1 needs to be radioactively labeled, which could be realized by replacing the central bromine residue with the radioactive isotope ^{18}F of fluorine. To address the question of PET application it could also be relied on compound **2** that already contains fluorine atoms at position *6* in the terminal benzene rings that could be radioactively labeled. Alternatively, also an ^{11}C isotope of carbon in the basic styrylbenzene structure of LT1 can be introduced. This strategy has also been used for Pittsburg compound B (PiB), which is a radioactive analog of ThT and routinely used as a PET tracer to detect Aβ plaques in neuronal tissue of AD patients[38].

In summary, even though various amyloid-targeting structures have been described over the last decades, their precise effect mechanism of action is still often only poorly understood. The Aβ42-FP assay represents a valuable tool to exactly address this point. It allows not only screening of aggregation modifying compounds in a high-throughput manner, but also their characterization and structure-activity optimization. The compound effects on disease-relevant amyloid structures *in vitro* can be also quantified, making the established FP-based method a powerful tool with unique capabilities and many applications in the drug discovery field. The newly synthesized small molecule LT1 represents an interesting advancement of the known amyloid binder K114. It may be a further starting point for additional structure-activity optimization.

6.5 Model for LT1's mechanism of action[2]

Small changes in the structure of K114 led to the di-hydroxylated compound LT1 that turned out to be the most potent structure in a focused compound screen with nine K114 derivatives. Its effect on both spontaneous and seed-induced Aβ42 aggregation was assessed using different substoichiometric concentrations (Fig. 56 and 58). The strong concentration-dependent extension of the lag phase that was observed in both experimental paradigms confirmed the hypothesis that LT1 perturbs early events in the amyloid polymerization cascade. Further analysis with various biochemical and biophysical methods revealed that LT1 seems to act as an Aβ42 nucleation modulator by targeting small on-pathway aggregate intermediates and delaying their extension into larger fibrillar structures. Polyacrylamid gel electrophoresis both under denaturating and native conditions revealed that substoichiometric concentrations of LT1 can delay but not prevent the aggregation process (Fig. 56 and 58). Furthermore, the increase in monomers and low molecular weight assemblies (LMWAs) that could be observed indicated that LT1 might slow down the conversion of transient oligomers into fibrillar structures. Analysis by atomic force microscopy unveiled that the Aβ42 fibrils formed in the lag phase in presence of LT1 were significantly thinner than control samples, indicating that compound treatment alters the thickness of spontaneously formed amyloid fibrils (Fig. 60). Furthermore, analysis with denaturating FRAs indicated that LT1 treatment seems to decrease the stability of spontaneously formed fibrils, probably due to incorporation into fibrillar structures (Fig. 59). Finally, it was shown that LT1-aggregates are less seeding-competent structures (Fig. 62).

A hypothetical model for LT1's potential mechanism of action is illustrated in Figure 68. The spontaneous Aβ42 aggregation (middle, blue curve) results in a sigmoidal curve due to the nucleation-dependent mechanism. Starting from monomers, small oligomeric nuclei are formed that presumably contain the first structural β-sheet elements. Addition of free unbound monomers (left, dark blue circles) to these nuclei can not only occur at their end points, but also by secondary nucleation events at the surface of nuclei and small aggregate intermediates. Due to the numerous available binding sites from surface-catalyzed reactions the aggregation is exponentially accelerated leading to the fast formation of protofibrils and fibrillar structures. In contrast, the lag phase is delayed in presence of LT1 (middle, purple curve). Due to its bis-styrylbenzene structure LT1 is very planar and thus it is hypothesized that it covers a large area of Aβ42 aggregate intermediates upon binding (right). As a result, many surface-catalyzed reactions are impeded and free monomers can predominantly bind to the reactive ends of formed assemblies in elongation events. By this, the aggregation reaction is delayed and monomers are withheld until the substoichiometrically added compound has bound and a critical concentration of nuclei is reached. Then, the aggregation reaction enters the exponential

growth phase and fibrillar structures are formed. However, due to the bound compound that might be partially incorporated different type of aggregates are formed, comprised by LT1-fibrils with a changed conformation and altered characteristics. The LT1-fibrils are thinner and by impression also longer, less SDS-stable and they feature a reduced seeding activity, which is likely also due to a change in aggregate conformation. Finally, this hypothesis can also be transferred to seed-mediated Aβ42 aggregations as LT1 is presumed to likewise bind to the surface of pre-formed aggregate seeds in seeded reaction as to emerging aggregate assemblies in spontaneous reaction.

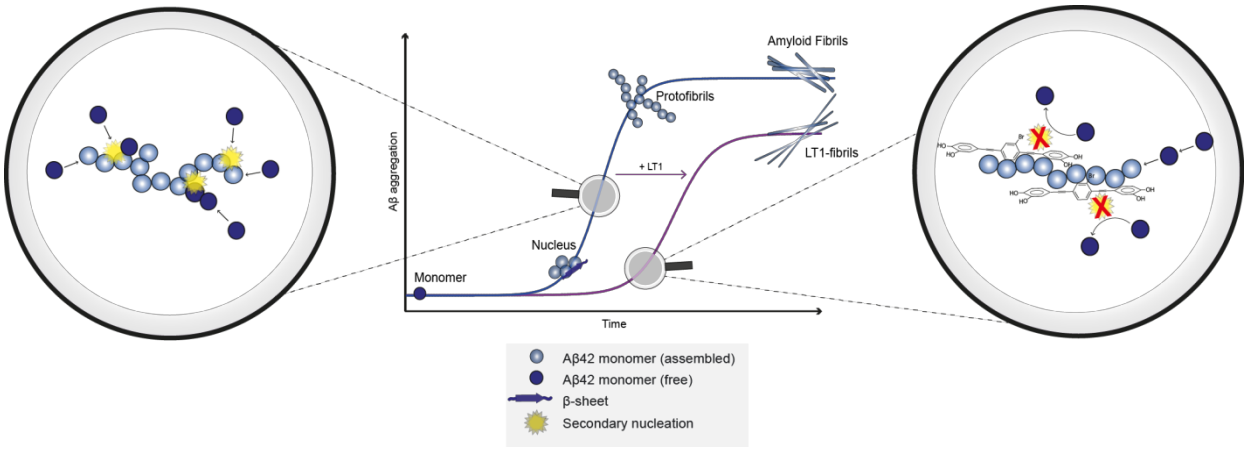

Figure 68 | Proposed mechanism of action of compound LT1 on spontaneous Aβ42 aggregation
Schematic model of a spontaneous Aβ42 aggregation reaction over time following a nucleation-dependent mechanism (middle). In compound-free reactions, many binding sites for free Aβ42 monomers are available on formed oligomeric nuclei (left). Particularly surface-catalyzed secondary nucleation events lead to a fast progress of the aggregation reaction until fibrillar structures are formed in the plateau phase. In presence of LT1 the surface of emerging nuclei is partially coverd by the planar compound and thereby secondary nucleation events occur less likely (right). As monomers rather bind to reactive ends of intermediate assemblies, the lag phase is delayed and another type of aggregates is formed.

In following experiments computational modeling could help to more precisely determine the molecular mechanism and the point of attack of LT1 in complex Aβ42 aggregation reactions that involve primary, secondary and elongation events. Using global fitting of quantitative kinetic data a molecular mechanism of Aβ42 aggregation reactions in the presence of LT1 could be postulated based on the comparison of integrated rate laws and experimental kinetic measurements[362]. Furthermore, thermodynamic measurements with Isothermal titration calorimetry (ITC) could deliver binding affinities, binding stoichiometry and enthalpy changes of LT1's interaction with Aβ42 assemblies and further also information about energy and entropy changes[363]. Circular dichroism measurements of Aβ assemblies formed in presence or absence of LT1 could deliver valuable information to better assess the impact of LT1 on secondary structure elements. Additionally, NMR experiments should help to elucidate the presumed conformational difference of LT1-treated Aβ42 aggregates in comparison to untreated fibrillar aggregates. Finally, *in vivo* experiments in suitable AD model organisms such as

C. elegans or *Drosophila* should help to assess if the compound LT1 with its aggregation delaying capacities also entails beneficial effects for the AD pathology.

7.

Material

7. Material

7.1 Biological material

7.1.1 Murine brain material

APPPS1 mouse brains were received from Josef Priller (Institut für Neuropathologie, Charité, Berlin) or kindly provided by Michael Willem (Ludwig-Maximilians-Universität, München). 5xFAD mouse brains were obtained from Thomas Willnow (MDC, Berlin). Samples from APP23 mice were kindly provided by Mathias Jucker (Deutsches Zentrum für Neurodegenerative Erkrankungen, Tübingen). Any available information can be found in the table below.

Charité, Berlin (Josef Priller)

Mouse ID	Strain	Gender	Genotype	Region	Age (month)
448	APP/PS1	M	APPS+/-	Hemisphere	22
449	APP/PS1	M	APPS+/-	Hemisphere	22
453	APP/PS1	M	APPS-/-	Hemisphere	22
455	APP/PS1	M	APPS-/-	Hemisphere	22
678	APP/PS1	M	APPS+/-	Hemisphere	18
723	APP/PS1	M	APPS-/-	Hemisphere	17

LMU, München (Michael Willem)

Mouse ID	Strain	Gender	Genotype	Region	Age (month)
844	APP/PS1	F	APPS-/-	Hemisphere	4
852	APP/PS1	F	APPS+/-	Hemisphere	4
5530	APP/PS1	M	APPS+/-	Hemisphere	6
5535	APP/PS1	M	APPS-/-	Hemisphere	6
5504	APP/PS1	F	APPS-/-	Hemisphere	9
400	APP/PS1	M	APPS+/-	Hemisphere	9

MDC, Berlin (Thomas Willnow)

Mouse ID	Strain	Gender	Genotype	Region	Age (month)
8951	5xFAD	F	C57Bl6/N	Cortex	1
8541	5xFAD	F	5xFAD x C57Bl6/N	Cortex	1
8857	5xFAD	F	C57Bl6/N	Cortex	2
8185	5xFAD	F	5xFAD x C57Bl6/N	Cortex	2
8710	5xFAD	F	C57Bl6/N	Cortex	5
7758	5xFAD	F	5xFAD x C57Bl6/N	Cortex	5

DZNE, Tübingen (Mathias Jucker)

Mouse ID	Strain	Gender	Volume / aliquot (µl)	Comment	Age (month)
14077	APP23	unknown	200	PBS homogenate	7
14078	APP23	unknown	200	PBS homogenate	7
Pool	APP23	unknown	50	Extract characterized *in vivo*	30
20686	APP23	unknown	Hemisphere	RIPA homogenization	27
20693	APP23	unknown	Hemisphere	RIPA homogenization	27

Table 9 | Information about used mouse brain material

7.1.2 Human brain material

Human patient and control brain material was obtained from Newcastle Brain Bank. Any available information is listed in Table 10.

Newcastle Brain Bank

#	Disease code	Age	Sex	Braak	ACATU	TRQ	Case ID
1	Alzheimer's Disease	71	F	/	2013056	2013,82	19960061
2	Alzheimer's Disease	71	M	5	2013056	2013,82	19960142
3	Alzheimer's Disease	79	F	/	2013056	2013,82	19970007
4	Alzheimer's Disease	80	F	/	2013056	2013,82	19970163
5	Alzheimer's Disease	68	M	5	2013056	2013,82	19980056
6	Alzheimer's Disease	78	M	4++	2013056	2013,82	19990291
7	Alzheimer's Disease	63	F	6	2013056	2013,82	20050083
8	Alzheimer's Disease	76	M	6	2013056	2013,82	20050086
9	Alzheimer's Disease	68	M	6	2013056	2013,82	20120530
10	Alzheimer's Disease	76	M	6	2013056	2013,82	20130325
11	Control	67	M	/	2013056	2013,82	19950025
12	Control	75	M	0	2013056	2013,82	19990275
13	Control	75	M	1	2013056	2013,82	20040091
14	Control	69	F	1	2013056	2013,82	20050053
15	Control	68	M	0	2013056	2013,82	20050087
16	Control	72	M	1	2013056	2013,82	20050102
17	Control	72	F	1	2013056	2013,82	20070049
18	Control	59	F	0	2013056	2013,82	20080005
19	Control	67	M	0	2013056	2013,82	20100742
20	Control	73	M	0	2013056	2013,82	20110891

Table 10 | Information about used human brain samples

Used abbreviations: ACATU (Application to the Committee for Approval of Tissue Use); TRQ (Tissue Request Number)

7.1.3 Human cerebrospinal fluid

Human cerebrospinal fluid (CSF) was kindly provided by PD Dr. Oliver Peters from Klinik für Psychiatrie und Psychotherapie (Charité, Berlin). In total, 36 CSF samples were analyzed comprising patients with mild cognitive impairment (MCI) and mild or moderate Alzheimer's disease diagnosis. Patients with a depressive episode or unknown etiology were used as controls as no liquor samples from healthy individuals were available. Briefly, liquor was extracted via lumbar puncture, aliquoted in polypropylene tubes and stored at -80°C without further centrifugation steps. Diagnosis after assessment of mental status as well as biomarker levels of analyzed patient samples can be found in Table 11. Numbers highlighted in red indicate striking values that suggest an AD diagnosis (Aβ42 <600 pg/ml; Aβ42/Aβ40 ratio <0.065 pg/ml; hTau >350 pg/ml).

#	Age	Diagnose	hTau (pg/ml)	Aβ42 (pg/ml)	Aβ40 (pg/ml)	Ratio Aβ40/Aβ42	Ratio tTau/Aβ42
5	75	Moderate AD, meningioma, remitted after surgery	655	208	3770	0,055	3,154
12	75	Depressive episode with cognitive deficits	154	856	9520	0,090	0,180
13	52	Depressive episode with cognitive deficits	84	625	6016	0,104	0,134
14	76	Mild cognitive impairment, neurodegenerative disorder	769	630	14230	0,044	1,221
15	42	Anxiety disorder without cognitive deficits	119	391	5452	0,072	0,305
18	80	Mild dementia, AD type; depressive episode	743	321	6667	0,048	2,315
19	74	Mild dementia, AD type	328	223	4136	0,054	1,471
20	68	Depressive episode with cognitive deficits	297	457	5890	0,078	0,650
21	61	Moderate AD	>1200	424	10077	0,042	2,830
23	61	Depressive episode with cognitive deficits	80	1452	10296	0,141	0,055
24	54	MCI, unknown etiology	194	1187	9630	0,123	0,163
25	67	Mild cognitive impairment (MCI), unknown etiology	156	1280	9940	0,129	0,122
26	61	Depressive episode with cognitive deficits, neurodegenerative disorder	175	537	6638	0,081	0,326
28	56	MCI, unknown etiology	303	575	7648	0,075	0,527
29	64	Depressive episode with cognitive deficits	219	185	3481	0,053	1,183
30	71	Mild dementia, AD type	559	166	3371	0,049	3,360
31	86	Depressive episode with cognitive deficits, neurodegenerative disorder	339	126	3572	0,035	2,681
32	84	Mild dementia, AD type; depressive episode	649	165	4963	0,033	3,939
33	78	Depressive episode with cognitive deficits, neurodegenerative disorder	412	294	6974	0,042	1,402
35	74	Moderate dementia, AD type	585	229	4699	0,049	2,556
35	67	Mild dementia, AD type	615	257	4650	0,055	2,392
36	54	Depressive episode with cognitive deficits	84	417	3959	0,105	0,201
37	83	Mild dementia, AD type	404	380	7810	0,049	1,064
38	54	Mild dementia, AD type; depressive episode	915	279	8046	0,035	3,285
52	76	Mild dementia, AD type	272	720	5297	0,136	0,378
51	73	Mild cognitive impairment, vascular etiology	735	252	3962	0,064	2,918
68	75	Mild cognitive impairment, vascular etiology	396	888	7636	0,116	0,446
69	65	Subjective memory complaints	530	990	8270	0,120	0,536
70	76	Mild cognitive impairment, unknown etiology	638	946	7937	0,119	0,675
71	88	Mild cognitive impairment, unknown etiology	650	1119	8527	0,131	0,581

72	79	Depressive episode with cognitive deficits, vascular encephalopathy	1024	343	7139	0,048	2,988
73	72	Mild cognitive impairment, unknown etiology	898	512	10424	0,049	1,755
75	70	Mild cognitive impairment, AD type	642	257	6408	0,040	2,495
76	71	Mild cognitive impairment, unknown etiology	205	745	5571	0,134	0,276
77	70	Mild cognitive impairment, unknown etiology	143	635	5048	0,126	0,226
78	79	Depressive episode with cognitive deficits	147	779	7495	0,104	0,189

Table 11 | Information about used human CSF samples
Used abbreviations: hTau (hyerphosphorylated Tau); tTau (total Tau)

7.1.4 Mammalian cell line

PC12	A rat cell line that was derived from a pheochromocytoma of the adrenal medulla. Upon treatment with nerve growth factor, PC12 cells stop proliferating and undergo terminal differentiation into a neuronal phenotype[276,277]
SH-EP	A subclone of a human neuroblastoma cell line and a widely used cellular model system[364]

Table 12 | Information about used cell lines

7.2 Chemicals and consumables

Chemical / Consumable	Supplier
Bovine Serum Albumin (BSA)	Sigma-Aldrich
cOmplete ™, EDTA-free Protease inhibitor cocktail tablets	Roche
Coomassie Brilliant Blue G-250M	Merck
Cycloheximid	Roth
Dimethylsulfoxide (DMSO)	Sigma-Aldrich
Dithiothreitol (DTT)	Serva
Dynabeads® Protein G (10003D)	Invitrogen
DynaMag™-96 Side Skirted Magnet (12027)	Life Technologies
Empore™ Sealing Tape Pads	3M™
Falcon™ 15 ml/50 ml Conical Centrifuge Tubes	BD Biosciences
Glutaraldehyde solution	Sigma-Aldrich
Glycerol	Merck
Glycine	Roth
HFIP (1,1,1,3,3,3-Hexafluor-2-propanol)	Sigma-Aldrich
K_2HPO_4	Roth
KH_2PO_4	Roth
Mica G250-2	PLANTO
Microplate 384-well Non-Binding Black (78190)	Greiner Bio-One
Microplate 96-well Non-Binding Transparent (651901)	Greiner Bio-One
Microplate 96-well black quartz (730.009B-QG)	Hellma
NaCl	Roth
Nitrocellulose Blotting Membrane Amersham™ Protran™ 0.1 µm NC 300 mm	GE Healthcare Life Sciences
Nitrocellulose Whatman™ Protran BA 85 0.45 µM	GE Healthcare Life Sciences
NaOH	Acros Organics
Novex® NativePAGE 4-16 % Bis-Tris Gel	Life Technologies
Novex® 20x NativePAGE Running Buffer	Life Technologies
Novex® 20x NativePAGE Running Buffer Additive	Life Technologies
Novex® NuPAGE4-12 % Bis-Tris Protein Gels	Life Technologies
Novex® 20x SDS-PAGE Running Buffer	Life Technologies
Pierce® Protein-Free Blocking Buffers	Pierce
Protein LoBind Tubes 0.5 / 1.5 / 2.0 / 5.0 ml	Eppendorf
Sodium Dodecyl Sulfate (SDS) Pellets	Roth
Thioflavin T	Sigma-Aldrich
Tris	Applichem
Triton™ X-100	Sigma-Aldrich
Trizma® base	Sigma-Aldrich
TWEEN® 20	Sigma-Aldrich
Ultra Micro cuvette (105.251-QS)	Helma
WesternBright™ Quantum	Advansta, Biozym
Whatman® Blotting Papers 0.8/1.0 mm	GE Healthcare Life Sciences
Whatman® OE 66 Membrane Filters (Cellulose acetate) 0.2 µm	GE Healthcare Life Sciences

7.3 Enzymes, proteins and markers

Enzymes	Supplier
Benzonase purity grade II	Merck
Proteinase K	NEB

Proteins	Supplier
Amyloid-beta 1-42 (Aβ42)	AnaSpec (#AS-20276), Bachem (#4014447)
Amyloid-beta 1-42 (Aβ42)	Peptide by laboratory of Dr. Volkmer-Engert (Institute for Medical Immunology, Charité, Berlin)
Amyloid-beta 1-42 peptide, 5-Carboxyfluorescein-labeled	AnaSpec
Amyloid-beta 1-42 peptide, 5-HiLyte™ Fluor 488-labeled	AnaSpec
Amyloid-beta 1-42 peptide, 5-TAMRA-labeled	Bachem
5-Carboxyfluorescein	Sigma-Aldrich
Albumin, bovine serum, FAM-labeled	Sigma-Aldrich; customized labeling by BioTez
Apoferritin from equine spleen, FAM-labeled	Sigma-Aldrich; customized labeling by BioTez
Carbonic Anhydrase, FAM-labeled	Sigma-Aldrich; customized labeling by BioTez
Ribonuclease A from bovine pancreas, FAM-labeled	Sigma-Aldrich; customized labeling by BioTez
Thyroglobulin from bovine thyroid, FAM-labeled	Sigma-Aldrich; customized labeling by BioTez

Markers	Supplier
NativeMark™ Unstained Protein Standard	Invitrogen
SeeBlue Plus2 Pre-stained Protein Standard	Thermo Fisher

7.4 Antibodies

Primary antibodies	Species	Dilution	Supplier
Mouse IgG1 Isotype control	Mouse	1:1000	Invitrogen
Purified Anti-β-Amyloid, 1-16 (6E10)	Mouse	1:1000	BioLegend
Purified Anti-β-Amyloid, 17-24 (4G8)	Mouse	1:1000	BioLegend
Purified Anti-β-Amyloid, 82E1	Mouse	1:1000	IBL
Purified Anti-β-Amyloid, 352	Mouse	1:1000	SynapticSystems (customized)
Anti-FITC (Fluorescein Isothiocyanate)	Mouse	1:50	Thermo Fisher

Secondary antibodies	Conjugate	Dilution	Supplier
Anti-Mouse IgG (Fc Specific)-Peroxidase	Peroxidase	1:2000	Sigma-Aldrich
Anti-Rabbit IgG (whole molecule)-Peroxidase	Peroxidase	1:2000	Sigma-Aldrich
12 nm Colloidal Gold AffiniPure Goat Anti-Mouse IgG	Gold	1:30	Dianova

7.5 Kits

Kits	Kits Supplier
Cell Proliferation Assay (MTT)	Promega
NativePAGE Novex® Bis-Tris gel-system	Invitrogen
Pierce™ BCA Protein Assay Kit	Thermo Fisher
SDS-PAGE Novex® Bis-Tris gel-system	Invitrogen
Western Bright™ Quantum	Biozym, Advansta

7.6 Buffers and media

Buffer	
Low salt buffer (LSB)	8.1 mM K_2HPO_4, 1.9 mM KH_2PO_4, 10 mM NaCl; pH 7.4 (adjusted with 85 % ortho-phosphoridc acid)
4x SDS loading buffer	200 mM Tris pH 6.8, 400 mM DTT, 8 % SDS, 40 % glycerol, bromophenol blue; 50 mM DTT (freshly added)
Electrophoresis buffer for SDS-PAGE	1x SDS-PAGE MES SDS running buffer
Electrophoresis buffer for NativePAGE:	
Light cathode buffer	1x NativePAGE running buffer
Dark cathode buffer	1x NativePAGE running buffer, 20x Cathode buffer additive
WetBlot transfer buffer (for SDS-PAGE)	25 mM Tris, 192 mM Glycine, 10 % Methanol
WetBlot transfer buffer (for NativePAGE)	25 mM Tris, 192 mM Glycine
Blocking buffer	3 % (w/v) skim milk powder in PBS-T
PBS	137 mM NaCl, 27 mM KCl, 100 mM Na_2HPO_4, 17.6 mM KH_2PO_4
PBS-Tween (PBS-T)	137 mM NaCl, 27 mM KCl, 100 mM Na_2HPO_4, 17.6 mM KH_2PO_4, 0.05 % (v/v) Tween-20
RIPA buffer	50 mM Tris, 150 mM NaCl, 0.1 % (v/v) SDS, 0.5 % (w/v) Sodium deoxycholat, 1 % (v/v) Triton, 0.25 U/µl Benzonase, 4 % v/v Complete protease inhibitor
RIPA wash buffer	50 mM Tris, 150 mM NaCl, 0.01 % (v/v) SDS, 0.05 % (w/v) Sodium deoxycholat, 0.1 % (v/v) Triton, 4 % v/v Complete protease inhibitor
Artificial CSF (ACSF)	124 mM NaCl, 2.5 mM KCl, 2.0 mM $MgSO_4$, 1.25 mM KH_2PO_4, 26 mM $NaHCO_3$, 10 mM Glucose, 4 mM Sucrose, 2.5 mM $CaCl_2$; pH 7.4
HEPES buffer	50 mM HEPES pH 7.5; 100 mM NaCl; 10 % Glycerin; 1 % NP40; 20 mM NaF; 1.5 mM $MgCl_2$; 1 mM EDTA; 0.25 U/µl Benzonase, Complete protease inhibitor

Cell culture supplies	Supplier
DMEM (31885-023)	Gibco
Fetal bovine serum (FBS)	Gibco
Fibronectin human plasma	Sigma-Aldrich
Fluorescence mounting medium	Dako
Hoechst 33342	Life Technologies
Horse Serum	Gibco
Poly-L-lysine solution	Sigma-Aldrich
RPMI 1640 Medium (1x) (31870-025)	Gibco
Trypsin	Gibco

7.7 Instruments and software

Instruments	
AFM, Nano Wizard II	JPK Instruments
CM100 transmission electron microscope	Philips
Cellomics™ ArrayScan VTI HCS	Thermo Fisher
Confocal microscope TCS SP5	Leica
Homogenisator Homogen plus	Schütt
Imaging System LAS-3000	Fujifilm
Infinite M200 / M1000 / M1000Pro / Spark microplate reader	Tecan
Magnetic Particle Concentrator MPC®-1	DynaL
Spectrophotometer SPECORD 250	Analytic Jena
Speedvacuum concentrator RVC 2-25 Cdplus	Christ, Germany
Sonic Dismembrator, Ultrasonic Processor	Thermo Fisher
Ultrasonic bath Sonorex TK52	Bandelin

Software	
AIDA	Free ware by Erik Hom
Array Scan VTI	Thermo Fisher
ChemDraw	Perkin Elmer
EndNote	Thomson Reuters
GraphPad Prism 5/7	GraphPad software
iControl	Tecan
Illustrator	Adobe
ImageJ	Wayne Rasband
JPK Data Processing	JPK Instruments AG
Microsoft Office 2007	Microsoft
Photoshop	Adobe

8.

Methods

8. Methods

8.1 Compound library

8.1.1 Synthesis of K114 derivatives

Synthesis of K114 and derivatives was carried out by ChiroBlock, Wolfen. All chemicals were purchased from commercial suppliers and used without further purification. The reaction was monitored by thin-layer chromatography on silica gel 60 F254 coated aluminium sheets (Merck KgaA). For preparative column chromatography silica gel 60, 0.063-0.2 nm (Fisher Scientific, #10723203) was used. As eluent dichloromethane (CVM, #101160), methanol (Fisher Scientific, #M/3950/PC25), ethyl acetate (Overlack, #813379), petroleum ether 40-60°C (Fisher Scientific, #180210250) or tert-butyl methyl ether (TBME, Carl Roth, #6746.3) or mixtures thereof were applied. NMR spectra were recorded on Bruker Avance 300 MHz and Bruker BioSpin 500 MHz spectrometer. Chemical shifts are reported in parts per million downfield from the internal standard tetramethylsilane (0.0 ppm) for 1H-NMR and 13C-NMR spectra. Samples were measured in d6-DMSO or CDCl3. The liquid chromatography (LC) measurements with or without mass determination were carried out on a LCMS2010EV LC system from Shimadzu coupled with an LC-10AD or a Shimadzu LC system with a LC-20AD double micro plunger system. For the analytical separation reverse phase columns, PackPro C18 (150 x 4.6 mm ID, 12 nm, S-3 µm) and Triart C18 (100 x 3.0 mm ID, 12 nm, S-5µm) from YMC were used (acetonitrile:water 8:2; 0.2 ml/min). Gas chromatography measurements were realized on CMS-QP 2010S or LCMS 2010 EV systems from Shimadzu. All CHN data were collected at HEKAtech GmbH, Wegberg, Germany. The following abbreviations are used in the subsequent description of compound synthesis and compound characterization: s: singulet; d: duplet; dd: duplet from duplet; m: multiplet; bs: broad singulet; bd: broad duplet; pd: pseudo duplet; pt: pseudo triplet; pq: pseudo quadruplet.

8.1.2 Characterization of K114 derivatives

2-Bromo-1,4-bis(bromomethyl)benzene (11)

To a solution of 2-bromo-1,4-dimethylbenzene (**12**, 85 g, 63.433 ml, 0.459 mmol) in (trifluoromethyl) benzene (1500 ml) *N*-bromosuccinimide (171,681 g, 0.964 mmol) and 2,2'-Azobis(2-methylpropio-nitrile) (754 mg, 4.6 mmol) were added. The mixture was heated under reflux for 2 h. Insoluble material was removed by filtration and the filtrate was evaporated. The residue was recrystallized from n-hexen (510 ml) to obtain **11** as off-white solid.

Yield: 74.0 g, 47 %; $C_8H_7Br_3$, M = 342.85 g/mol; ^{1}H-NMR (500 MHz, $CDCl_3$) ppm: 4.38 (s, 2H), 4.55 (s, 2H), 7.29 (dd, J = 7.9 Hz, J = 1.8 Hz. 1H), 7.40 (d, J = 7.9 Hz, 1H), 7.58 (d, J = 1.7 Hz, 1H); GC-MS 342 *m/z* $[M-H]^+$; Purity: 95 %

Tetraethyl (2-bromo-1,4-phenylene)bis(methylene)diphosphonate (10)

Compound **11** (50 g, 146 mmol) was combined with triethyl phosphite (48.46 g, 50.22 ml, 0.291 mmol) and heated to 160°C for 4 h. Volatile matters were removed by evaporation. The remaining residue was purified by silica gel chromatography using dichloromethane and methanol (95:5) as eluent to obtain **10** as orange oil.

Yield: 62.2 g, 84 %; $C_{16}H_{27}BrO_6P_2$, M = 457.23 g/mol, ^{1}H-NMR (500 MHz, $CDCl_3$) ppm: 1.15 – 1.20 (dt, J = 7.1 Hz, J = 1.3 Hz, 11H), 1.24 – 1.31 (m, 1H), 3.02 (d, J = 21.3 Hz, 2H), 3.30 (d, J = 21.4 Hz, 2H), 3.93 – 4.00 (m, 8 H), 7.15 (d, J = 7.9, Hz, 1H), 7.34 (dd, J = 2.6 Hz, J = 7.9 Hz), 7.44 (bs, 1H); GC-MS 377 *m/z* $[M-Br-H]^+$; Purity: 90 %

4,4'-(1E,1'E)-2,2'-(2-Bromo-1,4-phenylene)bis(ethene-2,1-diyl)bis(methoxybenzene) (6)

Compound **10** (30 g, 66 mmol) was solved in dry DMF (390 ml, 370.5 g, 5.1 mol). The solution was cooled to 12°C with a water bath. First, 4-methoxybenzaldehyde (17.87 g, 131 mmol) was added followed by potassium tert-butylate (29.449 g, 262 mmol). The mixture was stirred overnight at room temperature. The resulting suspension was spilled in ice water (1100 ml), the crude product was filtered off. The residue was 2-times purified by silica gel chromatography first using dichloromethane and ethyl acetate (100 to 20 %) and then using dichloromethane and petroleum ether (20 to 50 %) to obtain **6**.

Yield: 37.8 g, 38 %; $C_{24}H_{21}BrO_2$, M = 421.33 g/mol; ^{1}H-NMR (500 MHz, $CDCl_3$) ppm: 3.76 (s, 6H), 6.78 – 6.85 (m, 5H), 6.93 (d, J = 16.2 Hz, 1H), 6.98 (d, J = 16.3 Hz, 1H), 7.25 (d, J = 16.2 Hz, 1H), 7.32 (d, J = 8.2 Hz, 1H), 7.37 (d, J = 8.3 Hz, 2H), 7.42 (d, J = 8.4 Hz, 2H), 7.54 (d, J = 8.2 Hz, 1H), 7.62 (s, 1H), LC-MS 421 *m/z* (pos. ion); Purity: 95 %.

4,4'-(1E,1'E)-2,2'-(2-Bromo-1,4-phenylene)bis(ethene-2,1-diyl)diphenol (K114)

A mixture of compound **6** (500 mg, 1.2 mmol) and pyridine hydrochloride (10 g, 86.5 mmol) was heated to 160°C in an oil bath for 22 h. The molten reaction mixture was left to cool and combined with 1 molar HCl. The aqueous solution was 2-times extracted with ethyl acetate. The organic layers were combined, dried over anhydrous sodium sulfate and the solvent was removed. The residue was purified twice by silica gel chromatography using first dichloromethane and ethyl acetate (1:1) and

petroleum ether combined with TMBE (20 to 100 % within 30 min) for the second purification the CombiFlash device (Teledyne Isco, USA) was used to obtain **K114**.

Yield: 140 mg, 29 %; $C_{22}H_{17}BrO_2$, M = 393.27 g/mol; ^{1}H-NMR (300 MHz, d_6-DMSO) ppm: 6.73 (d, J = 8.6 Hz, 2H), 6.75 (d, J = 8.6 Hz, 2H), 6,95 (d, J = 16.4 Hz, 2H), 7.10 – 7.14 (m, 2H) 7.19 (d, J = 16.4 Hz, 2H), 7.39 (d, J = 8.6 Hz, 4H), 7.51 (bd, J = 8.2 Hz, 1H), 7.73 (d, J = 8.4 Hz, 1H), 7.75 (bd, J = 1.6 Hz, 1H), 9.61 (s, 1H), 9.65 (s, 1H); ^{13}C-NMR (75 MHz, d_6-DMSO) ppm: 115.48, 115.61, 122.52, 123.06, 123.29, 125.26, 126.33, 127.65, 127.73, 128.00, 128.07, 129.61, 129.93, 131.09, 134.69, 138.24; LC-MS 391 *m/z* (neg. ion), 395 *m/z* (pos. ion); Purity: 95.0 %; CHN: calc. C 67.19, H 4.36; anal. C 67.43, H 4.53.

4,4'-(2,2'-(2-Bromo-1,4-phenylene)bis(ethane-2,1-diyl))bis(methoxybenzene) (5a)

Compound **6** (421 mg, 1.0 mmol) was dissolved in trifluoroacetic acid (26.64 g, 18 ml, 233.6 mmol) and treated with triethylsilane (6.55 g, 9.1 ml, 56.3 mmol) under N_2 atmosphere. The reaction solution was heated to 60°C for 4 h. The mixture was evaporated and the crude product was purified by silica gel chromatography using dichloromethane and ethyl acetate (1:1) to obtain **5a**.

Yield: 280 mg, 65 %; $C_{24}H_{25}BrO_2$, M = 425.36 g/mol; ^{1}H-NMR (500 MHz, $CDCl_3$) ppm: 2.84 – 2.87 (m, 6H), 2.96 – 2.99 (m, 2H), 3.81 (pd, 6H), 6.85 (d, J = 8.7 Hz, 2H), 6.91 (d, J = 8.7 Hz, 2H), 7.00 (dd, J = 1.7 Hz, J = 7.8 Hz, 1H), 7.05 (d, J = 7.8 Hz, 1H), 7.09 (d, J = 8.6 Hz, 2H), 7.15 (d, J = 8.5 Hz, 2H), 7.4 (d, J = 1.1 Hz, 1H); Purity: 95.0 % (NMR).

4,4'-(2,2'-(2-Bromo-1,4-phenylene)bis(ethane-2,1-diyl))diphenol (5)

Compound **5a** (250 mg, 0.6 mmol) was dissolved in dry DCM (66.5 g, 50 ml, 783.0 mmol) and cooled down to -10°C under N_2 atmosphere. To this solution boron tribromide in dichloromethane (1 M, 10.6 g, 4.0 ml, 42.3 mmol) was added dropwise. The reaction solution was stirred and allowed to warm to room temperature within 5.5 h. The reaction solution was poured in saturated sodium bicarbonate solution. The aqueous solution was extracted with an additional amount of dichloro-methane (80 ml). The organic layer was dried over anhydrous sodium sulfate and the solvent removed. The residue was purified by silica gel chromatography using ethyl acetate and petroleum ether (1:2) to obtain **5**.

Yield: 190 mg, 81 %; $C_{22}H_{21}BrO_2$, M = 397.30 g/mol; ^{1}H-NMR (500 MHz, $CDCl_3$) ppm: 2.77 – 2.80 (m, 6H), 2.90 – 2.93 (m, 2H), 4.59 (s, 2H), 6.71 – 6.73 (m, Hz, 4H), 6.93 (dd, J = 1.5 Hz, J = 7.8 Hz, 1H), 6.98 – 6.99 (m, 3H), 7.03 (d, J = 8.4 Hz, 1H) , 7.33 (d, J = 1.5 Hz, 1H); ^{13}C-NMR (75 MHz, d_6-DMSO) ppm: 34.71, 35.92, 36.32, 37.46, 114.84, 114.93, 123.31, 127.74, 129.01, 129.9, 130.29, 131.08, 131.08, 131.18, 132.04,137.66, 141.81, 155.26, 155.35; LC-MS 397 *m/z* (neg. ion); Purity: 95.0 %; CHN: calc. C 66.51, H 5.33; anal. C 66.26, H 5.48.

4,4‘-(1E,1’E)-2,2‘-(2-(Trifluoromethyl)-1,4-phenylene)bis(ethene-2,1-diyl)bis(methoxybenzene) (8a)

Compound **6** (2.0 g, 4.7 mmol), copper (I) iodide (1.81 g 9.5 mmol) and sodium trifluoroacetate (3.23 g 23.7 mmol) were admit with vacuum for 30 min and then dissolved in dry DMF (38.0 g, 40 ml, 519.8 mmol). The mixture was stirred 1 h at 150°C. The reaction solution was diluted with dichloromethane und filtrated over celite. The filtrate was evaporated and the crude product was purified by silica gel chromatography using dichloromethane and petroleum ether (1:1). The product was resuspended in ethyl acetate (10 ml) and sucked off to obtain **8a**.

Yield: 930 mg, 48 %; $C_{25}H_{21}F_3O_2$, M = 410.43 g/mol; ^{1}H-NMR (500 MHz, $CDCl_3$) ppm: 3.77 (s, 6H), 6.83 – 6.85 (m, 4H), 6.90 (d, J = 16.3 Hz, 1H), 6.99 (d, J = 16.1 Hz. 1H), 7.04 (d, J = 16.3 Hz, 1H), 7.25 (dd, J = 16.0 Hz, J = 2.0 Hz, 1H), 7.40 (d, J = 8.7 Hz, 2H), 7.40 (d, J = 8.7 Hz, 2H), 7.54 (bd, J = 8.2 Hz, 1H), 7.67 – 7.69(m, 2H); GC-MS 410 *m/z* $[M]^+$; Purity: 95.0 %.

4,4‘-(1E,1’E)-2,2‘-(2-(Trifluoromethyl)-1,4-phenylene)bis(ethene-2,1-diyl)diphenol (8)

A mixture of **8a** (300 mg, 0.73 mmol) and pyridine hydrochloride (10 g, 86.5 mmol) was heated to 165°C in an oil bath for 7 h. The molten mass was left to cool and combined with 1 molar HCl. The aqueous solution was 2-times extracted with ethyl acetate. The organic layers were combined, dried over anhydrous sodium sulfate and the solvent was removed. The residue was purified by silica gel chromatography using TBME and petroleum ether (1:1) to obtain **8**. The final product was re-suspended in dichloromethane and anew sucked off and washed with dichloromethane.

Yield: 130 mg, 47 %; $C_{23}H_{17}F_3O_2$, M = 382.38 g/mol; ^{1}H-NMR (500 MHz, d6-DMSO) ppm: 6.74 (d, J = 8.6 Hz, 2H), 6.76 (d, J = 8.5 Hz, 2H), 7.07 (d, J = 16.5 Hz, 2H), 7.24 (d, J = 16.0 Hz , 1H), 7.26 (d, J = 16.4 Hz, 1H), 7.38 (d, J = 8.5 Hz, 1H), 7.42 (d, J = 8.5 Hz, 2H), 7.78 (s, 1H), 7.79 (d, J = 9.1 Hz, 1H), 7.90 (d, J = 8.2 Hz, 1H), 9.61 (s, 1H), 9.68 (s, 1H); ^{13}C-NMR (125,76 MHz, d6-DMSO) ppm: 115.64, 115.80, 119.34, 123.45, 123.54, 124.62 (q, CF3, 1J = 276 Hz), 125.82 (q, CCF3, 2J = 29 Hz) 127.00, 127.61, 127.82, 128.20, 128.30, 129.25, 129.99, 132.34,134.06, 136.64, 157.71, 158.03; LC-MS 381 *m/z* (neg. ion); Purity: 95.0 %; CHN: calc. C 72.24, H 4.48; anal. C 72.45, H 4.45

4,4‘-(1E,1’E)-2,2‘-(2-tert-butyl-1,4-Phenylene)bis(ethene-2,1-diyl)bis(methoxybenzene) (9a)

To a solution of compound **6** (1.0 g, 2.4 mmol) in THF (17.6 g, 20 ml 244.3 mmol) 1,3-dicyclohexylimidazolium tetrafluoroborate salt (76 mg, 0.24 mmol) and nickel(II) chloride (39 mg, 0.24 mmol) were added under dry conditions and N_2 atmosphere. The reaction mixture was cooled to -10°C and a 1 molar *tert*-butylmagnesium chloride solution in THF (1 M, 4.75 ml, 4.3 mmol) was added dropwise within 5 min. The reaction was carried out for 90 min at -10°C under stirring and 18 h at 4°C. The reaction was quenched by adding saturated NH_4Cl solution (50 ml). The aqueous layer was 2-

times extracted with ethyl acetate. The extracts were combined, dried over anhydrous sodium sulfate and evaporated. The residue was purified by silica gel chromatography via Combiflash device (Teledyne Isco, USA) using petroleum ether with TMBE (10 to 100 %) to obtain the crude product. **9a** was recrystallized from TMBE, the solid was sucked off and washed finally with petroleum ether.

Yield: 50 mg, 5 %; $C_{28}H_{30}O_2$, M = 398.54 g/mol; ^{1}H-NMR (500 MHz, $CDCl_3$) ppm: 1.53 (s, 9H), 3.86 (s, 3H), 3.87 (s, 3H), 6.80 (d, J = 15.9, Hz, 1H), 6.94 (pt, J = 8.7 Hz, 4H), 7.02 (d, J = 16.4, Hz, 1H), 7.10 (d, J = 16.3, Hz, 1H), 7.41 (bd, J = 8.1 Hz, 1H), 7.49 (pt, J = 8.8 Hz, 4H), 7.52 (d, J = 1.2 Hz, 1H), 7.54 (d, J = 8.0 Hz, 1H), 7.64 (d, J = 15.9 Hz, 1H); LC-MS 399 *m/z* (pos. ion).; Purity: 90.0 %.

4,4'-(1E,1'E)-2,2'-(2-tert-butyl-1,4-Phenylene)bis(ethene-2,1-diyl)diphenol (9)

A mixture of compound **9a** (190 mg, 0.48 mmol) and pyridine hydrochloride (10 g, 86.5 mmol) was heated to 165°C in an oil bath for 4 h. The molten reaction mixture was left to cool and combined with 1 molar HCl. The aqueous solution was 2-times extracted with ethyl acetate (50 ml).The organic layers were combined, dried over anhydrous sodium sulfate and the solvent was removed. The residue was purified by silica gel chromatography using a mixture of petroleum ether and TMBE (1:1) to obtain the crude product. This residue was purified further via Combiflash device (Teledyne Isco, USA) using petroleum ether with TMBE (20 to 100 %) to obtain **9**.

Yield: 90 mg, 46 %; $C_{26}H_{26}O_2$, M = 370.48 g/mol; ^{1}H-NMR (300 MHz, d_6-DMSO) ppm: 1.40 (s, 9H), 6.71 – 6.77 (m, 5H), 6.98 (d, J = 16.1 Hz, 1H), 7.07 (d, J = 16.4 Hz, 1H), 7.35 – 7.40 (m, 5H), 7.42 – 7.47 (m, 3H), 9.50 (s, 2H); ^{13}C-NMR (75 MHz, d_6-DMSO) ppm: 31.18, 71.95, 115.42, 115.53, 123.10, 124.24, 125.27, 136.08, 127.60, 127.80, 128.13, 128.42, 128.47, 128.71, 135.49, 135.98, 146.63, 157.10; LC-MS 369 *m/z* (neg. ion.); Purity: 90.0 %; CHN: calc. C 84.29, H 7.07; anal. C 84.04, H 7.08.

2,2'-(4,4'-(1E,1'E)-2,2'-(2-Bromo-1,4-phenylene)bis(ethene-2,1-diyl)bis(4,1- phenylene))bis(oxy)diacetic acid (7)

K114 (1.1 g, 2.8 mmol) was dissolved in absolute ethanol (79.0 g, 100 ml, 1.7 mol). To this solution bromoacetic acid (5.44 g, 2.82 ml, 39.2 mmol) and potassium hydroxide (2.83 g, 50.3 mmol) were added. The mixture was stirred under reflux for 5.3 h. The reaction mixture was left to cool and combined with 1 molar HCl (100 ml). The aqueous solution was 2-times extracted with ethyl acetate (100 ml, 50 ml).The organic layers were combined, dried over anhydrous sodium sulfate and the solvent was removed until the yellow product started to precipitate. The crude product was sucked off and re-crystallized from ethyl acetate to obtain **7**.

Yield: 550 mg, 39 %; $C_{26}H_{21}BrO_6$, M = 509.35 g/mol; ^{1}H-NMR (300 MHz, d_6-DMSO) ppm: 4.66 (s, 2H), 4.67 (s, 2H), 6.90 (pt, J = 8.6 Hz , 4H), 7.05 (d, J = 16.4, Hz, 1H), 7.21 (s, Hz, 2H), 7.26 (d, J = 16.4, Hz,

1H), 7.50 (d, J = 8.7 Hz, 4H), 7.56 (bd, J = 8.0 Hz, 1H) 7.77 (d, J = 8.4 Hz, 1H), 7.80 (bs, 1H), 12.99 (s, 2H); ^{13}C-NMR (75 MHz, d_6-DMSO) ppm: 64.36, 114.64, 114.75, 123.42, 123.81, 124.33, 125.45, 126.54, 127.84, 127.92, 129.23, 129.69, 129.79, 130.14, 130.73, 134.76, 138.26, 157.57, 157.75, 169.96, 169.99; LC-MS 509 *m/z* (neg. ion); Purity: 95.0 %; CHN: calc. C 61.31, H 4.16; anal. C 61.18, H 4.18.

4,4'-(1E,1'E)-2,2'-(2-Bromo-1,4-phenylene)bis(ethene-2,1-diyl)bis(1,2-dimethoxybenzene) (1a)

Compound **10** (5 g, 10.9 mmol) was solved in dry DMF (61.75 g, 65 ml, 844.7 mmol) under N_2 atmosphere. 3,4-Dimethoxybenzaldehyde (3.63 g, 21.9 mmol) and potassium tert-butylate (4.91 g, 43.7 mmol) were added and the reaction mixture was stirred for 20 h at room temperature. The reaction was quenched with ice water (120 ml), the precipitated crude product was sucked off and dried. The residue was purified by silica gel chromatography using dichloromethane to obtain **1a**. The final product was resuspended in ethyl acetate and filtered off.

Yield: 3.5 g, 47 %; $C_{26}H_{22}BrO_4$, M = 481.38 g/mol; ^{1}H-NMR (500 MHz, $CDCl_3$) ppm: 3.83 (s, 3H), 3.84 (s, 3H), 3.78 (s, 3H), 3.88 (s, 3H), 6.79 – 6.83 (m, 3H), 6.94 (d, J = 16.2 Hz, 1H), 6.95 – 7.04 (m, 5H), 7.25 (d, J = 16.2 Hz, 1H), 7.34 (dd, J = 8.2 Hz, J = 1.7 Hz, 1H), 7.56 (d, J = 8.2 Hz, 1H), 7.64 (d, J = 1.2 Hz, 1H); LC-MS 482 *m/z* (pos. ion); Purity: 95.0 %.

4,4'-(1E,1'E)-2,2'-(2-Bromo-1,4-phenylene)bis(ethene-2,1-diyl)dibenzene-1,2-diol (1)

Compound **1a** (1.1 g, 2.3 mmol) was dissolved in dry dichloromethane (66.5 g, 50 ml, 783.0 mmol) under N_2 atmosphere and cooled to -65°C. To this solution boron tribromide (5.7 g, 4.0 ml, 22.9 mmol) was added dropwise. The reaction solution was stirred for further 6 h at -65°C and was then quenched with saturated ammonia chloride solution (200 ml). The aqueous solution was extracted with ethyl acetate (100 ml). The organic layer was dried over anhydrous sodium sulfate and the solvent was removed. The residue was purified by silica gel chromatography using petroleum ether with TMBE (50 to 100 %) to obtain **1**.

Yield: 320 mg, 33 %; $C_{22}H_{17}BrO_4$, M = 425.27 g/mol; ^{1}H-NMR (500 MHz, d_6-DMSO) ppm: 6.70 (qt J = 9.4 Hz, 2H), 6.81 – 6.86 (m, 3H), 6.97 (d,d J = 14.2 Hz, J = 1.6 Hz, 2H), 7.06 (s,1H), 7.07 (s, 1H), 7.11 (d, J = 16.3 Hz, 1H), 7.51 (bd, J = 8.2 Hz, 1H), 7.73 (d, J = 8.4 Hz, 1H), 7.75 (bs 1H), 8.94 (s, 1H), 9.04 (s, 1H), 9.14 (qd, 2H); ^{13}C-NMR (75 MHz, d_6-DMSO) ppm: 112.87, 113.37, 115.59, 115.70, 118.79, 119.16, 122.31, 122.94, 123.28, 125.26, 126.22, 128.16, 128.28, 129.94, 129.98, 131.33, 134.53, 138.18, 145.30, 145.44, 145.84, 146.11; LC-MS 423 *m/z* (neg. ion); Purity: 95.0 %; CHN: calc. C 62.13, H 4.03; anal. C 62.17, H 4.49.

1,4-Bis(3,4-dimethoxystyryl)benzene (4a)

Tetraethyl 1,4-phenylenebis(methylene)diphosphonate (**13**, 2.5 g, 6.6 mmol) was dissolved in dry DMF (57.0 g, 60.0 ml, 779.7 mmol) under N_2 atmosphere. 3,4-Dimethoxybenzaldehyde (2.2 g, 13.2 mmol) and potassium tert-butylate (2.97 g, 26.4 mmol) were added and the reaction mixture was stirred at room temperature for 18 h. The reaction solution was poured in ice water (120 ml). The precipitated product was filtered off, washed with cooled water and dried to obtain **4a**.

Yield: 2.16 g, 73 %; $C_{26}H_{26}O_4$, M = 402.48 g/mol; ^{1}H-NMR (500 MHz, $CDCl_3$) ppm: 3.88 (s, 6H), 3.92 (s, 6H), 6.84 (d, J = 8.2 Hz, 2H), 6.94 (d, J = 16.3 Hz, 2H), 7.02 – 7.06 (m, 6H), 7.46 (s, 4H); Purity: 90.0 % (NMR).

4,4‘-(1E,1’E)-2,2‘-(1,4-Phenylene)bis(ethene-2,1-diyl)dibenzene-1,2-diol (4)

A mixture of **4a** (1.5 g, 3.7 mmol) and pyridine hydrochloride (30 g, 259.6 mmol) was heated to 175°C in an oil bath and stirred for 4 h. The molten reaction mixture was left to cool and combined with 1 molar HCl (250 ml). The aqueous solution was 2-times extracted with ethyl acetate (250 ml, 50 ml). The organic layers were combined, dried over anhydrous sodium sulfate and the solvent was removed to a residual volume of 20 ml. The precipitated crude product was sucked off and further purified via Combiflash device (Teledyne Isco, USA) using petroleum ether with TMBE (50 to 100 %) to obtain **4**. **4** was finally resuspended in dichloromethane and anew filtered off.

Yield: 650 mg, 51 %; $C_{22}H_{18}O_4$, M = 346.38 g/mol; ^{1}H-NMR (500 MHz, d_6-DMSO) ppm: 6.68 (d, J = 8.1 Hz, 2H), 6.82 (dd, J = 8.2 Hz, J = 1.5 Hz, 2H), 6.86 (d, J = 16.4 Hz, 2H), 6.95 (d, J = 1.5 Hz, 2H), 7.02 (d, J = 16.3 Hz, 2H), 7.46 (s, 4H), 8.89 (s, 2H), 9.06 (s, 2H); ^{13}C-NMR (75 MHz, d_6-DMSO) ppm: 113.15, 115.59, 118.47, 124.59, 126.22, 128.26, 128.63, 136.10, 145.29, 145.47; LC-MS 347 *m/z* (pos. ion); Purity: 95.0 %; CHN: calc. C 76.29, H 5.24; anal. C 76.46, H 5.35.

5,5‘-(1E,1’E)-2,2‘-(2-Bromo-1,4-phenylene)bis(ethene-2,1-diyl)bis(4-fluoro-1,2-dimethoxybenzene) (2a)

Compound **10** (2.0 g, 4.4 mmol) was solved in dry DMF (38.0 g, 40.0 ml, 519.8 mmol) under N_2 atmosphere. 2-Fluoro-4,5-dihydroxybenzaldehyde (1.61 g, 8.7 mmol) and potassium tert-butylate were added and the reaction mixture was stirred at room temperature for 22 h. The reaction solution was poured in ice water (40 ml). The precipitated product was filtered off, washed with cooled water and dried. The crude product was purified by silica gel chromatography using dichloromethane to obtain **2a**.

Yield: 990 mg, 44 %; $C_{26}H_{23}BrF_2O_4$, M = 517.36 g/mol ; ^{1}H-NMR (500 MHz, d_6-DMSO) ppm: 3.86 (bs, 6H), 3.89 (s, 3H), 3.91 (s, 3H), (d, J = 11.7 Hz, 2H), 6.90 (d, J = 16.4 Hz, 1H), 6.99 (d, 7.0 = Hz, 1H), 7.06

(d, J = 7.1 Hz, 1H), 7.16 (d, J = 16.0 Hz, 1H), 7.19 (d, J = 16.1 Hz, 1H), 7.33 (d, J = 16.4 Hz, 1H), 7.42 (bd, J = 7.9 Hz, 1H), 7.64 (d, J = 8.2 Hz, 1H), 7.70 (d, J = 0.9 Hz, 1H); Purity: 95.0 % (NMR).

5,5'-(1E,1'E)-2,2'-(2-Bromo-1,4-phenylene)bis(ethene-2,1-diyl)bis(4-fluorobenzene-1,2-diol) (2)

A mixture of **2a** (1.1 g, 2.1 mmol) and pyridine hydrochloride (32 g, 276.9 mmol) was heated to 175°C in an oil bath for 4 h. The reaction was quenched with 1 molar HCl (200 ml). The aqueous solution was 2-times extracted with ethyl acetate (100 ml, 50 ml). The organic layers were combined, washed with Brine (50 ml), dried over anhydrous sodium sulfate and evaporated. The obtained solid was dissolved in ethyl acetate (2 ml) and precipitated by adding dichloromethane (15 ml), **2** was sucked off and 2-times washed with dichloromethane.

Yield: 57 mg, 58 %; $C_{22}H_{15}BrF_2O_4$, M = 461.25 g/mol; ^{1}H-NMR (500 MHz, d_6-DMSO) ppm: 6.53 – 6.57 (m, 2H), 6.92 (d, J = 16.4 Hz, 1H), 6.99 – 7.02 (pq, 2H) 7.07- 7.17 (m, 3H), 7.54 (bd, J = 8.3 Hz, 1H), 7.75 (d, J = 8.4 Hz, 1H), 7.78 (bs, 1H), 9.85 (s, 1H), 9.08 (s, 1H), 9.67 (s, 2H); ^{13}C-NMR (75 MHz, d_6-DMSO) ppm: 103.48 (d, J_{C-F} = 25.8 Hz), 103.68 (d, J_{C-F} = 25.8 Hz), 112.83 (pt, J_{C-F} = 4.8 Hz), 114.56 (d, J_{C-F} = 8.7 Hz), 114.73 (d, J_{C-F} = 8.9 Hz), 122.56, 123.94, 124.11, 125.26 (d, J_{C-F} = 5.6 Hz), 125.74 (d, J_{C-F} = 4.8 Hz), 125.88, 126.89, 130.78, 135.30, 138.75, 142.54 (d, J_{C-F} = 6.6 Hz),147.28 (d, J_{C-F} = 14.4 Hz), 147.44 (d, J_{C-F} = 14.5 Hz), 153.96 (d, J_{C-F} = 238.8 Hz), 154.04 (d, J_{C-F} = 238.9 Hz); LC-MS 459 *m/z* (neg. ion); Purity: 95.0 %; CHN: calc. C 57.29, H 3.28; anal. C 57.41, H 3.31.

2,5-Bis(3,4-dimethoxystyryl)-4'-methoxybiphenyl (3a)

Compound **1** (1 g, 2.1 mmol) was dissolved in a degassed mixture of dioxin (41.2 g, 40 ml, 467.6 mmol) and water (4 ml) under N_2 atmosphere. 4-Methoxyphenylboronic acid (947 mg, 6.2 mmol) and cesium carbonate (1.35 g, 4.2 mmol) were added and the batch was anew degassed.

Tetrakis[triphenylphosphine]palladium(0) (480 mg, 415.5 mmol) was attached and the mixture was stirred for 2 h at 100°C. The reaction was quenched with saturated ammonia chloride solution (60 ml). The aqueous solution was extracted 2-times with ethyl acetate (60 ml, 50 ml). The organic layers were combined and dried over anhydrous sodium sulfate and evaporated. The residue was purified by silica gel chromatography using petroleum ether with dichloromethane (2:8) to obtain the crude product. **3a** was obtained after re-suspension (3 ml) and washing with ethyl acetate (1 ml).

Yield: 980 mg, 93 %; $C_{33}H_{32}O_5$, M = 508.60 g/mol; ^{1}H-NMR (500 MHz, $CDCl_3$) ppm: 3.79 (s, 3H), 3.80 (s, 3H), 3.81 (s, 3H), 3.84 (s, 3H), 3.88 (s, 3H), 6.75 (d, J = 8.3 Hz, 1H), 6.80 (d, J = 8.3 Hz, 1H), 6.83 (d, J = 1.6 Hz, 1H), 6.88 – 7.55 (m, 10 H), 7.30 (d, J = 8.6 Hz, 2H), 7.37 (bs, 1H), 7.40 – 7.42 (m, 1H), 7.64 (d, J = 8.2 Hz, 1H); Purity: 95.0 % (NMR)

4,4‘-(1E,1’E)-2,2‘-(4‘-Hydroxybiphenyl-2,5-diyl)bis(ethene-2,1-diyl)dibenzene-1,2-diol (3)

A mixture of **3a** (980 mg, 1.9 mmol) and pyridine hydrochloride (27 g, 233.6 mmol) was heated to 175°C in an oil bath for 3 h. The reaction was quenched with 1 molar HCl (200 ml). The aqueous solution was 2-times extracted with ethyl acetate (100 ml, 50 ml). The organic layers were combined, washed with Brine (50 ml), dried over anhydrous sodium sulfate and the solvent was removed. The obtained oil was solved in dichloromethane (20 ml), **3** precipitated immediately; it was sucked off and 2-times washed with dichloromethane.

Yield: 400 mg, 38 %; $C_{28}H_{22}O_5$, M = 438.47 g/mol; ^{1}H-NMR (500 MHz, d_6-DMSO) ppm: 6.33 (d, J = 2.4 Hz, 1H), 6.37 (dd, J = 8.1 Hz, J = 1.8 Hz, 1H), 6.46 (d, J = 1.8 Hz, 1H), 6.57 (d, J = 8.1 Hz, 1H), 6.64 – 6.70 (m, 3H), 6.82 – 6.84 (m, 2H), 6.89 (d, J = 16.4, Hz, 1H), 6.95 – 6.96 (m, 2H) 7.07 (d, J = 11.9 Hz, 1H), 7.08 (d, J = 12.3 Hz, 1H), 7.24 (bd, J = 7.8 Hz, 1H) 7.77 (d, J = 8.6, Hz, 1H), 7.83 (bs, 1H), 8.63 (s, 1H), 8.66 (s, 1H), 8.89 (s, 1H), 9.03 (s, 1H), 9.38 (s, 1H); ^{13}C-NMR (75 MHz, d_6-DMSO) ppm: 113.10, 113.89, 114.87 115.24, 115.33, 115.60, 118.35, 118.73, 120.03, 123.94, 124.88, 125.18, 127.87, 128.47, 128.78, 133.41, 134.07, 134.18, 136.10, 141.73, 143.58, 144.81, 145.31, 157.00; LC-MS 437 *m/z* (neg. ion); Purity: 95 %; CHN: calc. C 76.70, H 5.06; anal. C 76.44, H 4.97.

8.2 Protein biochemistry

8.2.1 Preparation of Aβ monomers and seeds

Synthetic β-amyloid (1-42) peptide was purchased from AnaSpec or Bachem. Peptides were dissolved in 1,1,1,3,3,3-Hexafluoro-2-propanol (HFIP) at a concentration of 5 mg/ml, vortexed for 1 min and sonicated for 10 min at 4°C in a sonicator bath. Then, the solution was incubated for 3 h at 22°C with 1 min vortexing and 1 min sonication every hour. After incubation for further 67 h at 22°C, samples were aliquoted and lyophilized in a SpeedVac for 1 h at 0.1 mbar and 45°C and stored at -20°C. Monomeric Aβ42 solutions were prepared by dissolving lyophilized peptide aliquots in 10 mM NaOH followed by 1 min vortexing and 5 min sonication yielding a final Aβ42 concentration of 200 µM. For the preparation of protofibrils (PF), synthetic β-amyloid (1-42) peptide produced by the laboratory of Dr. Volkmer-Engert (Institute for Medical Immunology, Charité Berlin, Germany) was used. Lyophylized HFIP-treated Aβ42 peptide was dissolved at a concentration of 10 mg/ml in 100 mM NaOH. After 1 min vortexing and 5 min sonication in a sonicator bath low salt buffer (LSB) was added yielding a Aβ42 concentration of 200 µM. After 6 h incubation at 37°C with 300 rpm shaking the Aβ42 solution was aliquoted and stored at -80°C until use. The morphology and stability of protofibrils were analyzed by atomic force microscopy, native gels, dot blots and ThT binding assays.

For the preparation of α-synuclein aggregates, lyophilized protein was dissolved in PBS at 500 µM and centrifuged (4°C, 265,000 x g) after a 5 min sonication step to remove aggregated material. The supernatant was incubated for 7 d at 37°C under constant shaking in the presence of a single glass bead. Synthetic human IAPP was aggregated as described previously[365]. Briefly, a human IAPP stock solution was incubated with 2x Tris-buffer (40 mM Tris/HCl, pH 7.4) at a final concentration of 30 µM at 37°C and constant shaking (300 rpm) for 48 h.

8.2.2 Measurement of protein concentrations

Protein concentration was determined with the BCA method, a coliometric assay that is based on a color change in proportion to protein concentration[366]. For the analysis of brain homogenates 10 µl sample (1:30 dilution) was incubated with 200 µl BCA solution (Pierce) at 37°C for 30 min in 96-well plate. Then, protein concentration was determined spectrophotometrically by measuring the absorption at 562 nm using a Tecan plate reader and by reference to a standard curve consisting of defined BSA concentrations in the appropriate buffer.

8.2.3 Denaturating SDS-PAGE

Polyacrylamide gel electrophoresis (PAGE) allows the separation of macromolecules according to their electrophoretic mobility which is dependent on the molecular weight, conformation and electric charge of the molecule. Use of the detergent SDS leads to denaturation of secondary structures and further supplementation with DTT causes breakage of disulfide bonds. Together, SDS and DTT result in full denaturation of proteins and cover the proteins inherent charge, making them accessible for a separation regarding their molecular weight only[215].

Invitrogen SDS-PAGE Bis-Tris 4-12 % gels were used for denaturating SDS-PAGE. Samples were prepared with 1x SDS-PAGE LDS Sample Buffer and 50 mM DTT before being boiled for 5 min at 95°C. 10 µl SeeBlue Plus 2 was used as marker. The electrophoresis was performed for 35 min at 200 V with 1x MES SDS Running Buffer. Following, proteins were transferred onto a nitrocellulose membrane using a wet blotting system from BioRad® and 1x Transfer buffer for 1 h at 100 V. The membrane was blocked in 3 % milk PBS-T for 30 min at room temperature followed by incubation with primary antibody in 3 % milk PBS-T overnight at 4°C or for 2 h at room temperature. After washing 3 x with PBS-T, antibodies were detected with appropriate HRP (horse-radish-peroxidase) coupled secondary antibodies (1:2000, Sigma-Aldrich) that were incubated 1 h at room temperature. After another 3 x 5 min washing step with PBS-T, detection of secondary antibody was performed by visualizing chemiluminescence after addition of WesternBright Quantum with an image reader (LAS 3000, Fujifilm).

8.2.4 NativePAGE

Polyacrylamide gel electrophoresis under native (non-denaturating) conditions lacks any detergents wherefore the proteins migration velocity depends on their size, electric charge and on the pH of the buffer[367]. The blue NativePAGE Novex® Bis-Tris gel system at near neutral pH uses Coomassie G-250 that supplies proteins with a net negative charge while maintaining them in their native state without denaturation.

Samples were prepared with NativePAGE 4x Sample Buffer. 10 µl NativeMark Unstained Protein Standard was used as a marker. The electrophoresis was performed for 1 h 50 min at 150 V with specific anode buffer (1x NativePAGE Running Buffer) and cathode buffer (1x NativePAGE Running Buffer + 20x NativePAGE Cathode Additive) for the inner cathode chamber. Subsequent blotting was performed as described for the SDS-PAGE but without methanol in the blotting buffer.

8.2.5 Dot blots and Filter retardation assay

Dot blot assays (DB) allow immunodetection of proteins without prior electrophoretical separation regarding size as in Western blot analysis. A sample is directly spotted on a membrane as a dot and detected afterwards with corresponding antibodies. For Dot blot assays a nitrocellulose membrane with a pore size of 0.1 µm was used. Membrane und Whatman-paper were equilibrated in PBS before the membrane was placed on top of the Whatman-paper in the 96-well vacuum apparatus. After washing the membrane with 100 µl PBS, 50-100 ng of Aβ42 samples were applied. Finally, the membrane was washed twice with 100 µl PBS.

Unlike dot blot assays where the total protein amount is spotted on a membrane, filter retardation assays (FRA) enable size-dependent retention of aggregates on nonbinding membranes. Filter retardation assays (FRA) were performed with a 0.2 µm cellulose acetate membrane and 200-400 ng samples were analyzed. The assay was performed similar to dot blot assays, however, the membrane was equilibrated in 0.1 % SDS and all washing steps were carried out with 100 µl 0.1 % SDS. The samples were prepared with equal volumes of denaturing buffer (4 % SDS and 100 mM DTT) and boiled for 5 min at 95°C. Both, membranes of dot blot or filter retardation analysis, were blocked in 1x PBS + 0.05% Tween with 3 % milk PBS-T for 30 min and immunological detection was performed as described above. Filters were quantified using AIDA image analyzer software.

8.2.6 Fluorescence polarization assay

Fluorescence polarization (FP) can be used to follow the aggregation of the Aβ peptide in a time-resolved manner. For the detection of Aβ42 aggregation a 5-Carboxyfluorescein labeled β-amyloid (1-42) peptide (^{FAM}Aβ42, tracer) was used that gets incorporated into aggregates throughout the aggregation process. The FAM-tracer was dissolved in 1 mM NaOH to 50 µM and stored at -20°C as a stock solution. The assay was performed in black non-binding 384-well microplates (Greiner Bio-One) with a transparent bottom and a 3M foil on top. Standard reactions contained 10 µM unlabeled Aβ42 monomer and 0.05 µM ^{FAM}Aβ42 in a total volume of 40 µl in low salt buffer (LSB). For seeded aggregations 100 nM (monomer equivalent) Aβ42 protofibrils were added as seeds. Tested compounds were used in a final concentration of 1 µM and 0.1 % DMSO was added to the according Aβ42 monomer control to ensure same DMSO concentrations. An example for a pipetting scheme can be seen in Table 13. Reactions without seeds or compound were replenished with 10 µl LSB buffer.

Component	(µl)	
Aβ42 (50 µM)	8	for 10 µM final
^{FAM}Aβ42 (0.17 µM)	12	for 0.05 µM final
PF (0.4 µM) / compound (4 µM)	10	for 100 nM / 1 µM final
LSB	10	
Σ	40	

Table 13 | Pipetting scheme for ^{FAM}Aβ4/Aβ42 co-polymerization assay

The fluorescence polarization measurements were carried out every 15 min at 37°C for a minimum of 14 h in a plate-reader (Infinite M1000/ Infinite M1000 PRO) at an excitation wavelength of 470 ± 5 nm and an emission wavelength of 528 ± 20 nm. Values are means of four technical replicates. Polarization values are expressed as dimensionless mP values, calculated by the plate-reader software i-control (Tecan, Switzerland).

For the analysis of fluorescence polarization (FP)-based aggregation profiles the GraphPad Prism software was used. The generated time-dependent FP data (four technical replicates per sample) was fitted to a four-parameter dose-response model with the following equation:

$$Y = Bottom + \frac{(Top - Bottom)}{(1 + 10^{((LogEC50 - X) * HillSlope)})}$$

After data fitting, the inflection point was determined for each aggregation profile (four technical replicates per sample), describing the time point where the half-maximal FP intensity is reached (t_{50}). To calculate the seeding activity of a sample ($\triangle t_{50}$), the t_{50} values were determined for the non-seeded (control) and the seeded (sample) ^{FAM}Aβ42/Aβ42 aggregation reactions and subtracted from each other to obtain the seeding activity of a sample ($\triangle t_{50} = t_{50}ctrl - t_{50}sample$).

To calculate the inhibitory effect of a compound ($\triangle t_{50}i$) the t_{50} values were determined from compound-treated (sample) and untreated (control) ^{FAM}Aβ42/Aβ42 aggregation reactions and subtracted from each other ($\triangle t_{50}i = t_{50}sample - t_{50}ctrl$). If not stated otherwise, average values were derived from four technical replicates in one experiment (mean ± SD of quadruplicates). Statistical significance was assessed by one-way ANOVA followed by Dunnett's or Bonferroni multiple comparison post hoc test or by unpaired t-test, two-tailed, respectively (*, p≤0.05; **, p≤0.01; ***, p≤0.001).

8.2.7 Thioflavin T assay

Thioflavin T (ThT) is a commonly used fluorescent dye to detect amyloid deposits[368] and to monitor Aβ aggregation *in vitro*[229,369]. The benzothiazol dye undergoes an absorbance maximum shift upon binding to β-sheet-rich amyloid structures from 385/445 nm to 450/482 nm[229]. The ThT assay was measured

in triplicates in black non-binding 384-well microplates (Greiner Bio-One). To determine the β-sheet content of endpoint aggregates, 10 µM Aβ42 monomers were mixed with 5 µM ThT and, if desired, 1 µM compounds.

Standard kinetic measurements contained 30 µM Aβ42 monomers and 30 µM ThT in LSB buffer in a total volume of 40 µl. The measurements were carried out every 15 min for 20 h at 37°C in a plate-reader (Infinite M1000/M1000 PRO). The excitation was performed at 420 nm and an emission was recorded at 485 nm after shaking 5 s with 2 mm amplitude before each measurement.

8.2.8 Fluorescence spectroscopy

LT1 fluorescence intensity measurements were performed in quadruplicates in black non-binding 384-well microplates (Greiner Bio-One). For single point measurements 5 µM Aβ42 species (monomer equivalent) were mixed with 10 µM LT1 in LSB buffer in a total volume of 60 µl. Fluorescence measurements of samples were performed in a plate reader (Infinite M1000/M1000 PRO) using the following wavelengths: Ex: 380 nm, Em: 560 nm.

For kinetic measurements 10 µM Aβ42 monomers and 5 µM LT1 were mixed in LSB buffer in a total volume of 40 µl. The measurements were carried out every 15 min for 20 h at 37°C after shaking 5 s with 2 mm amplitude before each measurement.

For LT1 fluorescence spectra, 10 µM compound was mixed with 10 µM Aβ42 species in a black 96-well quartz microplate (Hellma). Following, fluorescence was recorded at a constant excitation wavelength of 380 nm and varying the emission wavelength at 2 nm intervals between 400 nm to 680 nm using a plate reader (Infinite M1000 PRO).

8.2.9 Assessment of solubility of compound LT1

To assess the solubility of compound LT1, its concentration was gradually increased while measuring the absorption. Thus, an increase in turbidity upon a critical concentration can be correlated to the compounds insolubility. Steadily, 1 µl of 500 µM compound solution was added to 0.5 ml LSB buffer in a cuvette and the absorption was measured at 700 nm with a UV/Vis Spectrophotometers (Analytic Jena, Specord 250).

8.2.10 Homogenization of mouse and human brain tissue

Frozen tissue was weighed and homogenized in a 10-fold excess (w/v) of ice cold RIPA buffer (50 mM Tris-HCl pH 7.5, 150 mM NaCl, 0.1 % SDS, 0.5 % Sodium deoxycholate, 1 % Triton X-100, 0.25 U/µl Benzonase and a complete protease inhibitor cocktail) using a Schütt Homogen Plus semi-automatic homogenizer (700 rpm). The homogenate was centrifuged for 20 min at 1,500 x g at 4°C to remove

cell debris. The supernatant was then transferred to a new tube and the total protein concentration was determined with the Pierce BCA assay using BSA as a standard.

8.2.11 Immunoprecipitation of Aβ aggregate species and seeds release

Seeding-competent Aβ aggregate species were enriched from mouse brain homogenates (prepared from 0.25 mg brain tissue of APPPS1 transgenic mice) through immunoprecipitation with magnetic protein G beads coated with 6E10, 352 or IgG1 isotype control antibody (4 µg antibody/1.5 mg dynabeads). Antibody bound beads were incubated with homogenate at room temperature for 1 h or overnight at 4°C in a total volume of 0.5 ml RIPA buffer. Then, beads were washed once with RIPA wash buffer (50 mM Tris-HCl pH 7.5, 150 mM NaCl, 0.01 % SDS, 0.05 % Sodium deoxycholate, 0.1 % Triton X-100 and a complete protease inhibitor cocktail) and twice in LSB for buffer exchange. Subsequently, beads with extracted Aβ species were subjected to sonication to allow release of seeds. Therefore, beads in 100 µl LSB were transferred into a 96-well non-binding microplate and sonicated for 1 min at 60 % intensity using a Sonic Dismembrator Ultrasonic Processor with an 8-tip horn. Using a 96-well plate magnet (DynaMag™-96 Side Skirted Magnet) released seeding-competent Aβ material was separated from magnetic beads and the supernatant was finally analyzed in FP assays (10 µl/well). Alternatively, seeds could also be produced using a sonicator tip (Sonic Dismembrator Ultrasonic Processor (FB-120, 5/64" tip; sonication for 30 sec at 20 % amplitude) or a water bath for 15 min. For human brain samples 1-2 mg brain homogenate (supernatant) was used whilst likewise adjustment of antibody and beads amount. In case of the CSF samples 0.5 ml liquor with 0.05 % Tween was incubated with antibody bound beads overnight (16 h) at 4°C. Furthermore the RIPA wash buffer was replaced with artificial CSF (ACSF). All incubation steps were carried out while rotating.

8.3 Microscopy

8.3.1 Atomic force microscopy

In atomic force microscopy the surface of a sample is scanned and converted into a topographical map allowing high resolution images in the nanometer range under physiological conditions[218]. 20 µl of sample solution was added to freshly cleaved mica, incubated for 20 min and washed four times with ddH_2O. Atomic force micrographs were recorded using a Nano Wizard® II atomic force microscope operating in intermitted contact mode. The height of Aβ42 fibrils (n = 8) was quantified in two independent experiments (10 x 10 µm images) using the JPK Data Processing software.

8.3.2 Immunoelectron microscopy

Transmission electron microscopy (TEM) allows micro-structural examination with high-resolution and high magnification by passing a beam of electrons through the area of interest[370]. By use of a specific antibody for the protein of interest and a secondary antibody conjugated with colloidal gold particle, the presence of a specific protein can additionally be validated.

IEM images were acquired using a Zeiss 910 transmission electron microscope. 10 µl of sample solution were absorbed onto formvar-carbon-coated grids for 10 min and negatively stained using 2 % uranyl acetate. For immunogold-labeling absorbed samples were first incubated with primary antibody (6E10: 1:100; anti-5-Carboxyfluorescein monoclonal antibody: 1:50) for 15 min at room temperature. After washing 3 x with wash buffer (1xPBS, 1 % BSA, 0.12 % glycine), samples were incubated with the secondary antibody conjugated with 12 nm diameter gold particles (anti-mouse gold: 1:30) for 10 min at room temperature. After extensive washing (2 x PBS, 5 x ddH_2O), samples were stained with 5 % uranyl acetate. For the morphological analysis of the extracted Aβ aggregate species from transgenic mouse brain homogenate the whole Dynabeads including the extracted Aβ aggregate species were fixed in 2.5 % glutaraldehyde in 0.1 M phosphate buffer (pH 7.4) for 24 h at 4°C and embedded in epoxy resin. Ultrathin sections were contrasted with uranyl acetate/lead citrate.

8.3.3 Confocal microscopy

For confocal microscopy, cells were cultured in 24-well cell culture plates on fibronectin and polylysine coated coverslips ($9x10^4$ cells/well). SH-EP cells were washed with PBS before fixation with 2 % PFA for 15 mins at RT. After fixation, cover slips were transferred to conventional microscope slides using immersion solution before image acquisition with a Leica SP5 confocal microscope. HiLyte and LT1 fluorescent images were acquired at excitation wavelengths of 488 nm and 380 nm, respectively. Co-localization analysis of HiLyte and LT1 fluorescent puncta was performed using ImageJ software.

8.4 Cell biology

8.4.1 Cultivation of rat neuronal cells (PC12)

PC12 cells (rat pheochromocytoma, American Type Culture Collection) were cultured in RPMI 1640 (1x) medium supplemented with 10 % horse serum, 5 % FBS and 100 U/ml penicillin and streptomycin in a 5 % (v/v) CO_2 humidified environment at 37°C. All flasks as well as plates were coated with 10 % Poly-Lysine (v/v) prior to usage to allow PC12 cells to better attach to plastic surfaces. For splitting, medium was removed and cells were washed once with PBS. Then, trypsin containing 1 mM EDTA was added for ~1 min at 37°C to allow detachment of the cells. Trypsin was inactivated by adding fresh medium (4x volume of trypsin). Following, cells were partly transferred to a new flask to achieve the desired dilution.

8.4.2 MTT viability assay

PC12 cells were plated at a density of 20,000 cells per well on clear 96-well plates in 90 µl fresh medium. After 24 h, 10 µl seeds were added and cells were further incubated for 2-3 days at 37°C. 0.05 % Triton X-100 were used as toxicity control and incubated with the cells for 15 min. Cytotoxicity was measured using a MTT assay kit (Promega). Absorbance values of formazan were determined at 570 nm using an Infinite spectrometer (Tecan). Statistical significance was assessed by one-way ANOVA followed by Dunnett's or Bonferroni multiple comparison post hoc test. **, $p \leq 0.01$; ***, $p \leq 0.001$.

8.4.3 Cultivation of human neuroblastoma cells (SH-EP)

SH-EP cells (Human neuroblastoma cell line) were cultivated in DMEM supplemented with 4.5 g/l D-glucose, 10 % (v/v) FBS, 100 U/ml penicillin and streptomycin in a 5 % (v/v) CO_2 humidified environment at 37°C. Adherent mammalian cells were split twice a week. For splitting, medium was removed and cells were washed once with PBS. Then, trypsin containing 1mM EDTA was added for ~2 min at 37°C to detach the cells. Trypsin was inactivated by adding fresh medium (4x volume of trypsin). After centrifugation for 3 min at 150 x g, the cell pellet was resuspended in fresh medium and partly transferred to a new flask to achieve the desired dilution.

8.4.4 Detection of Aβ42 aggregates in neuroblastoma cells

For the intracellular detection of Aβ42 aggregates, unlabeled and fluorescently labeled Aβ42 aggregates were prepared by incubating 20 µM Aβ42 peptide with or without 5 %^{TAMRA}Aβ42 (Aβ42

N-terminally labeled with 5-Carboxytetramethyl-rhodamine) in LSB for 18 h at 37°C with constant agitation (300 rpm). Following, aggregates were sonicated 6 x 10 sec at 20 % intensity using a Sonic Dismembrator Ultrasonic Processor with a single tip. For Aβ42 aggregate internalization, cells ($90x10^4$ cells per 6-well) were treated with 600 nM Aβ42 aggregates (unlabeled or TAMRA-labeled) via direct infusion into the cell culture medium for 6 h. To ensure removal of surface-bound aggregates, cells were washed with PBS, trypsinized and seeded into 96-well cell culture plates ($45x10^4$ cells/well). After attachment of cells for 2 h, LT1 was added to the cells for a final concentration of 0.5 µM or 1 µM, respectively and LT1 fluorescence was measured after 1 h using a Tecan Spark plate reader at 37°C and 5 % (v/v) CO_2. Additionally, cellular ^{TAMRA}Aβ42 aggregate loads were determined using a Cellomics ArrayScan High-Content System device. After image acquisition, automated data analysis was performed using ArrayScan VTI software. For quantification, individual cells were detected via Hoechst fluorescent signals (Ex/Em: 350/461 nm) and average number of TAMRA spots per cell (Ex/Em: 544/572 nm) were measured and calculated from technical triplicates.

8.5 *In vivo* analysis: Blood brain barrier study

The pharmacokinetic evaluation of compound LT1 to assess the brain penetration after oral application was performed by Pharmacelsus (Saarbrücken, Germany). Concentrations of LT1 was determined in brain samples from male C57BL/6N mice after oral administration of 20 mg/kg (vehicle: 1 % methyl cellulose in water; application volume: 10 ml/kg) at three different time points (0.5, 1 and 4 h). For each time-point, samples were collected from three mice.

9.

Supplementary Information

9. Supplementary Information

9.1 Supplementary Data

9.1.1 Morphological characterization of seeds prepared from mouse brain

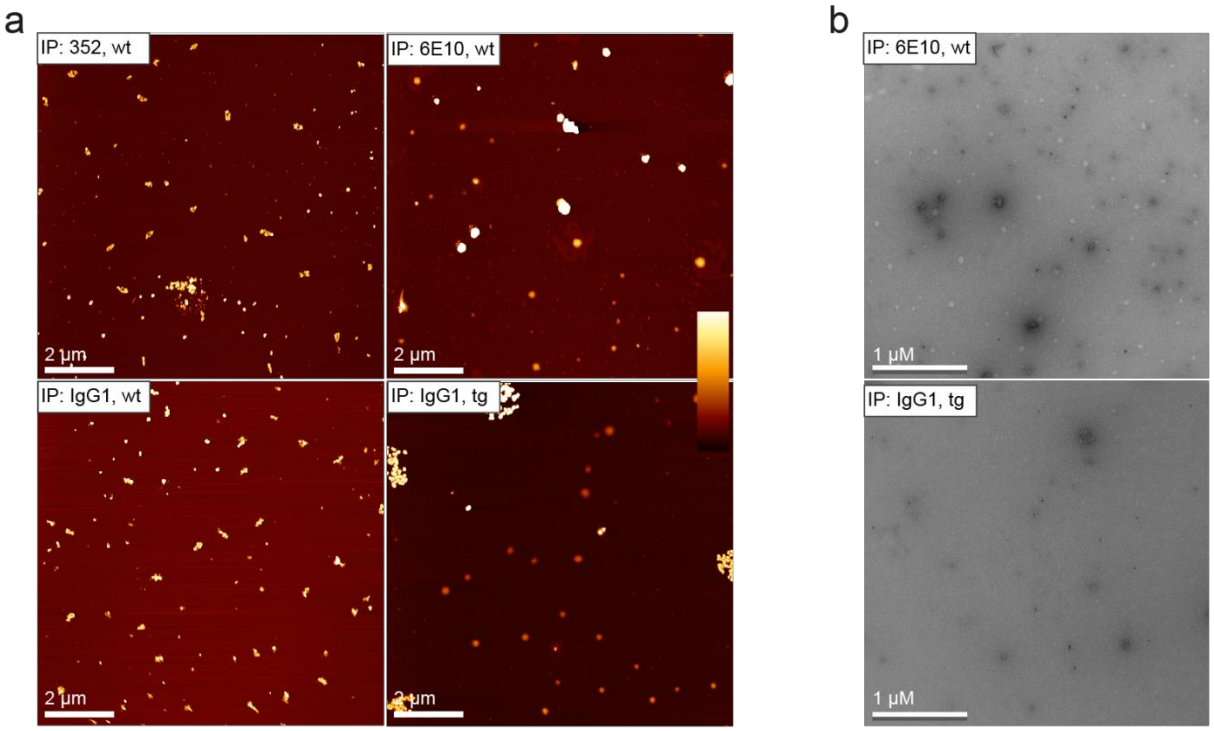

Figure S1 | AFM and TEM images of seeds prepared from wt and tg mouse brain homogenate
(a) Control AFM images of seeds prepared from wt or tg APPPS1 mouse brain after IP with 352, 6E10 or IgG1, respectively; 10 x 10 µm, scale bar: 2 µm, color gradient indicates 0-10 nm height. (b) Control TEM images seeds prepared from wt brain with 6E10 antibody and tg APPPS1 brain with IgG1 antibody; scale bar: 1 µm.

9.1.2 Analysis of CSF samples

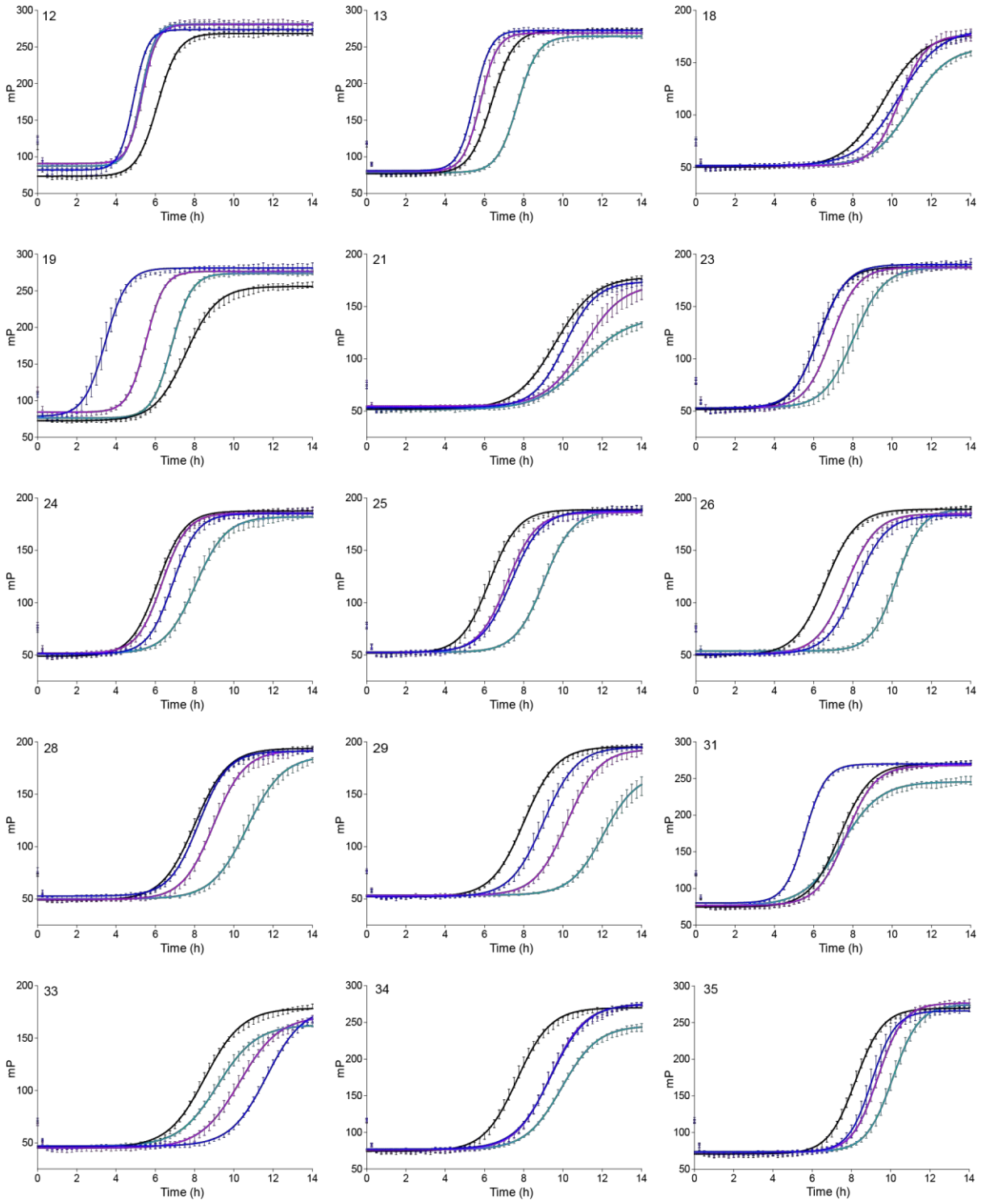

Figure S2 | Analysis of human CSF samples with ^{FAM}Aβ42/Aβ42 co-polymerization assays (I)
Aβ42-FP analysis of seeding activity of CSF samples. The color code applies for all samples: Black: 10 µM Aβ42 + 0.05 µM ^{FAM}Aβ42; turquoise: addition of seeds from 352-IP; purple: addition of seeds from 6E10-IP; blue: addition of seeds from IgG1-IP.

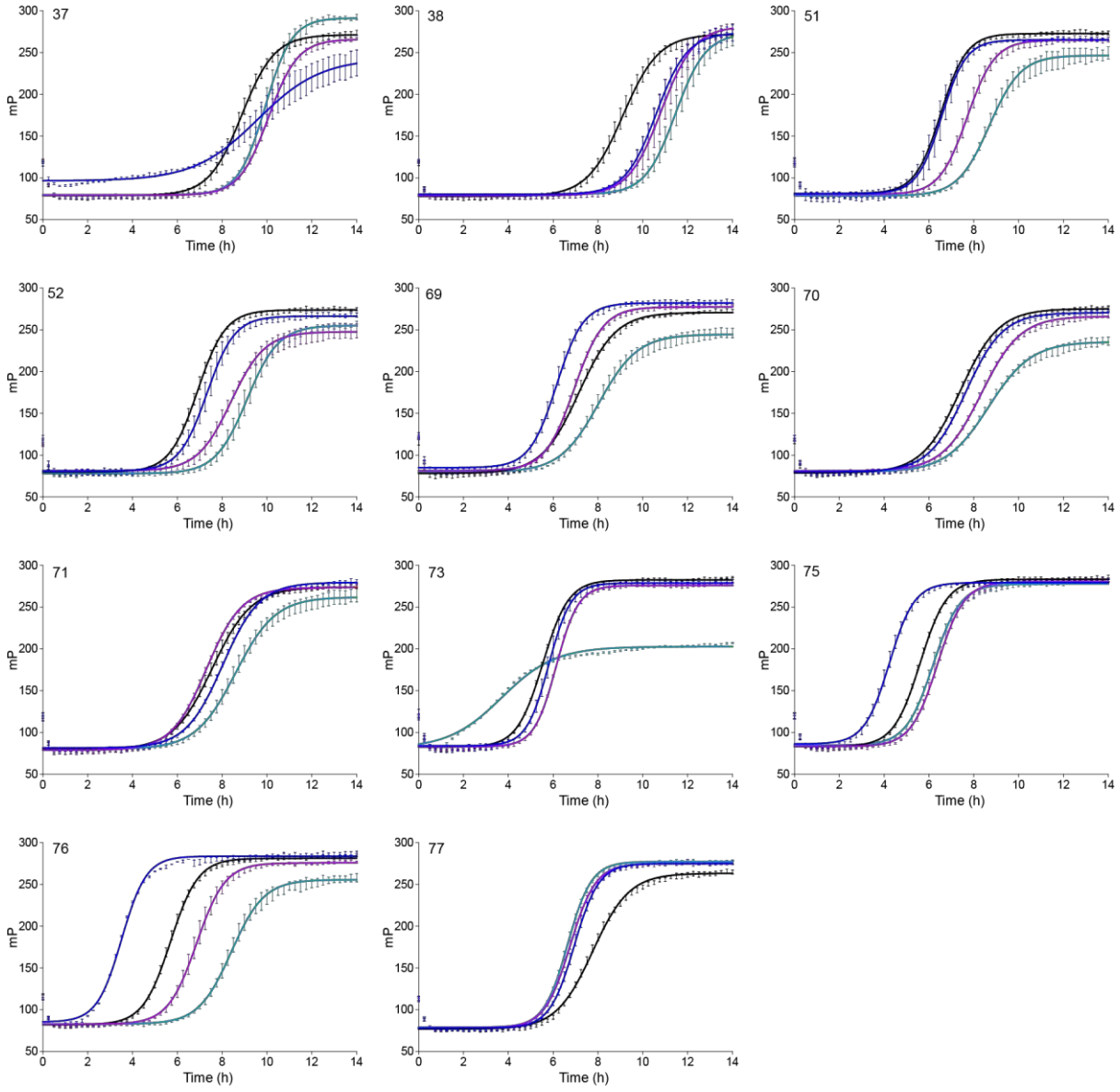

Figure S3 | Analysis of human CSF samples with ^{FAM}Aβ42/Aβ42 co-polymerization assays (II)
Aβ42-FP analysis of seeding activity of CSF samples. The color code applies for all samples: Black: 10 µM Aβ42 + 0.05 µM ^{FAM}Aβ42; turquoise: addition of seeds from 352-IP; purple: addition of seeds from 6E10-IP; blue: addition of seeds from IgG1-IP.

9.1 3 Compound synthesis

a

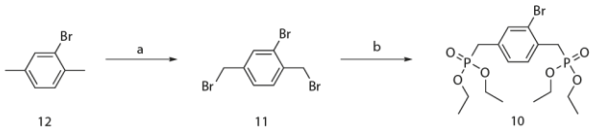

a) (trifluoromethyl)benzene, NSB, AIBN, reflux, 2 h. b) $P(Oet)_3$, 160°C, 4 h.

b

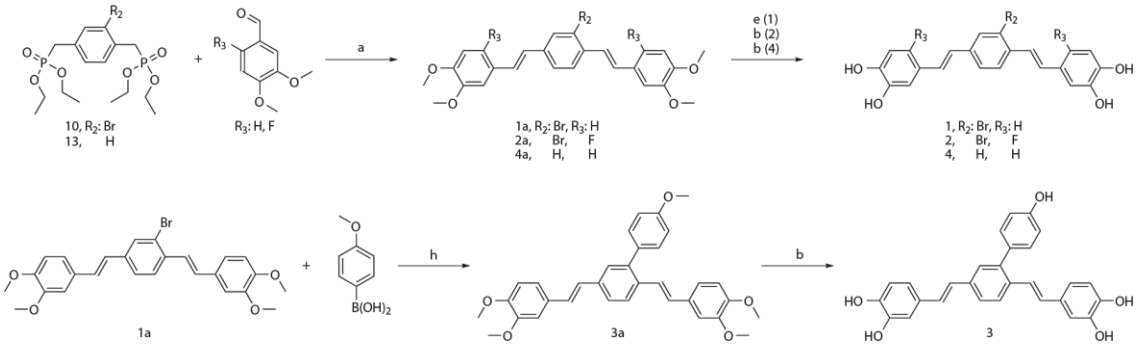

a) DMF, potassium tert-butylate, 4°C to RT or RT, 18-22 h. b) pyridine hydrochloride, 160-175°C, 3-22 h. e) DCM, BBr_3, -65°C to RT, 6h. h) dioxin:H_2O (10:1), $CsCO_3$, $Pd(PPh_3)_4$, 100°C, 1 h.

c

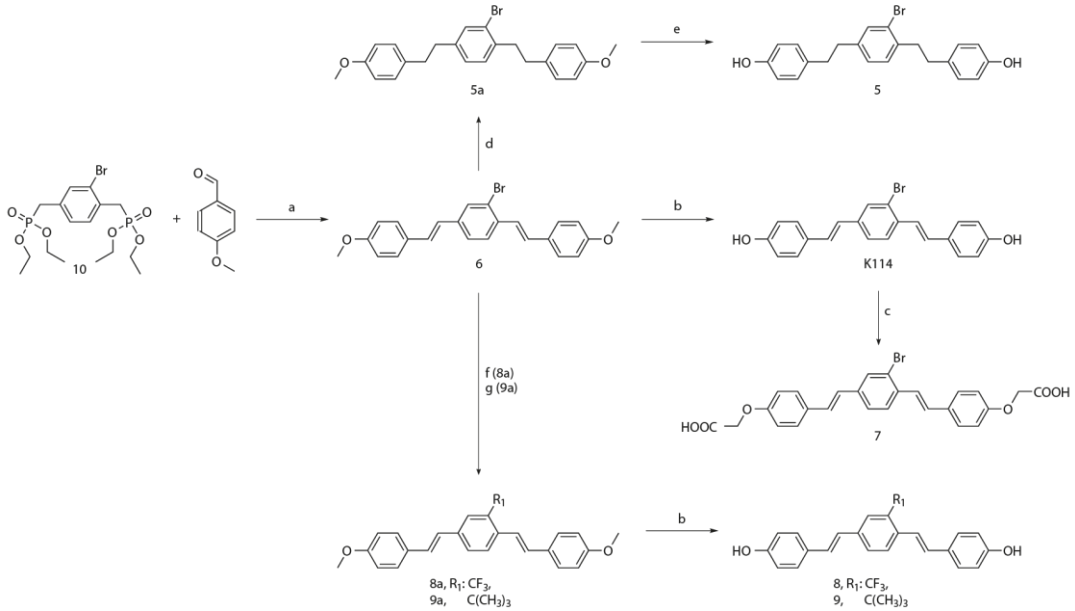

a) DMF, potassium tert-butylate, 4°C to RT or RT, 18-22 h. b) pyridine hydrochloride, 160-175°C, 3-22 h. c) EtOH, bromoacetic acid, KOH, reflux, 5.5 h. d) TFA, triethylsilane, 60°C, 4h. e) DCM, BBr_3, -65°C to RT, 6 h. f) DMF, CuI, sodium trifluoroacetate, 150°C, 1 h. g) THF, 1,3-dicyclohexylimidazolium tetrafluoroborate, $NiCl_2$, tert-butylmagnesium chloride, -10°C, 2 h.

Figure S4 | Synthesis route for K114 derivatives
(a) Synthesis of precursor compound 10 via Arbuzov reaction. Product 10 functions as precursor for synthesis in *b* and *c*. (b) Horner-Wadsworth-Emmons (HWE reaction) for compounds 1, 2, 4; Suzuki coupling for compound 3. (c) Horner-Wadsworth-Emmons (HWE reaction) for compounds 6, K114, 5, 7, 8 and 9.

9.1.4 Analysis of LT1-treated Aβ42 assemblies

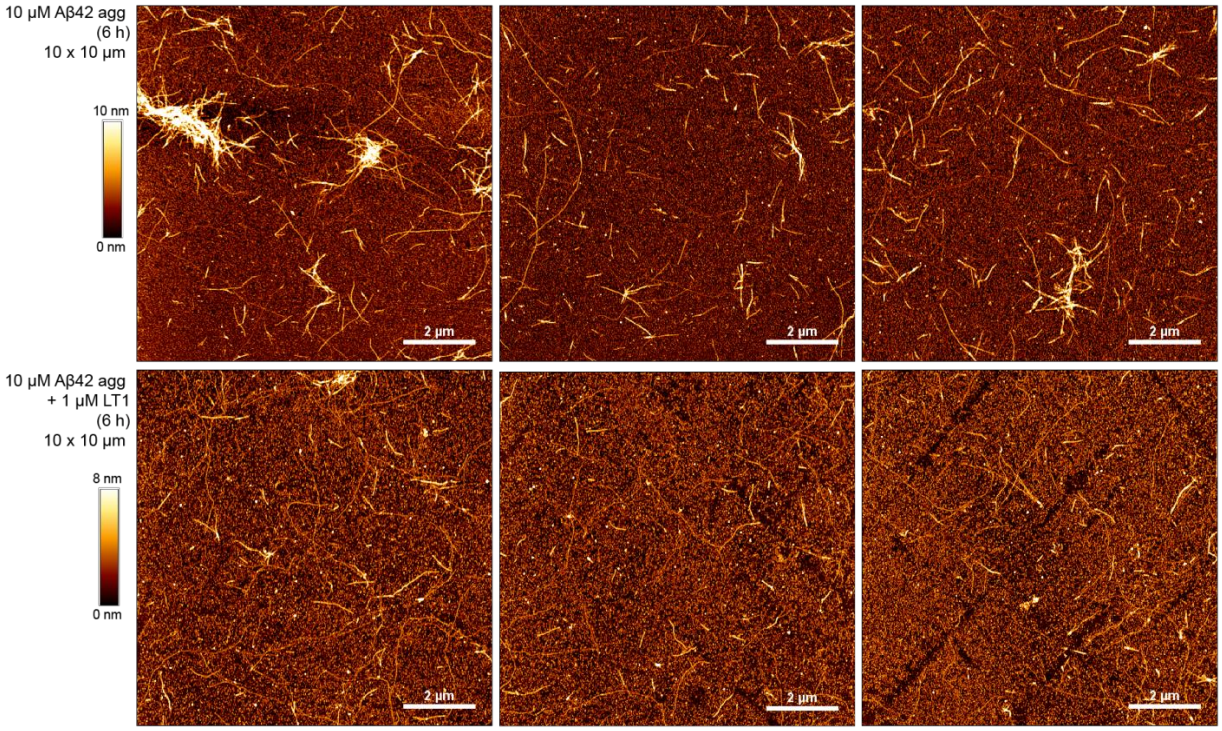

Figure S5 | AFM images of intermediate (6 h) Aβ42 assemblies in presence or absence of LT1
Additional AFM images of 6 h Aβ42 assemblies (10 µM) aggregated in presence or absence of LT1 (1 µM); 10 x 10 µm, scale bar: 2 µm, color gradient indicates 0-10 nm height for untreated samples an 0-8 nm height for LT1-treated samples.

9.2 List of Figures

Supplementary Figures

9.3 List of Tables

9.4 Abbreviations

°C	Degree celsius
Aβ40	Amyloid-beta 1-40
Aβ42	Amyloid-beta 1-42
ACh	Acetylcholine
AD	Alzheimer's disease
ADDLs	Aβ-derived diffusible ligands
AFM	Atomic force microscopy
AICD	APP intracellular domain
APOE	Apolipoprotein E
APP	Amyloid precursor protein
a.u.	Arbitrary units
BACE1	Beta-site amyloid precursor protein cleaving enzyme 1
BBB	Blood brain barrier
BCA	Bicinchoninic acid assay
BSA	Bovine serum albumin
CAA	Cerebral amyloid angiopathy
CD	Circular dichroism
CNS	Central nervous system
CSF	Cerebrospinal fluid
CT	Computer tomography
CTF	C-terminal fragment
ddH_2O	Double-distilled water
DLB	Dementia with Lewy bodies
DLS	Dynamic light scattering
DMSO	Dimethylsulfoxide
DTT	Dithiothreitol
EDTA	Ethylenediaminetetraacetic acid
ELISA	Enzyme-linked immunosorbent assay
EM	Electron microscopy
FAD	Familiar Alzheimer's disease
FAM	Carboxyfluorescein
FBS	Fetal bovine serum
FDA	Food and drug administration
FDG	Fluorodeoxyglucose
FRA	Filter retardation assay
FRET	Förster/Fluorescence resonance energy transfer
FP	Fluorescence polarization
FTDP-17	Frontotemporal dementia and parkinsonism linked to chromosome 17
FTLD	Frontotemporal lobar degeneration
g	Earth's gravity
GSK-3β	Glycogen synthase kinase 3
GWAS	Genome-wide association studies
h	Hour
H_2O	Water

HEPES	4-(2-hydroxyethyl)-1-piperazineethanesulfonic acid
HMWAs	High molecular weight Aβ assemblies
HRP	Horseradish peroxidase
IAPP	Islet amyloid polypeptide
IEM	Immunoelectron microscopy
IP	Immunoprecipitation
ITC	Isothermal titration calorimetry
$I_{\perp}$	Perpendicular or horizontal intensity
$I_{\parallel}$	Parallel or vertical intensity
kDa	Kilodalton
LED	Light emitting diode
LMWAs	Low molecular weight Aβ assemblies
LOAD	Late-onset Alzheimer's disease
LTP	Long-term potentiation
mA	Milliampere
MAP	Microtubule-associated protein
MAPT	Microtubule associated protein tau
MCI	Mild cognitive impairment
MES	2-(N-morpholino)ethanesulfonic acid
mg	Milligram
min	Minutes
ml	Milliliter
MMSE	Mini-mental state examination
mP	Millipolarization
MRI	Magnetic resonance imaging
MTT	3-(4,5-dimethylthiazol-2-yl)-2,5-diphenyltetrazolium bromide
NFT	Neurofibrillary tangle
ng	Nanogram
nm	Nanometer
NMDA	N-methyl D-aspartate
NMR	Nuclear magnetic resonance
PAGE	Polyacrylamid gel electrophoresis
PD	Parkinson's disease
PBS	Phosphate-buffered saline
PET	Positron emission tomography
PF	Protofibril
PHF	Paired helical filaments
PIB	Pittsburgh compound B
PMCA	Protein misfolding cyclic amplification
PS1/2	Presenilin-1/2
p-Tau	Phosphorylated tau
R	General gas constant
rpm	Rotations per minute
RT	Room temperature
SAD	Sporadic Alzheimer's disease
SEC	Size-exclusion chromatography
SEM	Standard error of mean

SD	Standard deviation
SDS	Sodium dodecyl sulfate
SDS-PAGE	Sodium dodecyl sulfate polyacrylamide gel electrophoresis
SF	Straight filaments
SORL1	Sortilin-related receptor gene
T	Temperature
TEM	Transmission electron microscopy
tg	Transgenic
ThT	Thioflavin T
TREM2	Triggering receptor expressed on myeloid cells 2
Tris	Tris(hydroxymethyl)aminomethane
t-tau	Total tau
U	Enzyme unit
V	Volume
wt	Wildtype
w/o	Without
w/v	Weight /volume
α-syn	Alpha synuclein
µg	Microgram
µl	Microliter
µM	Micromolar
η	Viscosity
ρ	Rotational relaxation time
τ	Fluorescence lifetime

Compound	IUAPC nomenclature
BSB	(trans,trans)-1-bromo-2,5-bis-(3- hydroxycarbonyl-4-hydroxy)styrylbenzene
Chrysamine G (CG)	4,4′-Bis(3-carboxy-4-hydroxyphenylazo)biphenyl disodium salt
Congo Red (CR)	disodium 4-amino-3-[4-[4-(1-amino-4-sulfonato-naphthalen-2-yl) diazenylphenyl]phenyl]diazenyl-naphthalene-1-sulfonate
Curcumin	(E,E)-1,7-bis(4-Hydroxy-3-methoxyphenyl)-1,6-heptadiene-3,5-dione
EGCG	(–)-Epigallocatechin gallate
K114	(trans,trans)-1-bromo-2,5-bis-(4-hydroxy)styrylbenzene
methoxy-X04	4,4‘-[(2-methoxy-1,4-phenylene)di-(1E)-2,1-ethenediyl]bisphenol
Ro 90-7501	2′-(4-Aminophenyl)-[2,5′-bi-1H-benzimidazol]-5-amine

10.

References

10. References

1 Alzheimer, A. Über einen eigenartigen schweren Erkrankungsprozeß der Hirnrinde. *Neurol Central*, 1134, (1906).

2 Hippius, H. & Neundorfer, G. The discovery of Alzheimer's disease. *Dialogues in clinical neuroscience* **5**, 101-108, (2003).

3 Ross, C. A. & Poirier, M. A. What is the role of protein aggregation in neurodegeneration? *Nat Rev Mol Cell Bio* **6**, 891-898, (2005).

4 Burns, A. & Iliffe, S. Dementia. *British medical journal* **338**, (2009).

5 Kelley, B. J. & Petersen, R. C. Alzheimer's disease and mild cognitive impairment. *Neurologic clinics* **25**, 577-609, v, (2007).

6 Association, A. s. 2017 Alzheimer's Disease Facts and Figures. *Alzheimer's Association*, 325-373, (2017).

7 Winblad, B. *et al.* Defeating Alzheimer's disease and other dementias: a priority for European science and society. *The Lancet. Neurology* **15**, 455-532, (2016).

8 Holtzman, D. M., Morris, J. C. & Goate, A. M. Alzheimer's disease: the challenge of the second century. *Science translational medicine* **3**, 77sr71, (2011).

9 Kurz, A. Verlauf der kognitiven Störungen. *Weiß. & Weber, G.*, 991- 1006, (1997).

10 Bamburg, J. R. & Bloom, G. S. Cytoskeletal pathologies of Alzheimer disease. *Cell motility and the cytoskeleton* **66**, 635-649, (2009).

11 Stefani, M. Protein misfolding and aggregation: new examples in medicine and biology of the dark side of the protein world. *Biochimica et biophysica acta* **1739**, 5-25, (2004).

12 Serrano-Pozo, A., Frosch, M. P., Masliah, E. & Hyman, B. T. Neuropathological alterations in Alzheimer disease. *Cold Spring Harbor perspectives in medicine* **1**, a006189, (2011).

13 Braak, H. & Braak, E. Neuropathological stageing of Alzheimer-related changes. *Acta neuropathologica* **82**, 239-259, (1991).

14 Thal, D. R., Rub, U., Orantes, M. & Braak, H. Phases of A beta-deposition in the human brain and its relevance for the development of AD. *Neurology* **58**, 1791-1800, (2002).

15 Goedert, M. NEURODEGENERATION. Alzheimer's and Parkinson's diseases: The prion concept in relation to assembled Abeta, tau, and alpha-synuclein. *Science* **349**, 1255555, (2015).

16 Liu, C. C., Kanekiyo, T., Xu, H. & Bu, G. Apolipoprotein E and Alzheimer disease: risk, mechanisms and therapy. *Nature reviews. Neurology* **9**, 106-118, (2013).

17 Goate, A. *et al.* Segregation of a missense mutation in the amyloid precursor protein gene with familial Alzheimer's disease. *Nature* **349**, 704-706, (1991).

18 Mullan, M. *et al.* A pathogenic mutation for probable Alzheimer's disease in the APP gene at the N-terminus of beta-amyloid. *Nature genetics* **1**, 345-347, (1992).

19 De Strooper, B. Loss-of-function presenilin mutations in Alzheimer disease. Talking Point on the role of presenilin mutations in Alzheimer disease. *EMBO reports* **8**, 141-146, (2007).

20 Weggen, S. & Beher, D. Molecular consequences of amyloid precursor protein and presenilin mutations causing autosomal-dominant Alzheimer's disease. *Alzheimer's research & therapy* **4**, 9, (2012).

21 Younkin, S. G. The role of A beta 42 in Alzheimer's disease. *Journal of physiology, Paris* **92**, 289-292, (1998).

22 Citron, M. *et al.* Mutation of the beta-amyloid precursor protein in familial Alzheimer's disease increases beta-protein production. *Nature* **360**, 672-674, (1992).

23 Harman, D. Alzheimer's disease pathogenesis: role of aging. *Annals of the New York Academy of Sciences* **1067**, 454-460, (2006).

24 Lambert, J. C. *et al.* Genome-wide association study identifies variants at CLU and CR1 associated with Alzheimer's disease. *Nature genetics* **41**, 1094-1099, (2009).

25 Harold, D. *et al.* Genome-wide association study identifies variants at CLU and PICALM associated with Alzheimer's disease. *Nature genetics* **41**, 1088-1093, (2009).

26 Farrer, L. A. *et al.* Effects of age, sex, and ethnicity on the association between apolipoprotein E genotype and Alzheimer disease. A meta-analysis. APOE and Alzheimer Disease Meta Analysis Consortium. *Jama* **278**, 1349-1356, (1997).

27 Wildsmith, K. R., Holley, M., Savage, J. C., Skerrett, R. & Landreth, G. E. Evidence for impaired amyloid beta clearance in Alzheimer's disease. *Alzheimer's research & therapy* **5**, 33, (2013).

28 Vardarajan, B. N. *et al.* Coding mutations in SORL1 and Alzheimer disease. *Annals of neurology* **77**, 215-227, (2015).

29 Lee, J. H., Barral, S. & Reitz, C. The neuronal sortilin-related receptor gene SORL1 and late-onset Alzheimer's disease. *Current neurology and neuroscience reports* **8**, 384-391, (2008).
30 Ulrich, J. D. & Holtzman, D. M. TREM2 Function in Alzheimer's Disease and Neurodegeneration. *ACS chemical neuroscience* **7**, 420-427, (2016).
31 Jin, S. C. *et al.* TREM2 is associated with increased risk for Alzheimer's disease in African Americans. *Molecular neurodegeneration* **10**, (2015).
32 Flicker, L. Modifiable lifestyle risk factors for Alzheimer's disease. *Journal of Alzheimer's disease : JAD* **20**, 803-811, (2010).
33 Arevalo-Rodriguez, I. *et al.* Mini-Mental State Examination (MMSE) for the detection of Alzheimer's disease and other dementias in people with mild cognitive impairment (MCI). *The Cochrane database of systematic reviews*, CD010783, (2015).
34 Jellinger, K. A. & Bancher, C. Neuropathology of Alzheimer's disease: a critical update. *Journal of neural transmission. Supplementum* **54**, 77-95, (1998).
35 Mueller, S., Keeser, D., Reiser, M. F., Teipel, S. & Meindl, T. Functional and structural MR imaging in neuropsychiatric disorders, Part 1: imaging techniques and their application in mild cognitive impairment and Alzheimer disease. *AJNR. American journal of neuroradiology* **33**, 1845-1850, (2012).
36 Priller, C. *et al.* Synapse formation and function is modulated by the amyloid precursor protein. *Journal of Neuroscience* **26**, 7212-7221, (2006).
37 Mosconi, L. *et al.* Pre-Clinical Detection of Alzheimer's Disease Using FDG-PET, with or without Amyloid Imaging. *Journal of Alzheimers Disease* **20**, 843-854, (2010).
38 Klunk, W. E. *et al.* Imaging brain amyloid in Alzheimer's disease with Pittsburgh Compound-B. *Annals of neurology* **55**, 306-319, (2004).
39 Reiber, H. Dynamics of brain-derived proteins in cerebrospinal fluid. *Clinica chimica acta; international journal of clinical chemistry* **310**, 173-186, (2001).
40 Andreasen, N., Sjogren, M. & Blennow, K. CSF markers for Alzheimer's disease: total tau, phospho-tau and Abeta42. *The world journal of biological psychiatry : the official journal of the World Federation of Societies of Biological Psychiatry* **4**, 147-155, (2003).
41 Blennow, K. & Hampel, H. CSF markers for incipient Alzheimer's disease. *The Lancet. Neurology* **2**, 605-613, (2003).
42 Sunderland, T. *et al.* Decreased beta-amyloid1-42 and increased tau levels in cerebrospinal fluid of patients with Alzheimer disease. *Jama* **289**, 2094-2103, (2003).
43 Jack, C. R., Jr. & Holtzman, D. M. Biomarker modeling of Alzheimer's disease. *Neuron* **80**, 1347-1358, (2013).
44 Mattsson, N. *et al.* CSF biomarker variability in the Alzheimer's Association quality control program. *Alzheimer's & dementia : the journal of the Alzheimer's Association* **9**, 251-261, (2013).
45 Maia, L. F. *et al.* Increased CSF Abeta during the very early phase of cerebral Abeta deposition in mouse models. *EMBO molecular medicine* **7**, 895-903, (2015).
46 Jack, C. R., Jr. *et al.* Tracking pathophysiological processes in Alzheimer's disease: an updated hypothetical model of dynamic biomarkers. *The Lancet. Neurology* **12**, 207-216, (2013).
47 Turner, P. R., O'Connor, K., Tate, W. P. & Abraham, W. C. Roles of amyloid precursor protein and its fragments in regulating neural activity, plasticity and memory. *Progress in neurobiology* **70**, 1-32, (2003).
48 Haass, C. & Selkoe, D. J. Soluble protein oligomers in neurodegeneration: lessons from the Alzheimer's amyloid beta-peptide. *Nature reviews. Molecular cell biology* **8**, 101-112, (2007).
49 Pearson, H. A. & Peers, C. Physiological roles for amyloid beta peptides. *The Journal of physiology* **575**, 5-10, (2006).
50 Kamenetz, F. *et al.* APP processing and synaptic function. *Neuron* **37**, 925-937, (2003).
51 Plant, L. D., Boyle, J. P., Smith, I. F., Peers, C. & Pearson, H. A. The production of amyloid beta peptide is a critical requirement for the viability of central neurons. *The Journal of neuroscience : the official journal of the Society for Neuroscience* **23**, 5531-5535, (2003).
52 Kumar, D. K. *et al.* Amyloid-beta peptide protects against microbial infection in mouse and worm models of Alzheimer's disease. *Science translational medicine* **8**, 340ra372, (2016).
53 Gandhi, S., Refolo, L. M. & Sambamurti, K. Amyloid precursor protein compartmentalization restricts beta-amyloid production: therapeutic targets based on BACE compartmentalization. *Journal of molecular neuroscience : MN* **24**, 137-143, (2004).
54 Bayer, T. A. W., O. Alzheimer-Demenz: Molekulare Pathologie, Tiermodelle und Therapiestrategien *Springer Medizin Verlag* (2008).

55 Ahmed, M. *et al.* Structural conversion of neurotoxic amyloid-beta(1-42) oligomers to fibrils. *Nature structural & molecular biology* **17**, 561-567, (2010).
56 Schmechel, A. *et al.* Alzheimer beta-amyloid homodimers facilitate A beta fibrillization and the generation of conformational antibodies. *The Journal of biological chemistry* **278**, 35317-35324, (2003).
57 Xu, Y. *et al.* Conformational transition of amyloid beta-peptide. *Proceedings of the National Academy of Sciences of the United States of America* **102**, 5403-5407, (2005).
58 Sontag, E. M. *et al.* Methylene blue modulates huntingtin aggregation intermediates and is protective in Huntington's disease models. *The Journal of neuroscience : the official journal of the Society for Neuroscience* **32**, 11109-11119, (2012).
59 Ehrnhoefer, D. E. *et al.* EGCG redirects amyloidogenic polypeptides into unstructured, off-pathway oligomers. *Nature structural & molecular biology* **15**, 558-566, (2008).
60 Kumar, S. & Walter, J. Phosphorylation of amyloid beta (Abeta) peptides - a trigger for formation of toxic aggregates in Alzheimer's disease. *Aging* **3**, 803-812, (2011).
61 Larson, M. E. & Lesne, S. E. Soluble A ss oligomer production and toxicity. *Journal of neurochemistry* **120**, 125-139, (2012).
62 Selkoe, D. J. Cell biology of protein misfolding: the examples of Alzheimer's and Parkinson's diseases. *Nature cell biology* **6**, 1054-1061, (2004).
63 Zhang, S. *et al.* The Alzheimer's peptide A beta adopts a collapsed coil structure in water. *Journal of structural biology* **130**, 130-141, (2000).
64 Barrow, C. J. & Zagorski, M. G. Solution structures of beta peptide and its constituent fragments: relation to amyloid deposition. *Science* **253**, 179-182, (1991).
65 Lazo, N. D., Grant, M. A., Condron, M. C., Rigby, A. C. & Teplow, D. B. On the nucleation of amyloid beta-protein monomer folding. *Protein science : a publication of the Protein Society* **14**, 1581-1596, (2005).
66 Garzon-Rodriguez, W., Sepulveda-Becerra, M., Milton, S. & Glabe, C. G. Soluble amyloid Abeta-(1-40) exists as a stable dimer at low concentrations. *The Journal of biological chemistry* **272**, 21037-21044, (1997).
67 Hilbich, C., Kisters-Woike, B., Reed, J., Masters, C. L. & Beyreuther, K. Substitutions of hydrophobic amino acids reduce the amyloidogenicity of Alzheimer's disease beta A4 peptides. *Journal of molecular biology* **228**, 460-473, (1992).
68 Nakabayashi, J. *et al.* Amyloid beta-protein (A beta) accumulation in the putamen and mammillary body during aging and in Alzheimer disease. *Journal of neuropathology and experimental neurology* **57**, 343-352, (1998).
69 Podlisny, M. B. *et al.* Aggregation of secreted amyloid beta-protein into sodium dodecyl sulfate-stable oligomers in cell culture. *The Journal of biological chemistry* **270**, 9564-9570, (1995).
70 Roher, A. E. *et al.* Morphology and toxicity of Abeta-(1-42) dimer derived from neuritic and vascular amyloid deposits of Alzheimer's disease. *The Journal of biological chemistry* **271**, 20631-20635, (1996).
71 Walsh, D. M., Tseng, B. P., Rydel, R. E., Podlisny, M. B. & Selkoe, D. J. The oligomerization of amyloid beta-protein begins intracellularly in cells derived from human brain. *Biochemistry* **39**, 10831-10839, (2000).
72 Lesne, S. *et al.* A specific amyloid-beta protein assembly in the brain impairs memory. *Nature* **440**, 352-357, (2006).
73 Townsend, M., Shankar, G. M., Mehta, T., Walsh, D. M. & Selkoe, D. J. Effects of secreted oligomers of amyloid beta-protein on hippocampal synaptic plasticity: a potent role for trimers. *The Journal of physiology* **572**, 477-492, (2006).
74 Bitan, G. *et al.* Amyloid beta -protein (Abeta) assembly: Abeta 40 and Abeta 42 oligomerize through distinct pathways. *Proceedings of the National Academy of Sciences of the United States of America* **100**, 330-335, (2003).
75 Cleary, J. P. *et al.* Natural oligomers of the amyloid-beta protein specifically disrupt cognitive function. *Nature neuroscience* **8**, 79-84, (2005).
76 Dahlgren, K. N. *et al.* Oligomeric and fibrillar species of amyloid-beta peptides differentially affect neuronal viability. *The Journal of biological chemistry* **277**, 32046-32053, (2002).
77 Kuo, Y. M. *et al.* Water-soluble Abeta (N-40, N-42) oligomers in normal and Alzheimer disease brains. *The Journal of biological chemistry* **271**, 4077-4081, (1996).
78 McLean, C. A. *et al.* Soluble pool of Abeta amyloid as a determinant of severity of neurodegeneration in Alzheimer's disease. *Annals of neurology* **46**, 860-866, (1999).
79 Walsh, D. M. *et al.* Naturally secreted oligomers of amyloid beta protein potently inhibit hippocampal long-term potentiation in vivo. *Nature* **416**, 535-539, (2002).

80 Walsh, D. M., Klyubin, I., Fadeeva, J. V., Rowan, M. J. & Selkoe, D. J. Amyloid-beta oligomers: their production, toxicity and therapeutic inhibition. *Biochemical Society transactions* **30**, 552-557, (2002).
81 Reed, M. N. *et al.* Cognitive effects of cell-derived and synthetically derived Abeta oligomers. *Neurobiology of aging* **32**, 1784-1794, (2011).
82 Chromy, B. A. *et al.* Self-assembly of Abeta(1-42) into globular neurotoxins. *Biochemistry* **42**, 12749-12760, (2003).
83 Georganopoulou, D. G. *et al.* Nanoparticle-based detection in cerebral spinal fluid of a soluble pathogenic biomarker for Alzheimer's disease. *Proceedings of the National Academy of Sciences of the United States of America* **102**, 2273-2276, (2005).
84 Harper, J. D., Wong, S. S., Lieber, C. M. & Lansbury, P. T., Jr. Assembly of A beta amyloid protofibrils: an in vitro model for a possible early event in Alzheimer's disease. *Biochemistry* **38**, 8972-8980, (1999).
85 Klein, W. L., Stine, W. B., Jr. & Teplow, D. B. Small assemblies of unmodified amyloid beta-protein are the proximate neurotoxin in Alzheimer's disease. *Neurobiology of aging* **25**, 569-580, (2004).
86 Lambert, M. P. *et al.* Diffusible, nonfibrillar ligands derived from Abeta1-42 are potent central nervous system neurotoxins. *Proceedings of the National Academy of Sciences of the United States of America* **95**, 6448-6453, (1998).
87 Gong, Y. *et al.* Alzheimer's disease-affected brain: presence of oligomeric A beta ligands (ADDLs) suggests a molecular basis for reversible memory loss. *Proceedings of the National Academy of Sciences of the United States of America* **100**, 10417-10422, (2003).
88 Kagan, B. L., Hirakura, Y., Azimov, R., Azimova, R. & Lin, M. C. The channel hypothesis of Alzheimer's disease: current status. *Peptides* **23**, 1311-1315, (2002).
89 Lashuel, H. A., Hartley, D., Petre, B. M., Walz, T. & Lansbury, P. T., Jr. Neurodegenerative disease: amyloid pores from pathogenic mutations. *Nature* **418**, 291, (2002).
90 Le, Y. *et al.* Amyloid (beta)42 activates a G-protein-coupled chemoattractant receptor, FPR-like-1. *The Journal of neuroscience : the official journal of the Society for Neuroscience* **21**, RC123, (2001).
91 Mattson, M. P. & Chan, S. L. Neuronal and glial calcium signaling in Alzheimer's disease. *Cell calcium* **34**, 385-397, (2003).
92 Quist, A. *et al.* Amyloid ion channels: a common structural link for protein-misfolding disease. *Proceedings of the National Academy of Sciences of the United States of America* **102**, 10427-10432, (2005).
93 Arimon, M. *et al.* Fine structure study of Abeta1-42 fibrillogenesis with atomic force microscopy. *FASEB journal : official publication of the Federation of American Societies for Experimental Biology* **19**, 1344-1346, (2005).
94 Harper, J. D. & Lansbury, P. T., Jr. Models of amyloid seeding in Alzheimer's disease and scrapie: mechanistic truths and physiological consequences of the time-dependent solubility of amyloid proteins. *Annual review of biochemistry* **66**, 385-407, (1997).
95 Harper, J. D., Wong, S. S., Lieber, C. M. & Lansbury, P. T. Observation of metastable Abeta amyloid protofibrils by atomic force microscopy. *Chemistry & biology* **4**, 119-125, (1997).
96 Hartley, D. M. *et al.* Protofibrillar intermediates of amyloid beta-protein induce acute electrophysiological changes and progressive neurotoxicity in cortical neurons. *The Journal of neuroscience : the official journal of the Society for Neuroscience* **19**, 8876-8884, (1999).
97 Kheterpal, I. *et al.* Abeta protofibrils possess a stable core structure resistant to hydrogen exchange. *Biochemistry* **42**, 14092-14098, (2003).
98 Rochet, J. C. & Lansbury, P. T., Jr. Amyloid fibrillogenesis: themes and variations. *Current opinion in structural biology* **10**, 60-68, (2000).
99 Walsh, D. M. *et al.* Amyloid beta-protein fibrillogenesis. Structure and biological activity of protofibrillar intermediates. *The Journal of biological chemistry* **274**, 25945-25952, (1999).
100 Walsh, D. M., Lomakin, A., Benedek, G. B., Condron, M. M. & Teplow, D. B. Amyloid beta-protein fibrillogenesis. Detection of a protofibrillar intermediate. *The Journal of biological chemistry* **272**, 22364-22372, (1997).
101 Williams, A. D. *et al.* Structural properties of Abeta protofibrils stabilized by a small molecule. *Proceedings of the National Academy of Sciences of the United States of America* **102**, 7115-7120, (2005).
102 Klunk, W. E., Jacob, R. F. & Mason, R. P. Quantifying amyloid by congo red spectral shift assay. *Methods in enzymology* **309**, 285-305, (1999).
103 LeVine, H., 3rd. Quantification of beta-sheet amyloid fibril structures with thioflavin T. *Methods in enzymology* **309**, 274-284, (1999).

104 Luhrs, T. *et al.* 3D structure of Alzheimer's amyloid-beta(1-42) fibrils. *Proceedings of the National Academy of Sciences of the United States of America* **102**, 17342-17347, (2005).
105 Malinchik, S. B., Inouye, H., Szumowski, K. E. & Kirschner, D. A. Structural analysis of Alzheimer's beta(1-40) amyloid: protofilament assembly of tubular fibrils. *Biophysical journal* **74**, 537-545, (1998).
106 Stromer, T. & Serpell, L. C. Structure and morphology of the Alzheimer's amyloid fibril. *Microscopy research and technique* **67**, 210-217, (2005).
107 Lansbury, P. T., Jr. Evolution of amyloid: what normal protein folding may tell us about fibrillogenesis and disease. *Proceedings of the National Academy of Sciences of the United States of America* **96**, 3342-3344, (1999).
108 Muller-Hill, B. & Beyreuther, K. Molecular biology of Alzheimer's disease. *Annual review of biochemistry* **58**, 287-307, (1989).
109 Terry, R. D. *et al.* Physical basis of cognitive alterations in Alzheimer's disease: synapse loss is the major correlate of cognitive impairment. *Annals of neurology* **30**, 572-580, (1991).
110 Finder, V. H. & Glockshuber, R. Amyloid-beta aggregation. *Neuro-degenerative diseases* **4**, 13-27, (2007).
111 Benilova, I., Karran, E. & De Strooper, B. The toxic Abeta oligomer and Alzheimer's disease: an emperor in need of clothes. *Nature neuroscience* **15**, 349-357, (2012).
112 Selkoe, D. J. The molecular pathology of Alzheimer's disease. *Neuron* **6**, 487-498, (1991).
113 Hardy, J. A hundred years of Alzheimer's disease research. *Neuron* **52**, 3-13, (2006).
114 Mucke, L. & Selkoe, D. J. Neurotoxicity of amyloid beta-protein: synaptic and network dysfunction. *Cold Spring Harbor perspectives in medicine* **2**, a006338, (2012).
115 Chapman, P. F. *et al.* Impaired synaptic plasticity and learning in aged amyloid precursor protein transgenic mice. *Nature neuroscience* **2**, 271-276, (1999).
116 Tu, S., Okamoto, S., Lipton, S. A. & Xu, H. Oligomeric Abeta-induced synaptic dysfunction in Alzheimer's disease. *Molecular neurodegeneration* **9**, 48, (2014).
117 Jan, A. *et al.* Abeta42 neurotoxicity is mediated by ongoing nucleated polymerization process rather than by discrete Abeta42 species. *The Journal of biological chemistry* **286**, 8585-8596, (2011).
118 Biffi, A. & Greenberg, S. M. Cerebral amyloid angiopathy: a systematic review. *J Clin Neurol* **7**, 1-9, (2011).
119 McLauchlan, D., Malik, G. A. & Robertson, N. P. Cerebral amyloid angiopathy: subtypes, treatment and role in cognitive impairment. *J Neurol* **264**, 2184-2186, (2017).
120 Ross, C. A. & Poirier, M. A. Protein aggregation and neurodegenerative disease. *Nature medicine* **10 Suppl**, S10-17, (2004).
121 Fandrich, M. & Dobson, C. M. The behaviour of polyamino acids reveals an inverse side chain effect in amyloid structure formation. *The EMBO journal* **21**, 5682-5690, (2002).
122 Serpell, L. C. *et al.* The protofilament substructure of amyloid fibrils. *Journal of molecular biology* **300**, 1033-1039, (2000).
123 Fitzpatrick, A. W. *et al.* Atomic structure and hierarchical assembly of a cross-beta amyloid fibril. *Proceedings of the National Academy of Sciences of the United States of America* **110**, 5468-5473, (2013).
124 Cohen, T., Frydman-Marom, A., Rechter, M. & Gazit, E. Inhibition of amyloid fibril formation and cytotoxicity by hydroxyindole derivatives. *Biochemistry* **45**, 4727-4735, (2006).
125 Arosio, P., Knowles, T. P. & Linse, S. On the lag phase in amyloid fibril formation. *Physical chemistry chemical physics : PCCP* **17**, 7606-7618, (2015).
126 Collins, S. R., Douglass, A., Vale, R. D. & Weissman, J. S. Mechanism of prion propagation: amyloid growth occurs by monomer addition. *PLoS biology* **2**, e321, (2004).
127 Tanaka, M., Collins, S. R., Toyama, B. H. & Weissman, J. S. The physical basis of how prion conformations determine strain phenotypes. *Nature* **442**, 585-589, (2006).
128 Bishop, M. F. & Ferrone, F. A. Kinetics of nucleation-controlled polymerization. A perturbation treatment for use with a secondary pathway. *Biophysical journal* **46**, 631-644, (1984).
129 Wegner, A. Spontaneous fragmentation of actin filaments in physiological conditions. *Nature* **296**, 266-267, (1982).
130 Ferrone, F. Analysis of protein aggregation kinetics. *Methods in enzymology* **309**, 256-274, (1999).
131 Cohen, S. I., Vendruscolo, M., Dobson, C. M. & Knowles, T. P. Nucleated polymerization with secondary pathways. II. Determination of self-consistent solutions to growth processes described by non-linear master equations. *J Chem Phys* **135**, 065106, (2011).

132 Cohen, S. I. *et al.* Proliferation of amyloid-beta42 aggregates occurs through a secondary nucleation mechanism. *Proceedings of the National Academy of Sciences of the United States of America* **110**, 9758-9763, (2013).
133 Ferrone, F. A., Hofrichter, J. & Eaton, W. A. Kinetics of sickle hemoglobin polymerization. II. A double nucleation mechanism. *Journal of molecular biology* **183**, 611-631, (1985).
134 Ferrone, F. A., Hofrichter, J. & Eaton, W. A. Kinetics of sickle hemoglobin polymerization. I. Studies using temperature-jump and laser photolysis techniques. *Journal of molecular biology* **183**, 591-610, (1985).
135 Naiki, H., Higuchi, K., Nakakuki, K. & Takeda, T. Kinetic analysis of amyloid fibril polymerization in vitro. *Laboratory investigation; a journal of technical methods and pathology* **65**, 104-110, (1991).
136 Du, D. *et al.* A kinetic aggregation assay allowing selective and sensitive amyloid-beta quantification in cells and tissues. *Biochemistry* **50**, 1607-1617, (2011).
137 Cohen, S. I., Vendruscolo, M., Dobson, C. M. & Knowles, T. P. From macroscopic measurements to microscopic mechanisms of protein aggregation. *Journal of molecular biology* **421**, 160-171, (2012).
138 Colby, D. W. *et al.* Prion detection by an amyloid seeding assay. *Proceedings of the National Academy of Sciences of the United States of America* **104**, 20914-20919, (2007).
139 Jarrett, J. T. & Lansbury, P. T., Jr. Seeding "one-dimensional crystallization" of amyloid: a pathogenic mechanism in Alzheimer's disease and scrapie? *Cell* **73**, 1055-1058, (1993).
140 Jucker, M. & Walker, L. C. Pathogenic protein seeding in Alzheimer disease and other neurodegenerative disorders. *Annals of neurology* **70**, 532-540, (2011).
141 Kane, M. D. *et al.* Evidence for seeding of beta -amyloid by intracerebral infusion of Alzheimer brain extracts in beta -amyloid precursor protein-transgenic mice. *The Journal of neuroscience : the official journal of the Society for Neuroscience* **20**, 3606-3611, (2000).
142 Rosen, R. F. *et al.* Exogenous seeding of cerebral beta-amyloid deposition in betaAPP-transgenic rats. *Journal of neurochemistry* **120**, 660-666, (2012).
143 Walker, L. C. *et al.* Exogenous induction of cerebral beta-amyloidosis in betaAPP-transgenic mice. *Peptides* **23**, 1241-1247, (2002).
144 Meyer-Luehmann, M. *et al.* Exogenous induction of cerebral beta-amyloidogenesis is governed by agent and host. *Science* **313**, 1781-1784, (2006).
145 Eisele, Y. S. *et al.* Peripherally applied Abeta-containing inoculates induce cerebral beta-amyloidosis. *Science* **330**, 980-982, (2010).
146 Brundin, P., Melki, R. & Kopito, R. Prion-like transmission of protein aggregates in neurodegenerative diseases. *Nature reviews. Molecular cell biology* **11**, 301-307, (2010).
147 Brettschneider, J., Del Tredici, K., Lee, V. M. & Trojanowski, J. Q. Spreading of pathology in neurodegenerative diseases: a focus on human studies. *Nature reviews. Neuroscience* **16**, 109-120, (2015).
148 Jucker, M. & Walker, L. C. Self-propagation of pathogenic protein aggregates in neurodegenerative diseases. *Nature* **501**, 45-51, (2013).
149 Guo, J. L. & Lee, V. M. Cell-to-cell transmission of pathogenic proteins in neurodegenerative diseases. *Nature medicine* **20**, 130-138, (2014).
150 Vogiatzi, T., Xilouri, M., Vekrellis, K. & Stefanis, L. Wild type alpha-synuclein is degraded by chaperone-mediated autophagy and macroautophagy in neuronal cells. *The Journal of biological chemistry* **283**, 23542-23556, (2008).
151 Jaiswal, J. K., Fix, M., Takano, T., Nedergaard, M. & Simon, S. M. Resolving vesicle fusion from lysis to monitor calcium-triggered lysosomal exocytosis in astrocytes. *Proceedings of the National Academy of Sciences of the United States of America* **104**, 14151-14156, (2007).
152 Lee, H. J. *et al.* Assembly-dependent endocytosis and clearance of extracellular alpha-synuclein. *The international journal of biochemistry & cell biology* **40**, 1835-1849, (2008).
153 Binder, L. I., Frankfurter, A. & Rebhun, L. I. The distribution of tau in the mammalian central nervous system. *The Journal of cell biology* **101**, 1371-1378, (1985).
154 Mandelkow, E. M. & Mandelkow, E. Tau in Alzheimer's disease. *Trends in cell biology* **8**, 425-427, (1998).
155 Lee, V. M., Goedert, M. & Trojanowski, J. Q. Neurodegenerative tauopathies. *Annual review of neuroscience* **24**, 1121-1159, (2001).
156 Wang, J. Z., Xia, Y. Y., Grundke-Iqbal, I. & Iqbal, K. Abnormal hyperphosphorylation of tau: sites, regulation, and molecular mechanism of neurofibrillary degeneration. *Journal of Alzheimer's disease : JAD* **33 Suppl 1**, S123-139, (2013).
157 Johnson, G. V. & Jenkins, S. M. Tau protein in normal and Alzheimer's disease brain. *Journal of Alzheimer's disease : JAD* **1**, 307-328, (1999).

158 Lovestone, S., Hartley, C. L., Pearce, J. & Anderton, B. H. Phosphorylation of tau by glycogen synthase kinase-3 beta in intact mammalian cells: the effects on the organization and stability of microtubules. *Neuroscience* **73**, 1145-1157, (1996).
159 Siuda, J., Fujioka, S. & Wszolek, Z. K. Parkinsonian syndrome in familial frontotemporal dementia. *Parkinsonism & related disorders* **20**, 957-964, (2014).
160 Wolfe, M. S. The role of tau in neurodegenerative diseases and its potential as a therapeutic target. *Scientifica* **2012**, 796024, (2012).
161 Hutton, M. *et al.* Association of missense and 5'-splice-site mutations in tau with the inherited dementia FTDP-17. *Nature* **393**, 702-705, (1998).
162 Poorkaj, P. *et al.* Tau is a candidate gene for chromosome 17 frontotemporal dementia. *Annals of neurology* **43**, 815-825, (1998).
163 Feinstein, S. C. & Wilson, L. Inability of tau to properly regulate neuronal microtubule dynamics: a loss-of-function mechanism by which tau might mediate neuronal cell death. *Bba-Mol Basis Dis* **1739**, 268-279, (2005).
164 Roy, S., Zhang, B., Lee, V. M. & Trojanowski, J. Q. Axonal transport defects: a common theme in neurodegenerative diseases. *Acta neuropathologica* **109**, 5-13, (2005).
165 Trojanowski, J. Q., Smith, A. B., Huryn, D. & Lee, V. M. Microtubule-stabilising drugs for therapy of Alzheimer's disease and other neurodegenerative disorders with axonal transport impairments. *Expert opinion on pharmacotherapy* **6**, 683-686, (2005).
166 Trojanowski, J. Q. & Lee, V. M. Pathological tau: a loss of normal function or a gain in toxicity? *Nature neuroscience* **8**, 1136-1137, (2005).
167 Goedert, M. The ordered assembly of tau is the gain-of-toxic function that causes human tauopathies. *Alzheimer's & dementia : the journal of the Alzheimer's Association* **12**, 1040-1050, (2016).
168 Andorfer, C. *et al.* Hyperphosphorylation and aggregation of tau in mice expressing normal human tau isoforms. *Journal of neurochemistry* **86**, 582-590, (2003).
169 Hardy, J. A. & Higgins, G. A. Alzheimer's disease: the amyloid cascade hypothesis. *Science* **256**, 184-185, (1992).
170 Blennow, K., Hampel, H., Weiner, M. & Zetterberg, H. Cerebrospinal fluid and plasma biomarkers in Alzheimer disease. *Nature reviews. Neurology* **6**, 131-144, (2010).
171 Citron, M. Strategies for disease modification in Alzheimer's disease. *Nature reviews. Neuroscience* **5**, 677-685, (2004).
172 Takashima, A. *et al.* Activation of tau protein kinase I/glycogen synthase kinase-3beta by amyloid beta peptide (25-35) enhances phosphorylation of tau in hippocampal neurons. *Neuroscience research* **31**, 317-323, (1998).
173 Karran, E. & De Strooper, B. The amyloid cascade hypothesis: are we poised for success or failure? *Journal of neurochemistry* **139 Suppl 2**, 237-252, (2016).
174 Braak, H., Thal, D. R., Ghebremedhin, E. & Del Tredici, K. Stages of the pathologic process in Alzheimer disease: age categories from 1 to 100 years. *Journal of neuropathology and experimental neurology* **70**, 960-969, (2011).
175 Price, J. L. & Morris, J. C. Tangles and plaques in nondemented aging and "preclinical" Alzheimer's disease. *Annals of neurology* **45**, 358-368, (1999).
176 Walsh, D. M. & Selkoe, D. J. A beta oligomers - a decade of discovery. *Journal of neurochemistry* **101**, 1172-1184, (2007).
177 Hasselmo, M. E. The role of acetylcholine in learning and memory. *Current opinion in neurobiology* **16**, 710-715, (2006).
178 Anand, R., Gill, K. D. & Mahdi, A. A. Therapeutics of Alzheimer's disease: Past, present and future. *Neuropharmacology* **76 Pt A**, 27-50, (2014).
179 Rees, T. M. & Brimijoin, S. The role of acetylcholinesterase in the pathogenesis of Alzheimer's disease. *Drugs Today (Barc)* **39**, 75-83, (2003).
180 McEntee, W. J. & Crook, T. H. Glutamate: its role in learning, memory, and the aging brain. *Psychopharmacology* **111**, 391-401, (1993).
181 Budson, A. E. & Solomon, P. R. *Memory Loss, Alzheimer's Disease, and Dementia E-Book: A Practical Guide for Clinicians*. (Elsevier Health Sciences, 2015).
182 Danysz, W. & Parsons, C. G. Alzheimer's disease, beta-amyloid, glutamate, NMDA receptors and memantine--searching for the connections. *British journal of pharmacology* **167**, 324-352, (2012).
183 Ghosh, A. K., Brindisi, M. & Tang, J. Developing beta-secretase inhibitors for treatment of Alzheimer's disease. *Journal of neurochemistry* **120 Suppl 1**, 71-83, (2012).

184 Eriksen, J. L. *et al.* NSAIDs and enantiomers of flurbiprofen target gamma-secretase and lower Abeta 42 in vivo. *The Journal of clinical investigation* **112**, 440-449, (2003).
185 Olsauskas-Kuprys, R., Zlobin, A. & Osipo, C. Gamma secretase inhibitors of Notch signaling. *OncoTargets and therapy* **6**, 943-955, (2013).
186 Selkoe, D. & Kopan, R. Notch and Presenilin: regulated intramembrane proteolysis links development and degeneration. *Annual review of neuroscience* **26**, 565-597, (2003).
187 Wolfe, M. S. Inhibition and modulation of gamma-secretase for Alzheimer's disease. *Neurotherapeutics : the journal of the American Society for Experimental NeuroTherapeutics* **5**, 391-398, (2008).
188 Page, R. M. *et al.* Generation of Abeta38 and Abeta42 is independently and differentially affected by familial Alzheimer disease-associated presenilin mutations and gamma-secretase modulation. *The Journal of biological chemistry* **283**, 677-683, (2008).
189 Bard, F. *et al.* Peripherally administered antibodies against amyloid beta-peptide enter the central nervous system and reduce pathology in a mouse model of Alzheimer disease. *Nature medicine* **6**, 916-919, (2000).
190 Sevigny, J. *et al.* The antibody aducanumab reduces Abeta plaques in Alzheimer's disease. *Nature* **537**, 50-56, (2016).
191 Nalivaeva, N. N., Beckett, C., Belyaev, N. D. & Turner, A. J. Are amyloid-degrading enzymes viable therapeutic targets in Alzheimer's disease? *Journal of neurochemistry* **120 Suppl 1**, 167-185, (2012).
192 Maezawa, I. *et al.* Congo red and thioflavin-T analogs detect Abeta oligomers. *Journal of neurochemistry* **104**, 457-468, (2008).
193 Mathis, C. A., Wang, Y. & Klunk, W. E. Imaging beta-amyloid plaques and neurofibrillary tangles in the aging human brain. *Current pharmaceutical design* **10**, 1469-1492, (2004).
194 Bohrmann, B. *et al.* Self-assembly of beta-amyloid 42 is retarded by small molecular ligands at the stage of structural intermediates. *Journal of structural biology* **130**, 232-246, (2000).
195 Ma, D. L. & Leung, C. H. Editorial: Small molecule therapeutics for Alzheimer's disease. *Current Alzheimer research* **12**, 400-402, (2015).
196 Kochi, A. *et al.* Inhibitory Activity Of Curcumin Derivatives Towards Metal-free And Metal-induced Amyloid-beta Aggregation. *Current Alzheimer research* **12**, 415-423, (2015).
197 Kampa, M., Nifli, A. P., Notas, G. & Castanas, E. Polyphenols and cancer cell growth. *Reviews of physiology, biochemistry and pharmacology* **159**, 79-113, (2007).
198 Yang, F. *et al.* Curcumin inhibits formation of amyloid beta oligomers and fibrils, binds plaques, and reduces amyloid in vivo. *The Journal of biological chemistry* **280**, 5892-5901, (2005).
199 Bieschke, J. *et al.* EGCG remodels mature alpha-synuclein and amyloid-beta fibrils and reduces cellular toxicity. *Proceedings of the National Academy of Sciences of the United States of America* **107**, 7710-7715, (2010).
200 Riviere, C. *et al.* Inhibitory activity of stilbenes on Alzheimer's beta-amyloid fibrils in vitro. *Bioorganic & medicinal chemistry* **15**, 1160-1167, (2007).
201 Orlando, R. A., Gonzales, A. M., Royer, R. E., Deck, L. M. & Vander Jagt, D. L. A chemical analog of curcumin as an improved inhibitor of amyloid Abeta oligomerization. *Plos One* **7**, e31869, (2012).
202 Klunk, W. E., Debnath, M. L. & Pettegrew, J. W. Development of small molecule probes for the beta-amyloid protein of Alzheimer's disease. *Neurobiology of aging* **15**, 691-698, (1994).
203 Klunk, W. E., Debnath, M. L. & Pettegrew, J. W. Chrysamine-G binding to Alzheimer and control brain: autopsy study of a new amyloid probe. *Neurobiology of aging* **16**, 541-548, (1995).
204 Pardridge, W. M. Alzheimer's disease drug development and the problem of the blood-brain barrier. *Alzheimer's & dementia : the journal of the Alzheimer's Association* **5**, 427-432, (2009).
205 Lipinski, C. A., Lombardo, F., Dominy, B. W. & Feeney, P. J. Experimental and computational approaches to estimate solubility and permeability in drug discovery and development settings. *Advanced drug delivery reviews* **46**, 3-26, (2001).
206 Leeson, P. Drug discovery: Chemical beauty contest. *Nature* **481**, 455-456, (2012).
207 Skovronsky, D. M. *et al.* In vivo detection of amyloid plaques in a mouse model of Alzheimer's disease. *Proceedings of the National Academy of Sciences of the United States of America* **97**, 7609-7614, (2000).
208 Klunk, W. E. *et al.* Imaging Abeta plaques in living transgenic mice with multiphoton microscopy and methoxy-X04, a systemically administered Congo red derivative. *Journal of neuropathology and experimental neurology* **61**, 797-805, (2002).
209 Zhuang, Z. P. *et al.* Radioiodinated styrylbenzenes and thioflavins as probes for amyloid aggregates. *Journal of medicinal chemistry* **44**, 1905-1914, (2001).
210 Crystal, A. S. *et al.* A comparison of amyloid fibrillogenesis using the novel fluorescent compound K114. *Journal of neurochemistry* **86**, 1359-1368, (2003).

211 LeVine, H., 3rd. Mechanism of A beta(1-40) fibril-induced fluorescence of (trans,trans)-1-bromo-2,5-bis(4-hydroxystyryl)benzene (K114). *Biochemistry* **44**, 15937-15943, (2005).
212 Zhang, Y. H. *et al.* K114 inhibits A-beta aggregation and inflammation in vitro and in vivo in AD/Tg mice. *Current Alzheimer research* **11**, 299-308, (2014).
213 Casas-Terradellas, E. *et al.* Simultaneous electrophoretic analysis of proteins of very high and low molecular weights using low-percentage acrylamide gel and a gradient SDS-PAGE gel. *Electrophoresis* **27**, 3935-3938, (2006).
214 Davis, B. J. Disc Electrophoresis. Ii. Method and Application to Human Serum Proteins. *Annals of the New York Academy of Sciences* **121**, 404-427, (1964).
215 Laemmli, U. K. Cleavage of structural proteins during the assembly of the head of bacteriophage T4. *Nature* **227**, 680-685, (1970).
216 Berne, B. J. *Dynamic Light Scattering: With Applications to Chemistry, Biology, and Physics*. (Dover Publications Inc., 2003).
217 Shirahama, T. & Cohen, A. S. High-resolution electron microscopic analysis of the amyloid fibril. *The Journal of cell biology* **33**, 679-708, (1967).
218 Goldsbury, C. S., Scheuring, S. & Kreplak, L. Introduction to atomic force microscopy (AFM) in biology. *Current protocols in protein science* **Chapter 17**, Unit 17 17 11-19, (2009).
219 Bruggink, K. A., Muller, M., Kuiperij, H. B. & Verbeek, M. M. Methods for analysis of amyloid-beta aggregates. *Journal of Alzheimer's disease : JAD* **28**, 735-758, (2012).
220 Wirths, O. *et al.* Identification of low molecular weight pyroglutamate A{beta} oligomers in Alzheimer disease: a novel tool for therapy and diagnosis. *The Journal of biological chemistry* **285**, 41517-41524, (2010).
221 Santos, A. N., Simm, A., Holthoff, V. & Boehm, G. A method for the detection of amyloid-beta1-40, amyloid-beta1-42 and amyloid-beta oligomers in blood using magnetic beads in combination with Flow cytometry and its application in the diagnostics of Alzheimer's disease. *Journal of Alzheimer's disease : JAD* **14**, 127-131, (2008).
222 Necula, M., Kayed, R., Milton, S. & Glabe, C. G. Small molecule inhibitors of aggregation indicate that amyloid beta oligomerization and fibrillization pathways are independent and distinct. *The Journal of biological chemistry* **282**, 10311-10324, (2007).
223 Frid, P., Anisimov, S. V. & Popovic, N. Congo red and protein aggregation in neurodegenerative diseases. *Brain research reviews* **53**, 135-160, (2007).
224 Howie, A. J. & Brewer, D. B. Optical properties of amyloid stained by Congo red: History and mechanisms. *Micron* **40**, 285-301, (2009).
225 Sipe, J. D. & Cohen, A. S. Review: History of the amyloid fibril. *Journal of structural biology* **130**, 88-98, (2000).
226 Porat, Y., Abramowitz, A. & Gazit, E. Inhibition of amyloid fibril formation by polyphenols: Structural similarity and aromatic interactions as a common inhibition mechanism. *Chemical biology & drug design* **67**, 27-37, (2006).
227 Kim, Y. S., Randolph, T. W., Manning, M. C., Stevens, F. J. & Carpenter, J. F. Congo red populates partially unfolded states of an amyloidogenic protein to enhance aggregation and amyloid fibril formation. *Journal of Biological Chemistry* **278**, 10842-10850, (2003).
228 Caughey, B., Ernst, D. & Race, R. E. Congo Red Inhibition of Scrapie Agent Replication. *J Virol* **67**, 6270-6272, (1993).
229 LeVine, H., 3rd. Thioflavine T interaction with synthetic Alzheimer's disease beta-amyloid peptides: detection of amyloid aggregation in solution. *Protein science : a publication of the Protein Society* **2**, 404-410, (1993).
230 Vassar, P. S. & Culling, C. F. Fluorescent stains, with special reference to amyloid and connective tissues. *Archives of pathology* **68**, 487-498, (1959).
231 Buell, A. K., Dobson, C. M., Knowles, T. P. & Welland, M. E. Interactions between amyloidophilic dyes and their relevance to studies of amyloid inhibitors. *Biophysical journal* **99**, 3492-3497, (2010).
232 Hudson, S. A., Ecroyd, H., Kee, T. W. & Carver, J. A. The thioflavin T fluorescence assay for amyloid fibril detection can be biased by the presence of exogenous compounds. *The FEBS journal* **276**, 5960-5972, (2009).
233 Singh, P. K., Mora, A. K. & Nath, S. Ultrafast fluorescence spectroscopy reveals a dominant weakly-emissive population of fibril bound thioflavin-T. *Chem Commun* **51**, 14042-14045, (2015).
234 Berezin, M. Y. & Achilefu, S. Fluorescence Lifetime Measurements and Biological Imaging. *Chem Rev* **110**, 2641-2684, (2010).

235 Lea, W. A. & Simeonov, A. Fluorescence polarization assays in small molecule screening. *Expert opinion on drug discovery* **6**, 17-32, (2011).
236 Perrin, F. Polarization of light of fluorescence, average life of molecules. *J Phys Radium* **7**, 390-401, (1926).
237 Zaccai, N. R., Serdyuk, I. N. & Zaccai, J. *Methods in Molecular Biophysics: Structure, Dynamics, Function for Biology and Medicine*. (Cambridge University Press, 2017).
238 Weber, G. Polarization of the Fluorescence of Macromolecules .1. Theory and Experimental Method. *Biochemical Journal* **51**, 145-155, (1952).
239 Nasir, M. S. & Jolley, M. E. Fluorescence polarization: an analytical tool for immunoassay and drug discovery. *Combinatorial chemistry & high throughput screening* **2**, 177-190, (1999).
240 GmbH, T. A. Tecan Instructions for Use for infinite M1000 No. 30036266 Rev. No. 1.6. (2011).
241 Serdyuk, I. N., Zaccai, N. R. & Zaccai, J. *Methods in Molecular Biophysics: Structure, Dynamics, Function*. (Cambridge University Press, 2007).
242 Owicki, J. C. Fluorescence polarization and anisotropy in high throughput screening: perspectives and primer. *Journal of biomolecular screening* **5**, 297-306, (2000).
243 Jameson, D. M. & Ross, J. A. Fluorescence polarization/anisotropy in diagnostics and imaging. *Chem Rev* **110**, 2685-2708, (2010).
244 Terpetschnig, E. ISS Technical Notes Fluorescence Polarization (FP).
245 Invitrogen. Technical Resource Guide Invitrogen: Fluorescence Polarization Fourth Edition. (2006).
246 Weber, G. Polarization of the fluorescence of macromolecules. II. Fluorescent conjugates of ovalbumin and bovine serum albumin. *The Biochemical journal* **51**, 155-167, (1952).
247 Weber, G. Polarization of the fluorescence of macromolecules. I. Theory and experimental method. *The Biochemical journal* **51**, 145-155, (1952).
248 Ding, Z. *et al.* Binding of inositol 1,4,5-trisphosphate (IP3) and adenophostin A to the N-terminal region of the IP3 receptor: thermodynamic analysis using fluorescence polarization with a novel IP3 receptor ligand. *Molecular pharmacology* **77**, 995-1004, (2010).
249 Li, C. *et al.* Development of a screening fluorescence polarization immunoassay for the simultaneous detection of fumonisins B(1) and B(2) in maize. *Journal of agricultural and food chemistry* **63**, 4940-4946, (2015).
250 Ozers, M. S. *et al.* Equilibrium binding of estrogen receptor with DNA using fluorescence anisotropy. *The Journal of biological chemistry* **272**, 30405-30411, (1997).
251 Leissring, M. A. *et al.* Kinetics of amyloid beta-protein degradation determined by novel fluorescence- and fluorescence polarization-based assays. *The Journal of biological chemistry* **278**, 37314-37320, (2003).
252 Ahn, H. J. *et al.* Alzheimer's disease peptide beta-amyloid interacts with fibrinogen and induces its oligomerization. *Proceedings of the National Academy of Sciences of the United States of America* **107**, 21812-21817, (2010).
253 Allsop, D. *et al.* Fluorescence anisotropy: a method for early detection of Alzheimer beta-peptide (Abeta) aggregation. *Biochemical and biophysical research communications* **285**, 58-63, (2001).
254 Ban, T., Hamada, D., Hasegawa, K., Naiki, H. & Goto, Y. Direct observation of amyloid fibril growth monitored by thioflavin T fluorescence. *The Journal of biological chemistry* **278**, 16462-16465, (2003).
255 Brusendorf, L. *Entwicklung fluoreszenzbasierter Assays zur Analyse des Beta-Amyloid-Proteins*, TU Berlin (2013).
256 GmbH, T. A. Tecan Instructions for Use for infinite M1000Pro. (2011).
257 Atarashi, R. *et al.* Simplified ultrasensitive prion detection by recombinant PrP conversion with shaking. *Nature methods* **5**, 211-212, (2008).
258 Salvadores, N., Shahnawaz, M., Scarpini, E., Tagliavini, F. & Soto, C. Detection of misfolded Abeta oligomers for sensitive biochemical diagnosis of Alzheimer's disease. *Cell reports* **7**, 261-268, (2014).
259 Tsigelny, I. F. *et al.* Mechanisms of hybrid oligomer formation in the pathogenesis of combined Alzheimer's and Parkinson's diseases. *Plos One* **3**, e3135, (2008).
260 Clinton, L. K., Blurton-Jones, M., Myczek, K., Trojanowski, J. Q. & LaFerla, F. M. Synergistic Interactions between A beta, Tau, and alpha-Synuclein: Acceleration of Neuropathology and Cognitive Decline. *Journal of Neuroscience* **30**, 7281-7289, (2010).
261 Mandal, P. K., Pettegrew, J. W., Masliah, E., Hamilton, R. L. & Mandal, R. Interaction between A beta peptide and alpha synuclein: Molecular mechanisms in overlapping pathology of Alzheimer's and Parkinson's in dementia with Lewy body disease. *Neurochem Res* **31**, 1153-1162, (2006).
262 O'Nuallain, B., Williams, A. D., Westermark, P. & Wetzel, R. Seeding specificity in amyloid growth induced by heterologous fibrils. *Journal of Biological Chemistry* **279**, 17490-17499, (2004).

263 Hu, R. D., Zhang, M. Z., Chen, H., Jiang, B. B. & Zheng, J. Cross-Seeding Interaction between beta-Amyloid and Human Islet Amyloid Polypeptide. *ACS chemical neuroscience* **6**, 1759-1768, (2015).
264 Gotz, J., Lim, Y. A. & Eckert, A. Lessons from two prevalent amyloidoses-what amylin and Abeta have in common. *Frontiers in aging neuroscience* **5**, 38, (2013).
265 Westermark, P., Andersson, A. & Westermark, G. T. Islet amyloid polypeptide, islet amyloid, and diabetes mellitus. *Physiological reviews* **91**, 795-826, (2011).
266 Seki, T. *et al.* Congo red, an amyloid-inhibiting compound, alleviates various types of cellular dysfunction triggered by mutant protein kinase cgamma that causes spinocerebellar ataxia type 14 (SCA14) by inhibiting oligomerization and aggregation. *Journal of pharmacological sciences* **114**, 206-216, (2010).
267 Zhang, J. H., Chung, T. D. & Oldenburg, K. R. A Simple Statistical Parameter for Use in Evaluation and Validation of High Throughput Screening Assays. *Journal of biomolecular screening* **4**, 67-73, (1999).
268 Toombs, J., Paterson, R. W., Schott, J. M. & Zetterberg, H. Amyloid-beta 42 adsorption following serial tube transfer. *Alzheimer's research & therapy* **6**, 5, (2014).
269 Broersen, K. *et al.* A standardized and biocompatible preparation of aggregate-free amyloid beta peptide for biophysical and biological studies of Alzheimer's disease. *Protein engineering, design & selection : PEDS* **24**, 743-750, (2011).
270 Nichols, M. R. *et al.* Amyloid-beta protofibrils differ from amyloid-beta aggregates induced in dilute hexafluoroisopropanol in stability and morphology. *The Journal of biological chemistry* **280**, 2471-2480, (2005).
271 Zagorski, M. G. *et al.* Methodological and chemical factors affecting amyloid beta peptide amyloidogenicity. *Methods in enzymology* **309**, 189-204, (1999).
272 Serpell, L. C. Alzheimer's amyloid fibrils: structure and assembly. *Biochimica et biophysica acta* **1502**, 16-30, (2000).
273 Soto, C., Saborio, G. P. & Anderes, L. Cyclic amplification of protein misfolding: application to prion-related disorders and beyond. *Trends Neurosci* **25**, 390-394, (2002).
274 Wanker, E. E. *et al.* Membrane filter assay for detection of amyloid-like polyglutamine-containing protein aggregates. *Methods in enzymology* **309**, 375-386, (1999).
275 Bieschke, J. *et al.* Small-molecule conversion of toxic oligomers to nontoxic beta-sheet-rich amyloid fibrils. *Nature chemical biology* **8**, 93-101, (2011).
276 Greene, L. A. Nerve growth factor prevents the death and stimulates the neuronal differentiation of clonal PC12 pheochromocytoma cells in serum-free medium. *The Journal of cell biology* **78**, 747-755, (1978).
277 Greene, L. A. & Tischler, A. S. Establishment of a noradrenergic clonal line of rat adrenal pheochromocytoma cells which respond to nerve growth factor. *Proceedings of the National Academy of Sciences of the United States of America* **73**, 2424-2428, (1976).
278 Liu, Y., Peterson, D. A., Kimura, H. & Schubert, D. Mechanism of cellular 3-(4,5-dimethylthiazol-2-yl)-2,5-diphenyltetrazolium bromide (MTT) reduction. *Journal of neurochemistry* **69**, 581-593, (1997).
279 Berridge, M. V. & Tan, A. S. Characterization of the cellular reduction of 3-(4,5-dimethylthiazol-2-yl)-2,5-diphenyltetrazolium bromide (MTT): subcellular localization, substrate dependence, and involvement of mitochondrial electron transport in MTT reduction. *Archives of biochemistry and biophysics* **303**, 474-482, (1993).
280 Vistica, D. T. *et al.* Tetrazolium-based assays for cellular viability: a critical examination of selected parameters affecting formazan production. *Cancer research* **51**, 2515-2520, (1991).
281 Alzforum. 5xFAD. (n.d.).
282 Oakley, H. *et al.* Intraneuronal beta-amyloid aggregates, neurodegeneration, and neuron loss in transgenic mice with five familial Alzheimer's disease mutations: potential factors in amyloid plaque formation. *The Journal of neuroscience : the official journal of the Society for Neuroscience* **26**, 10129-10140, (2006).
283 Alzforum. APPPS1. (n.d.).
284 Radde, R. *et al.* Abeta42-driven cerebral amyloidosis in transgenic mice reveals early and robust pathology. *EMBO reports* **7**, 940-946, (2006).
285 Rupp, N. J., Wegenast-Braun, B. M., Radde, R., Calhoun, M. E. & Jucker, M. Early onset amyloid lesions lead to severe neuritic abnormalities and local, but not global neuron loss in APPPS1 transgenic mice. *Neurobiology of aging* **32**, 2324 e2321-2326, (2011).
286 Serneels, L. *et al.* gamma-Secretase heterogeneity in the Aph1 subunit: relevance for Alzheimer's disease. *Science* **324**, 639-642, (2009).
287 Alzforum. APP23 (n.d.).

288 Elder, G. A., Gama Sosa, M. A. & De Gasperi, R. Transgenic mouse models of Alzheimer's disease. *The Mount Sinai journal of medicine, New York* **77**, 69-81, (2010).
289 Snellman, A. *et al.* Longitudinal amyloid imaging in mouse brain with 11C-PIB: comparison of APP23, Tg2576, and APPswe-PS1dE9 mouse models of Alzheimer disease. *Journal of nuclear medicine : official publication, Society of Nuclear Medicine* **54**, 1434-1441, (2013).
290 Stalder, M. *et al.* Association of microglia with amyloid plaques in brains of APP23 transgenic mice. *The American journal of pathology* **154**, 1673-1684, (1999).
291 Sturchler-Pierrat, C. *et al.* Two amyloid precursor protein transgenic mouse models with Alzheimer disease-like pathology. *Proceedings of the National Academy of Sciences of the United States of America* **94**, 13287-13292, (1997).
292 Calhoun, M. E. *et al.* Neuron loss in APP transgenic mice. *Nature* **395**, 755-756, (1998).
293 Kelly, P. H. *et al.* Progressive age-related impairment of cognitive behavior in APP23 transgenic mice. *Neurobiology of aging* **24**, 365-378, (2003).
294 Van Dam, D. *et al.* Age-dependent cognitive decline in the APP23 model precedes amyloid deposition. *Eur J Neurosci* **17**, 388-396, (2003).
295 Mok, Y. F. & Howlett, G. J. Sedimentation velocity analysis of amyloid oligomers and fibrils. *Methods in enzymology* **413**, 199-217, (2006).
296 Langer, F. *et al.* Soluble Abeta seeds are potent inducers of cerebral beta-amyloid deposition. *The Journal of neuroscience : the official journal of the Society for Neuroscience* **31**, 14488-14495, (2011).
297 Lee, S. J. *et al.* A detergent-insoluble membrane compartment contains A beta in vivo. *Nature medicine* **4**, 730-734, (1998).
298 Cook, D. G. *et al.* Alzheimer's A beta(1-42) is generated in the endoplasmic reticulum/intermediate compartment of NT2N cells. *Nature medicine* **3**, 1021-1023, (1997).
299 Hartmann, T. *et al.* Distinct sites of intracellular production for Alzheimer's disease A beta 40/42 amyloid peptides. *Nature medicine* **3**, 1016-1020, (1997).
300 WildBode, C. *et al.* Intracellular generation and accumulation of amyloid beta-peptide terminating at amino acid 42. *Journal of Biological Chemistry* **272**, 16085-16088, (1997).
301 Xu, H. X. *et al.* Generation of Alzheimer beta-amyloid protein in the trans-Golgi network in the apparent absence of vesicle formation. *Proceedings of the National Academy of Sciences of the United States of America* **94**, 3748-3752, (1997).
302 Sivanathan, V. & Hochschild, A. Generating extracellular amyloid aggregates using E. coli cells. *Genes & development* **26**, 2659-2667, (2012).
303 OpenWetWare. *Critical micelle concentration (CMC)*, <https://openwetware.org/wiki/Critical_micelle_concentration_(CMC)> (2014).
304 Choe, W., Durgannavar, T. A. & Chung, S. J. Fc-Binding Ligands of Immunoglobulin G: An Overview of High Affinity Proteins and Peptides. *Materials (Basel)* **9**, (2016).
305 Devi, L., Prabhu, B. M., Galati, D. F., Avadhani, N. G. & Anandatheerthavarada, H. K. Accumulation of amyloid precursor protein in the mitochondrial import channels of human Alzheimer's disease brain is associated with mitochondrial dysfunction. *The Journal of neuroscience : the official journal of the Society for Neuroscience* **26**, 9057-9068, (2006).
306 Anandatheerthavarada, H. K., Biswas, G., Robin, M. A. & Avadhani, N. G. Mitochondrial targeting and a novel transmembrane arrest of Alzheimer's amyloid precursor protein impairs mitochondrial function in neuronal cells. *The Journal of cell biology* **161**, 41-54, (2003).
307 Eisele, Y. S. *et al.* Induction of cerebral beta-amyloidosis: intracerebral versus systemic Abeta inoculation. *Proceedings of the National Academy of Sciences of the United States of America* **106**, 12926-12931, (2009).
308 Khan, J. M. *et al.* SDS Can Be Utilized as an Amyloid Inducer: A Case Study on Diverse Proteins. *Plos One* **7**, (2012).
309 Watt, A. D. *et al.* Oligomers, fact or artefact? SDS-PAGE induces dimerization of beta-amyloid in human brain samples. *Acta neuropathologica* **125**, 549-564, (2013).
310 Braak, H. & Braak, E. Staging of Alzheimer's disease-related neurofibrillary changes. *Neurobiology of aging* **16**, 271-278; discussion 278-284, (1995).
311 Klein, W. L., Krafft, G. A. & Finch, C. E. Targeting small Abeta oligomers: the solution to an Alzheimer's disease conundrum? *Trends Neurosci* **24**, 219-224, (2001).
312 Hardy, J. & Selkoe, D. J. The amyloid hypothesis of Alzheimer's disease: progress and problems on the road to therapeutics. *Science* **297**, 353-356, (2002).
313 Selkoe, D. J. Deciphering the genesis and fate of amyloid beta-protein yields novel therapies for Alzheimer disease. *The Journal of clinical investigation* **110**, 1375-1381, (2002).

314 Gelfanova, V. *et al.* Quantitative analysis of amyloid-beta peptides in cerebrospinal fluid using immunoprecipitation and MALDI-Tof mass spectrometry. *Briefings in functional genomics & proteomics* **6**, 149-158, (2007).
315 Portelius, E. *et al.* Distinct cerebrospinal fluid amyloid beta peptide signatures in sporadic and PSEN1 A431E-associated familial Alzheimer's disease. *Molecular neurodegeneration* **5**, 2, (2010).
316 Garcia-Ayllon, M. S. *et al.* CSF Presenilin-1 complexes are increased in Alzheimer's disease. *Acta neuropathologica communications* **1**, 46, (2013).
317 Sako, K. *et al.* Emi2 mediates meiotic MII arrest by competitively inhibiting the binding of Ube2S to the APC/C. *Nature communications* **5**, 3667, (2014).
318 ACSF (Artificial cerebrospinal fluid). *Cold Spring Harbor Protocols* **2007**, pdb.rec10804, (2007).
319 Toombs, J. *et al.* The impact of Tween 20 on repeatability of amyloid beta and tau measurements in cerebrospinal fluid. *Clinical chemistry and laboratory medicine* **53**, e329-332, (2015).
320 Riddoch, D. & Thompson, R. A. Immunoglobulin levels in the cerebrospinal fluid. *British medical journal* **1**, 396-399, (1970).
321 Wisniewski, T., Castano, E., Ghiso, J. & Frangione, B. Cerebrospinal fluid inhibits Alzheimer beta-amyloid fibril formation in vitro. *Annals of neurology* **34**, 631-633, (1993).
322 Reinke, A. A. & Gestwicki, J. E. Structure-activity relationships of amyloid beta-aggregation inhibitors based on curcumin: influence of linker length and flexibility. *Chem Biol Drug Des* **70**, 206-215, (2007).
323 Young, L. M. *et al.* Screening and classifying small-molecule inhibitors of amyloid formation using ion mobility spectrometry-mass spectrometry. *Nature chemistry* **7**, 73-81, (2015).
324 Feng, B. Y. *et al.* Small-molecule aggregates inhibit amyloid polymerization. *Nature chemical biology* **4**, 197-199, (2008).
325 Jiang, L. *et al.* Structure-based discovery of fiber-binding compounds that reduce the cytotoxicity of amyloid beta. *eLife* **2**, e00857, (2013).
326 Masters, C. L. *et al.* Amyloid plaque core protein in Alzheimer disease and Down syndrome. *Proceedings of the National Academy of Sciences of the United States of America* **82**, 4245-4249, (1985).
327 Hardy, J. Framing beta-amyloid. *Nature genetics* **1**, 233-234, (1992).
328 Luk, K. C., Hyde, E. G., Trojanowski, J. Q. & Lee, V. M. Sensitive fluorescence polarization technique for rapid screening of alpha-synuclein oligomerization/fibrillization inhibitors. *Biochemistry* **46**, 12522-12529, (2007).
329 Krafft, G. A., Pray, T. & Goure, W. F. Methods of modifying amyloid ß oligomers using non-peptidic compounds. Canada patent (2009).
330 Sharma, S. K. & Rank, K. B. Assays for assessing A Beta-Tau aggregation USA patent (2002).
331 Pray, T. R. Method for detecting oligomerization of soluble amyloid beta oligomers USA patent (2008).
332 Ryan, T. M. *et al.* Ammonium hydroxide treatment of Abeta produces an aggregate free solution suitable for biophysical and cell culture characterization. *PeerJ* **1**, e73, (2013).
333 Shen, C. L. & Murphy, R. M. Solvent effects on self-assembly of beta-amyloid peptide. *Biophysical journal* **69**, 640-651, (1995).
334 Shammas, S. L. *et al.* A mechanistic model of tau amyloid aggregation based on direct observation of oligomers. *Nature communications* **6**, 7025, (2015).
335 Holloway, P. W. A simple procedure for removal of Triton X-100 from protein samples. *Analytical biochemistry* **53**, 304-308, (1973).
336 Shechter, I. & Bloch, K. Solubilization and purification of trans-farnesyl pyrophosphate-squalene synthetase. *The Journal of biological chemistry* **246**, 7690-7696, (1971).
337 Momoi, T. The presence of lipophilic glycoprotein interacting with insulin. *Biochemical and biophysical research communications* **87**, 541-549, (1979).
338 Ye, L. *et al.* Abeta seeding potency peaks in the early stages of cerebral beta-amyloidosis. *EMBO reports* **18**, 1536-1544, (2017).
339 Selkoe, D. J. Soluble oligomers of the amyloid beta-protein impair synaptic plasticity and behavior. *Behavioural brain research* **192**, 106-113, (2008).
340 Schmidt, M. *et al.* Comparison of Alzheimer Abeta(1-40) and Abeta(1-42) amyloid fibrils reveals similar protofilament structures. *Proceedings of the National Academy of Sciences of the United States of America* **106**, 19813-19818, (2009).
341 Paravastu, A. K., Leapman, R. D., Yau, W. M. & Tycko, R. Molecular structural basis for polymorphism in Alzheimer's beta-amyloid fibrils. *Proceedings of the National Academy of Sciences of the United States of America* **105**, 18349-18354, (2008).
342 Petkova, A. T. *et al.* Self-propagating, molecular-level polymorphism in Alzheimer's beta-amyloid fibrils. *Science* **307**, 262-265, (2005).

343 Xiao, Y. *et al.* Abeta(1-42) fibril structure illuminates self-recognition and replication of amyloid in Alzheimer's disease. *Nature structural & molecular biology* **22**, 499-505, (2015).
344 Lu, J. X. *et al.* Molecular structure of beta-amyloid fibrils in Alzheimer's disease brain tissue. *Cell* **154**, 1257-1268, (2013).
345 Ownby, R. L., Crocco, E., Acevedo, A., John, V. & Loewenstein, D. Depression and risk for Alzheimer disease: systematic review, meta-analysis, and metaregression analysis. *Archives of general psychiatry* **63**, 530-538, (2006).
346 Eisele, Y. S. *et al.* Targeting protein aggregation for the treatment of degenerative diseases. *Nature reviews. Drug discovery* **14**, 759-780, (2015).
347 Arosio, P., Vendruscolo, M., Dobson, C. M. & Knowles, T. P. Chemical kinetics for drug discovery to combat protein aggregation diseases. *Trends Pharmacol Sci* **35**, 127-135, (2014).
348 Habchi, J. *et al.* Systematic development of small molecules to inhibit specific microscopic steps of Abeta42 aggregation in Alzheimer's disease. *Proceedings of the National Academy of Sciences of the United States of America* **114**, E200-E208, (2017).
349 Meier, J. J. *et al.* Inhibition of human IAPP fibril formation does not prevent beta-cell death: evidence for distinct actions of oligomers and fibrils of human IAPP. *American journal of physiology. Endocrinology and metabolism* **291**, E1317-1324, (2006).
350 Aitken, J. F., Loomes, K. M., Konarkowska, B. & Cooper, G. J. Suppression by polycyclic compounds of the conversion of human amylin into insoluble amyloid. *The Biochemical journal* **374**, 779-784, (2003).
351 McKoy, A. F., Chen, J., Schupbach, T. & Hecht, M. H. Structure-activity relationships for a series of compounds that inhibit aggregation of the Alzheimer's peptide, Abeta42. *Chem Biol Drug Des* **84**, 505-512, (2014).
352 Doig, A. J. & Derreumaux, P. Inhibition of protein aggregation and amyloid formation by small molecules. *Current opinion in structural biology* **30**, 50-56, (2015).
353 Masuda, M. *et al.* Small molecule inhibitors of alpha-synuclein filament assembly. *Biochemistry* **45**, 6085-6094, (2006).
354 Meanwell, N. A. Synopsis of Some Recent Tactical Application of Bioisosteres in Drug Design. *Journal of medicinal chemistry* **54**, 2529-2591, (2011).
355 Lima, L. M. A. & Barreiro, E. J. Bioisosterism: A useful strategy for molecular modification and drug design. *Curr Med Chem* **12**, 23-49, (2005).
356 Kroth, H. *et al.* Discovery and Structure Activity Relationship of Small Molecule Inhibitors of Toxic beta-Amyloid-42 Fibril Formation. *Journal of Biological Chemistry* **287**, 34786-34800, (2012).
357 Nakagami, Y. *et al.* A novel beta-sheet breaker, RS-0406, reverses amyloid beta-induced cytotoxicity and impairment of long-term potentiation in vitro. *British journal of pharmacology* **137**, 676-682, (2002).
358 O'Hare, E. *et al.* RS-0406 Arrests Amyloid-beta Oligomer-Induced Behavioural Deterioration In Vivo. *Behavioural brain research* **210**, 32-37, (2010).
359 Thooft, A. M., Cassaidy, K. & VanVeller, B. A Small Push-Pull Fluorophore for Turn-on Fluorescence. *The Journal of organic chemistry* **82**, 8842-8847, (2017).
360 Goldey, G. J. *et al.* Removable cranial windows for long-term imaging in awake mice. *Nature protocols* **9**, 2515-2538, (2014).
361 Robbins, E. M. *et al.* Kinetics of cerebral amyloid angiopathy progression in a transgenic mouse model of Alzheimer disease. *The Journal of neuroscience : the official journal of the Society for Neuroscience* **26**, 365-371, (2006).
362 Meisl, G. *et al.* Molecular mechanisms of protein aggregation from global fitting of kinetic models. *Nature protocols* **11**, 252-272, (2016).
363 Pierce, M. M., Raman, C. S. & Nall, B. T. Isothermal titration calorimetry of protein-protein interactions. *Methods-a Companion to Methods in Enzymology* **19**, 213-221, (1999).
364 Reddy, U. R. *et al.* Characterization of two neuroblastoma cell lines expressing recombinant nerve growth factor receptors. *Journal of neurochemistry* **56**, 67-74, (1991).
365 Gao, M. *et al.* Modulation of human IAPP fibrillation: cosolutes, crowders and chaperones. *Physical chemistry chemical physics : PCCP* **17**, 8338-8348, (2015).
366 Smith, P. K. *et al.* Measurement of protein using bicinchoninic acid. *Analytical biochemistry* **150**, 76-85, (1985).
367 Wittig, I. & Schagger, H. Native electrophoretic techniques to identify protein-protein interactions. *Proteomics* **9**, 5214-5223, (2009).
368 Westermark, G. T., Johnson, K. H. & Westermark, P. Staining methods for identification of amyloid in tissue. *Methods in enzymology* **309**, 3-25, (1999).

369 Naiki, H., Higuchi, K., Hosokawa, M. & Takeda, T. Fluorometric determination of amyloid fibrils in vitro using the fluorescent dye, thioflavin T1. *Analytical biochemistry* **177**, 244-249, (1989).
370 Williams, D. B., Carter, C. Barry (Springer, 2009).

11.

Contributions

11. Contributions

- Basic establishment of the Aβ42-FP assay was performed by Lydia Brusendorf during her diploma thesis (TU Berlin, 2013)
- Fig. 20: Data of time-resolved FP analysis were partly obtained from Nicole Groenke within her master thesis (Universität Potsdam, 2015)
- Fig. 25: Data to assess homogeneity of the fluorescence polarization values within one 384-well plate were taken from Nicole Groenke within her master thesis (Universität Potsdam, 2015)
- Fig. 47: Filter analysis were performed by Nancy Neuendorf
- Fig. 64: Confocal microscopy images were acquiered with the help of Christopher Secker
- Synthesis of K114 and compounds 1-9 was carried out by Chiroblock GmbH

12.

Acknowledgments

12. Acknowledgments

I would like to thank **Erich** for his guidance, support and help within the last years. I really appreciated his trust to let me pursue my work very independently and with great freedom. Despite his packed schedule he always found the time to discuss with me my project and contribute with valuable ideas, critical appraisal and consistent motivation and vision. I am very grateful for everything I have learned.

I would also like to thank **Prof. Stephan Sigrist**, who kindly agreed to supervise my thesis.

I would like to thank our collaboration partners within this project, **PD Dr. Oliver Peters** and **Dr. Carola Schipke** as well as **Prof. Josef Priller** from the Klinik für Psychiatrie und Psychotherapie, Charité. Furthermore, I would like to thank **Prof. Mathias Jucker** from the DZNE. Thank you all for the provision of valuable biosamples and the scientific discussion.

Furthermore, I thank **Dr. Bettina Purfürst** from the EM core facility for a great collaboration within the last years and assistance with electron microscopy. Thank you, **Aline**, for providing primary neurons to exciting past projects.

Huge thanks goes to all my colleagues, from whom everyone contributed enormously to provide the most pleasant working atmosphere.

Thank you, **Annett**, for guidance, assistance and a sympathetic ear throughout my whole project. **Thomas**, thank you for all your help, crucial discussions and answering one billion of chemical questions. And for very good coffee!

Nancy and **Martina**, without you nothing would run that smoothly in the lab. Thank you both so much for all your help within my project, for assisting with experiments or purchasing orders. Thank you, **Gerlinde,** for all your help with the AFM and you, **Christian**, for fixing any IT issue. **Frau Pisch** and **Sigrid**, thank you both for keeping my back free from any organizational and administrative issues, allowing me to completely focus on my project.

I would also like to thank you **Philipp**, for all your valuable ideas, discussions and assistance and always believing in my project, I really appreciated that. Thank you, **Chris,** for your help with the confocal microscope.

Thank you **Lydia**, first of all for your preliminary work on the assay establishment during your diploma thesis. But even more for loads of fun times in the lab, in the office and in our free time. The food supply was also always top-notch!

Anne, **Simona**, **Annika, Konrad, Marta, Sabrina** and **'Queen Bee' Stephie,** the whole **AG Wanker** and **Prigione**, thank you all for a great time!

Sometimes working in science can give you a hard time. That is why my amazing friends were of no less importance. **Ani** and **Tamara**, **Nora**, **Simon** and **Yoko**, **Stefan and Stephi**: I am so lucky to have you.

Last but not least, all my gratitude goes to my wonderful **family**. Ich danke euch von Herzen für eure unendliche Unterstützung. Danke euch für all die (un)gewollten Ratschläge, die ich nach und nach mehr zu schätzen gewusst habe. Danke für eure Motivation, eure ermutigenden Worte und euer grenzenloses Vertrauen in mich, wann immer ich gezweifelt habe.

Danke für alles.